



HAL
open science

Electrochemical pesticide detection and film deposition at liquid-liquid interface

Guofeng Lu

► **To cite this version:**

Guofeng Lu. Electrochemical pesticide detection and film deposition at liquid-liquid interface. Analytical chemistry. Université de Lorraine, 2020. English. NNT : 2020LORR0231 . tel-03264568

HAL Id: tel-03264568

<https://hal.univ-lorraine.fr/tel-03264568>

Submitted on 18 Jun 2021

HAL is a multi-disciplinary open access archive for the deposit and dissemination of scientific research documents, whether they are published or not. The documents may come from teaching and research institutions in France or abroad, or from public or private research centers.

L'archive ouverte pluridisciplinaire **HAL**, est destinée au dépôt et à la diffusion de documents scientifiques de niveau recherche, publiés ou non, émanant des établissements d'enseignement et de recherche français ou étrangers, des laboratoires publics ou privés.



AVERTISSEMENT

Ce document est le fruit d'un long travail approuvé par le jury de soutenance et mis à disposition de l'ensemble de la communauté universitaire élargie.

Il est soumis à la propriété intellectuelle de l'auteur. Ceci implique une obligation de citation et de référencement lors de l'utilisation de ce document.

D'autre part, toute contrefaçon, plagiat, reproduction illicite encourt une poursuite pénale.

Contact : ddoc-theses-contact@univ-lorraine.fr

LIENS

Code de la Propriété Intellectuelle. articles L 122. 4

Code de la Propriété Intellectuelle. articles L 335.2- L 335.10

http://www.cfcopies.com/V2/leg/leg_droi.php

<http://www.culture.gouv.fr/culture/infos-pratiques/droits/protection.htm>



UNIVERSITÉ
DE LORRAINE



Détection électrochimique de pesticide et dépôt de film

à l'interface liquide-liquide

Sujet de thèse :

Présenté par

Guofeng LU

Pour l'obtention de titre de Docteur

Spécialité : Chimie

Soutenance publique prévue le **15 Décembre 2020** devant le jury:

Directeur:

Dr. Gregoire Herzog — Charge de recherche (LCPME, Université de Lorraine)

Invité:

Dr. Liang Liu — Charge de recherche (LCPME, Université de Lorraine)

Rapporteurs:

Dr. Martin Jönsson-Niedziolka — Professeur (IPC, Polish Academy of Science)

Dr. Corinne Lagrost — Directrice de Recherche (ISCR - UMR CNRS 6226)

Examineurs:

Dr. Talia Jane Stockmann — Professeur (Memorial University of Newfoundland)

Dr. Andréea Pasc — Professeur (Institut Jean Lamour, Université de Lorraine)

Dr. Sophie Griveau — Maître de Conférence (Chimie ParisTech, PSL Université)

Ecole doctorale:

C2MP (Chimie - Mécanique - Matériaux- Physique)



UNIVERSITÉ
DE LORRAINE



A thesis:

**Electrochemical pesticide detection and film deposition
at liquid-liquid interface**

by

Guofeng LU

For obtaining a **Doctoral title**

Speciality : Chemistry

Public defense scheduled **on 15 December 2020** in front of the jury:

Supervisor:

Dr. Grégoire Herzog — Research fellow (LCPME, University of Lorraine)

Invite:

Dr. Liang Liu — Research fellow (LCPME, University of Lorraine)

Reviewers:

Dr. Martin Jönsson-Niedziolka — Professor (IPC, Polish Academy of Science)

Dr. Corinne Lagrost — Research Director (Institut des Sciences Chimiques de Rennes)

Examiners:

Dr. T. Jane Stockmann — Professor (Memorial University of Newfoundland)

Dr. Andréea Pasc — Professor (Institut Jean Lamour, University of Lorraine)

Dr. Sophie Griveau — Lecturer (Chimie ParisTech, PSL University)

Doctoral School:

C2MP (Chemistry - Mechanics - Materials - Physics)

Electrochemical pesticide detection and film deposition at liquid-liquid interface

by

Guofeng Lu

A dissertation submitted in partial satisfaction of the
requirements for the degree of
Doctor of C2MP(Chemistry-Mechanics-Materials-Physics)

in

Chemistry

in the

Graduate Division
of the
University of Lorraine, Nancy

Committee in charge:

Dr. Grégoire Herzog, Chair
Dr. Liang Liu, Co-chair
Dr. Martin Jönsson-Niedziolka
Dr. Corinne Lagrost
Dr. Talia Jane Stockmann
Dr. Andréea Pasc
Dr. Sophie Griveau

Winter 2020

The dissertation of Guofeng Lu, titled Electrochemical pesticide detection and film deposition at liquid-liquid interface, is approved:

Chair Date

Co-chair Date

Date

Date

University of Lorraine, Nancy

**Electrochemical pesticide detection and film deposition at liquid-liquid
interface**

Copyright 2020

by

Guofeng Lu

Abstract

Electrochemical pesticide detection and film deposition at liquid-liquid interface

by

Guofeng Lu

Doctor of C2MP (Chemistry-Mechanics-Materials-Physics) in Chemistry

University of Lorraine, Nancy

Dr. Grégoire Herzog, Chair

Dr. Liang Liu, Co-chair

Modern electrochemistry at the liquid-liquid interface, also termed the interface between two immiscible electrolyte solutions (ITIES), has been investigated for over a century due to its special interface properties. It provides a unique platform to allow the non-redox electrochemical detection of ions ranging from protons to macromolecules across the soft molecular interface that is intrinsically defect-free and self-healing. Additionally, the ITIES can act as a scaffold to electrodeposit nanometer-sized objects or charged molecules in arranged film. The electro-generated film at liquid-liquid interfaces has numerous advantages such as control the ion transfer, improve the sensitivity and the selectivity. Therefore, the present thesis is devoted to pesticide detection and electrodeposited films at the ITIES and further investigation of model ion transfer behaviour and electrochemical properties. The thesis consists of three large parts: first is mainly to achieve pesticide detection, second is devoted to silica electrodeposition at the micro liquid-liquid interface, and third is to develop chitosan film generation at the interface. Research at ITIES is ongoing into their use as a unique platform for sensors and membranes application.

In the first part, we made an effort to detect pesticides at micro-ITIES due to its cost-effectiveness. Thus, Ametryn, Imidacloprid and Metam sodium were selected as model ions that belong to triazine, neonicotinoid, and organosulfur family, respectively. These drugs were chosen as they are commonly used and have been placed on the European

watch list of emerging pollutants. Their over-usage around the world created a big issue for soil or river security and bring health problems to humans. Thus, it is very critical to develop an in-situ sensor. Thanks to the miniaturization of ITIES, the micro-pore capillary can be as a support to construct a liquid-liquid interface. Combining with the stripping voltammetry at ITIES, this kind sensor does not require the analyte to be electrochemically oxidized or reduced, or adsorbed on the solid electrode surface, but instead requires the analyte to be ionic so that it transfers from one phase to another upon applying a potential. Thus, the accumulation of analytes from a solution close to neutral pH into an organic phase through an automatic transfer at open-circuit potential is possible and increasing the detection signal. This strategy is successful for ametryn but is failed for the detection of Imidacloprid and Metam sodium.

In the second part, we developed silica deposition at Micro-ITIES. The objective of the silica membrane at ITIES is to focus on improving the selectivity for ion transfer. Electrochemical experiments at the liquid-liquid interface revealed that the TMA^+ transfer is blocked by the presence of silica film. However, electrodeposit silica at Micro-ITIES is not accurately reproduced due to the geometry limitation. Furthermore, the ex-situ measures are hardly achieved.

In the third part, we realized chitosan electrodeposition at ITIES. Chitosan films act as membrane for ion transfer and presented positive charge, which could provide the adsorption effect for negative ion. Unlike silica film, electrogenerated chitosan film is free-stranding and has excellent mechanic properties, which can be work as subtract for co-deposition with other materials. To improve the structure of chitosan film, the cross-linker Terephthalaldehyde (TPA) is introduced into the organic phase. We demonstrated a protocol for controlling the interfacial reaction with the variable concentration of cross-linker in the organic phase, and the precursor is limited in the aqueous phase. Therefore, we obtained different types of chitosan films.

Résumé

L'électrochimie moderne à l'interface liquide-liquide, également appelée interface entre deux solutions électrolytiques non miscibles (ITIES), est étudiée depuis plus d'un siècle en raison de ses propriétés d'interface particulières. Elle offre une plateforme unique permettant la détection électrochimique non redox d'ions allant des protons aux macromolécules à travers l'interface moléculaire molle qui est intrinsèquement sans défaut et autoguérissant. En outre, l'ITIES peut servir de support pour le dépôt électrolytique d'objets de la taille du nanomètre ou de molécules chargées dans un film arrangé. Le film électro-généré aux interfaces liquide-liquide présente de nombreux avantages tels que le contrôle du transfert d'ions, l'amélioration de la sensibilité et de la sélectivité. Par conséquent, la présente thèse est destinée à la détection des pesticides et aux films électro-déposés à l'ITIES et à l'étude plus approfondie du comportement modèle du transfert d'ions et des propriétés électrochimiques. La thèse se compose de trois grandes parties : la première vise principalement à réaliser la détection des pesticides, la deuxième est consacrée à l'électrodéposition de silice à l'interface micro liquide-liquide, et la troisième est de développer la génération de films de chitosane à l'interface. Les recherches à l'ITIES se poursuivent en vue de leur utilisation comme plate-forme unique pour l'application de capteurs et de membranes.

Dans la première partie, nous avons fait un effort pour détecter les pesticides dans les micro-ITIES en raison de son rapport coût-efficacité. Ainsi, l'Ametryn, l'Imidacloprid et le Metam sodium ont été sélectionnés comme ions modèles qui appartiennent respectivement à la famille des triazines, des néonicotinoïdes et des organosulfures. Ces pesticides ont été choisis car ils sont couramment utilisés et ont été placés sur la liste de surveillance européenne des polluants émergents. Leur surconsommation dans le monde entier a créé un grand problème pour la sécurité des sols ou des rivières et entraîne des problèmes de santé pour les humains. Il est donc très important de développer un capteur sur place. Grâce à la miniaturisation des ITIES, le capillaire à micropores peut servir de support pour construire une interface liquide-liquide. Combiné à la voltampérométrie, ce type de capteur ne nécessite pas que l'analyte soit oxydé ou réduit électrochimiquement, ou adsorbé sur la surface de l'électrode solide, mais exige au contraire que l'analyte soit

ionique afin qu'il passe d'une phase à l'autre lors de l'application d'un potentiel. Ainsi, l'accumulation des analytes d'une solution proche du pH neutre dans une phase organique par un transfert automatique à un potentiel en circuit ouvert est possible et augmente le signal de détection. Cette stratégie a réussi pour l'amétryne mais a échoué pour la détection de l'imidaclopride et du métam-sodium.

Dans la deuxième partie, nous avons développé le dépôt de silice à Micro-ITIES. L'objectif de la membrane de silice à l'ITIES est de se concentrer sur l'amélioration de la sélectivité pour le transfert d'ions. Des expériences électrochimiques à l'interface liquide-liquide ont révélé que le transfert de TMA^+ est bloqué par la présence d'un film de silice. Cependant, la silice déposée par électrolyse à Micro-ITIES n'est pas reproduite avec précision en raison de la limitation de la géométrie. En outre, les mesures ex-situ sont à peine réalisées.

Dans la troisième partie, nous avons réalisé l'électrodéposition du chitosane à ITIES. Les films de chitosane agissent comme une membrane pour le transfert d'ions et présentent une charge positive, qui pourrait fournir l'effet d'adsorption pour l'ion négatif. Contrairement au film de silice, le film de chitosane électrogénéré est flexible et possède de bonnes propriétés mécaniques, qui peuvent être travaillées comme soustraction pour la co-déposition avec d'autres matériaux. Pour améliorer la structure du film de chitosane, le réticulant téréphtalaldéhyde (TPA) est introduit dans la phase organique. Nous avons démontré un protocole pour contrôler la réaction interfaciale avec la concentration variable de réticulant dans la phase organique, et le précurseur est limité dans la phase aqueuse. Nous avons donc obtenu différents types de films de chitosane.

To my beloved parents Ronquan LU and Yinjiao Guan. You raised me up and gave me unconditional love and supports to pursue my dream.

Contents

List of Figures	v
List of Tables	ix
List of General Abbreviations	x
Abbreviations for Technically Important Chemicals	xii
1 Résumé long de la thèse en français	1
2 Bibliographical introduction	8
2.1 Aspects of Liquid-Liquid Interface	9
2.2 Basis of Liquid-Liquid Interface	9
2.3 Electrochemistry at Liquid-Liquid Interface	12
2.3.1 A brief history	12
2.3.2 The structure of the liquid/liquid interface	13
2.3.3 Simple ion transfer reaction	15
2.3.4 Assisted ion transfer reaction	19
2.3.5 Electron transfer reaction	23
2.3.6 Ionic distribution diagrams	26
2.3.7 Nonpolarized ITIES	28
2.3.8 Polarized ITIES	30
2.4 Miniaturization of the ITIES	32
2.4.1 Interface modifications	36
2.4.1.1 Top-down method	36
2.4.1.2 Bottom-up method	40
2.4.2 Methodologies for ITIES	43
2.4.2.1 Electroanalytical methods	44
2.4.2.2 Experimental system	44
2.4.3 ITIES Applications	47
2.4.3.1 Pharmacokinetics	47
2.4.3.2 Amperometric sensors	48

3	Experimental and Instrumentation	51
3.1	Introduction	52
3.2	Chemicals	52
3.3	Electrochemical set-ups	53
3.3.1	Four-electrode system for macro-ITIES	53
3.3.2	Three-electrode system for micro-ITIES	55
3.4	Protocols	56
3.4.1	Preparation of BTPPA ⁺ TPBCl ⁻ as organic supporting electrolyte	56
3.4.2	Preparation of CTA ⁺ TPBCl ⁻ as organic supporting electrolyte	57
3.4.3	Preparation of counter electrode	58
3.4.4	Preparation of single pore micro-ITIES capillary	59
3.5	Instrumentation	61
3.6	Experimental section	62
3.6.1	Experimental section of pesticide detection	62
3.6.2	Experimental section of silica deposition	64
3.6.3	Experimental section of chitosan deposition	66
4	Pesticides detection	69
4.1	Introduction	70
4.1.1	Imidacloprid	70
4.1.2	Metam sodium	73
4.1.3	Ametryn	74
4.2	Results and discussion	75
4.2.1	Ametryn	75
4.2.2	Imidacloprid	93
4.2.3	Metam sodium	94
4.3	Conclusions	97
5	Silica electrodeposition study	99
5.1	Introduction	100
5.2	Results and discussion	102
5.2.1	Macro scale electrogeneration of silica film	102
5.2.2	Micro scale electrogeneration of silica film	108
5.3	Conclusions	116
6	Chitosan electrodeposition at ITIES	118
6.1	Introduction	119
6.1.1	The structure and properties of chitosan	119
6.1.2	Cross-linking modification	122
6.1.3	Electrodeposition for chitosan film	123
6.1.4	Chitosan study at liquid-liquid interface	125
6.2	Results and discussion	126

6.2.1	Macro-scale experiments	126
6.2.2	Ex-situ characterization of dried chitosan films	137
6.2.3	Micro-scale experiments	144
6.3	Conclusions	148
7	Conclusions and Perspectives	149
	Bibliography	154

List of Figures

2.1	Evolution of views on the structure of ITIES	14
2.2	Standard ion transfer potentials for different species	18
2.3	Schematic plot of an ion across the interface	19
2.4	Thermodynamic constants for assisted-ion-transfer reactions	21
2.5	The four mechanisms of possible assisted ion	21
2.6	Scheme of the shuttling mechanism of IT	22
2.7	Schematic plot of electron transfer	24
2.8	Redox potential in water and 1,2 DCE	25
2.9	Ionic distribution diagram	27
2.10	Blank ITIES cyclic voltammogram	31
2.11	Ion transfer at polarized ITIES	32
2.12	Schematic representation of the different simulated geometries	34
2.13	Schematic representation of voltammetric experiments	35
2.14	Scanning electron micrographs	37
2.15	Scheme of the laser entry and exit in the glass substrate	38
2.16	Fabrication process flowchart for the preparation of nanopore arrays in Si ₃ N ₄ membranes	39
2.17	formation of surfactant-templated silica	41
2.18	The surface of different membranes for ITIES	43
2.19	Macro-ITIES and Micro-ITIES set up	46
2.20	Nano-ITIES set up	47
2.21	pH-lipoplicity profile for different drugs on ITIES	48
3.1	Four-electrode electrochemical cell	54
3.2	Four-electrode electrochemical cell	55
3.3	Components used for the counter electrode assembly	58
3.4	Platinum mesh based counter electrode	59
3.5	Glass capillary with melted gold wire	60
3.6	Borosilicate glass capillary with fixed diameter of gold wire	61
3.7	Experimental capture for silica deposition	65

4.1	Nine popular neonicotinoid insecticides	72
4.2	Major breakdown pathways of metam sodium	74
4.3	Calibration for the half-wave potential ametryn with TBA ⁺ at different pH mixed solution and Cyclic voltammograms obtained for variable pH value of aqueous solution within 70 μ M AME	77
4.4	Ionic partition diagrams for AME transfer	78
4.5	The distribution of each compound of AME with different pH	80
4.6	The zones of AME ion transfer with its proposed mechanism	81
4.7	Cyclic voltammograms obtained for mix solution of 50 μ M AME and 50 μ M TBA ⁺ at different scan rate	82
4.8	Cyclic voltammograms obtained using smaller capillary with diameter = 25 μ m.	83
4.9	Cyclic voltammograms obtained for AME with variable scan rate	84
4.10	Cyclic voltammograms comparison with two kinds measurement for AME.	86
4.11	Calibration point of employing preconcentration and its peak current cyclic response	87
4.12	Cyclic evolution of the experimental peak currents for two-step measurement	88
4.13	Octanoic acid in organic capillary for AME detection	89
4.14	Cyclic voltammograms of 8 μ M AME in a 10 mM LiCl aqueous solution containing phosphate buffer	90
4.15	Background subtracted AC voltammograms for increasing concentrations of AME and Calibration curve for AME obtained from the AC voltammograms	91
4.16	AC voltammograms for increasing spiked concentrations of AME in real river samples	92
4.17	Imidacloprid detection at single Micro-ITIES	94
4.18	Metam sodium detection using 5 mM BTPPA ⁺ TPBCl ⁻ and 10 mM BTPPA ⁺ TPBCl ⁻ at single Micro-ITIES	95
4.19	Decay of Cl ⁻ transfer potential with increasing the concentration of MET and the stable potential window	96
4.20	Methylamine detection using 5 mM BTPPA ⁺ TPBCl ⁻ at single Micro-ITIES	97
5.1	Co-condensation and post-synthesis grafting routes for for the functionalization of silica mesochannel walls	101
5.2	Cyclic voltammograms recorded in electrodeposition of macro silica film	102
5.3	Galvanostatic deposit curves for silica film at macro ITIES	103
5.4	CVs of 1 mM TMA ⁺ crossing the silica interface with different deposit time.	105
5.5	Forward peak current of TMA ⁺ from 0.2 mM to 1.0 mM as a function of silica formation time	106
5.6	TMA ⁺ detection across the silica membrane at modified Macro-ITIES	107
5.7	The mechanical problem for macro silica membranes	108
5.8	Single pore capillary testing by using TMA ⁺ ion transfer	109

5.9	The calibration dotted line for the capillary with diameter 25 μm and the capillary with diameter 50 μm	110
5.10	Recorded cyclic voltammogram of surfactant-template CTA^+ silica film electrodeposition at single pore capillary	111
5.11	CV checking before silica electrodeposition and potential transient during the galvanostatic deposition of silica film at -5.2 nA.	111
5.12	Optical capture for micro silica film at the single pore capillary	112
5.13	Recorded cyclic voltammograms in the presence of TMA^+ ion transfer at μITIES using silica modified capillary	114
5.14	The calibration of TMA^+ using the modified capillary 60s and 120s	114
5.15	Cyclic voltammograms recorded from the failed capillaries with modified silica membrane	115
6.1	The structure of Chitin and Chitosan	120
6.2	Chitosan's versatility	122
6.3	Cathodic electrodeposition of chitosan film	124
6.4	Biphasic reaction controlled by common cation transfer and the model chitosan solution	127
6.5	Typical cyclic voltammograms obtained in the presence of CS solution in the aqueous phase	128
6.6	The electrodeposition of chitosan film at macro-ITIES	129
6.7	Cyclic voltammogram in the presence of different concentrations of TEA and TMA	130
6.8	Cyclic voltammogram of different time period for same electrochemical cell and its calibration curve between the time and the peak current	131
6.9	Cyclic voltammogram of numerous cycle study for same electrochemical cell and its calibration curve between the number of cycle and the peak current	131
6.10	The potentiostatic deposition for simple chitosan film at liquid-liquid interface	132
6.11	The electrochemical characterization by model ion TEA^+ and TMA^+ at the modified liquid-liquid interface	133
6.12	Cyclic voltammetry of protonated chitosan with different concentration of TPA in water-DCE system and water-TFT system individually	135
6.13	Calibration curves obtained of model ion TMA and TEA at chitosan modified interface with different potentiostat process	136
6.14	SEM for No TPA film and TPA film	137
6.15	Raman spectrum of chitosan electrodeposit following different TPA concentrations	139
6.16	Infra-red spectrum of chitosan electrodeposit following different TPA concentrations	140
6.17	DSC curves for chitosan powder and chitosan films	141
6.18	The macro force measurement to obtain the stiffness	143

6.19	Cyclic voltammograms recorded at micro ITIES using single pore capillary	145
6.20	Cyclic voltammograms and linear fit for different concentration of TMA ⁺ in the aqueous phase across chitosan film	146
6.21	Potential dependence of the interfacial capacitance of the presence chitosan film (red curve) and the absence of chitosan film (black curve)	146
6.22	Comparison of Cyclic voltammograms for different concentration of TMA in the aqueous phase across different chitosan film	147
6.23	Optical images of the formation of cross-liner with chitosan film at the micro ITIES	148
7.1	pH modulation for ametryn detection	150

List of Tables

2.1	Ion sensing achieved by ITIES	49
2.2	Organic compounds sensing achieved by ITIES	50
2.3	Proteins sensing achieved by ITIES	50
3.1	Aqueous and organic electrolytes used for the protocols of electrolytes	53
3.2	Full list of pesticides and other used chemicals	63
3.3	Aqueous and organic electrolytes used at silica modified ITIES	66
3.4	Full list of chemicals used in chitosan electrodeposition	67
4.1	Physical properties of the neonicotinoids	73
4.2	Physicochemical Properties of Ametryn used in this study	75
4.3	Analytical performance and chemical composition of the river solution analyzed	93
5.1	Calibration points of forward peak current as the electrochemical response at unmodified μ ITIES	110
6.1	Chemical and biological properties of chitosan	121
6.2	Polarized liquid-liquid interface by common ion transfer	127
6.3	TMA ⁺ transfer slope across macro-scale chitosan film	136
6.4	TEA ⁺ transfer slope across macro-scale chitosan film	137
6.5	Thickness measurement of four types TPA-chitosan film	142
6.6	Stiffness and Young's modulus obtained for each chitosan film	144

List of General Abbreviations

A	electrode surface area
a	activity
c	concentration
$c_i^{0,o}$	initial concentration of the ion i in organic phase
$c_i^{0,w}$	initial concentration of the ion i in aqueous phase
D	diffusion coefficient
e	elementary charge
F	Faraday constant
i	ion or current
i_p	peak current
I_{ss}	steady state current
K	equilibrium constant
k^0	standard rate constant
L	ligand or neutral carrier
n	charge number
N_A	Avogadro's constant
P	partition constant
pK_a	acidity constant
r	radius
R	universal gas constant
T	Thermodynamic temperature

v	scan rate
V^o	volume of the organic phase
V^w	volume of the aqueous phase
γ	activity coefficient
δ_d	diffusion layer
η	solvent viscosity
μ_i^α	chemical potential in phase α
$\tilde{\mu}_i^\alpha$	electrochemical potential in phase α
$\mu_i^{0,\alpha}$	standard chemical potential in phase α
ϕ	inner potential
ΔE^0	standard cell potential
ΔG^0	standard reaction Gibbs energy change
$\Delta G_{0,w \rightarrow o}^{tr,i}$	standard Gibbs transfer energy of i from the aqueous to the organic phase
$\Delta_o^w \phi$	Galvani potential difference
$\Delta_o^w \phi_{1/2}$	half-wave potential
$\Delta_o^w \phi_i^0$	formal transfer potential of i between the aqueous and the organic phase
CE	Counter electrode
CV	Cyclic Voltammetry
LOD	limit of detection
RE	Reference electrode
v%	volume percent
wt%	weight percent

Abbreviations for Technically Important Chemicals

AME	Ametryn
BTPPA⁺	Bis(triphenylphosphoranyldiene) cation
CTA⁺	Cetyltrimethylammonium cation
CS	Chitosan
DCE	Dichloroethane
EDOT	3,4-Ethylenedioxythiophene
EtOH	Ethanol
IMI	Imidacloprid
MET	Metam sodium
TBA⁺	Tetrabutylammonium cation
TEA⁺	Tetraethylammonium cation
TEOS	Tetraethoxysilane

TMA⁺	Tetramethylammonium cation
TPA	Terephthalaldehyde
TPBCl⁻	Tetrakis(4-chlorophenylborate) anion

Acknowledgments

The path towards finishing this work is long and writing up this dissertation is arduous. It is not possible for me to finish this thesis without the guidance and support from my committee members and the colleagues at the Laboratory of Physical Chemistry and Microbiology for the Environment (LCPME).

First and foremost, I express my heartiest gratitude to my supervisor Dr. Grégoire Herzog for introducing me to this particular research field of ITIES and giving me his trust for letting me work liberally. During my PhD years, Dr Herzog not only taught me the advanced knowledge in electrochemistry but also supported me on various online conferences during COVID-19 that helped me to catch the most recent research topics and technology advances.

I also owe my deepest gratitude to my other respected supervisor Dr. Liang Liu. Dr. Liu had directly mentored me through my tough early days in Nancy. The highly motivated attitude, the honest and hard-working work ethics I have learned from Dr. Liu will benefit me for life.

I know I was not good at speaking and writing in English. Both advisors had always been very patient while discussing with me and correcting my papers. Working under their guidance helped me grow to be a professional researcher. I would not be able to finish my first research paper and my first conference presentation without their patient guidance. I had been deeply impressed by their dedication to research, their detail-oriented working ethic, and their passion for exploring. Those spirits will always be inspirations for me to achieve more progress in the future.

I would also like to express my appreciation to Dr. Micheál D. Scanlon and Dr. Sofiane EL KIRAT CHATEL as members on my dissertation committee by giving feedbacks for the research area. Through the annual meetings with them, I strengthened my skillset for presenting knowledge. I appreciate their efforts in helping me with exploring my research interests and their encouragements for me to pursue my career goal.

I wish to acknowledge those that have contributed to this work; Dr. Manuel Dosot for Raman and IR analysis, Clare Genois for chemical product purchase, Jean-Paul Moulin and Gérard Paquot for technical support to solve mechanical problems arose during experiments. Thank you to Marie Tercier, Christelle Charbaut for their help with administration issues.

I want to thank for the colleagues and some former colleagues who also worked in ITIES for supporting my research. Thanks to Dr. Alonso Gamero-Quijano for providing micro capillary fabrication support for the examination. Thanks to Dr. Lukasz Poltorak and Dr. Martha C. Collins for detailed discussion and giving instructions in electrochemical cell set-up.

Thanks to Dr. Alain Walcarius who is leading the multi-cultural ELAN team. With students coming and going over the three years, it has always a lovely group to work. Thanks to my fellow lab-mates: Samuel, Christelle, Ning, Wang, Deomila, Himanshu, Joanna, Wahid, Taisia, Xie, Qiao for your friendship and all the valuable discussions and help on my projects. The experience I spent with you was invaluable and unforgettable.

I wish to express my sincere thanks to Dr. Poulard Christophe for recommending me to pursue double diploma and giving me the confidence in continuing finishing my master degree. I would also like to thank to Dr. Thibaud Hildebrandt and Dr. Vincent Ji for their encouragement during my internship. Your words inspired me to stick to my goals whenever I met any obstacles.

I also want to thank these chinese students in France. For their company, for the good time we spent together. Mengjie Xu, Kou Du, Xing Liu, Jingjing Liao, Junmei Qi, Hang Wan, Fang Yuan, Hui Ying, Xin Li and many others.

Special thanks to financial support by the China Scholarship Council. Special thanks also to my cousin Jiying Gao for her guarantee.

I am very much indebted to my wife Xinya Zhu, who is willing to accompany me and encourage me in France during these years. I cannot find any words to express my gratitude to her.

Last but not least, I want to thank my parents Mr. Rongquan Lu and Ms. Yinjiao Guan, for the unconditional love, support and understanding they have given me at every stage of my life. Thank you, and I dedicate my work to you.

Chapitre 1

Résumé long de la thèse en français

L'électrochimie moderne à l'interface liquide-liquide, également appelée interface entre deux solutions électrolytiques non miscibles (ITIES), est étudiée depuis plus d'un siècle en raison de ses propriétés d'interface particulières. Elle offre une plateforme unique permettant la détection électrochimique non redox d'ions allant des protons aux macromolécules à travers l'interface moléculaire molle qui est intrinsèquement sans défaut et auto-guérisant. En outre, l'ITIES peut servir de support pour le dépôt électrolytique d'objets de la taille du nanomètre ou de molécules chargées dans un film arrangé. Le film électro-généré aux interfaces liquide-liquide présente de nombreux avantages tels que le contrôle du transfert d'ions, l'amélioration de la sensibilité et de la sélectivité. Par conséquent, la présente thèse est destinée à la détection des pesticides et aux films électrodéposés à l'ITIES et à l'étude plus approfondie du comportement modèle du transfert d'ions et des propriétés électrochimiques. La thèse se compose de trois grandes parties : la première vise principalement à réaliser la détection des pesticides, la deuxième est consacrée à l'électrodéposition de silice à l'interface micro liquide-liquide, et la troisième est de développer la génération de films de chitosane à l'interface. Les recherches à l'ITIES se poursuivent en vue de leur utilisation comme plate-forme unique pour l'application de capteurs et de membranes.

Actuellement, deux liquides sont non miscibles s'ils forment un mélange hétérogène et forment une interface Eau/Huile similaire. Cependant, ils ne sont pas strictement immiscibles, et il y a nécessairement une petite quantité d'eau dissoute dans la phase organique. Ainsi, lorsque les phases aqueuse et organique sont mises en contact, c'est nécessaire d'attendre un certain temps que les phases soient saturées. Néanmoins, il s'avère que lors de l'équilibrage, il se produit une émulsification spontanée de l'eau dans le solvant organique, conduisant à la formation d'un léger "voile" blanc sur l'interface. Les charges en deux phases formant une double couche électrique, il existe donc divers phénomènes électriques aux interfaces.

De plus, la structure d'une interface liquide-liquide est à peine définie en raison de les fluctuations. Jusqu'à présent, nos connaissances proviennent de recherches expérimentales et de calculs de dynamique moléculaire si nous la traitons comme une interface moléculaire dynamique. La structure de l'interface liquide-liquide a été proposée pour la première fois en 1939 par Verwey et Niessen et al. Puis, Gouy-Chapman et al. ont suggéré une double couche électrique comme deux doubles couches électriques dos à dos avec la charge

opposée à séparer comme limite géométrique. Plus tard, le modèle précédent a été amélioré pour devenir le modèle "Verwey-Niessen modifié" que nous connaissons aujourd'hui par Gavach et al. par l'ajout d'une couche d'ions spécifiquement adsorbés à l'interface comme une "couche compacte" de molécules dipolaires orientées (dite couche de Stern) afin de compromettre la diminution exponentielle des potentiels électriques.

Au milieu des années 80, le concept d'une région de solvants mixtes a été introduite par Girault et Schiffrin et al. en considérant un changement continu des propriétés du solvant à travers la couche mélangée qui se forme à partir de des molécules des deux liquides afin d'expliquer l'adsorption ionique spécifique qui se produit à la région interfaciale. Si un ion a un potentiel de transfert standard plus élevé situé près de la limite ou en dehors de la fenêtre potentielle, son transfert ne peut pas être examiné par transfert direct d'ions. Ainsi, les réactions de transfert d'ions assisté ont été considéré avec le ligand. Si un porteur d'ions chargé/neutre pouvant former un complexe avec l'ion cible est ajouté dans le phase appropriée, la barrière de transfert peut alors être abaissée, et par conséquent, l'objectif ion est assistée pour être détectable.

Dans la première partie, nous avons fait un effort par ce principe pour détecter les pesticides dans les micro-ITIES en raison de son rapport coût-efficacité. Ainsi, l'Ametryn, l'Imidacloprid et le Metam sodium ont été sélectionnés comme ions modèles qui appartiennent respectivement à la famille des triazines, des néonicotinoïdes et des organosulfures. Ces pesticides ont été choisis car ils sont couramment utilisés et ont été placés sur la liste de surveillance européenne des polluants émergents. Leur surconsommation dans le monde entier a créé un grand problème pour la sécurité des sols ou des rivières et entraîne des problèmes de santé pour les humains. Il est donc très important de développer un capteur sur place. Grâce à la miniaturisation des ITIES, le capillaire à micropores peut servir de support pour construire une interface liquide-liquide. Combiné à la voltampèremètre, ce type de capteur ne nécessite pas que l'analyte soit oxydé ou réduit électrochimiquement, ou adsorbé sur la surface de l'électrode solide, mais exige au contraire que l'analyte soit ionique afin qu'il passe d'une phase à l'autre lors de l'application d'un potentiel. Ainsi, l'accumulation des analytes d'une solution proche du pH neutre dans une phase organique par un transfert automatique à un potentiel en circuit ouvert est possible et augmente ensuite le signal de détection.

Cette stratégie a réussi pour l'amétryne mais a échoué pour la détection de l'imidaclopride et du métam-sodium. Dans notre travail, nous avons accumulé de l'AME diluée dans la solution organique par la réaction de dissociation environ 30 minutes d'agitation à pH 6 dans la solution aqueuse. Nous avons faire la détection dans la deuxième solution. Les résultats de l'expérience ont montré cette méthode en deux étapes ont un signal amélioré que la mesure directe assistée par les protons. De plus, elle a obtenu une amélioration évidente d'environ trois fois en deux étapes. Afin d'obtenir une concentration maximale de l'AME organique dans le capillaire, l'AME à pH 8 en phase aqueuse a également été mesurée en deux étapes. En détail, chaque capillaire a été lavé par ultrasons dans une solution d'éthanol pendant 5 minutes, puis remplacé par la solution organique afin de collecter l'AME se trouvant en solution aqueuse. Grâce à la première étape de préconcentration, l'accumulation de l'AME est obtenue par sa propriété hydrophobe avec sa protonation au micro interface à l'aide de la micropipette.

Néanmoins, cette méthode de préconcentration posait encore un gros problème. La valeur maximale de l'AME dans la solution aqueuse était normalement détectée pour le premier cycle en utilisant la voltamétrie cyclique. En outre, la détection en deux étapes n'a pas amélioré la sensibilité. Et cette méthode a une barre d'erreur plus grande pour chaque concentration. Pour dépasser ces limites, nous avons enquêté l'effet de l'ajout de tampon à la solution aqueuse. La présence de tampon dans la solution aqueuse assure une concentration constante de protons disponibles pour le transfert à travers l'interface. De plus, lorsque la concentration du tampon de phosphate était de 1 mM, un courant de pointe pour le transfert de ametryn a été bien observé, permettant ainsi la détection de l'ametryn en une seule étape. La voltampérométrie AC a été aussi utilisée ici pour améliorer la sensibilité de la détection de l'amétryne afin de surmonter la médiocre limite de détection atteinte avec la voltampérométrie cyclique.

Dans la deuxième partie, nous avons développé le dépôt de silice à Micro-ITIES. L'objectif de la membrane de silice à l'ITIES est de se concentrer sur l'amélioration de la sélectivité pour le transfert d'ions. La membrane de silice des Macro-ITIES a été optimisée grâce au temps d'électrodéposition. La propriété de ces films, telle que la sélectivité des ions, dépendait en fait du processus d'électrodéposition. En même temps, la macro membrane ne peut pas éviter l'inconvénient d'un point de vue mécanique puisque le dur-

cissement et la solidification n'ont pas été réalisés in situ. Nous sommes donc passés à la micro-électrodéposition au niveau du capillaire à un seul micropore. D'après les captures optiques du capillaire de la pointe, nous pouvons être sûrs que les membranes de silice se sont formées à la sortie de la pointe même après le durcissement en four. Cependant, la caractérisation électrochimique par ion d'analyte a malencontreusement échoué car aucune détection de courant et une grande résistance lors de la mesure. Complication en voltampérométrie cyclique des mesures ont été effectuées pour l'interface silice modifiée en raison de la résistance de la membrane de silice et l'ajout à peine de solution organique dans le capillaire. Ces a rendu l'analyse voltampérométrique difficile et ambiguë. Nous pouvons conclure que les deux coefficients, l'épaisseur et le coefficient de diffusion à l'intérieur de la membrane de silice jouent un rôle essentiel pour qui limiterait clairement le transfert d'ions. C'est la raison pour laquelle il est difficile d'obtenir le signal de courant provenant du micro capillaire après le dépôt de silice.

En détail, le capillaire modifié a perdu le signal électrochimique dans une expérience ultérieure lorsque nous avons utilisé le capillaire modifié à la silice pour étudier sa sélectivité du membranaire. Il y a deux raisons à cela : la première est que le tensioactif CTA⁺ est toujours présent dans le film et dans la plupart des cas, la seconde est le film de silice mésoporeux à la solution du bloc d'extrémité et alors les ITIES ne peuvent pas être établies. Si l'on compare à grande échelle, le signal caractéristique du TMA⁺ a été entravé dans les Macro-ITIES. Malgré cela, le signal électrochimique présenté devait clairement indiquer la membrane de silice à l'interface. En raison de l'interface miniaturisée, la reproductibilité d'expérience était encore un grand problème. Entre-temps, la mesure expérimentale de l'épaisseur de la micro-membrane de silice n'a guère été réalisée en raison des limites de l'expérimentation à l'échelle micro. Une méthode de caractérisation fiable pour les expériences ex-situ la caractérisation du dépôt de silice reste à établir.

Dans la troisième partie, nous avons réalisé l'électrodéposition du chitosane à ITIES. Les films de chitosane agissent comme une membrane pour le transfert d'ions et présentent une charge positive, qui pourrait fournir l'effet d'adsorption pour l'ion négatif. Contrairement au film de silice, le film de chitosane électrogénéré est flexible et possède de bonnes propriétés mécaniques, qui peuvent être travaillées comme soustraction pour la co-déposition avec d'autres matériaux. Pour améliorer la structure du film de chitosane,

le réticulant téréphtalaldéhyde (TPA) est introduit dans la phase organique. Dans ce travail, nous avons développé une nouvelle méthode basée sur le transfert d'ions à l'ITIES pour former un film de chitosane autonome à l'interface liquide-liquide qui convient aux applications de transfert sélectif d'ions, visant à la détection des pesticides. La solution de chitosane est préparée dans la phase aqueuse; le film est généré par chronoampérométrie et est réticulé avec x mM TPA (téréphtalaldéhyde) dans la phase organique. Les propriétés du film sont liées à la durée variable du dépôt électrolytique et à la concentration en TPA.

Les réactions de transfert de charge enregistrées par voltampérométrie cyclique montrent une réduction du pic de courant inverse sur le côté positif de la fenêtre de potentiel en raison de la formation d'un film de chitosane au LLI. Tous les films de chitosane générés par voie électrique offrent d'excellentes propriétés mécaniques qui peuvent être extraites de la solution. Après l'évaporation totale de l'eau, les valeurs de module d'Young des films ont été mesurées à environ 10 kPa sous le système de macro-force. Il est en outre caractérisé par la spectroscopie infrarouge et la spectroscopie Raman. La caractérisation des résultats ont démontré que la liaison covalente de C=N a été introduite dans le film de chitosane. La membrane molle du chitosane à l'interface liquide-liquide donnerait la sélectivité nécessaire à la détection in situ de l'analyte. Nous avons effectué des tests avec du TMA^+ et du TEA^+ et leurs voltampérogrammes cycliques ont illustré différents répondeurs pour le transfert d'ions interfaciaux. Ainsi, le chitosane déposé par électrolyse in situ serait une nouvelle membrane synthétisée qui fonctionne comme une membrane souple à l'interface et permet d'analyser l'adsorption avec détection sélective pour le capteur ITIES.

Nous avons alors démontré un protocole pour contrôler la réaction interfaciale avec la concentration variable de réticulant dans la phase organique, et le précurseur est limité dans la phase aqueuse. Nous avons donc obtenu différents types de films de chitosane à l'aide de micropipette en ce protocole. L'étude électrochimique présente le même mécanisme de la formation d'un film au micro interface liquide-liquide, qui a protoné l'adsorption du chitosane à l'interface et son film généré. Néanmoins, comme le même problème rencontré dans les micro dépôts de silice, le film de chitosane a le défi d'un processus précis qui conduit à un film homogène. Des études supplémentaires sont nécessaires pour améliorer les propriétés de la microstructure des matériaux synthétisés pour le chi-

tosane et la silice. Les facteurs qui affectent la structure de ces deux types de film peut varier entre l'étape de l'électrodéposition et l'état chimique initial. Même la manipulation du film d'extraction des solutions peut jouer un rôle important. En résumé, il convient de reconsidérer le film de micro-dépôt à l'interface liquide-liquide et d'optimiser la précision du dispositif expérimental.

Chapter 2

Bibliographical introduction

2.1 Aspects of Liquid-Liquid Interface

Liquid-liquid interfaces play an essential role in some physical, chemical, and biochemical processes in order to sustain the regular function of living cells. Furthermore, the related examples of liquid-liquid interface application in industry are crude oil demulsification, asphalt emulsification, the fabrication of food, cosmetics etc. In the interest of well understanding the liquid-liquid interface structure, physics can give us the information about surface tension, spreading coefficient, work of adhesion or work of cohesion etc. However, with a view to know the process involving the ion at the liquid-liquid interface, electrochemistry is a powerful and suitable method to study ion transfer and oxidation-reduction behaviour at the interface and reveal the corresponding processes of their formation and destruction with ligand across the membrane. In terms of the present viewpoint, the liquid-liquid interface itself is a dynamic soft interface and its structure is obviously affected by the distribution of ions in the liquid phase next to the interface forming the electrical double layer. Furthermore, adsorption and desorption events at the liquid-liquid interface can be modified by a function of applied potential, time, and solution conditions. In order to grasp what is taking place in an electrochemical cell, it links to traditional electrochemical techniques such as cyclic voltammetry to observe directly the interfacial processes. Their characteristic methods include scanning probe based approaches (scanning electrochemical microscopy) and optical spectroscopy, such as Surface plasmon resonance (SPR), dark field microscopy (DFM), surface-enhanced Raman spectroscopy (SERS). Therefore, it is of a high scientific challenge to investigate electrochemistry at the liquid-liquid interface to understand the processes occurring at them and to make wise use of them. This interdisciplinary lead us to recherche beyond the traditional fields of study and applications. Thus, in the beginning, bibliographical introduction for the current state of the art is made in this chapter.

2.2 Basis of Liquid-Liquid Interface

An interface is an area that separates two phases from each other. If we generally consider the solid, liquid, and gas phase (S, L, G), we immediately get five combinations

of interfaces: the solid-liquid, the solid-gas, the solid-solid, the liquid-gas, and the liquid-liquid interface. Besides, these interfaces involve at least one condensed phase, such as liquid and solid. Gas-gas interfaces do not exist because of the gas mix. These five interfaces are presented respectively by the symbol: SLI, SGI, SSI, LGI, LLI. Surfaces and interfaces are “phase boundaries”, that is, they delimit distinct regions of matter (phases) and define the shape of these regions as long as they are stable. The respective process, of course, depends on the nature of the two phases on either side of the phase boundary. More precisely, the individual process depends on the properties of both aspects within their area of immediate contact. These interface properties ultimately determine the mechanism, the speed, and the final product of the process. Typically, the interface width in real materials is of the order of Angstroms. If chemicals across phase boundary, it means that interfacial energy is related to the interface width and the energy barrier associated with the interface are changed. Thus, phase boundaries are the locations of gradients, and gradients are a driving force of chemicals mass transfer. With regard to liquid-liquid interface, it appears quite intuitive that the mere contact between two immiscible phases leads to an alteration of their properties at the interface from their respective properties in bulk.

For one phase, molecular interactions play an essential role inside for its properties. For instance, when salt is added in water, electrostatic interactions between a positively charged ion (cation) and a water molecule will occur readily in an aqueous environment. This ion-dipole interaction involves the orientation of the partially localized negative charge of the water molecule toward the positively charged cation, forming a hydration shell. This hydration force is particularly crucial for ions or molecules in solution as it minimizes their direct contact due to the van der Waals attraction, controlling the stability of the solution. Meanwhile, a hydrogen atom will be attached with an electronegative group of the molecule to form a hydrogen bonding as a particular case of dipole interaction. Usually, we distinguish and classify two types of electrolyte solutions. The first is formed from strong electrolytes, also called ionophores. Strong electrolytes exist as ions in the solid-state, a well-known example being NaCl. When they dissolve in a polar solvent such as water, the individual ions are stabilized by ion-dipole interactions with solvent molecules. The second is formed from a weak electrolyte which does not completely dis-

sociate in the solvent, and we need to consider one extra parameter called the dissociation constant. Cations and anions in the solvent will keep electrostatic interactions. These attractive interactions construct the ordering of liquids and their properties. For example, viscosity is the physical property of a fluid which characterizes its resistance to flow. It is often measured by timing the flow of a liquid through a cylindrical tube under the influence of gravity. However, the origin of this friction is from intermolecular forces. With the development of the theory of ionic conductance, it has been shown that the viscosity of the solvent is an important parameter determining ionic mobility (diffusion coefficient).¹

Thus, the interface has unique properties when combining two different liquids. Take into account the interface of a macroscopic water/oil system, the interfacial tension between water and oil pendant on the surfactant molecules properties and the volume concentration of surfactant in the system. Moreover, a selective transfer of a substance from one phase toward the other can be realized through a partitioning method base on differential solubility in each solvent. Otherwise, the liquid/liquid interface acts as a simple model for simulating bio-films has developed rapidly over the past decades. Thus, the liquid/liquid interface has promising applications in the study of electrochemical sensing, phase transfer catalysis, drug release, solvent extraction and mimic bio-films. For example, liquid-liquid interface precipitation (LLIP) method is commonly used to form Self-Assembly film for 3D crystals due to the heterogeneous nucleation reaction at an immiscible liquid-liquid interface, with high dimensional uniformity. Moreover, drug's solubility is different between the aqueous phase and the the organic phase. The migration from one phase into another phase of analytes would be facilitated like a detergent for solubilizing the salts. Therefore, the system of liquid-liquid interface with membrane are the core recherche of bioelectrochemical science and sol-gel technology, and is still in its infancy.

2.3 Electrochemistry at Liquid-Liquid Interface

2.3.1 A brief history

Two immiscible liquids form a similar Water/Oil interface. However, they are not strictly immiscible, and there is necessarily a small quantity of water dissolved in the organic phase. Thus, when the aqueous and organic phases are put in contact, it is necessary to wait a specific time until the phases are saturated. Nevertheless, it turns out that during equilibration, spontaneous emulsification of water in organic solvent occurs, leading to the formation of a light white "veil" on the interface. The charges at the two-phase interface, forming an electric double layer, so there are various electrical phenomena at interfaces.

In comparison to other interfaces, the particularity of liquid-liquid interfaces is that the condensed phases are both fluids. They can be continuously deformed and self-healing. In this respect, this interface is a highly reproducible, defect-free surface that allows matter diffusion. The first work for electrochemistry at the Interface between Two Immiscible Electrolyte Solutions (ITIES) was dated back to 1902 when Nernst and Riesenfeld found that ion can transfer across the water/phenol interface.² In the 1970s, Gavach et al. demonstrated that ion transfer could be observed at the ITIES by polarizing similarly to a conventional electrode-electrolyte interface, and popularized the acronym of ITIES.³⁻⁶ At the same time, the four electrode potentiostat was introduced to compensate iR drop at ITIES by Samec et al.⁷ Almost at the same time, functionalization of the liquid-liquid interface had started mainly with phospholipid. Koryta et al. pioneered the observation of ion transfer reaction across a phospholipid monolayer at ITIES.⁸ Meanwhile, many other types of functionalizations have been studied, such as metallic nanoparticles.⁹⁻¹¹ Since then, various types of research, such as electrochemical techniques, theories, and systems are carried out on ITIES and turned into a fundamental part of the modern electrochemistry. In recent years, with the continuous development of nanotechnology and life sciences, analytical applications for liquid/liquid interface electrochemistry would be possible to unveil the complex biochemical reactions that simulate biofilm interfaces, oxygen reduction electrocatalytic reactions, phase transfer catalytic reactions, photoconversion

processes, ion electrochemical sensors, and drug release processes.

2.3.2 The structure of the liquid/liquid interface

First of all, the structure of a liquid-liquid interface is hardly defined due to thermal fluctuations if we deal with it as a dynamic molecular interface. So far, our knowledge stems from experimental investigations and molecular dynamic calculations. The structure of the liquid-liquid interface was proposed for the first time in 1939 by Verwey and Niessen et al. through with Gouy-Chapman theory to describe an electric double layer as two back-to-back electric double layers with the opposite charge to separate as a continuous geometric boundary (Figure 1.1 a).¹² Therefore, the ions are present throughout the interfacial phase, and the boundary between the two liquid phases is a dimensionless geometrical surface separating two space-charge layers. Experimental evidence was then reported by Gavach et al. almost 40 years later.⁶ In the same article, the previous model was improved what we know today as the ‘modified Verwey-Niessen’ model (Figure 1.1b) by Gavach et al. through the addition of a layer of specifically adsorbed ions at the interface as a ‘compact layer’ of oriented dipole molecules (so-called, Stern layer) in order to compromise the exponential electric potentials decrease into the bulk of both phases. However, the capacity of the inner layer at ITIES is more exceptional than the capacity of the inner layer at the metal/solution indicated that the contribution from the inner layer is less pronounced than has been expected according to later studies.¹³⁻¹⁶ Because it can not ignore the formation of an ion-free layer at the water/oil interface which is associated with the presence of the specific ions in the double layer and the properties of the inner layer may depend on the nature of entering ions.¹⁷⁻²⁰ In the middle of the 80s, the concept of a mixed solvent region was introduced by Girault and Schiffrin et al. with considering a continuous change of solvent properties across the mixed layer which form from the molecules of the two liquids to explain significant ionic specific adsorption occurs at the interfacial region (Figure 1.1c).²¹⁻²⁴ Over the past two decades, molecular dynamics has provided a pictorial view of the interface and has developed some new concepts regarding such as surface dynamics. With the help of these computer simulations, Benjamin et al. have shown that ITIES is molecularly sharp with nanoscale protrusions at short time

scale (Figure 1.1d), but at longer time scale it still appears as a mixed layer for averaging around 10\AA .^{25–28} Notably, he also figured out that 2-3 layers of water should have dipoles which are parallel to the interface due to water fingers are likely to form.

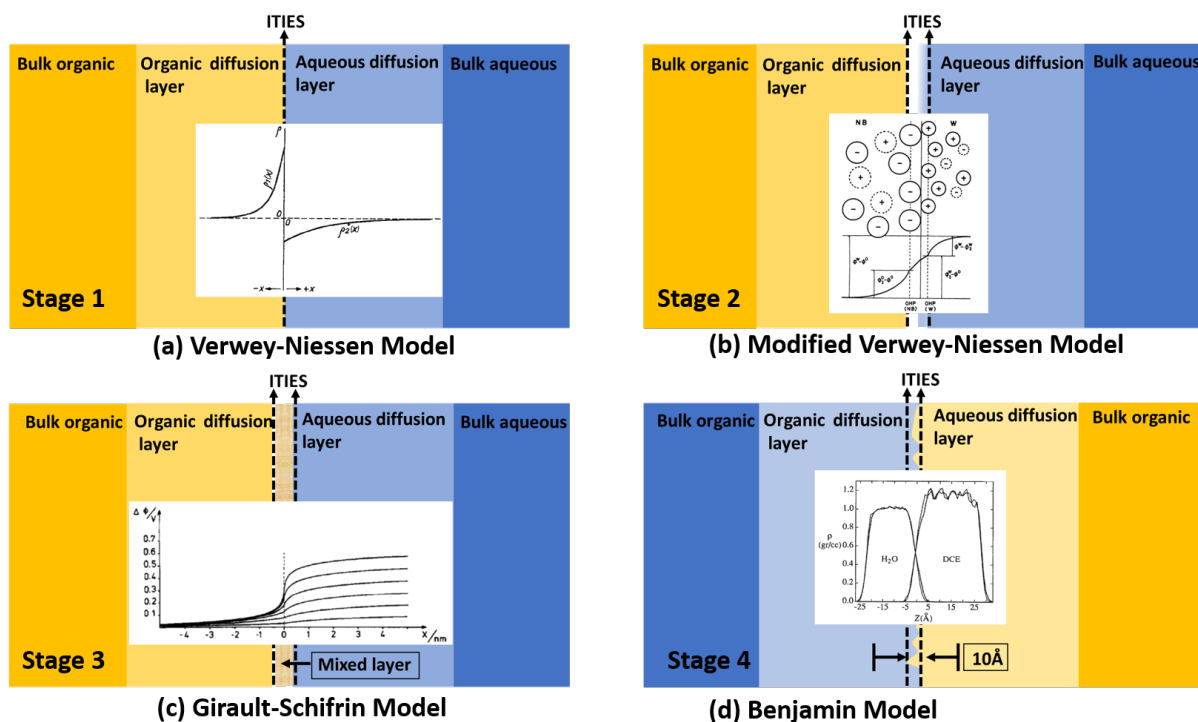


Figure 2.1: Evolution of views on the structure of ITIES: (a) Verwey-Niessen Model using two back-to-back based on Gouy-Chapman theory and its distribution of the charges, (b) Modified-Verwey-Niessen Model using a compact layer of two oriented dipole molecules at the interface and its double layer structure with representative potential profile of the interface, (c) Girault-Schiffrin Model using a mixed layer of two solvents at the interface and its various potential distribution, (d) Benjamin Model using Molecular Dynamics Computer Simulation with its calculated densities profiles of water and 1,2 DCE.

Right now, recent research still focuses on understanding the complex nature and probing the unique structure of the liquid-liquid interface through spectroscopic techniques: the scattering of X-ray,²⁹ non-linear optical methods by sum-frequency vibrational spectroscopy,³⁰ and second-order optical spectroscopy.³¹ Recent studies have shown that the tight interaction of the ions in the double layer makes them virtually insensitive to the presence of other ions. Thus, it means that the capacitance of the interface is constant. In addition, the interface has no diffusion layer, which makes the potential difference drops

in its totality between two sharp ionic layers. Thus, the polarization of the interface is supported by ionic interactions over short distances (typically less than 5 Å), which allow direct compensation of their charge and prevent the charge screening mechanisms.³²

2.3.3 Simple ion transfer reaction

In classical electrochemical experiments, the electron transfer reaction (ET) occurs at the interface between a working electrode and an electrolyte solution i.e. solid/liquid interface, with an exchange of electrons between the electrode and the oxidizing/reducing agent present in the solution. The electrochemistry of the liquid/liquid interface is used for charge transfer reaction studies by means of working electrodes at the interface of two insoluble liquids. In contrast to conventional solid/liquid interface electrochemistry, it is possible to study not only the oxidation-reduction reactions in water or organic phases, but also the transfer reactions of charged species at the liquid/liquid interface, such as the ion transfer reaction (IT). Taking account into the simple ion transfer reaction across the liquid-liquid interface, the partial molar Gibbs energy named the electrochemical potential ($\tilde{\mu}$) of the species **i** in phase α is expressed as equation 1.1:

$$\tilde{\mu}_i^\alpha = \mu_i^\alpha + z_i F \phi^\alpha \quad (2.1)$$

where μ_i^α is the chemical contribution and called the chemical potential, z_i is the charge number of species **i**, F is the Faraday's constant, ϕ^α is the Galvani potential in phase α . And the chemical potential μ_i^α can be developed in the form of equation 1.2:

$$\mu_i^\alpha = \mu_i^{0,\alpha} + RT \ln a_i^\alpha \quad (2.2)$$

in which, $\mu_i^{0,\alpha}$ is the standard chemical potential of species **i** in phase α , R is the gas constant, T is absolute temperature in Kelvin and a_i^α is the activity of species **i** in phase α . By combining these two equations, the electrochemical potential can be written as Equation 1.3:

$$\tilde{\mu}_i^\alpha = \mu_i^{0,\alpha} + RT \ln a_i^\alpha + z_i F \phi^\alpha \quad (2.3)$$

Since molecular species are dissolved in aqueous and organic phases and have different chemical potentials, in liquid-liquid equilibrium, we consider the two phases to be in

contact and have equal electrochemical potentials as following equation 1.4:

$$\tilde{\mu}_i^o = \tilde{\mu}_i^w \quad (2.4)$$

If we consider that species **i** is transferred from the aqueous to the organic phase via simple ion transfer reaction, then the standard transfer Gibbs energy ($\Delta_o^w G_i^{0,w \rightarrow o}$) will be defined as the difference between standard Gibbs energy of solvation ($\mu_i^{0,o}$) and hydration ($\mu_i^{0,w}$):³³

$$\Delta_o^w G_i^{0,w \rightarrow o} = \mu_i^{0,o} - \mu_i^{0,w} \quad (2.5)$$

Standard transfer Gibbs energy ($\Delta_o^w G_i^{0,w \rightarrow o}$) can be converted to standard transfer potential ($\Delta_o^w \phi_i^0$) by introducing the factor of $z_i F$ according to equation 1.6:

$$\Delta_o^w \phi_i^0 = \frac{\Delta_o^w G_i^{0,w \rightarrow o}}{z_i F} \quad (2.6)$$

After rearranging equation 1.4 with the standard transfer potential of species **i** ($\Delta_o^w \phi_i^0$), a Galvani potential difference $\Delta_o^w \phi$ defined as $\Delta_o^w \phi = \phi^w - \phi^o$ can be expressed through a formal Nernst equation 1.7:

$$\Delta_o^w \phi = \Delta_o^w \phi_i^0 + \frac{RT}{z_i F} \ln \frac{a_i^o}{a_i^w} \quad (2.7)$$

where ϕ^w and ϕ^o are the inner potential of the bulk aqueous and organic phases respectively, a_i^o and a_i^w are the activities of the species **i** in organic and aqueous phases respectively. Concentration c can be related to activity using the activity coefficient γ leads to the following equation:

$$a_i = \gamma_i c_i \quad (2.8)$$

Thus, equation 1.7 can be expressed with concentration instead of activity:

$$\Delta_o^w \phi = \Delta_o^w \phi_i^0 + \frac{RT}{z_i F} \ln \frac{c_i^o}{c_i^w} \quad (2.9)$$

where $\Delta_o^w \phi_i^0$ correspond to formal transfer potential, is defined as:^{33,34}

$$\Delta_o^w \phi_i^0 = \Delta_o^w \phi_i^0 + \frac{RT}{z_i F} \ln \frac{\gamma_i^o}{\gamma_i^w} \quad (2.10)$$

Ions with a large positive or large negative $\Delta_o^w G_i^0$ are denoted as hydrophilic or hydrophobic ions, respectively. The ratio of the ion activities or the ion concentrations in

the two phases is the ion partition coefficient Pi or the apparent ion partition coefficient Pi' can be rewritten as equation 1.11 and 1.12 respectively:

$$Pi = \frac{a_i^o}{a_i^w} = \exp\left[\frac{z_i F (\Delta_o^w \phi - \Delta_o^w \phi_i^0)}{RT}\right] \quad (2.11)$$

$$Pi' = \frac{c_i^o}{c_i^w} = \exp\left[\frac{z_i F (\Delta_o^w \phi - \Delta_o^w \phi_i^0)}{RT}\right] \quad (2.12)$$

Therefore, the potential difference across the interface (Galvani potential difference, $\Delta_o^w \phi$) is controlled by the reference electrode in each phase and is linked to the concentration of ionic species (c_i) distributed across the interface.

Simple ion transfer reaction is considered as an easy electrochemical technique to analyze qualitatively the standard transfer potential or the standard Gibbs energy difference across the water/oil interface. Figure 1.2 gives the standard potential differences obtained for univalent cations (H^+ , Li^+ , Na^+ , K^+ etc) and anions (Cl^- , Br^- , I^- etc).^{34,35} For more recent data and details, we can check on the website of the electrochemical database.³⁶

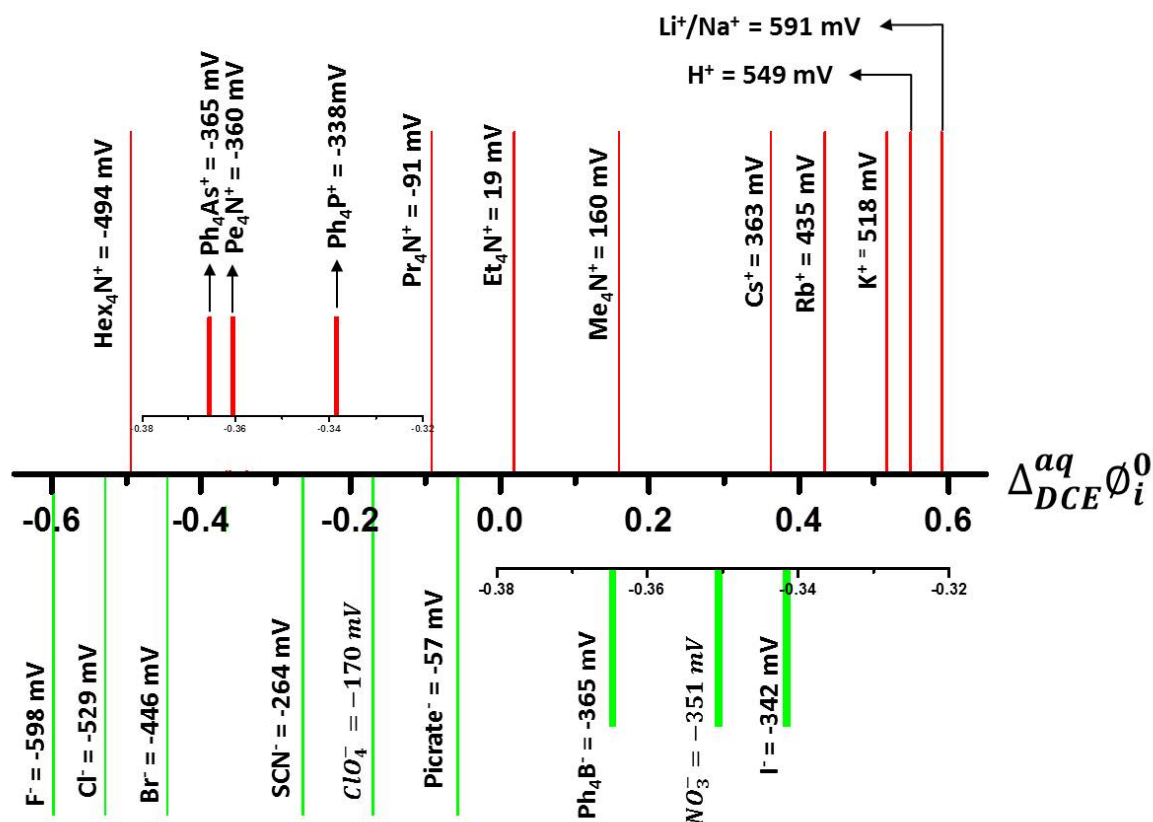


Figure 2.2: Standard ion transfer potentials for different univalent cations and anions across the water/DCE interface.³⁷

The reported absolute values of the rate constants for the “exchange” current (current at zero electrochemical Gibbs energy of ion transfer), are apparently usually about 0.01–0.1 $cm\ s^{-1}$.³⁸ Computational studies under conditions of zero-electrochemical free energy ion transfer would be useful in ascertaining which of the following factors are dominant in controlling the rate of ion transfer across the interface. Figure 1.3 illustrates 3 steps for ion transfer across the immiscible interface considering the conjunction on protrusions at the interface and the relative rate constant. Firstly, an ion initially in solvent A first attaches itself to a protrusion of solvent B. The attachment of the ion to the tip of the protrusion of solvent B has a “bimolecular” attachment rate. Secondly, once the attached ion diffuses across the interface toward solvent B. The recession of the protrusion presumably assists the solvation of the ion by the new solvent B, and this solvation and the desolvation from

A continues as the ion diffuses across the interface. Thirdly, when the change of solvation is nearly complete, the ion begins to detach itself from the interface at some point, , which may now be from the tip of a protrusion of solvent A extending into solvent B. Thus, the higher hydration energy of an ion, the harder it is to overcome this barrier which is reflected in slower anion-transfer kinetics.^{39,40}

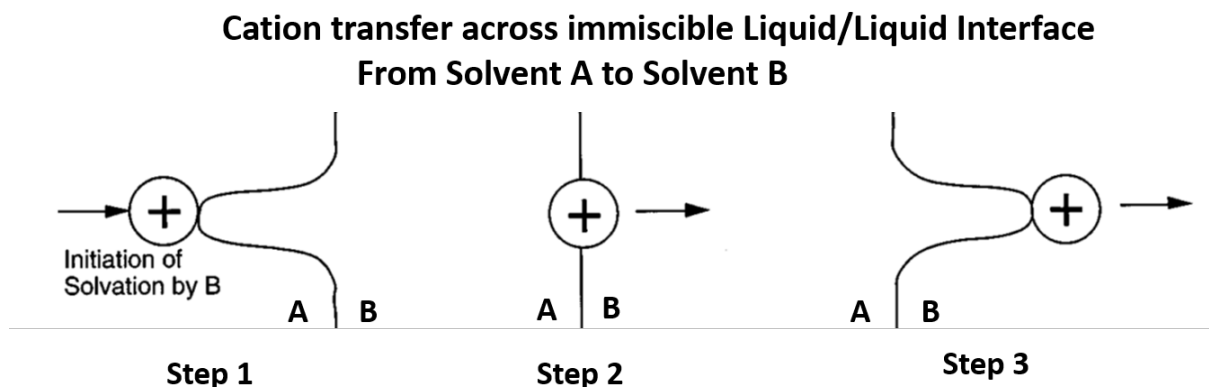


Figure 2.3: Schematic plot of an ion in solvent A approaching a protrusion from solvent B at the A/B interface, passing through the interface and exiting into solvent B from another protrusion, now of B into A.³⁸

2.3.4 Assisted ion transfer reaction

If an ion has a higher standard potential of transfer located near the limit or outside of potential windows, its transfer cannot be studied by merely polarizing the ITIES. However, if a charged/neutral ion carrier that can form a complex with the target ion is added in the appropriate phase, the transfer barrier can then be lowered, and consequently, the target ion is assisted to be detectable. Assisted ion transfer reactions were reported by Koryta in 1979.⁴¹ He used dibenzo-18-crown-6 ionophores in the organic phase to form a complex with potassium ions in the aqueous phase, demonstrated the concept of a facilitated ion transfer by decreasing the Gibbs energy of transfer and allowing the ions to transfer at lower interfacial potential difference values. Thus, in ITIES electrochemistry, it is possible to target specific analytes using a facilitated/assisted ion transfer. The usage of a ligand to 'assist' the transfer of the ion between phases is involved, by employing a host-guest interaction. This concept was inspired by the ion pump/channel existing in nature – an

integral protein embedded at a biomembrane forming a hydrophilic pore facilitating ion transfer inside and outside of the cell.^{42,43} To describe the process, one assumes the ligand is in the organic phase, with the ion in the aqueous phase. Complexation occurs in the phase the ligand is present in (i.e. organic phase). This facilitated cation transfer with the ligand in a 1:1 stoichiometry at the ITIES can be depicted in equation 1.13:



For given reaction the association constant K_a can be rewritten as equation 1.15:

$$K_{iL^+} = \frac{a_{iL^+}^o}{a_L^o a_{i^+}^w} \quad (2.14)$$

With the apparent standard transfer potential,

$$\Delta_o^w \phi_{iL^+}^0 = \Delta_o^w \phi_{i^+}^0 + \frac{RT}{F} \ln(K_a a_L^o) \quad (2.15)$$

If all the species (the cation, the ligand, and the complex) are partitioned, the Nernst equation can be written either for the ion or the complex:

$$\Delta_o^w \phi = \Delta_o^w \phi_{i^+}^0 + \frac{RT}{F} \ln \frac{a_{i^+}^o}{a_{i^+}^w} = \Delta_o^w \phi_{iL^+}^0 + \frac{RT}{F} \ln \frac{a_{iL^+}^o}{a_{iL^+}^w} \quad (2.16)$$

An excess concentration of the ion is present in the aqueous phase compared with the organic phase and under open circuit potential, complex formation in the organic phase is high. Thus, ion concentration in the organic phase and ligand concentration in the aqueous phase can be neglected while ion diffusion need not be considered. For the half-wave potential in CV, we have the condition:⁴⁴

$$\sqrt{D_{iL^+} c_{iL^+}^0} = \sqrt{D_L c_L^0} \quad (2.17)$$

where D_{iL^+} and D_L are the diffusion coefficients of the complex and of the complex former in the organic phase and the index 0 indicates the concentrations close to the interface. Finally we can get the half-wave potential for the facilitated ion transfer as equation 1.18:

$$\Delta_o^w \phi_{1/2, iL^+} = \Delta_o^w \phi_{i^+}^0 + \frac{RT}{2F} \ln \left(\frac{D_L}{D_{iL^+}} \right) - \frac{RT}{F} \ln(K_{iL^+} a_{i^+}^w) \quad (2.18)$$

In view of this equation, stronger complexation and higher concentration of the metal ion cause larger shift of the half-wave potential to more negative potential and it is *vice*

versa for anions. Figure 1.4 illustrates a thermodynamic viewpoint of this reaction with considering the partition coefficient of the ion i^+ , of the ligand L , and of the complex iL^+ .

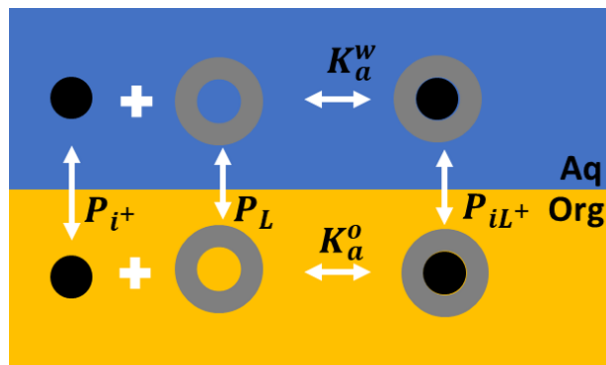


Figure 2.4: Thermodynamic constants for assisted-ion-transfer reactions.

From which, equation 1.18 can be developed by substitution with equation 1.19:

$$\Delta_o^w \phi_{iL^+}^0 = \Delta_o^w \phi_{i^+}^0 - \frac{RT}{F} \ln\left(\frac{K_a^o}{K_a^w}\right) - \frac{RT}{F} \ln(P_L) \quad (2.19)$$

The nature of assisted ion transfer reactions is quite complex but four mechanisms have been put forward to describe the processes occurring as Figure 1.5 illustrated: ACT – aqueous complexation followed by transfer, TOC – transfer followed by complexation, TIC – transfer by interfacial complexation and TID – transfer by interfacial dissociation.⁴⁵

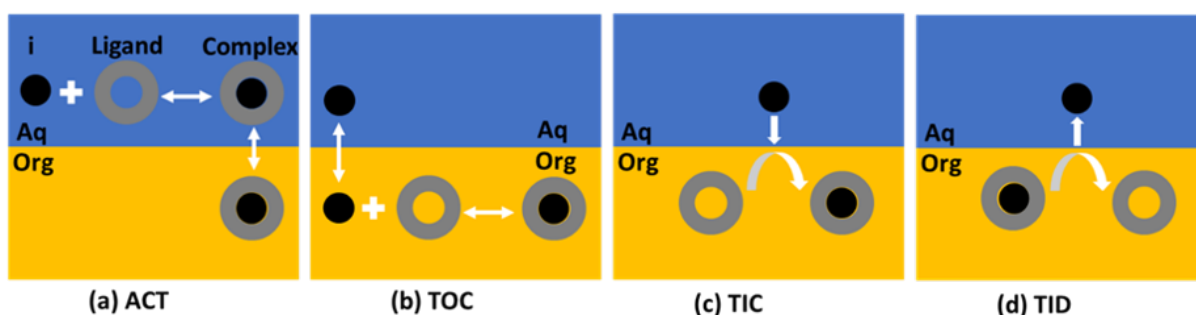


Figure 2.5: The four mechanisms of possible assisted ion (i) transfer with Ligand: (a) Aqueous Complexation followed by Transfer (ACT), (b) Transfer to the Organic phase followed by Complexation (TOC), (c) Transfer by Interfacial Complexation (TIC), (d) Transfer by Interfacial Dissociation.

Comparing these two thermodynamic diagrams, we can get:

ACT: $pK_a^w < 0$, $pK_a^o > 0$, and $\log P_L < 0$ (hydrophilic ligand)

TOC: $pK_a^w > 0$, $pK_a^o < 0$, and $\log P_L > 0$ (lipophilic ligand)

TIC and TID: $pK_a^w > 0$, $pK_a^o < 0$, and $\log P_L > 0$ (hydrophilic ligand)

However, it needs indicate that the simple ion transfer as described before can be a relative phenomenon. It has been demonstrated that the transfer of hydrophilic alkali metal cations is facilitated by hydrophobic organic counterions at the interface by Mirkin et al.⁴⁶ Figure 1.6 shows simple ion transfer occurs via a shuttling mechanism in which the counter anion forms an ion pair with the target cation in the mixed solvent layer of the liquid/liquid interface and releases it to the bulk of the organic phase.

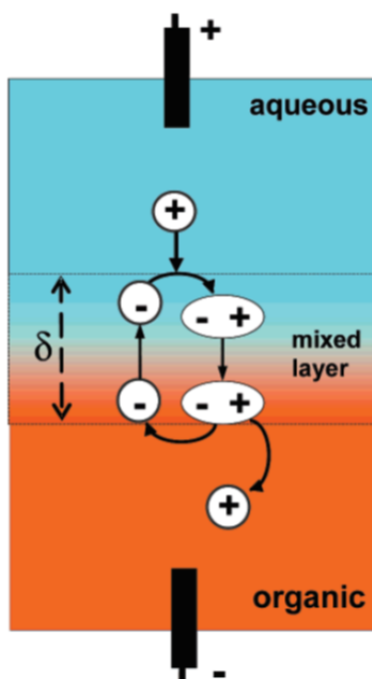


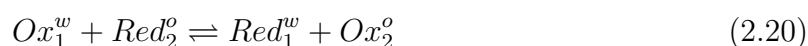
Figure 2.6: The shuttling mechanism for the transfer of a cation from water to the organic phase involves the formation of a short-lived ion pair with a hydrophobic anion at interface.⁴⁶

In detail, the water molecules present even in trace amounts in the organic phase can facilitate the hydrophilic metal ions significantly. However, it is also clear that the behaviour of more hydrophobic cations (e.g., TMA⁺), which can be readily transferred

to neat DCE, is almost unaffected by $[\text{H}_2\text{O}]$ in the organic phase.⁴⁷ So it seems that TMA^+ transfer is a true simple ion transfer. Another example of ion pair formation at ITIES is the transfer of protamines through strong adsorption of the protamine–organic anion pair at the interface by using dinonylnaphthalenesulfonate (DNNS) as presented by Amemiya et al.^{48,49} and also by Trojanek et al.⁵⁰ The environment-related drug detection and relative ion sensors based on ITIES would be realized because FIT mechanism can be applied for the design of potentiometric ion-selective electrodes and the understanding of their hydrophilicity or hydrophobicity in the liquid phase. For example, if the analyte is very hydrophobic and this strongly hinders their partition from the organic to the aqueous phase; the proton transfer reagents are therefore confined to the organic phase. Dependent on the pH of the aqueous phase, the transfer of substituted analyte as well as the transfer of protons facilitated by the ligand.^{51,52}

2.3.5 Electron transfer reaction

Electron transfer reactions involve the study of charge transfer of redox-active species at the ITIES. A redox reaction between an oxidized form of the redox couple in one phase and a reduced form in the other can occur under conditions where the driving force is large enough to trigger this reaction. This process can be expressed by equation 1.20 and shown schematically in Figure 1.7:



where Ox_1^w is the oxidized species in aqueous phase and Red_1^w is its reduced form, Red_2^o is the oxidized species in organic phase and Ox_2^o is its reduced form. The number of electrons involved in the interfacial redox reaction is assumed to be 1.

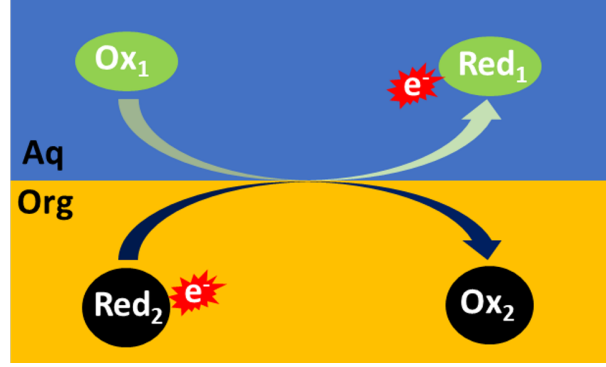


Figure 2.7: Schematic plot of heterogeneous redox reaction within electron transfer across the immiscible liquid/liquid interface.

For the reaction 1.21 at constant temperature and pressure, the following equality of the electrochemical potentials at equilibrium will be given as:

$$\tilde{\mu}_{Red_1}^w + \tilde{\mu}_{Ox_2}^o = \tilde{\mu}_{Ox_1}^w + \tilde{\mu}_{Red_2}^o \quad (2.21)$$

Developing this, the equivalent of the Nernst equation for this reaction of electron transfer at the interface can be expressed in equation 1.22:

$$\Delta_o^w \phi = \Delta_o^w \phi_{ET}^0 + \frac{RT}{F} \ln \left(\frac{a_{Red_1}^w a_{Ox_2}^o}{a_{Ox_1}^w a_{Red_2}^o} \right) \quad (2.22)$$

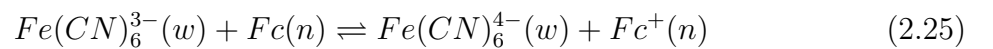
with $\Delta_o^w \phi_{ET}^0$ is the standard redox potential for the interfacial transfer of electrons:

$$\Delta_o^w \phi_{ET}^0 = [\tilde{\mu}_{Red_1}^{0,w} + \tilde{\mu}_{Ox_2}^{0,o} - \tilde{\mu}_{Ox_1}^{0,w} - \tilde{\mu}_{Red_2}^{0,o}] / F \quad (2.23)$$

It is interesting to bring into this equation on the same aqueous SHE scale by simplifying the difference of the standard redox potential between these two redox couples in equation 1.24:

$$\Delta_o^w \phi_{ET}^0 = [E_{Ox_2/Red_2}^0]_{SHE}^o - [E_{Ox_1/Red_1}^0]_{SHE}^w \quad (2.24)$$

From an experimental viewpoint, this standard redox potential can be measured by referring all the standard redox potential to a reference redox couple such as ferrocinium/ferrocene. This interfacial electron transfer reaction was first time observed by Samec et al. for the system composed from hexacyanoferrate redox couple in the aqueous phase and ferrocene in the nitrobenzene phase:⁷



where n indicate the organic phase is nitrobenzene, For instance it has been determined that in DCE (organic phase = DCE):⁵³

$$[E_{Fc^+/Fc}^0]_{SHE}^{DCE} = [E_{Fc^+/Fc}^0]_{SHE}^w + \Delta_o^w \phi_{Fc^+}^0 - \Delta_o^w G_{Fc}^{0,w \rightarrow o} / F \quad (2.26)$$

where the parameter $\Delta_o^w G_{Fc}^{0,w \rightarrow o} = -24.3 \text{ kJmol}^{-1}$ corresponds to the Fc Gibbs energy of transfer from water to the DCE phase and has been estimated from extraction methods. The average value for the Fc redox potential of $\Delta_o^w \phi_{Fc^+}^0 = 0.381 \text{ V}$ was derived from voltammetry at ultramicroelectrodes,⁵⁴ while the parameter $\Delta_o^w \phi_{Fc^+}^0 = 0.005 \text{ V}$ was estimated by cyclic voltammograms featuring the transfers of Fc^+ and the standard TMA^+ , $[E_{Fc^+/Fc}^0]_{SHE}^{DCE} = 0.64 \text{ V}$ is then calculated. Finally, equation 1.27 can be more conveniently to be expressed as:

$$\Delta_o^w \phi_{ET}^0 = [E_{Ox_2/Red_2}^0]_{Fc}^{DCE} - [E_{Ox_1/Red_1}^0]_{SHE}^w + 0.64 \text{ V} \quad (2.27)$$

If the standard redox potential in aqueous phase is known, it is possible to calculate its value in DCE with respect to the aqueous SHE if the standard Gibbs transfer energies of all the participated species at the w/DCE interface are known as Figure 1.8 illustrated.⁵⁵

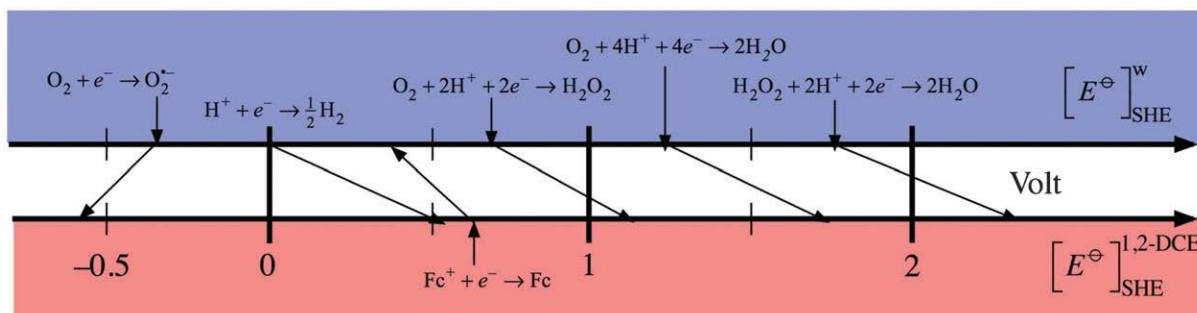


Figure 2.8: Redox potential scale for oxygen in water (top scale) and in 1,2-dichloroethane (bottom scale) versus the Standard Hydrogen Electrode (SHE).⁵⁵

Although this particular type of interfacial charge transfer reaction is rarely used for sensing, it can accompany other disciplines such as electrocatalysis,⁵⁶ photoinduced electron transfer process, *i.e.* artificial photosynthesis,⁵⁷⁻⁶⁰ interfacial modification with the metals.⁶¹⁻⁶³ The modification at ITIES will be discussed in more details in the next section of this chapter.

2.3.6 Ionic distribution diagrams

Due to the equivalent Nernst equation at ITIES, the concept of zone diagrams for the distribution of ionizable species such as acids or bases was proposed by Reymond et al.⁶⁴⁻⁶⁶ Ionic partition diagrams can provide a useful representation of thermodynamic equilibrium involving ionizable species in biphasic liquid systems and is an important illustration of many physicochemical and biological processes such as solvent extraction, drug absorption. For instance, let us consider the distribution diagrams for hydrophilic monobasic acid AH in the water-organic system. At a high aqueous pH, the acid is ionized in the anionic form. The Nernst equation for the distribution without considering the activity coefficients can be written as:

$$\Delta_o^w \phi = \Delta_o^w \phi_{A^-}^0 - \frac{RT}{F} \ln \frac{c_{A^-}^o}{c_{A^-}^w} \quad (2.28)$$

The separation limit between the anion in water and the organic phase ($c_{A^-}^o = c_{A^-}^w$) is a horizontal straight line. Simultaneously, the separation limit between the acid and basic forms in water ($c_{AH}^w = c_{A^-}^w$) is a vertical given by $\text{pH}=\text{pK}_a$. Finally, the line separation the neutral acid in water and the anion A^- in the organic phase is given by equation 1.32:

$$\Delta_o^w \phi = \Delta_o^w \phi_{A^-}^0 + \frac{RT}{F} \ln K_a^w - \frac{RT}{F} \ln \left(\frac{a_{A^-}^o a_{H^+}^w}{c_{AH}^w} \right) \quad (2.29)$$

Considering the AH acid is lipophilic and neglecting the activity coefficients, the Partition coefficient ($P_{AH} = c_{AH}^o / c_{AH}^w$) is taken into account the distribution of the acid in the organic phase:

$$K_a^w = \frac{a_{A^-}^w a_{H^+}^w}{c_{AH}^w} = \frac{c_{A^-}^w c_{H^+}^w}{c_{AH}^w} P_{AH} \quad (2.30)$$

then the separation limit between the aqueous anion ion A_w^- and the neutral form in the organic phase is expressed as:

$$\text{pH} = \text{pK}_a^w + \log P_{AH} \quad (2.31)$$

This equation shows that, to extract an organic acid into water, one should work at a pH higher than that given by equation 1.32. Without taking the phase ration into consideration, the separation limit between the two ionic forms ($c_{A^-}^o = c_{A^-}^w$) is still the

one given by equation 1.31. The separation line between the anion in the water and the acid in the organic phase is rewritten as below:

$$\Delta_o^w \phi = \Delta_o^w \phi_{A^-}^0 + \frac{RT}{F} \ln \frac{K_a^w}{P_{AH}} - \frac{RT}{F} \ln \left(\frac{c_{A^-}^o - c_{H^+}^w}{c_{AH}^w} \right) \quad (2.32)$$

This limit depends on the pH. In Figure 1.9 , A1 shows a hydrophilic acid ionic distribution diagram and A2 shows a lipophilic acid distribution diagram. The illustration of ionic partition for a hydrophilic monobasic compound and a lipophilic monobasic compound is presented in picture B1, B2 respectively.

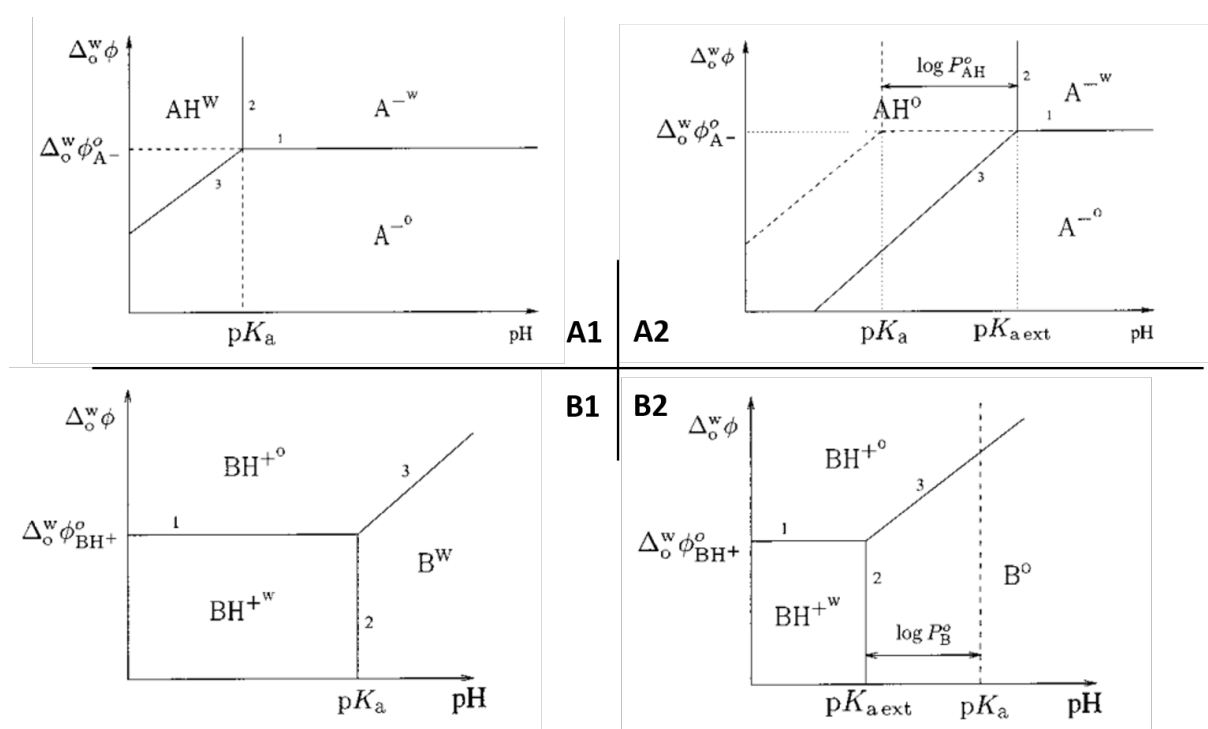


Figure 2.9: Ionic distribution diagram: (A1) a hydrophilic monoacidic compound, (A2) a lipophilic monoacidic compound; (B1) a hydrophilic monobasic compound, (B2) a lipophilic monobasic compound.⁶⁶

Besides, several parameters can influence the drawing of ionic distribution diagram such as the role of the biological membranes,^{67,68} double protonation.^{64,65}

2.3.7 Nonpolarized ITIES

In electrochemistry theory, there are two classes of electrode/electrolyte interfaces, i.e. ideally polarizable electrode (IPE) and ideally non-polarizable electrode (INPE). The ITIES can also be classified into polarizable and nonpolarizable depending on the ions or electrolytes present in solvent. For example, nonpolarizable ITIES can be simply built by the partition of a single binary electrolyte AB , which is assumed to dissociate completely in both phases into A^+ and B^- , and the biphasic system can be described as below:



At equilibrium, the electrochemical potentials of both cation and anion are equal between the two phases:

$$\mu_{A^+}^{0,w} + RT \ln a_{A^+}^w + F\phi^w = \mu_{A^+}^{0,o} + RT \ln a_{A^+}^o + F\phi^o \quad (2.34)$$

$$\mu_{B^-}^{0,w} + RT \ln a_{B^-}^w + F\phi^w = \mu_{B^-}^{0,o} + RT \ln a_{B^-}^o + F\phi^o \quad (2.35)$$

Combining equations 1.34 and 1.35, the Galvani potential difference $\Delta_o^w\phi$ at the ITIES will be defined as equation below.^{69,70}

$$\Delta_o^w\phi = \frac{\Delta_o^w\phi_{A^+}^0 + \Delta_o^w\phi_{B^-}^0}{2} + \frac{RT}{2F} \ln \left(\frac{a_{A^+}^o a_{B^-}^w}{a_{A^+}^w a_{B^-}^o} \right) \quad (2.36)$$

where $\Delta_o^w\phi_{A^+}^0$ and $\Delta_o^w\phi_{B^-}^0$ are the standard transfer potentials of A^+ and B^- respectively, R , T and F have their usual meanings. With taking the charge neutrality into account, Equation 1.36 implies that $\Delta_o^w\phi$ is regardless of the electrolyte concentration and the volume ratio between the two adjacent solutions. It is the reason that this system is nonpolarizable.

Another special nonpolarizable interface occurs when both immiscible phases contain at least one common ion, which can freely cross the interface. In that case, the current originating from common ion transfer in any direction would not induce any changes in potential interfacial difference. According to Nernst-like equation for ion transfer reaction, the potential distribution is only dependent on the ionic species separated between two immiscible phases. Therefore, binary electrolyte (A^+B^-) or electrolytes containing common ion ($A^+B^-|A^+C^-$) are distributed between two phases, and hence the potential interfacial

difference does not depend on their concentration and present an ideally non-polarized interface.^{71,72} For example, if the organic phase contains bis (triphenylphosphoranylidene) ammonium tetrakis (pentafluorophenyl) borate (BA^+TB^-) as the supporting electrolyte, the Ref. water phase will contain bis (triphenylphosphoranylidene) ammonium chloride (BA^+Cl^-). The potential at the Ref. Water/organic interface will be given through the Nernst equation for BA^+ partition between the two phases, listed as follows:

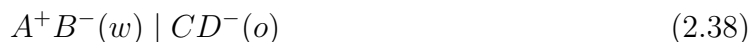
$$\Delta_o^w \phi = \Delta_o^w \phi_{BA^+}^0 + \frac{RT}{F} \ln \frac{a_{BA^+}^o}{a_{BA^+}^w} \quad (2.37)$$

where $\Delta_o^w \phi$ is the Galvani potential difference at the Ref. water/organic interface, $\Delta_o^w \phi_{BA^+}^0$ is the standard transfer potential of BA^+ , $a_{BA^+}^w$ and $a_{BA^+}^o$ are the activity of BA^+ in aqueous phase and organic phase respectively, R , T , F have been constant. When the two phases contain equal concentrations or activity of BA^+ , then the last term equal to 0. Thus, the potential difference at Ref. water/organic interface is equal to standard transfer potential of BA^+ ($\Delta_o^w \phi_{BA^+}^0$) at $-0.70V$.⁷³ In this condition, this non-polarized interface can be usually employed as a similar reference electrode at ITIES. Practically, a silver wire coated with a layer of silver chloride ($Ag|AgCl$) can be easily employed as the reference electrode in the aqueous phase connecting with the external power source. The reference electrode ($Ag|AgCl|BA^+Cl^-(w)|BA^+TB^-(o)$) was called an oil/water-type reference electrode created by Senda et al.,²⁴ and was widely used as the organic phase reference at ITIES because it can find a stable reference electrode directly immersed into the organic phase. Systems employing non-polarized interface can also be used to study the kinetics of electron transfer reactions in application of new techniques such as scanning electrochemical microscopy (SECM), microelectrochemical measurements at expanding droplets (MIMED), thin-layer cyclic voltammetry (CV), and spectroelectrochemical methods.⁷⁴ In brief, this interface is nonpolarizable by the common ion redistribution to readjust the activity ratio of the common ion between the two adjacent phases, returning the system into equilibrium. However, we can say that the interface is polarized chemically by the common ion, as a distinct potential difference has been established.

2.3.8 Polarized ITIES

An ideally polarizable electrode is an electrode at which the potential across the electrode/electrolyte interface can be changed significantly without observable charge transfer, so only capacitive double-layer charging current can be observed. In other words, a polarizable electrode can be considered to be equivalent to a perfect capacitor without leakage. Similar behaviour can be found at the ITIES. Eventually, the solid conductor is replaced by an immiscible electrolyte phase and the polarization becomes an ionic process purely. From the viewpoint of electrochemistry, polarized ITIES are more attractive because more different kinds of charge transfer reactions would be investigated such as ion-selective electrodes, biological systems across the Membrane transport, extraction of useful ions.⁷⁵

Take, for example, the electrolyte between the organic phase and aqueous phase would form a potential window because of its self-transfer. In detail, the aqueous phase contains highly hydrophilic salt (A^+B^-) of ideally zero solubility in the organic phase, and the organic phase contains highly lipophilic salt (C^+D^-) of ideally zero solubility in the aqueous phase then the ideally polarized interface can be described as the interface impermeable to the charged particles transfer in whole potential range. It is illustrated as below:



The standard Gibbs transfer energies of A^+ and B^- are very positive from w to o and they are very negative for C^+ and D^- , can be expressed in Galvani potential scale as below:

$$\begin{aligned} \Delta_o^w \phi_{A^+}^o &\gg 0, \quad \Delta_o^w \phi_{B^-}^o \ll 0 \\ \Delta_o^w \phi_{C^+}^o &\ll 0, \quad \Delta_o^w \phi_{D^-}^o \gg 0 \end{aligned} \quad (2.39)$$

The Galvani potential difference ($\Delta_o^w \phi$) at the ITIES is controlled by the excess electrical charge at the double layer, which can be supplied by an external power source. For example, lithium chloride (LiCl) as a hydrophilic salt in water and Bis-(triphenylphosphoranylidene) ammonium tetrakis-(4-chlorophenyl) borate ($BTPPA^+TPBCl^-$) as a lipophilic salt in 1,2-Dichloroethene (1,2 DCE) can form a polarizable interface w|1,2 DCE. The polarization of interface can be realized by changing the Galvani potential difference. Thus,

voltammetry is a powerful characterization to detect the polarization of interface and ions transfer across the interface. Figure 1.10 illustrates a standard blank cyclic voltammogram recorded at a polarized ITIES. The middle region shows the polarizable part of the interface and is known as the potential window.

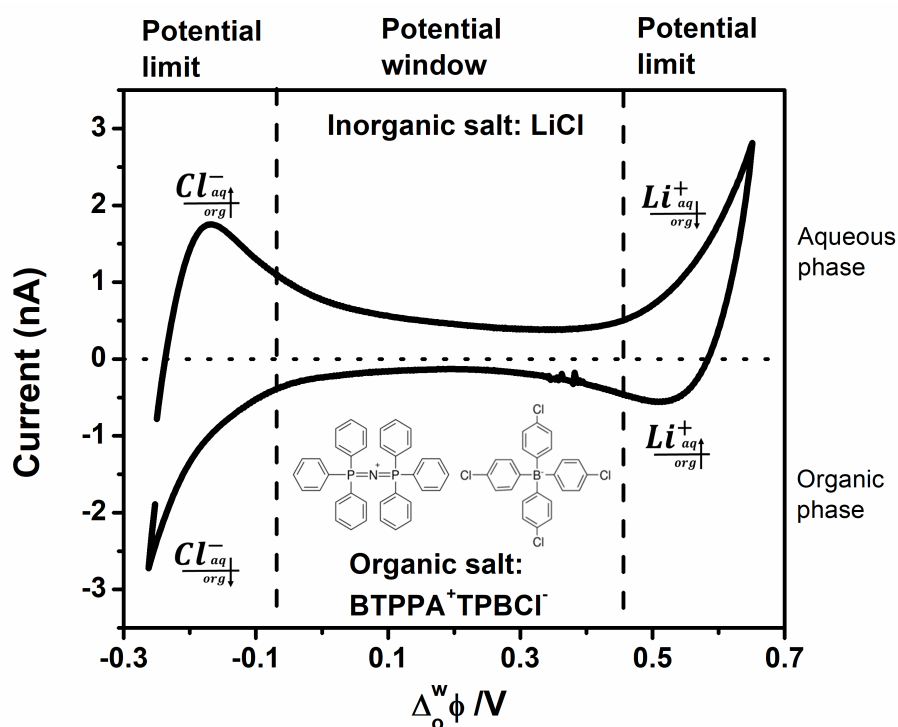


Figure 2.10: Voltammogram recorded at micro-ITIES only in the presence of the aqueous ($LiCl$) and the organic ($BTPPA^+ TPBCl^-$) supporting electrolytes. The left and right regions show ion transfer of the background electrolyte ions and limit the middle region as a potential window which the interface is impermeable for all ionic species present in both phases.

When monitoring the transfer of probe ions at the interface, their charge and direction of ion transfer determines will be visible by a peak on the voltammogram. Figure 1.11 shows the direction of cation and anion transfers with corresponding current responses. The application of a Galvani potential which become more positive than the standard Galvani potential Applying a Galvani potential ($\Delta_o^w \phi$) that is more positive than the standard Galvani potential ($\Delta_o^w \phi^0$), during the forward scan, cations are transferred from the aqueous phase to the organic phase, and anions are transferred from the organic phase

to the water phase. On the contrary, in the backward scan, cations are transferred from the organic phase to the water phase, and anions are transferred from the water phase to the organic phase.⁷⁶

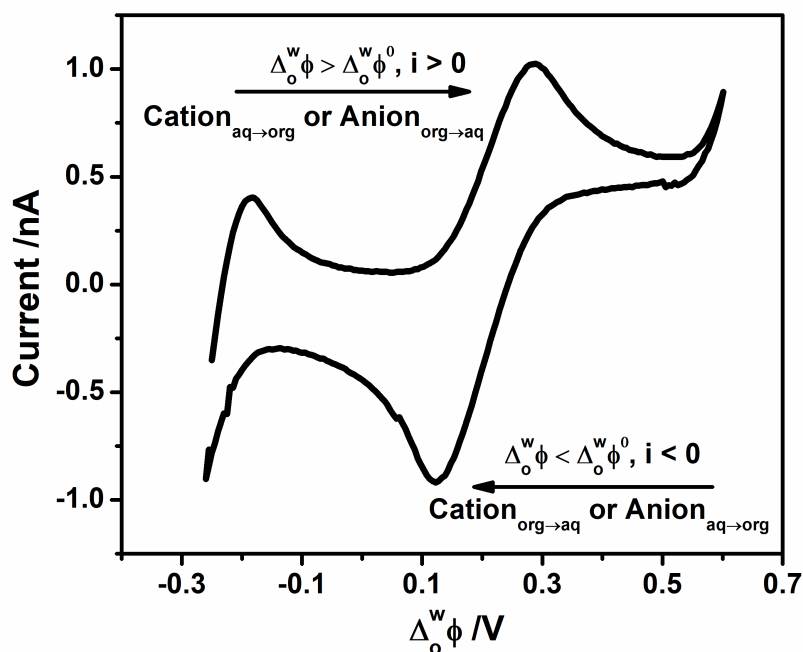


Figure 2.11: Direction of cation and anion transfer with corresponding current response at polarized ITIES.

2.4 Miniaturization of the ITIES

The miniaturization of the ITIES will bring many advantages such as relative iR drop and reduced charging current. Mass transport is also improved and results in better sensitivities and limits of detection due to the radical diffusion at the interface.⁷⁷ In the views of analytical chemistry, sensitivity is a quantitative parameter which indicates the performance of an analytical procedure.⁷⁸ However, some unwanted species presented in the solution can arise the background noise and hardly quantify the real analyte. Improvement of selectivity is then sought after for based on ITIES sensor.

The construction methods of miniaturization can be divided into Micro scale and Nano scale and classify three categories according to the materials used: (1) pulled glass tubules, within micron tip, nano-meter tip, and double pipettes;⁷⁹⁻⁸³ (2) polymer films or silicon films, including micro-porous and nano-porous arrays;⁸⁴⁻¹⁰¹ (3) micro-cavity or nano-cavity.^{102,103} Historically, The concept of miniaturization was first introduced in 1986 by Taylor et Girault who have reported the transfer tetrathylammonium ion at an H₂O-DCE interface supported at the fine tip of a glass micropipette.⁷⁹ The laser micro-machine technique was also used to form a micro-porous array in polyester film at ITIES.⁸⁰ Repeatable single pore micro-ITIES could be prepared by using a metal wire with a fixed diameter as a template, and a glass tube melted around. The wire removal of a wire by etching releases the pore that can be subsequently used to fill an organic phase or aqueous phase.^{104,105} As a similar condition in the solid-liquid interface, mass transfer is then enhanced due to edge effect.¹⁰⁶ In order to know the main characteristics of asymmetric diffusion fields, Girault et al. proposed that the mode of diffusion of ions at the interface is affected the length of the pore and the position of the interface.¹⁰⁷ This influence is illustrated in Figure 1.12 which shows three major diffusion profiles of ion transfer at different interface positions in a single micropore with δ_o and δ_w represent the steady-state thicknesses of the diffusion layers in the two phases.

However, the precise location of the interface is a major difficulty of micro-ITIES with regards to experimental reproducibility. It has been shown that the ratio between pore diameter and channel length or thickness of the array support is critical for reproducible measurements when using different arrays. The hydrophilic or hydrophobic nature of the micropipette and filling procedure will also make a significant impact on the interface position.¹⁰⁸ Thus, the geometry of the interface must be taken into account, including orifice radius, wall thickness, the angle, the inside or outside pore radius, the pore spacing of an array, thickness of the organic film for the study of ion transfer at the liquid/liquid interface.

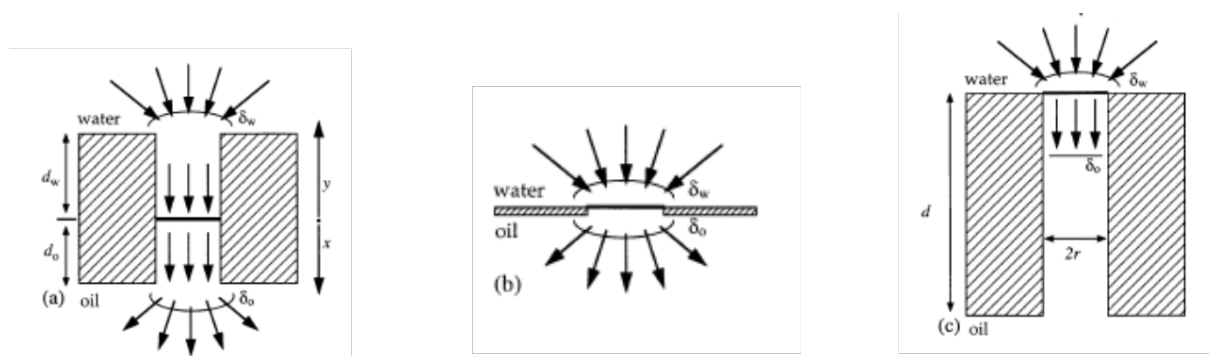


Figure 2.12: Schematic representation of the different simulated geometries. (a) Recessed microdisc interface, spherical-linear linear-spherical diffusion. (b) Quasi inlaid microdisc interface, spherical spherical diffusion. (c) Long micro-hole (or short diffusion time) with quasi inlaid interface, spherical linear diffusion. (d) Micro-hole with small organic recessed interface, spherical linear-spherical diffusion.¹⁰⁷

Figure 1.12 demonstrated four possible ion transfer happened at micro ITIES. (a) Recessed micro-disc interface: The position of the liquid/liquid interface is inside the orifice, due to the micron radius of the orifice, the ions are spherically diffused outside the orifice and linearly diffused inside the orifice; (b) Quasi inlaid micro-disc interface: Due to the small length of the pore channel, ions diffuse through the pore channel can be neglected and it is approximated that ions diffuse spherically symmetrically at the interface. (c) Long micro-hole (or short diffusion time) with a quasi inlaid interface: The organic phase fills the entire pore channel causing the interface to be located near the aqueous phase of the pore, so that the ions diffuse spherically on the aqueous side of the interface and linearly in the pore channel. It is an asymmetric diffusion profile. The organic phase is filled with micron pore channels with the interface positioned close to the aqueous side, The ions diffuse spherically in the orifice near the aqueous phase, linearly in the orifice, and spherically in the orifice near the organic phase. The radial diffusion in the micro-ITIES generates a faster mass transport (as opposed to linear diffusion), thus giving a higher sensitivity, consequently allowing detection limits at the scale of nM.¹⁰⁹ As a result, cyclic voltammetric response for each condition would differ as Figure 1.13 illustrated.

It has been shown experimentally, that micropore of a μ ITIES behaves in the same way as a solid micro-electrode and that the steady state current can be calculated according

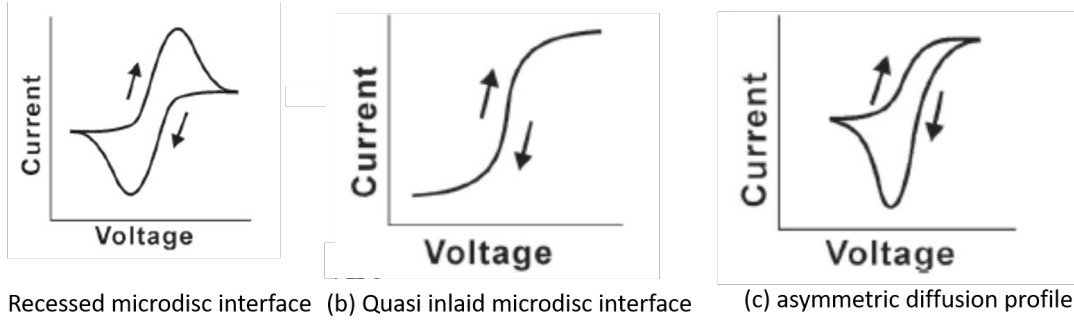


Figure 2.13: Schematic representation of voltammetric experiments at (a) Recessed micro-disc interface; (b) Quasi inlaid micro-disc interface (c) Micro-hole (or short diffusion time) with quasi inlaid interface.

to different different interface as Figure 1.14 shown,¹¹⁰⁻¹¹³

(a) inlaid disc interface:

$$I_{ss} = 4z_i F D_i c_i r_a N \quad (2.40)$$

(b) cylinder-recessed interface:

$$I_{ss} = \frac{4\pi z_i F D_i c_i r_a^2 N}{4L + \pi r_a} \quad (2.41)$$

(c) cone-recessed disc interface:

$$I_{ss} = \frac{4\pi z_i F D_i c_i r_a r_L N}{4L + \pi r_a} \quad (2.42)$$

where z_i is the charge on the transferring ion, r_a is the radius of the micropore that defines the interface area, D_i is the diffusion coefficient of the ion, N is the number of micropores if in the array and c_i is the concentration of ion species in the bulk, r_L is the outside radius of the cone.

Furthermore, Nano-ITIES have a diffusion profile similar to that of micro-ITIES which can be applied by Equation 1.40.¹¹³ Nano-ITIES can offer a better electroanalytical response, as, under proper geometrical conditions, the array can be treated as a sum of individual ITIES, thereby maximizing the mass transport and thus greatly improving sensitivity. For instance, using an array of nano-ITIES resulted in the detection of propranolol at values 5 – 10 times lower than the limit of detection achieved at the larger micro/macro interfaces.¹¹⁴

To summarize, Micro-ITIES (μ ITIES) has four significant advantages over conventional macro ITIES electrochemistry: (1) Problems associated with the high iR -drop effect across the interface are minimized leading to the separation of the faradaic current from the double layer charging current which achieve a lower limit of detection. (2) Significantly improved mass transport leads to superior sensitivity. (3) The mechanical stability of the μ ITIES is also enhanced, leading to more consistent measurements. (4) Miniaturization is more environmentally friendly as lower volume of highly toxic organic solvent are needed and simplify the experiment set-up with two or three electrodes detection.

2.4.1 Interface modifications

Micro or nano pipettes are widely used to build miniaturized liquid-liquid interfaces due to their simple preparation process and unique geometry structure. However, the charge transfer of analyte at a single liquid/liquid interface generates low current values which are several nanoampere(nA). Porous membranes are then developed to support micro or nano scale liquid/liquid interfaces to overcome this deficiency and facilitate the analytical detection of the drug. The preparation methods of porous membranes have been diversifying with the advanced nanotechnology. We have broadly divided the fabrication of porous membranes in two ways. One is the top-down method by removing mass from a substrate in macro or nanoscale, leaving micro or nanopores. The other is called the bottom-up method, which membranes are built up through the molecular self-assembly phenomenon related to physical and chemical interactions.

2.4.1.1 Top-down method

Highly ordered micro/nanoporous channels with uniform pore sizes can be achieved top-down on a variety of substrates using physicochemical processing such as the laser micro-machining technique and reactive ion etching. In 1989, Campbell and Girault developed the first microhole array supported micro-ITIES which was made on a polyester film consisting of 66 holes prepared by ablation with a UV excimer laser.⁸⁰ Uneven etching results in an inverted tapered aperture, with a larger aperture on the incident side and a smaller aperture on the exit side of the laser. Figure 1.15 illustrates this geometry with

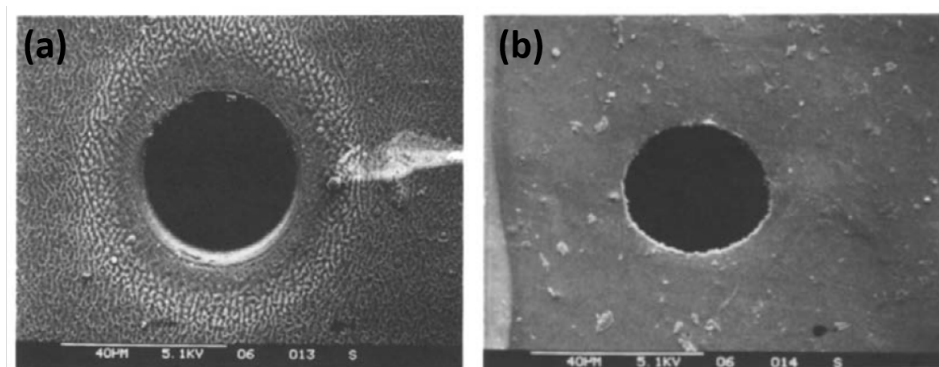


Figure 2.14: Scanning electron micrographs of a 38 μm single microhole membrane: (a) laser entrance side (hydrophilized) and (b) laser exit side.¹¹⁵

scanning electron micrographs of 38 μm single microhole membrane.¹¹⁵

This special geometry influenced ion transfer, and was characterized by Eulate et al.¹¹⁶ Figure 1.16 shows one hundred pores in an array (10×10 pores) were drilled at the borosilicate glass membrane by UV laser ablation. The size of the pores formed in the glass on the laser entry and exit sides differed and resulted a unique cyclic voltammetry response. It provides a solid answer to confirm that the interfaces located at the laser exit side improved the sensitivity of ITIES in comparison to the laser entry side of the membrane.

Beside the glass and polyester, UV eximer laser can fabricate the microhole at other substrates such as polyimide (PI),¹¹⁷ polyethylene terephthalate (PET),^{96,118} However, it is generally difficult to obtain smaller micrometer porous membranes due to UV wavelength limitation. The smallest micron-sized porous membranes ($6.5\mu\text{m}$) was firstly fabricated by Zazpe et al., who used Deep reactive ion etching (DRIE).¹¹⁹ The DRIE process is a gas-phase plasma etch of the silicon, based on the alternate introduction of SF_6 and C_4F_8 into the plasma reaction chamber. The SF_6 etches the exposed silicon, and the subsequent exposure of the etched surface to C_4F_8 produces a fluorocarbon passivation coating on all exposed silicon. All non-vertical surfaces are then stripped of the fluorocarbon coating (but not the vertical surfaces) by exposure to a high-energy ion beam. The thus freshly exposed silicon can then be etched by the SF_6 , while the fluorocarbon-coated vertical walls remain unchanged. This process continues until the etching process stops at the

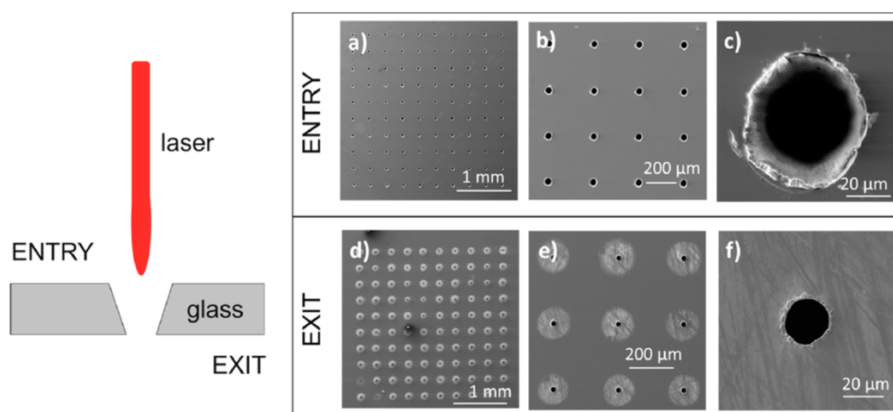


Figure 2.15: Scheme of the laser entry and exit in the glass substrate (left-hand side) along with SEM images of the pores at the laser entry side (a–c) and the laser exit side (d–f).¹¹⁶

bottom of the designed pore length.¹¹⁹

Due to technique process limitation, UV excimer laser ablation and deep reactive ion etching techniques can only create micron-sized holes. Polyester ‘track-etched’ membranes with pore radii of 100 and 15 nm can be served as nanoporous membranes.¹²⁰ Track-etch membranes (TMs) are produced by irradiating polymer films with highly ionizing particles followed by chemical etching. They differ from most conventional polymeric membranes because of their precisely controlled structure. Their pore size, shape, and density can be varied in a controllable manner to produce membranes with the required retention and transport properties. The process of track etching then converts the latent tracks into hollow channels. Different etching methods have been developed that allow for the formation of cylindrical, conical, funnel-like, cigar-like, and other shapes of track-etched pores. Commercial TMs are produced from polycarbonate, polyethylene terephthalate and polyimide.¹²¹ However, it is not easy to control the hole spacing precisely because the generated tracks are not consistent.

With the development of nanotechnology, accurate fabrication of nano-sized pore channels is possible. Scanlon et al. obtained the nanopore array membranes of Silicon nitride (Si_3N_4) by combining the Electron-Beam Lithography (EBL) with reactive ion etching (RIE), wet etching and other techniques.¹²² This membrane fabrication can well yield a

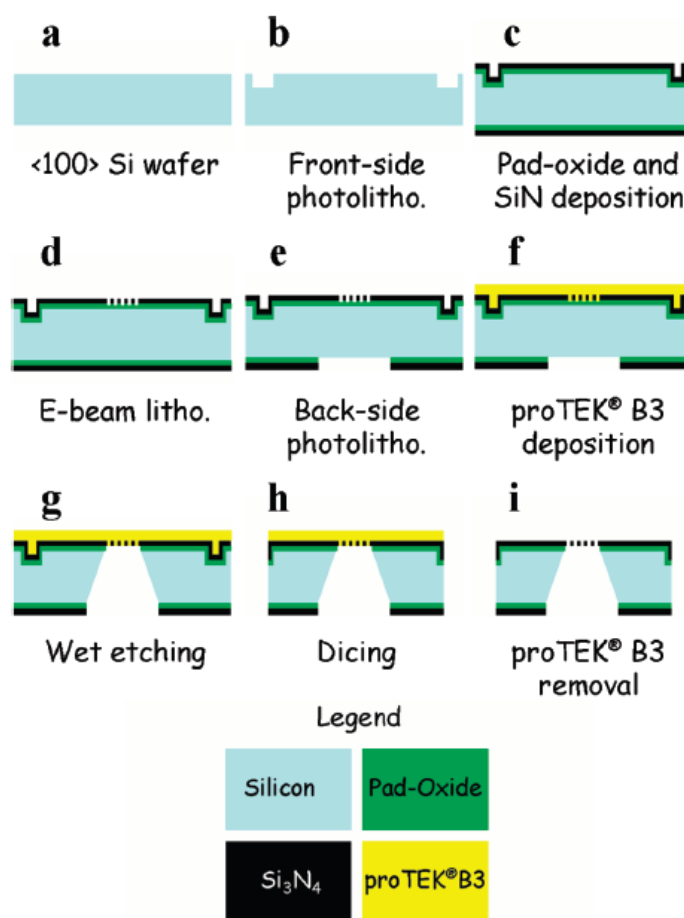


Figure 2.16: Fabrication process flowchart for the preparation of nanopore arrays in Si₃N₄ membranes. Note: this flowchart is not to scale. The bulk silicon layer is 525 μm thick, the pad-oxide layer is 35 nm thick; the proTEKB3 layer is 8 μm thick, and, finally, the patterned Si₃N₄ layer is 100 nm thick.¹²²

range of membranes, each with a unique value for the nanopore radius (r_a), the interpore (centre-centre) separation (r_c), and the total numbers of pores in the array (N_p). Figure 1.17 presents its preparation process of a nanopore array membrane.

At present, this fabrication of nanopore arrays in silicon nitride membranes can obtain the radii down to down to 17 nm.¹²³ Cyclic voltammetry at these nano-interface arrays demonstrated the sensitivity depended directly on the inverse of the nano-interface radius. However, the voltammetric wave-shape became progressively worse as the interface size decreased due to the nucleation of an insoluble ion-pairing at the interface. When prepar-

ing ultra-small size nanopore membranes of Silicon nitride (Si_3N_4), the charge effect of the insulation can cause the shape of the hole to deviate. The conductance measurements showed that the nanopores prepared by the EBL method have several concerns.¹²⁴

1. some of the pores were not completely formed.
2. not fully formed cylindrical pores and were instead conical.
3. do not even extend through the entire membrane thickness.
4. the silanization process may have resulted in reduced pore diameters due to formations of cross-linked multi-layers during the fabrication procedure.

The fabrication of single and array nanopores through (focused ion beam) FIB milling provides an alternative to EBL as it is a direct-write method, and thus facilitates the fast prototyping of nanopore membranes. Silicon nitride (Si_3N_4) and silicon dioxide are frequently used materials for nanopore structures generated by FIB. Focused ion beam (FIB) micro-machining uses highly focused ion beams such as Ga^+ beam to scan and cut the substrate surface inside a vacuum chamber. This technique was originally developed for sample preparation in electron microscopy. The spot size of the FIB is less than 10 nm. The removal rates can further be improved by introducing reactive halogen gases into the processing chamber. Due to the ion bombardment, neutral and ionized atoms are removed from the substrate, enabling micro-machining of the substrate.¹²⁵

There is no doubt that the use of nano-fabrication technologies employed in semiconductor device fabrication will allow the formation of numerous nano-interfaces within a defined area through controlling the geometric parameters of the pore array, namely the pore radius and the pore-to-pore separation.

2.4.1.2 Bottom-up method

The Bottom-up approaches assemble primary building blocks into macroscopic structures based on physical and chemical interactions at the nanoscale. The molecular interactions include non-covalent bonds, such as hydrogen and ionic bonds, van der Waals forces and water-mediated hydrogen bonds. In particular, the bottom-up approach refers to the accumulation of material from the bottom: atom by atom and molecule by molecule. Atomic deposition leads to self-assembly of atoms/molecules and clusters. Together, these

clusters form a single-layer molecular layer by self-assembly.

The typical example is the in-situ mesoporous silica electrodeposition by Poltorak et al.^{126–128} Figure 1.18 illustrates the formation of surfactant-templated silica material at μ ITIES.

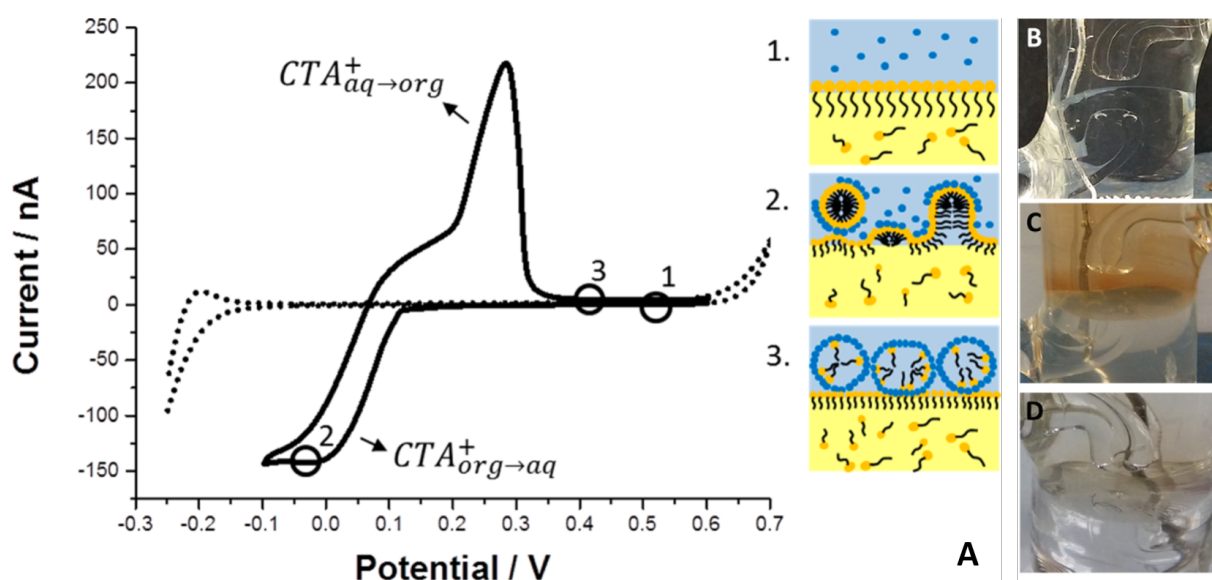


Figure 2.17: A. Typical cyclic voltammogram representing the formation of surfactant-templated silica material at μ ITIES with the pictures on the right correspond to the proposed mechanism for silica deposits formation at μ ITIES at distinct potential regions,¹²⁷ B is the photo recorded before interfacial modification, C is the photo recorded after Hb co-deposition, D is the photo recorded after AP co-deposition.¹²⁹

The generation of mesoporous silica membrane is based on the electrochemical transfer of cetyltrimethylammonium cations (CTA^+) from an organic phase to an aqueous solution of hydrolyzed tetraethoxysilane (TEOS), and catalyzed self-assembly polycondensation of hydrolyzed silica precursors to a free-standing mesoporous silica films at liquid-liquid interface. The mesoporous silica membranes offers the advantages of both microscopic and nanoscopic scale by improving mass transport and fictionalizing of the silica matrix with chemical groups of interest would provide selectivity at the nanoscale.¹²⁷

Recently, Poltorak extended silica deposition with different proteins at the LLI since the interfacial transfer of H^+ to the organic phase, where it catalyzes tetraethoxysilane (TEOS – silica precursor) hydrolysis and condensation reactions, controll interfacial ad-

sorption in the silica matrix.¹²⁹

Moreover, the organic/inorganic hybrid mesoporous silica membrane (HMSM) inside the channels of polycarbonate filtration membrane (PC) was synthesized by using aspiration-induced infiltration, and the surfactant in as-prepared membrane was removed by employing template-extraction.¹³⁰ Zeolite membrane was calcined in a flow of air at 450°C to remove the tetrapropylammonium cations from the silicalite pores: these cations act as structure-directing agents during the growth of the film. The sinusoidal channels are elliptical with pore dimensions of 0.55x0.51 nm. Its stable chemical thermodynamic properties and skeletal structure can well support ITIES and offer the selectivity for ion transfer. Besides, Anodic aluminum oxide (AAO) can also serve as porous alumina membrane due to its properties of easy to use, reproducible, inexpensive, and nondestructive.¹³¹⁻¹³⁵ The surface of each membrane is illustrated in Figure 1.18.

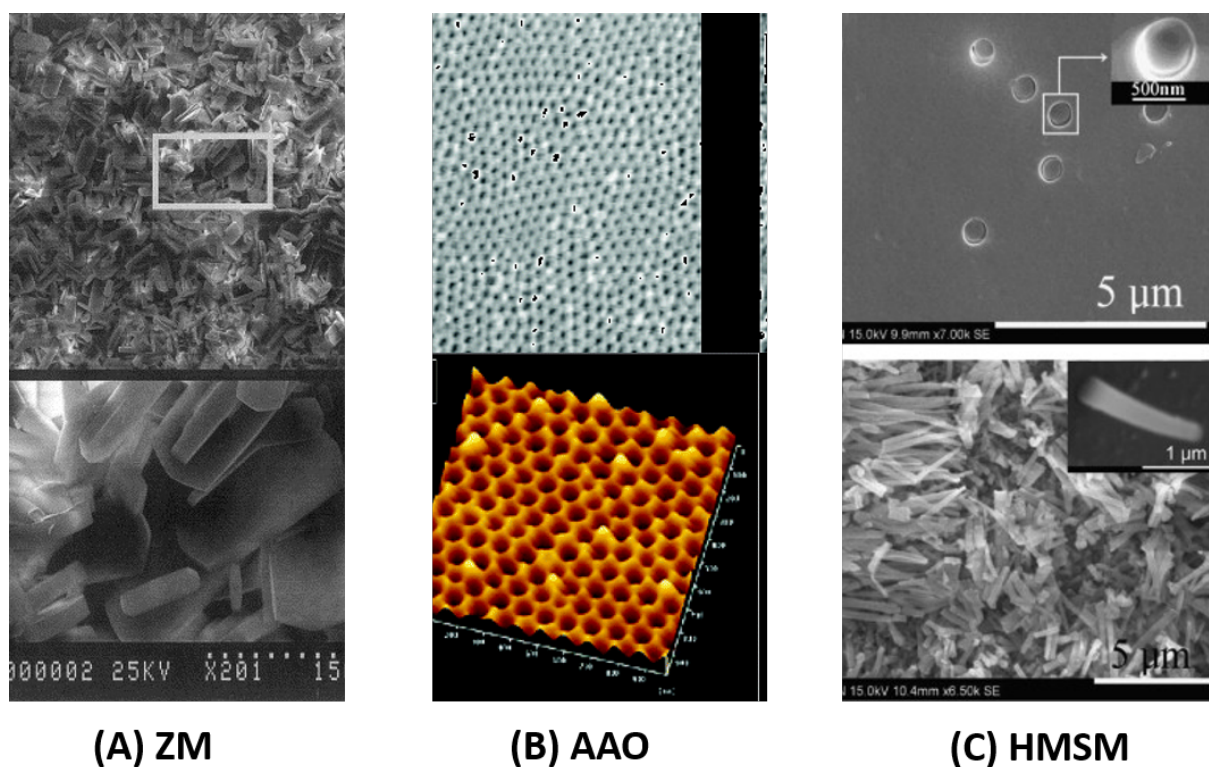


Figure 2.18: (A) SEM images of the zeolite membrane,¹³⁰ (B) SEM images of the anodic alumina layer (top) and AFM image of the top view of the barrier layer on the Al base (bottom),¹³⁴ (C) SEM images of the surface PET-templated HMSM (top) and released silica rods from PET-templated HMSM(bottom).¹³⁶

Furthermore, the bottom-up approach would be a cost-effective way for mesoporous membrane due to the miniaturization of material components down to the atomic level, and further self-assembly processes lead to the formation of nanostructures.

2.4.2 Methodologies for ITIES

From an experimental viewpoint, the difficulties encountered for electrochemical measurements at a liquid/liquid interface are even more severe than that at a solid/electrolyte interface. It is because of the inherent problems of using organic solvents, such as high iR drop and the difficulty in separating the faradaic and charging currents. Despite these problems, almost all modern electrochemical techniques have been applied to study charge transfer reactions at liquid/liquid interfaces. For example, methods, including

cyclic voltammetry and various spectroscopic techniques, have all been employed. Computer simulations have been used in solving problems in this field in the past decade.

2.4.2.1 Electroanalytical methods

There is a wide variety of electrochemical methods; common techniques include cyclic voltammetry (CV), differential square wave voltammetry (DSWV), differential pulse voltammetry (DPV), stripping voltammetry (SV), square wave voltammetry (SWV) and chronoamperometry (CA). They can all be applied to electrochemical studies at the liquid/liquid interface. The cyclic voltammetry method is the most commonly used technique in electrochemical studies at the liquid/liquid interface. The thermodynamic constant associated with the analyte across the interface can be obtained from the CV curve such as $\Delta_o^w \phi$, $\Delta_o^w G_i^{0,w \rightarrow o}$. Differential pulse stripping voltammetry (DPSV) could be considered as one of the most sensitive voltammetry to detect the ion transfer at the ITIES.¹³⁷ DPSV generally has a lower detection limit and higher sensitivity (at least by order of magnitude) than the cyclic voltammetry. Simulation results prove firmly that stripping voltammetry could make asymmetric diffusion behavior of ions at the interface to be more efficient. The stripping signal was enhanced by increasing length of the pores within which the organic phase is located, and then slowing down the diffusion speed of the analyte in the organic phase. The latter is achieved by increasing the viscosity of the organic phase by employing a gelled organic phase. These collective effects are then manifested to enhance stripping currents because the analyte is not lost from the organic phase but instead is retained within the pores close to the interface and thus is available for the back-extraction (stripping) process.^{138,139} Furthermore, adsorptive stripping voltammetry can be a powerful way to detect protein via adsorption-desorption process.^{84,86,95}

2.4.2.2 Experimental system

For all experiment at a large ITIES (mm^2 or cm^2 scale), a four-electrode system is usually adopted with the electrical charge supplied by the external source. The advantage of the four-electrode system is the compensation of the iR drop from both phases. The cell design used is shown in Figure 1.19a. The interface is not fully planar in experimental

because of curvature due to surface tension effects. Although this non-ideality causes non-uniformity of electric field and difficulty in calculations related to the interfacial area, it is not a big problem for analysis. Two counter electrodes made of platinum (wire or plate) are used for passing the current. Usually, The two reference electrodes are Ag/AgCl can be employed to control the external polarization. Besides, the majority of earlier thermodynamic and kinetic data before 90s were gathered from such macro-ITIES set up. However, the limitations for this four-electrode setup are:

1. Both phases need supporting electrolytes resulting in a relatively narrow potential window.
2. The number of available organic solvents is small.
3. Both phases and the dissolved electrolytes are in large quantity that is related to the issues of cost and environmental concern.

As described before, the micro-ITIES electrochemistry started in 1986 due to the application of a pulled glass micropipette by Girault et al.⁷⁹ Unlike macro-ITIES, such pipets or holes are easily made, which means Micro-ITIES can establish more conveniently. The minimization of capacitive current and iR drop, as well as a dramatic improvement of mass transfer rate, are also achieved. So a three-electrode setup, shown in Figure 1.19b, can be employed to simplify the complicated electronics and replace the classical four-electrode system. Moreover, the geometry of the pipette in micro-scale causes an asymmetrical diffusion field – hemispherical for ingress and linear for egress of the transported species. Hence, the voltammogram of ion transfer shows a peak for ion egress and a steady-state wave for ion ingress the pipette.

Later on, with the advanced micro-fabrication in the semiconductor industry, nano-ITIES turns to be possible and has also significantly changed the electrochemistry at liquid/liquid interfaces. Figure 1.20 shows the typical electrochemical cell of a glass U-tube for nano-ITIES, which contains the organic reference solution in contact with the organic phase. The organic phase is covered with the organic reference solution to offer the ideally non-polarizable interface and to limit evaporation of the organic solvent during the experiment. Meanwhile, the nanoporous membrane can be applied at the liquid/liquid interface to improve the selectivity and sensitivity of ion sensing.

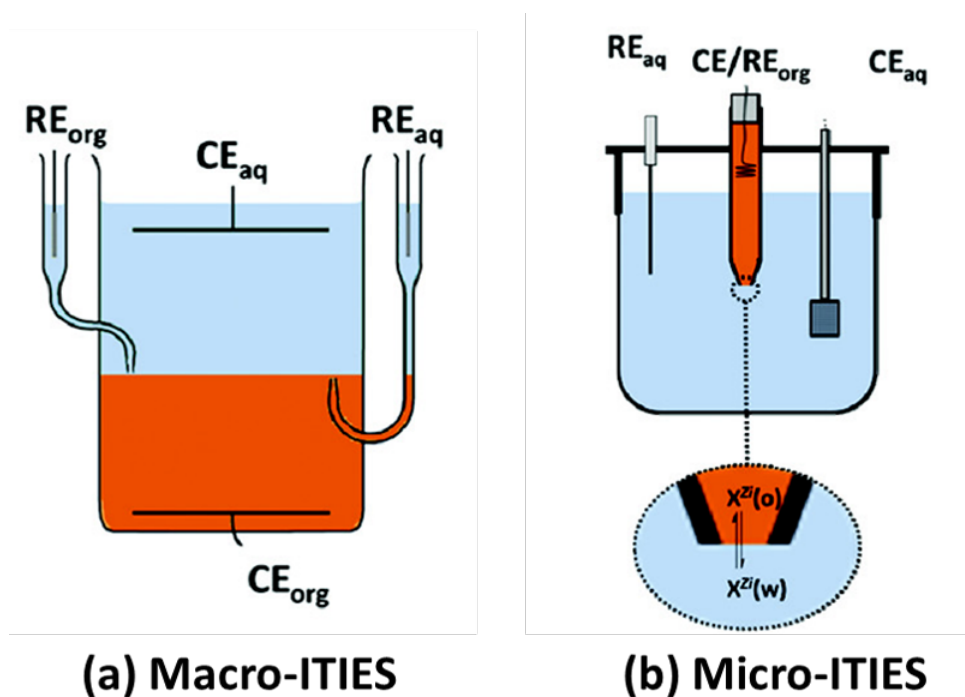


Figure 2.19: Most common experimental set-ups for electrochemistry at the ITIES: (a) macro-ITIES, (b) micro-ITIES. The aqueous phase is represented in blue and the organic phase in orange. RE_{org}: reference electrode for the organic phase, RE_{aq}: reference electrode for the aqueous phase, CE_{org}: counter electrode for the organic phase, CE_{aq}: counter electrode for the aqueous phase.⁷⁷

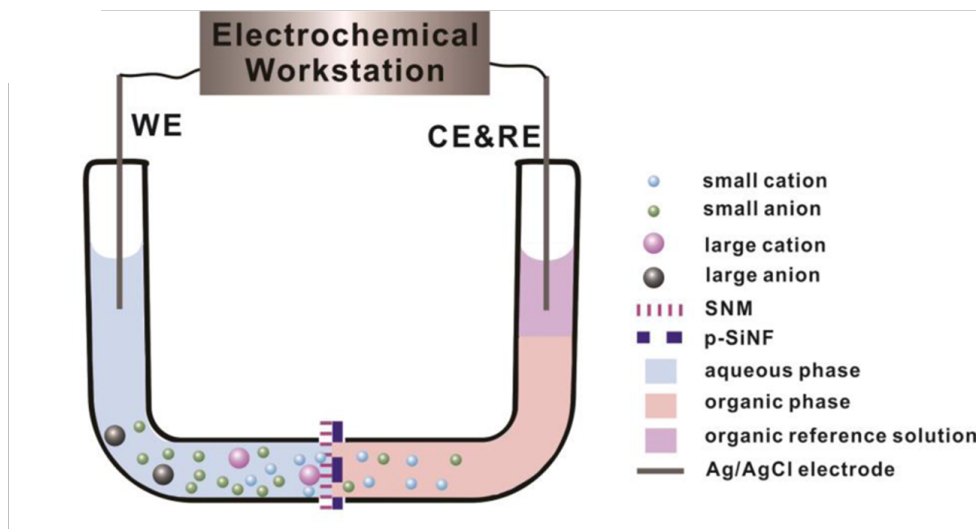


Figure 2.20: A two-electrode setup with the support of nano porous membrane at a glass U-Tube Cell for Nano-ITIES.¹⁴⁰

2.4.3 ITIES Applications

Recent developments in the field of electrochemistry at the ITIES have emerged over the past 30 years. Although they have not necessarily resulted in commercial analytical applications yet, they still offer promising perspectives for the future. More and more application examples of charge transfer reactions at liquid/ liquid interfaces have been demonstrated. This section introduces the ITIES application of ion sensors, kinetic studies, and SECM imaging to illustrate the unique nature of liquid-liquid interface.

2.4.3.1 Pharmacokinetics

In pharmaceutical sciences, $\log P$ is an important parameter to define drugs' lipophilicity or hydrophilicity and plays an important role to predict adsorption in soils and sediments.^{141,142} It is commonly measured by its partition coefficient in the octanol/water biphasic system. This parameter has been widely used in equations as to estimate bio-accumulation in animals and plants and to predict the toxic effects of a drug in Quantitative structure–activity relationship (QSAR) studies.¹⁴³ However, in many systems, ionic species enter the aqueous phase would have protonation and a more complex approach is

then required.¹⁴⁴ For instance, measurement of K_{ow} of 10 phenols and carboxylic acids at pH 12 indicates that both free ions and ion-pairs were present in the octanol phase at significant concentrations.^{145,146} Thus, the octanol–water partition coefficient for ionic species P_i is introduced. Moreover, the determination of the partition coefficient of the neutral and ionic form requires a pH modification of the octanol–water system, and this must be done very carefully.

Since the transfer Gibbs energy of species can be easily determined by cyclic voltammetry at a liquid/liquid interface, the water/DCE system could be used to replace the water/n-octanol system and established the ionic partition diagram as described in subsection 1.1.5 because DCE-water partition coefficients can be correlated with n-octanol-water coefficients.¹⁴⁷ Figure 1.20A shows the regression plotting between $\log P_{\text{octanol}}$ and $\log P_{\text{DCE}}$, and Figure 1.20B illustrates the ion partition diagram of the quinidine drug. It generally offers pH-lipophilicity profile and direct visualization of all the transfer mechanisms.

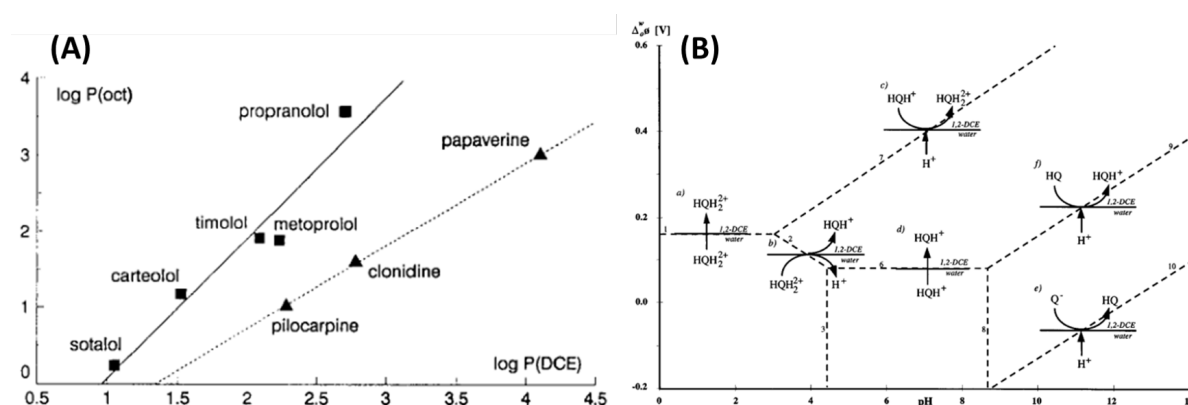


Figure 2.21: (A) Comparison of $\log P_{\text{octanol}}$ values and $\log P_{\text{DCE}}$ for different drugs,¹⁴⁷ (B) Schematic transfer mechanisms of the various forms of quinidine at the water/1,2-DCE interface. The following transfers are outlined: (a) simple HQH₂²⁺ transfer; (b) HQH₂²⁺ transfer by interfacial dissociation; (c) assisted proton transfer facilitated by HQH⁺(o); (d) simple HQH⁺ transfer; (e) assisted proton transfer facilitated by Q⁻; (f) assisted proton transfer facilitated by HQ(o).⁶⁴

2.4.3.2 Amperometric sensors

The application of ion sensors based on ITIES technique in environmental monitoring and clinical diagnosis is still great challenge. Due to the miniaturization of liquid-liquid

interface, such ion sensors have been developing. Until now, some ions including drugs, pollutants, proteins having been tested. Table 1.1 lists ion sensing achieved by ITIES. Table 1.2 lists organic compounds sensing achieved by ITIES. Table 1.3 lists proteins sensing achieved by ITIES.

Table 2.1: ion sensing by ITIES technique.

Targeted ion	Support	Method	LOD
Na ⁺	micropipette	DPV	25μM ¹⁴⁸
	PVC-NPOE array	CV	50ppb ¹⁴⁹
NH ₄ ⁺	PVC-NPOE array	CV	50ppb ¹⁴⁹
	PET array	DSWV	0.12μM ⁹⁷
K ⁺	micropipette	CV	50μM ¹⁵⁰
	micropipette	DPV	50μM ¹⁵¹
Ag ⁺	PVC-NPOE array	CV	50ppb ¹⁴⁹
	micropipette	CV	0.2μM ¹⁵²
Cu ²⁺	PET array	DPSV	1μM ¹⁵³
Cd ²⁺	PET array	DPSV	20ppb ¹¹⁸
Cr ⁶⁺	PET array	LSV	0.5μM ¹⁵⁴
NO ₃ ⁻	PET array	DPV	0.2mM ¹⁵⁵
	PET array	DPV	1ppt ¹⁵⁶
F ⁻ , Cl ⁻ , Br ⁻ , SO ₄ ²⁻	PET array	DPV	1ppt ¹⁵⁶
ClO ₄ ⁻	PET array	DPSV	10ppb ⁹⁰

Table 2.2: Small organic compounds sensing by ITIES technique.

Targeted drug	Support	Methods	LOD
Propranolol	Silicon array	DPSV	0.02 μM ⁸⁷
	Silicon array	DPSV	0.05 μM ¹⁵⁷
Dopamine	PET array	SWV	0.35 μM ⁹⁹
	PET array	DPV	0.05 μM ¹⁵⁸
Noradrenaline	Silicon array	SWV	0.5 μM ¹⁵⁹
	PET array	SWV	0.17 μM ⁹⁹
Choline	PET array	SV	3 μM ¹⁶⁰
Paraoxon	PVC array	DPSV	0.5 μM ¹³⁷
Parathion	PVC array	DPSV	0.5 μM ¹⁶¹
Vitamin-B1	micropipette	CV	4.6 μM ¹⁶²
Daunorubicin	PET array	DPV	0.8 μM ⁹⁸
Topotecan	micropipet	DPSV	0.1 μM ¹⁶³
Serotonin	nanopipet	CV	77 μM ¹⁶⁴
Acetylcholine	nanopipet	CV	205 μM ¹⁶⁴
Tryptamine	nanopipet	CV	86 μM ¹⁶⁴

Table 2.3: Proteins sensing by ITIES technique.

Targeted protein	Support	Method	LOD
Protein digests	Silicon array	DPSV	0.55 μM ⁸⁸
Hen-Egg-White-Lysozyme	Silicon array	AdSV	0.03 μM ⁸⁴
Myoglobin	Silicon array	CV	1 μM ⁹³
Albumin	PTFE array	CA	1.2 μM ¹⁶⁵
haemoglobin	Silicon array	AdSV	48 nM ⁸⁶
Rat amylin	Silicon array	CV	2 μM ⁸⁵
Insulin	Silicon array	AdSV	1 μM ⁹⁵

Chapter 3

Experimental and Instrumentation

3.1 Introduction

In this chapter, experimental techniques and chemicals will be presented. The experimental techniques are mainly classified into two categories: shake-flask experiments and electrochemical measurements. Electrochemical measurements include the four-electrode system for macro ITIES and the three-electrode system for micro ITIES. All chemicals were used as received without further purification. All aqueous solutions were prepared with ultra-pure water (Millipore Milli-Q, specific resistivity 18.2 M Ω .cm). Other characterization techniques such as Raman spectroscopy will be detailed in the corresponding place.

3.2 Chemicals

All chemicals are analytical grade and used as received without further purification. The table 2.1 gives the common used chemical for the protocols of electrolytes at the ITIES.

Table 3.1: Full list of chemicals used for the protocols of electrolytes and single pore micro capillaries.

Name	Abbreviation	CAS Number	Molar mass g/mol	Source
Bis(triphenylphosphoranyldiene) ammonium chloride	BTPPA ⁺ Cl ⁻	21050-13-5	574.03	Aldrich
Potassium tetrakis (4-chlorophenylborate)	K ⁺ TPBCl ⁻	14680-77-4	496.11	Fluka
Sodium chloride	NaCl	7647-14-5	58.44	Prolabo
Lithium chloride	LiCl	7447-41-8	42.39	
Cetyltrimethylammonium bromide	CTAB	57-09-0	364.45	
1,2-dichloroethane	1,2-DCE	107-06-2	98.96	
Ethanol	EtOH	64-17-5	46.07	Sigma
Methanol	MeOH	67-56-1	32.04	
Acetone	Ace	67-64-1	58.08	
Hydrochloric acid	HCl	7647-01-0	36.46	
Nitric acid	HNO ₃	7697-37-2	63.01	

3.3 Electrochemical set-ups

Different set-ups were used among this work and their descriptions are divided in agreement with the successive parts of the thesis i.e. macroscopic ITIES modification with the chitosan electrodeposition, microscopic ITIES modification

3.3.1 Four-electrode system for macro-ITIES

The custom made electrochemical cells used to study the electrochemical deposition at the macroscopic ITIES are presented in Figure 2.1. The cells were custom made from glass tubes with inner diameters 12 mm and its interfacial surface area ($A_{\text{interface}}$) equal to 1.13 cm². The reference electrodes placed in the Luggin capillaries of each phase were Ag/AgCl

wires whereas the counter electrodes were made from platinum wire or platinum mesh. In detail, the Ag/AgCl electrode was prepared by oxidation of silver wire in a saturated solution of FeCl_3 .

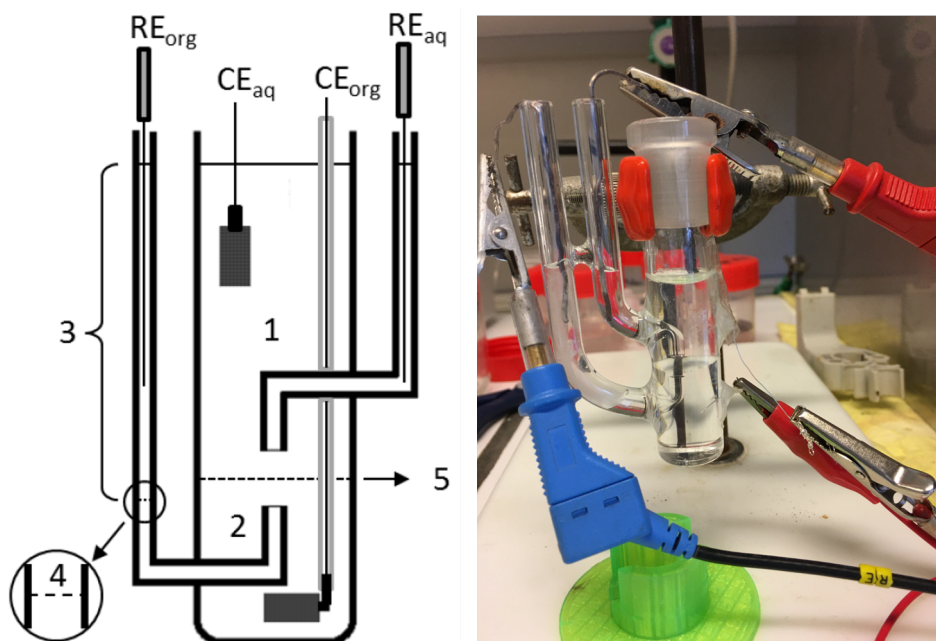


Figure 3.1: Four-electrode electrochemical cell with macroscopic liquid-liquid interface. RE_{org} and RE_{aq} represent the organic and aqueous reference electrodes, CE_{org} and CE_{aq} corresponding to the organic and aqueous counter electrodes respectively. 1 – Aqueous phase; 2 – Organic phase; 3 – Organic reference phase; 4 – Liquid-liquid interface between the organic and organic reference phases; 5 – ITIES

During the electrochemical measurement or electrodeposition, the organic reference solution was prepared with the mixed aqueous solution of 10 mM $\text{BTPPA}^+\text{Cl}^-$ and 10 mM LiCl . Thus, for one electrochemical cell, it can be written as:



The electrochemical cell compositions were modified depending on the specific experimental requirements.

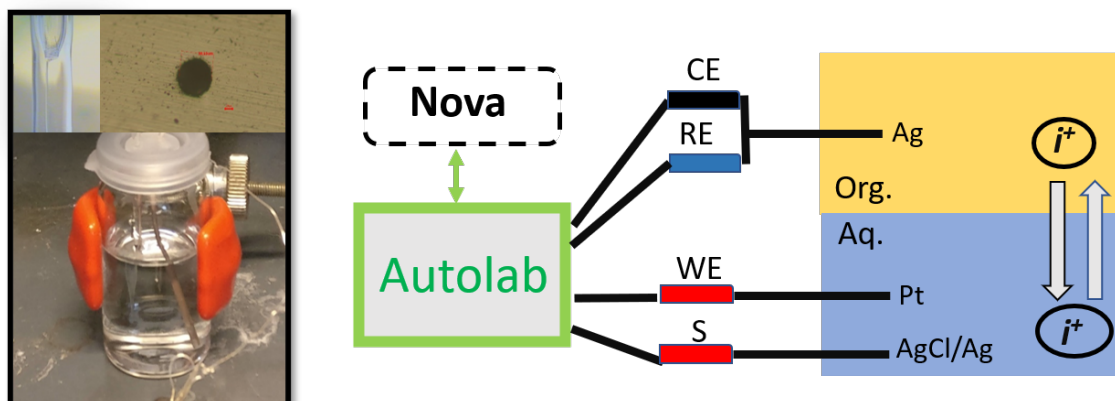


Figure 3.2: Three electrode system Set-up used during pesticide measurement (\varnothing is the pore diameter of capillary tip equal to 50 μm). Electrochemistry at the liquid-liquid interface was controlled with the CEaq – aqueous counter electrode (platinum mesh), REaq – reference counter electrode (Ag/AgCl) and REorg/CEorg – Ag wire used as organic quasi- reference and counter electrode in one.

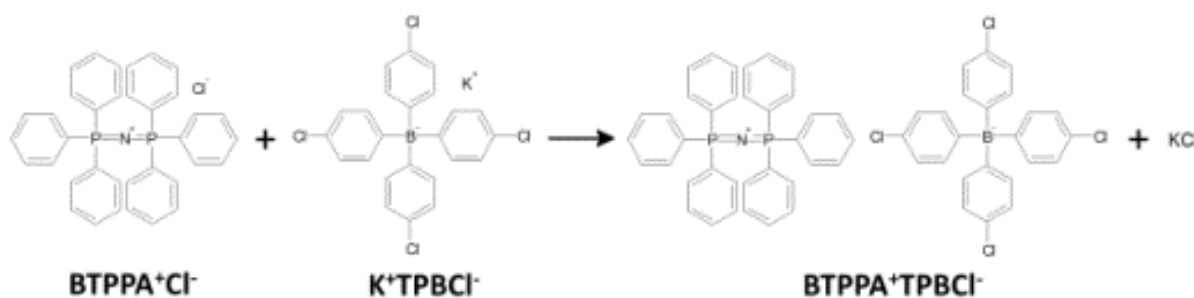
3.3.2 Three-electrode system for micro-ITIES

The three-electrode cell is the most commonly used system in electrochemical measurements due to the simplified set-up and the less usage of chemical materials. Typically, a solid and inert electrode (such as Ag) is used as the working electrode and the quasi-reference electrode in the organic phase with the support of micro or nano pore capillary. A platinum electrode as the counter electrode and an Ag/AgCl wire as the reference are immersed in the aqueous phase. In this arrangement, the potential of the working electrode is controlled with respect to the reference electrode, while the current passes the loop between the working and the counter electrodes. Figure 2.2 illustrates the experimental set-up and its mechanism.

3.4 Protocols

3.4.1 Preparation of $BTPPA^+TPBCl^-$ as organic supporting electrolyte

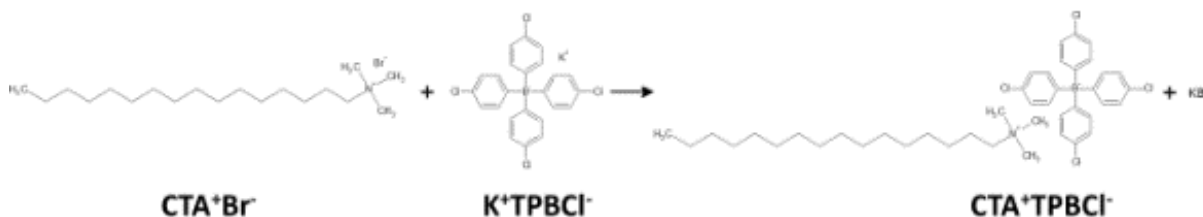
Bis(triphenylphosphoranyldiene)ammonium tetrakis(4-chlorophenylborate) was used as the organic electrolyte salt and prepared according to the following reaction:



1. 1.25 g of $BTPPA^+Cl^-$ and 1 g of K^+TPBCl^- were dissolved in 10 ml and 20 ml of a 1:2 mixture $H_2O : MeOH$ solution respectively. The $BTPPA^+Cl^-$ solution was added to the K^+TPBCl^- drop-wise while stirring, forming a white precipitate. The beaker was then covered in parafilm® and left in the fridge for 48 hours, continuously stirring.
2. After this time, the solution was filtered under vacuum for approximately 30 minutes to remove the solvent. The resulting product was transferred to a dry beaker, covered with aluminum foil and stored in a desiccator overnight.
3. The reaction product was then rinsed with acetone to dissolve the $BTPPA^+TPBCl^-$ and the solution was filtered under gravity using filter paper. The beaker was covered with parafilm that had holes in it to allow the acetone to evaporate and then stored in the fridge, until crystals had formed.
4. The rectangular crystals were rinsed with a 1:1 *Acetone* : H_2O mixture, filtered under vacuum and placed in a desiccator overnight.
5. The resulting crystals of $BTPPA^+TPBCl^-$ were stored in the fridge, with the sample vial covered in aluminum foil to prevent degradation from light exposure.

3.4.2 Preparation of CTA^+TPBCl^- as organic supporting electrolyte

Cetyltrimethylammonium tetrakis(4-chlorophenylborate) (CTA^+TPBCl^-) – surfactant template salt soluble in the organic phase was prepared according to following metathesis reaction:



1. Equimolar amounts of CTA^+Br^- (0.800 grams) and K^+TPBCl^- (1.089 gram) were weighted and dissolved in 5 ml and 10 ml of a 1:2 mixture of H_2O : $MeOH$, respectively. Then a solution of CTA^+Br^- was added drop-wise to a vigorously stirring solution of K^+TPBCl^- . The product of reaction - white precipitate - was then left under stirring in the fridge for 48h.
2. After this time suspension was filtered under vacuum and then dried overnight in a desiccator.
3. Dry CTA^+TPBCl^- was dissolved in acetone and was filtered under gravity using a paper filter. The beaker containing CTA^+TPBCl^- was covered with the Parafilm® and placed under the fume hood. Small holes were made in Parafilm® to allow acetone evaporation.
4. Recrystallized CTA^+TPBCl^- is very dense and viscus liquid residual at the bottom of the beaker.
5. Lastly, this component was dissolved in 1,2-DCE as the organic phase and was stored at 4°C.

3.4.3 Preparation of counter electrode

Due to the excellent electrochemical inertness, superb electrical conductivity and good mechanical stability in both aqueous and organic solutions, platinum (Pt) has been widely employed as counter electrode material. The fabrication steps are described below with essential components used in Figure 2.3.



Figure 3.3: Components used for the counter electrode assembly.

1. A small amount of platinum mesh was welded around a platinum wire of ca. 1 cm in length.
2. The wire was then placed inside a borosilicate capillary. Using a Bunsen burner, the glass around the platinum wire was gently melted to seal the platinum mesh and wire to the capillary.
3. With a long needle syringe, the conductive resin was inserted inside the capillary, just above the wire. Next, ca. 15 cm of copper-tinned wire was placed inside the glass capillary until it came into contact with the conductive resin, then left in the oven at 130 °C for a few hours to set. The length of the copper-tinned wire needs to be longer than that of the capillary as a few centimeters needs to extend out for electrical contact.
4. Once the resin was cured, a micro-needle was used to fill the interior of the capillary with silicon sealant, and it was placed the oven overnight to set.
5. Finally, rubber tubing was added to the top of the capillary to secure the contact wire as Figure 2.4 shown.



Figure 3.4: Platinum mesh based counter electrode.

3.4.4 Preparation of single pore micro-ITIES capillary

The reproducible procedure of preparation of single pore capillaries supporting miniaturized liquid-liquid interface is described in here.

1. Initially, the borosilicate glass capillary has been closed in the middle. One end of the capillary was clogged with the Parafilm® and then the capillary has been placed vertically with the opened end directed upwards so that its half-length was placed in the middle of the ring made from several scrolls of the nickel/chrome 80/20 wire (Figure 2.5a). With an external power supply, the current was passed through the wire and increased the temperature in the vicinity of the capillary (Figure 2.5b), which in turn decreased the glass viscosity. Next, the pump was attached to the top of the capillary. Under vacuum, the walls in the heating region were collapsed, closing the capillary in the mid-length.

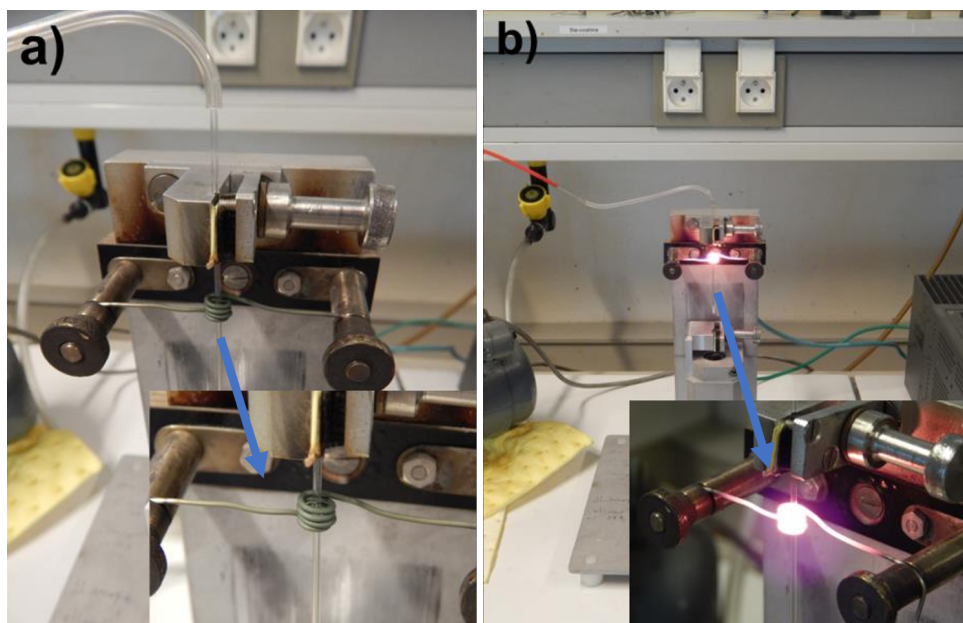


Figure 3.5: The vertical capillaries puller was used to close the capillary in the middle and to melt the gold wire into the glass: (a) shows the capillary placed in the nickel/chrome wire ring before current passage, (b) after current was passed through the wire.

2. Next step was to place a short piece of gold wire (length 3-5 mm, diameter $\varnothing = 25$ or $50 \mu\text{m}$) just above the collapsed part of the capillary. The gold wire was melted into the glass in the same manner as the capillary was closed. The second piece of the gold wire was melted into the glass as it is shown in Figure 2.6a. Subsequently, the capillary was cut with the diamond knife in the mid-length (Figure 2.6b).

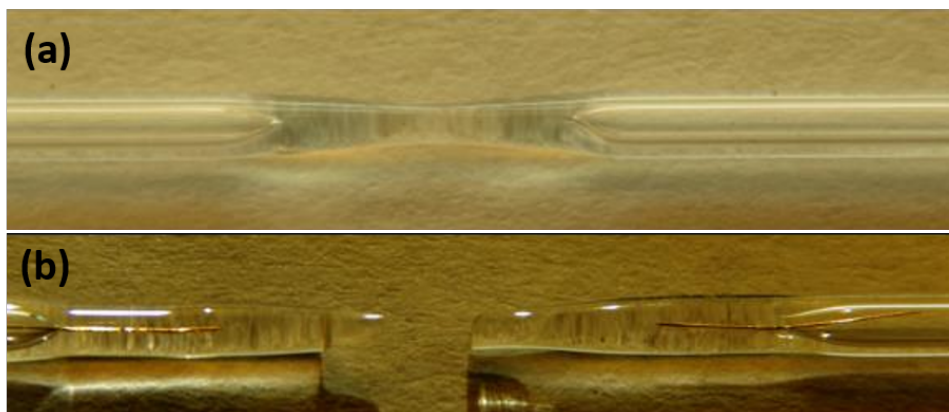
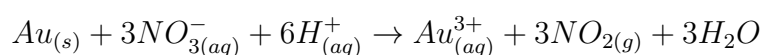


Figure 3.6: (a) Borosilicate glass capillary with collapsed walls closing the capillary in the middle, (b) Borosilicate glass capillary contains the 50 μm gold wires melted into the glass on double side of the capillary mid-length and splitted into two pieces, each contained gold wire.

3. Two resulting pieces have been polished (initially with 250 granulation sandpaper) in order to remove the redundant layer of glass up to the gold wire. The polishing was repeated three more times with the increasing - 1000, 2500 and 4000 - granulation of sandpaper in order to smooth the surface.
4. The gold from the glass was removed by placing the capillary overnight into the beaker containing aqua regia which is a mixture of nitric acid and hydrochloric acid, in a molar ratio of 1:3. The gold etching has to be held under the fume hood due to the toxic nitrogen dioxide evolution during the reaction:



5. On the following day, remains of aqua regia inside the capillary were carefully removed by rinsing them a few minutes with distilled water. The capillary contained a fixed diameter of micropore, which will support the liquid-liquid interface.

3.5 Instrumentation

Electrochemical measurements – All electrochemical measurements were performed with a potentiostat (PGSTAT 302N Metrohm, Switzerland) with the four-electrode

configuration or the three-electrode configuration. The potentiostat was controlled by NOVA software.

Raman spectroscopy – The chitosan films obtained were characterized by Raman spectroscopy (Jobin Yvon T64000 high resolution confocal Raman spectra with a nitrogen-cooled CCD detector with green laser light).

Fourier-transform infrared spectroscopy – The chitosan films obtained were also characterized by Fourier-transform infrared spectroscopy (Thermo Nicolet 8700 FTIR - near/middle/far infrared).

Profilometry based on shear force measurement –The thickness of chitosan films was estimated from profilometry measurements using the Dektak XT apparatus with Vision 64 software (Brüker).

Differential scanning calorimetry (DSC) - As the most frequently used thermal analysis technique, DSC measures enthalpy changes in samples due to changes in their physical and chemical properties as a function of temperature or time. Differences in heat flow arise when a sample absorbs or releases heat due to thermal effects such as melting, crystallization, chemical reactions, polymorphic transitions, vaporization and many other processes. Specific heat capacities and changes in heat capacity, for example during a glass transition, can also be determined from the difference in heat flow. The experiment was carry with DSC 3 from METTLER TOLEDO and its software STAR^e System.

3.6 Experimental section

3.6.1 Experimental section of pesticide detection

The schematic presentation of experimental measurement is demonstrated with the three-electrode system for micro-ITIES. In detail, metam sodium is hydrophilic, and its initial solution (10 mM) was prepared with deionized water. Ametryn and imidacloprid are hydrophobic, and they were dissolved in EtOH to have initial solution 10 mM. All of the initial solutions were kept in the refrigerator to avoid degradation.

The electrochemical experiment was carried out in a glass cell which was filled with 2 mL aqueous phase solution. Single micropore capillary was filled with 10 mM BTPPA⁺TPBCl⁻

and was immersed in aqueous phase. A platinum wire was worked as a working electrode and an Ag/AgCl wire was worked as a counter electrode. Both of them were placed in the aqueous phase solution. An Ag wire was placed into capillary as the counter electrode and the working electrode for the organic phase. We then applied cyclic voltammetry to characterize the blank solution to confirm that there was no contamination in the potential window. Subsequently, we placed the initial solution of the analyte pesticide into the aqueous phase and tested it again by cyclic voltammetry to obtain its electrochemical response.

In details, commercial solutions of 1 M HCl or 1 M NaOH were used for pH adjustment. 50 mM Tetramethylammonium chloride (TMA^+Cl^- , 98% Aldrich) was prepared in deionized water to characterize the size of single pore capillary. 50 mM Tetrabutylammonium chloride (TBA^+Cl^- , 97% Aldrich) was also prepared in deionized water and was used to calibrate the half-wave Galvani potential if necessary. All the tested pesticides and related chemicals are listed in Table 3.3.

Table 3.2: Full list of tested pesticides and other used chemicals.

Name	Abbreviation	CAS Number	Molar mass $\text{g}\cdot\text{mol}^{-1}$	Source	
Imidacloprid	IMI	138261-41-3	255.66	Aldrich	
Ametryn	AME	834-12-8	227.33		
Metam-sodium hydrate	MET	137-42-8	129.18		
Methylamine	MA	74-89-5	31.06		
Octanoic acid	OA	124-07-2	144.21		
Hydrochloric acid	HCl (1M)	7647-01-0	36.46		
Sodium hydroxide	NaOH (1M)	1310-73-2	39.99		
Tetramethylammonium chloride	TBA^+Cl^-	75-57-0	109.60		Fluka
Tetrabutylammonium chloride	TMA^+Cl^-	214-195-7	277.92		

3.6.2 Experimental section of silica deposition

The macroscopic electrochemical cell was prepared under a fume hood using special luggin capillary. It contained c.a. 2.5 mL 10 mM BTPPA⁺TPBCl⁻ in 1,2 DCE at the bottom while c.a. 3 mL of 5 mM LiCl solution at the top. The organic reference solution 10 mM BTPPA⁺Cl⁻ in 5 mM LiCl is connected with the organic solution. The four electrodes are assembled with the potentiostat following the description in chapter 2 and the operating software is the Nova 2.10 software. A first so-called blank acquisition can be carried out. It is used to check that all the connections have In order to make sure the aqueous or organic solutions do not present any contamination or other contamination, blank test was generally carried on firstly. Thus, the electrochemical cell-ups were:

Ag | AgCl | 14 mM CTA⁺TPBCl⁻ in 1,2 DCE || 50 mM TEOS in H₂O | AgCl | Ag (silica electrodeposition)

Ag | AgCl | 14 mM CTA⁺TPBCl⁻ in 1,2 DCE || x mM TMA⁺Cl⁻ 10 mM LiCl in H₂O | AgCl | Ag (electrochemical characterization)

The microscopic electrochemical cell was using borosilicate glass capillary. The silica precursor use in this study was TEOS and the pH for TEOS hydrolysis of in the aqueous phase was set at pH=3. This pH of aqueous phase was adjusted until pH=9 to have enough OH⁻ for the silica film electrodeposit at micro-interface. 1 M HCl solution and 1 M NaOH solution were used to modify the pH value. Trimethylchlorosilane was used as salinizing agent to improve hydrophobicity of capillary. Lastly, TMA⁺ was chosen as the model ion to characterize the performance of silica film at the liquid-liquid interface. Thus, the micro-electrochemical cell-ups were:

Ag | 14 mM CTA⁺TPBCl⁻ in 1,2 DCE || 50 mM TEOS in H₂O | AgCl | Ag (silica electrodeposition)

Ag | 10 mM BTPPA⁺TPBCl⁻ in 1,2 DCE || x mM TMA⁺Cl⁻ 10 mM LiCl in H₂O | AgCl | Ag (electrochemical characterization)

All the measurements were carried by PGSTAT 302N (Metrohm, Switzerland) and Figure 2.7 shows experimental capture for macro-scale electrochemical cell experiment (A) and micro-scale electrochemical cell experiment (B). In addition, the surface morphology of the capillary tip was registered by optical microscopy using an optical microscope

Nikon-japan to observe the difference at each stage.

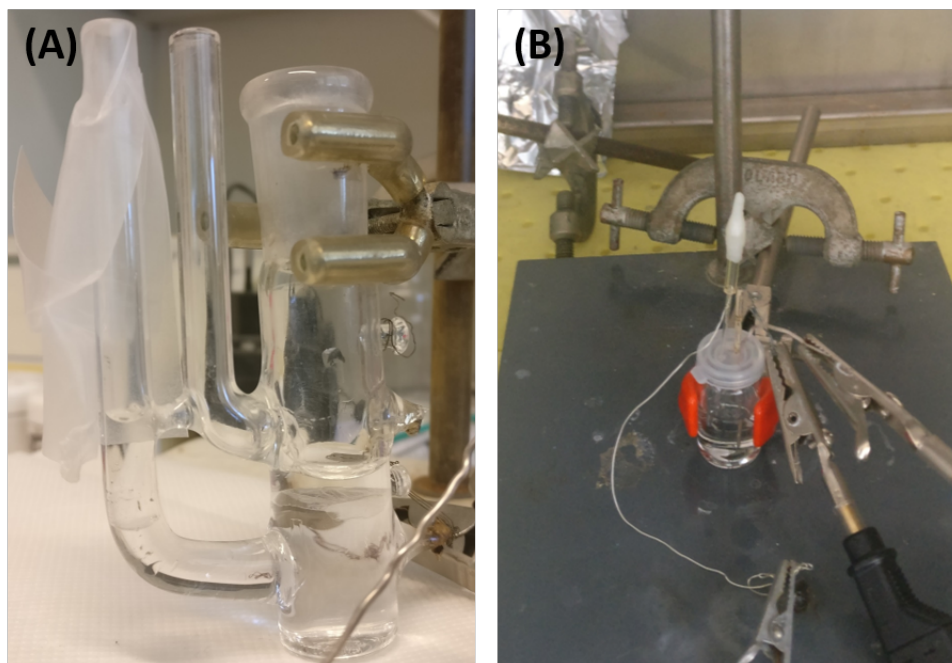


Figure 3.7: Experimental capture of silica modification at liquid-liquid interface: (A) macro ITIES, (B) micro ITIES after galvanostatic deposition.

All the experimental materials about silica deposition are listed in Table 2.3.

Table 3.3: Full list of chemicals used for the protocols of electrolytes at silica modified ITIES.

Name	Abbreviation	CAS Number	Molar mass g/mol	Source
Bis(triphenylphosphoranyldiene) (4-chlorophenylborate)	BTPPA ⁺ TPBCl ⁻	-	995.59	Synthesized
Cetyltrimethylammonium (4-chlorophenylborate)	CTA ⁺ TPBCl ⁻	-	786.01	Synthesized
Sodium chloride	NaCl	7647-14-5	58.44	Prolabo
Lithium chloride	LiCl	7447-41-8	42.39	Aldrich
Cetyltrimethylammonium bromide	CTAB	57-09-0	364.45	Aldrich
Tetraethoxysilane	TEOS	74-10-4	208.33	Alfa Aesar
Tetramethylammonium chloride	TMA ⁺ Cl ⁻	75-57-0	109.60	Fluka
Tetraethylammonium chloride	TEA ⁺ Cl ⁻	56-34-8	165.70	Fluka
Tetrabutylammonium chloride	TBA ⁺ Cl ⁻	214-195-7	277.92	Fluka
1,2-dichloroethane	1,2-DCE	107-06-2	98.96	
Ethanol	EtOH	64-17-5	46.07	
Hydrochloric acid	HCl	7647-01-0	36.46	Sigma
Sodium hydroxide	NaOH	1310-73-2	39.99	

3.6.3 Experimental section of chitosan deposition

The chitosan solution was prepared by a known amount of chitosan powder in deionized water, adding acetic acid drop by drop and mix them with the magnetic force for several hours (ca.6 hours) until it is completely dissolved, and then store the 1 wt% chitosan (CS) solution in a refrigerator at 4°C . For 0.1 wt% chitosan solution using in micro ITIES, the

acetic acid was replaced by HCl. All the chemicals are listed in Table 2.4.

Table 3.4: Full list of chemicals used in chitosan electrodeposition.

Name	Abbreviation	CAS Number	Molar mass g/mol	Source
Chitosan low molecular weight	CS-LM	9012-76-4	50,000 - 190,000 Da	
Chitosan medium molecular weight	CS-MM	9012-76-4	-	
Chitosan high molecular weight	CS-HM	9012-76-4	310,000 - 375,000 Da	
Acetic acid	HAc	64-19-7	60.05	Sigma
Lithium chloride	LiCl	7447-41-8	42.39	
Methyle yellow	MY	60-11-7	225.29	
Terephthalaldehyde	TPA	623-27-8	134.13	
decamethylferrocene	DmFc	12126-50-0	326.30	
Ethanol	EtOH	64-17-5	46.07	
Hydrochloric acid	HCl	7647-01-0	36.46	
Sodium hydroxide	NaOH	1310-73-2	39.99	

The macroscopic electrochemical cell was prepared and contained c.a. 1.5 mL 10 mM BTPPA⁺TPBCl⁻ in 1,2 DCE at the bottom while c.a. 2 mL of 1 wt% CS in 5 mM LiCl solution at the top. The organic reference solution 10 mM BTPPACl in 5 mM LiCl is connected with the organic solution. The four electrodes are assembled the potentiostat following the description in chapter 2 and the operating software is the Nova 2.10 software. Thus, the electrochemical cells were:

Ag | AgCl | x mM TPA + 10 mM BTPPA⁺TPBCl⁻ in 1,2 DCE || 1 wt% CS 5 mM LiCl in H₂O | AgCl | Ag (macro chitosan film deposition)

Ag | AgCl | 10 mM BTPPA⁺TPBCl⁻ in 1,2 DCE || x mM TMA⁺Cl⁻ or x mM TEA⁺Cl⁻ | AgCl | Ag (electrochemical characterization)

The microscopic electrochemical cell was using borosilicate glass capillary. The chi-

tosan hydrogel in this study was the same solution from macroscopic experiment. Trimethylchlorosilane was also used as salinizing agent to improve hydrophobicity of capillary. Lastly, TMA and TEA was chosen to characteristics the performance of micro chitosan film. Thus, the electrochemical cell-ups were:

Ag | x mM TPA + 10 mM BTPPA⁺TPBCl⁻ in 1,2 DCE || 1 wt% CS 5mM LiCl in H₂O | AgCl | Ag (micro chitosan film deposition)

Ag | 10mM BTPPA⁺TPBCl⁻ in 1,2 DCE || x mM TMA⁺Cl⁻ + 10 mM LiCl in H₂O | AgCl | Ag (electrochemical characterization)

Chapter 4

Pesticides detection

4.1 Introduction

Pesticides have been over-used to increase food yields in modern agriculture. The number of pesticide molecules developed has also been steadily rising along with the massive demand for pesticides in specific food production period. In 2008, approximately 2.36 million kg of pesticides were used worldwide.¹⁶⁶ Currently, there are more than 536 and 1,055 different registered pesticides molecules in the EU and the USA.¹⁶⁶ However, these compounds may not be easily degraded and would accumulate in soil and river such as ametryn.^{167,168} They may be cause of environmental pollution and will cause severe ecological damage and health risk. Food may be contaminated by these small organic molecules (e.g., herbicides, pesticides, residues of these drugs). Recently, the role of neonicotinoid insecticides has a negative impact in the decline of populations of pollinator bees. Imidacloprid-contaminated bumble bee colonies were found to be smaller in size and then produced less honey than non-contaminated colonies.¹⁶⁹ As we all know, the decline of bee populations threatens crop production potentially on a global scale because of their crucial role as pollinators. In order to monitor pesticide concentration and understand the behavior of pesticides in the environment, developing relative sensors has become a critical research in science today.

Meanwhile, pesticide detection is achieved by sophisticated laboratory equipment such as liquid chromatography,^{168,170–172} Raman spectroscopy¹⁷³ or nuclear magnetic resonance.^{174,175} All of the above methods are ex-situ measurements and require long-time sample preparation. Thus, it is essential to provide reliable in-situ detection for farmers to monitor ametryn residue in the environment and turn to electrochemical sensors. In this chapter, we will try to detect three types of pesticides: Imidacloprid (IMI), Metam sodium (MET), Ametryn (AME) at micro-ITIES with single pore capillary.

4.1.1 Imidacloprid

Imidacloprid is the most widely used insecticide in the world and belongs to the neonicotinoid family. Worldwide annual sales of neonicotinoids are approximately one billion dollars, accounting for 11%–15% of the total insecticide market. They are readily ab-

sorbed by plants and act quickly, at low doses, on piercing-sucking insect pests (aphids, leafhoppers, and whiteflies) of major crops. Neonicotinoid is the newest primary class of neuro-active insecticides chemically similar to nicotine and has outstanding potency and systemic action for crop protection against piercing-sucking pests.¹⁷⁶ The neonicotinoid family is listed in Figure 3.1 with including acetamiprid, clothianidin, imidacloprid, nitenpyram, nithiazine, thiacloprid and thiamethoxam. The physical properties of the neonicotinoids and nicotine are compared in Table 3.1. Their Molecular weights range from 160 to 292 $\text{g} \cdot \text{mol}^{-1}$ and log P values from -0.66 to 1.26. The compounds vary in water solubility from 0.185 $\text{g} \cdot \text{l}^{-1}$ for thiacloprid, to 590 $\text{g} \cdot \text{l}^{-1}$ for Nitenpyram. Compared to organophosphate and carbamate insecticides, neonicotinoids cause less toxicity in birds and mammals than insects. Some breakdown products are also toxic to insects. Due to the lowest log P values, these molecules are potent toxic for insects targeting the nervous system. In detail, the commercial neonicotinoids, acetamiprid, IMI, and thiacloprid are the most toxic to birds, and thiacloprid to fish. Several neonicotinoids are harmful to honeybees, either by direct contact or ingestion.^{177,178}

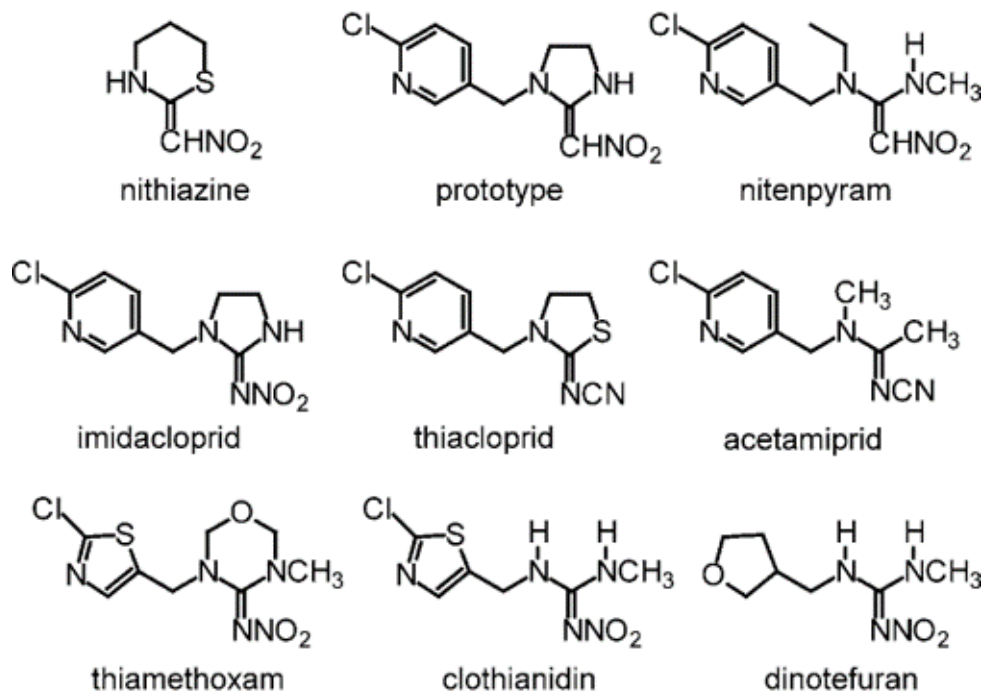
NEONICOTINOIDS

Figure 4.1: Nine neonicotinoid insecticides and four nicotinoids. The neonicotinoids are nitromethylenes ($\text{C}=\text{CHNO}_2$), nitroguanidines ($\text{C}=\text{NNO}_2$), and cyanoamidines ($\text{C}=\text{NCN}$). Compounds with 6-chloro-3-pyridinylmethyl, 2-chloro-5-thiazolylmethyl, and 3-tetrahydrofuranmethyl moieties are referred to chloropyridinyls (or chloronicotinyls), chlorothiazolyls (or thianicotinyls), and tefuryl, respectively.¹⁷⁶

Table 4.1: Physical properties of the neonicotinoids.

Compound	Molecular weight ($\text{g} \cdot \text{mol}^{-1}$)	Water solubility ($\text{g} \cdot \text{l}^{-1}$)	Log P
Acetamiprid	222.7	4.25	0.80
Clothianidin	249.7	0.30–0.34	0.7
Dinotefuran	202.2	54.3	−0.64
Imidacloprid	255.7	0.61	0.57
Nitenpyram	270.7	>590	−0.66
Nithiazine	160.0	200	−0.60
Thiacloprid	252.7	0.185	1.26
Thiamethoxam	291.7	4.1	−0.13
Nicotine	162.2	1000	1.17

Currently, gas chromatography,¹⁷⁹ high performance liquid chromatography,^{180–182} are the conventional analysis methods which have been tested for imidacloprid. With the developing of technology, the enzyme-linked immunosorbent assay,¹⁸³ colorimetric sensor¹⁸⁴ and electrochemical methods^{185,186} have been also employed in the design of imidacloprid pesticides probes. In spite of the precision, those instrumental analysis methods require lengthy sample preparation, and are not suitable for real-time detection. Hence, it is still necessary to develop an on-site sensor based on ITIES for real-time detection of imidacloprid.

4.1.2 Metam sodium

Metam sodium is the third most commonly used agricultural pesticide (by weight) in the U.S. It is used in agriculture as a fungicide, nematocide, and weed killer in soil. In 1991, 19,000 gallons of metham sodium were spilled into the Sacramento River, an event that demonstrated the extremely adverse ecological and human health effects of a large release of this pesticide. In addition, the incident demonstrated that the primary degradation product of induced sodium methanesulfonate (methyl isothiocyanate, MITC) also had a continuing environmental impact, significantly increasing the cost of remediation. As Figure 3.2 shown, once the solution is diluted and applied to the soil, metham sodium

is rapidly decomposed to produce methyl isothiocyanate (MITC) and H_2S . MITC is considered to be the active biocide product of metham sodium due to its strong reaction with amines and mercaptans in biological molecules. In addition, another decomposition pathway is under acidic conditions (common in some types of contaminated soils), where CS_2 and methylamine are products. Both of these decomposition reactions can occur in pure solution, so apparently they do not require enzyme catalysis.^{187,188}

Except from the classical chromatography detection, there are few reports for metam sodium. Flow Injection Analysis (FIA) with amperometric detection is a valuable technique for the MET determining with good accuracy and precision.¹⁸⁹ To understand metam behaviour in aqueous solution, we will try to analyze its ion transfer at ITIES.

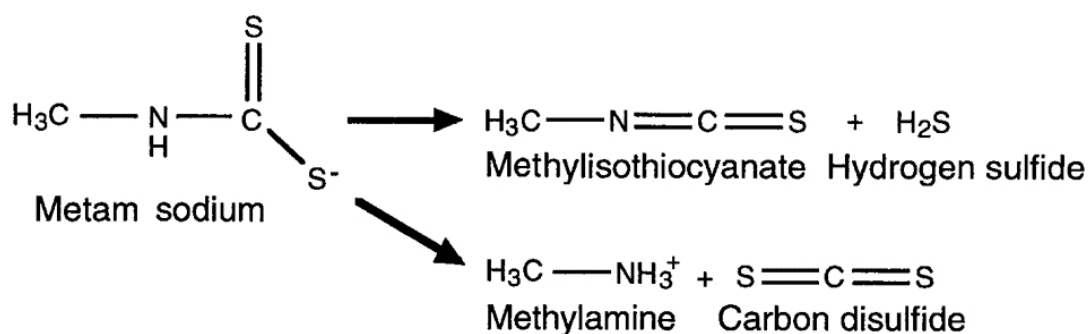
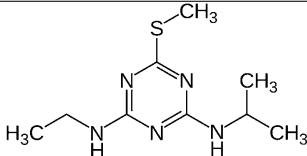


Figure 4.2: Major breakdown pathways of metam sodium in vivo in mammals and in vitro in soil.¹⁸⁷

4.1.3 Ametryn

Ametryn is a selective herbicide belonging to the triazine family which is applied in farming on fruit and vegetables for the sake of yield and product quality, and its usage is alarmingly increasing in agriculture. However, this compound cannot be easily degraded and would accumulate in soil and river.^{167,168} It is moderately soluble in water over several years. Meanwhile, it is slightly toxic to humans and is moderately irritating to the eyes, skin, and respiratory tract. Therefore, ametryn can accumulate in the water environment and cause human health risks. Detection of ametryn has been achieved by conventional laboratory equipment such as liquid chromatography,^{168,170-172} Raman spectroscopy¹⁷³ or nuclear magnetic resonance.^{174,175} All of the above methods are ex-

Table 4.2: Selected Physicochemical Properties of Ametryn used in this study.

	Structure	pKa	logP (25°C)
Ametryn		4.1	2.63

situ measurement and are required technique-skilled sample preparation. Thus, it is of particular importance to provide reliable cost effective detection for farmers to monitor ametryn residue in the environment and it turns to electrochemical sensor. But the triazine family are molecules difficult to detect by electrochemistry. Most electrochemical sensor are based on reduction process with mercury electrode,¹⁹⁰⁻¹⁹² gold electrode,¹⁹³⁻¹⁹⁵ modified carbon electrode.^{196,197} Such a detection method brings one major problem. The presence of dissolved oxygen, which is reduced at the electrode and would disturb the detection of triazine. The demand for portable sensors with features of facile in operation, high sensitivity and good selectivity keep surging. In consideration of above-mentioned features, it has turned another type of electrochemical sensor by using the interface between two immiscible electrolyte solutions (ITIES). Table 3.2 gives selected physicochemical properties of ametryn used in this study including its pKa and logP.¹⁹⁸

4.2 Results and discussion

4.2.1 Ametryn

The electrochemical behavior of AME at the liquid-liquid interface was investigated by cyclic voltammetry with varying pH values from pH 1.1 to 2.9 in Figure 3.3A. In these pH conditions where $\text{pH} < \text{pKa}$ (4.1), AME was protonated to form AMEH^+ because it is a weak base and then became detectable as cation at the ITIES. The transfer current increased with the pH and the transfer potential was shifted towards more positive potential difference values since its logP are over 1. In order to identify the Galvani potential

of ametryn, a mixed solution contained 250 μM TBA⁺ and 10 μM AME was tested in different pH and its result was illustrated in Figure 3.3B. The half-wave potential ($\Delta_o^w\phi_{1/2}$) of ametryn was measured in accordance with the ion transfer of TBA⁺ at the same potential scale, which formal transfer potential for TBA⁺ at the aqueous-DCE interface was established at $\Delta_o^w\phi_{TBA^+}^0 = -0.280\text{V}$ ($\Delta G_{TBA^+}^0 = -27 \text{ kJmol}^{-1}$).⁷³ Since the half-wave potential of TBA⁺ is known, the half-wave potential of AMEH⁺ was calculated through the equation below:

$$y = -0.28 + b - a$$

where b is the experimental half-wave of AMEH⁺ at pH = x and a is the experimental half-wave potential of TBA⁺ at pH = x during the same cyclic voltammetry. Therefore, the formal transfer potential at pH = 1.1 for AMEH⁺ was determined at -0.15 V ($\Delta_o^w\phi_{AMEH^+}^0 = -0.15\text{V}$) which was used to construct its ionic partition diagram lately. In this pH range study, , the transfer potential of protonated ametryn as a function of pH value was predicted by equation below when pH > pKa - log P (1.47):

$$\Delta_o^w\phi = \Delta_o^w\phi_{AMEH^+}^0 + \frac{2.3RT}{zF}(\log P - pKa) + \frac{2.3RT}{zF}pH \quad (4.1)$$

Where R is gas constant ($8.31 \text{ Jmol}^{-1}\text{K}^{-1}$), T is the temperature in K, z is the charge number of transferred ion (+1) and F is the Faraday constant (96485.2 C). As the ionic partition diagram shown in Figure 3.4, there was a good agreement between the experimental data measured in dotted line from the cyclic voltammograms and the theoretical curve shown in solid lines.

Therefore, three dominant types of ametryn species were considered, which corresponded to the pH and $\Delta_o^w\phi$ conditions for which (i), AMEH⁺, was predominantly in the aqueous phase, (ii) AMEH⁺ was predominantly in the organic phase and (iii) the neutral form of AME is predominantly in the organic phase. However, the ionic partition diagram could not explain the variation of the recorded peak currents in different pH aqueous phase. Precisely, for an initial concentration of 70 μM AME present in the aqueous phase, a transfer current of 0.69 nA was recorded at pH 1.1. This peak current increased to 6.2 nA at pH 2.9 after we adjusted the pH value of the aqueous phase using NaOH solution. Meanwhile, this improved peak currents were linked to an symmetric

peak current response for the forward scan and the backward scan. As supposed, an asymmetric peak current profiles should be observed at single μ ITIES together with the volume differences between the organic and the aqueous phase. The organic volume was about 50 μ L and the aqueous phase volume was 2 mL, and the volumetric ratio $V_{\text{aq}}/V_{\text{org}}$ was then about 40. Thus, it is of importance to describe specifically AME reactions in the solutions in agreement with the volumetric ratio.

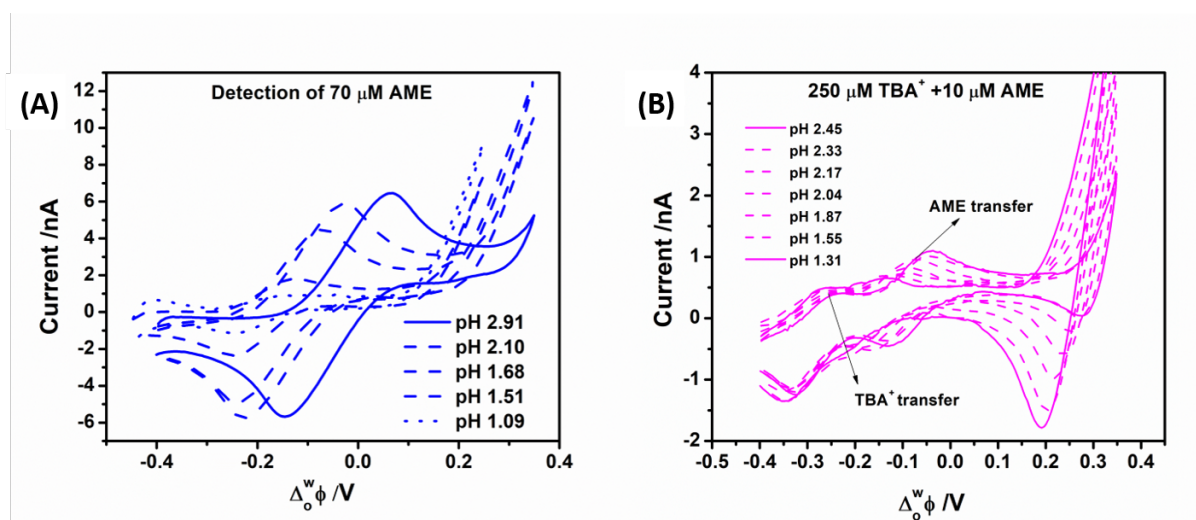


Figure 4.3: (A) Calibration for the half-wave potential ($\Delta_o^w \phi_{1/2} \text{AME}$) ametryn with 250 μ M TBA⁺ at different pH mixed solution. (B) Cyclic voltammograms obtained for variable pH value (from pH 1 to pH 3) of aqueous solution within 70 μ M AME.

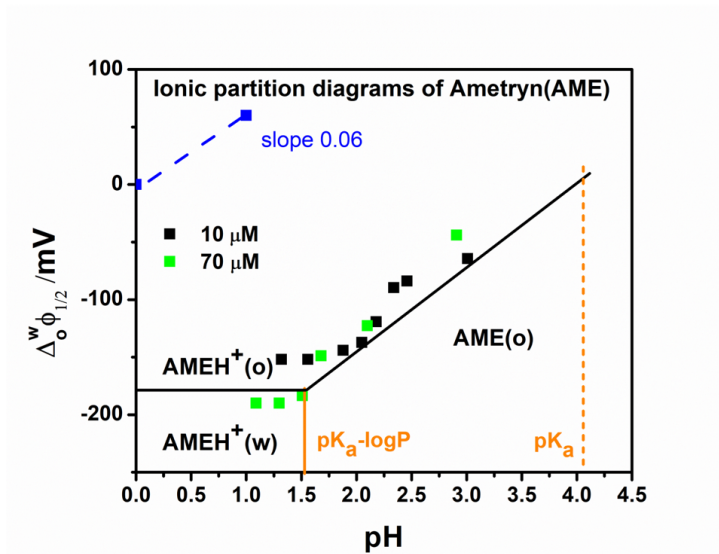
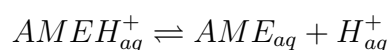


Figure 4.4: Ionic partition diagrams for AME transfer energy based on the cyclic voltammograms measured at variable pH value of the aqueous phase with TBA mutually. The vertical line (orange solid line) represents the estimated value of $(pK_a - \log P)$. The concentration of AME was tested twice at $10 \mu\text{M}$, $70 \mu\text{M}$.

Firstly, ametryn is weak base. So there was a dissociation reaction for ametryn when dissolved it in the aqueous solution. AME is dissociated according to equilibrium reaction, for which the dissociation constant, K_a , could be written as described by equation 4.2:



$$K_a = \frac{[AME]_{aq}[H^+]_{aq}}{[AMEH^+]_{aq}} \quad (4.2)$$

And neutral ametryn is distributed in both phases. Thus, partition coefficient P is necessary to take into account. Furthermore, AME is a lipophilic molecule and its neutral species is probably transferred into the organic phase. The spontaneous distribution between the organic and aqueous phase can be written as following equation 4.3:

$$AME_{aq} \rightleftharpoons AME_{org}$$

$$P = \frac{[AME]_{org}}{[AME]_{aq}} \quad (4.3)$$

Lastly, the amount of each ametryn species in both solutions is constant following the law of mass conservation. The equation 4.4 describes the mass conservation in terms of the number of moles:

$$V_{org} * [AME]_{org} + V_{aq} * [AME]_{aq} + V_{aq} * [AMEH^+]_{aq} = n \quad (4.4)$$

Where n is the total number of moles initially present in the system, V_{org} and V_{aq} were the volumes of the organic and aqueous phases, respectively. By combining equations 4.5, 4.6 and 4.7, we can express the concentrations $[AME]_{aq}$, $[AME]_{org}$ and $[AMEH^+]_{aq}$ as a function of the aqueous volume, the organic volume and the proton concentration where Ka , P and the mole n are constants. Extensively, we assume that in the absence of polarized potential application, the protonated form $AMEH^+$ and H^+ were only present in the aqueous phase.

$$[AME]_{aq} = \frac{nKa}{Ka(PV_{org} + V_{aq}) + [H^+]_{aq}V_{aq}} \quad (4.5)$$

$$[AMEH^+]_{aq} = \frac{n[H^+]_{aq}}{Ka(PV_{org} + V_{aq}) + [H^+]_{aq}V_{aq}} \quad (4.6)$$

$$[AME]_{org} = \frac{nPKa}{Ka(PV_{org} + V_{aq}) + [H^+]_{aq}V_{aq}} \quad (4.7)$$

Using the following experimental conditions: $n = 25$ nmol, $V_{aq} = 2$ mL and $V_{org} = 50$ μ L, the distribution of AME in the biphasic system as a function of pH can be distinguished three regions by ranging pH value from 0 to 6. three regions are clearly identified: (i) the first zone is the predominated ion of $[AMEH^+]_{aq}$ in aqueous phase; (ii) the second zone is neutral AME in the organic phase and the concentration of dominated $[AME]_{org}$ remain lower than the proton concentration of $[H^+]_{aq}$; (iii) the third zone is limited $[H^+]_{aq}$ when $[AME]_{org} > [H^+]_{aq}$. These three zones can be distinguished by solving the separated limitation in accordance with these two equations 4.8 and 4.9:

$$[AMEH^+]_{aq} = [AME]_{org} \quad (4.8)$$

$$[H^+]_{aq} = [AME]_{org} \quad (4.9)$$

After applying the equation above, the AME partition as a function of pH value is further draw in Figure 3.5, where the first intersection is $[AMEH^+]_{aq} = [AME]_{org}$, $[H^+]_{aq} = Ka * P$ which is constant , that's $pH = pKa - \log P = 1.47$, the second intersection is $pH_{aq}^{lim} = [AME]_{org}$ which can be written in the equation 51 and the $pH_{aq}^{lim} = 3.5$ in our example.

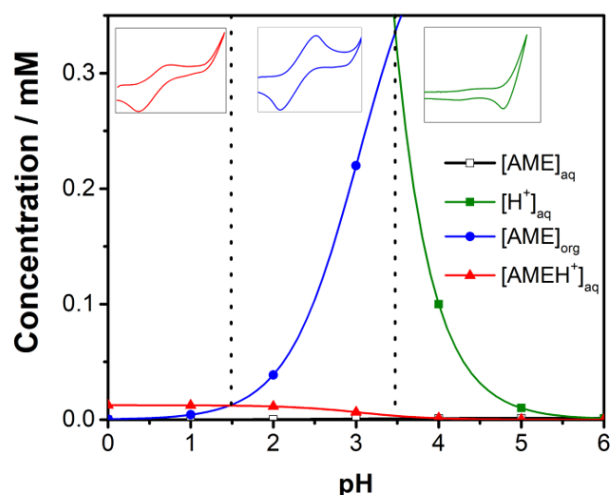


Figure 4.5: The distribution of each compound of AME in organic phase $[AME]_{org}$, AME in aqueous phase $[AME]_{aq}$ and protonated AME in aqueous phase $[AMEH^+]_{aq}$ as a function of pH value in the aqueous solution under the condition of $V_{aq} = 2$ mL, $V_{org} = 50$ μ L, $n = 25$ nMol. The ion transfer behaviors of each condition in conformity with their special CV responses are inset at the top: simple ion transfer of $[AMEH^+]_{aq}$ @ $pH < pKa - \log P$ (red curve), Proton assisted transfer of $[AME]_{org}$ @ $pKa - \log P < pH < pH_{lim}$ (blue curve), Proton limited transfer of $[AME]_{org}$ @ $pKa - \log P < pH$ (green curve).

From this theoretical approximation, we can conclude that the predominant ions are protonated AME in aqueous phase when the aqueous solution pH is lower than pH 1.47. Later, there would exist a facilitated ion transfer of AME in organic phase with proton after pH 1.47. This facilitated ion transfer is controlled by the concentration of neutral AME in organic phase. However, this facilitated ion transfer is limited by proton concentration after pH 3.5. Hence, these three transfer behaviors could offer individually their specific current signals during cyclic voltammetry. Therefore, we would like to propose its correspondent mechanism as Figure 3.6 demonstrated:

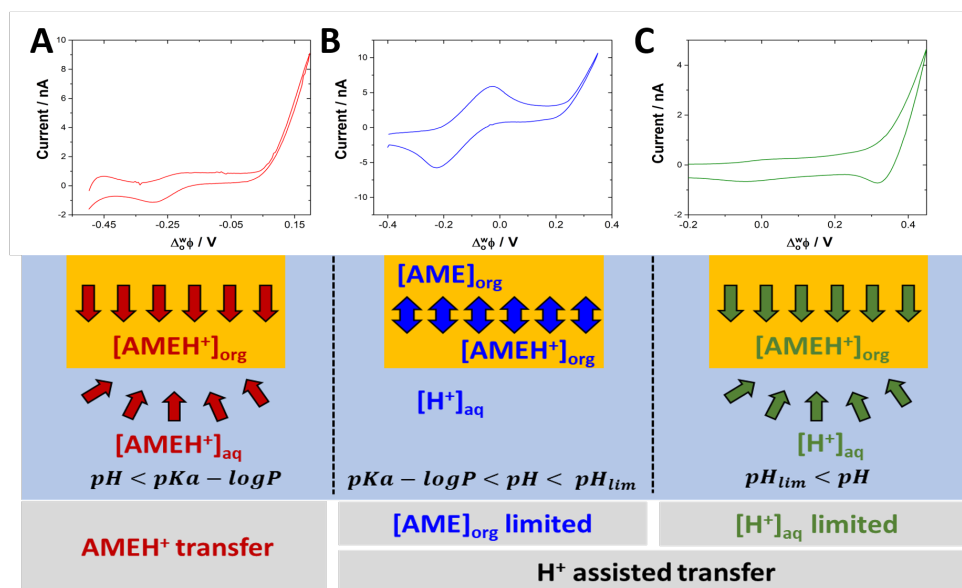


Figure 4.6: The zones of AME ion transfer with its proposed mechanism and its classification.

Condition (A): $pH < \log P - pKa$, AME is mostly protonated because of its dissociation reaction, AME is transferred across the interface by simple ion transport and that's why its cyclic voltammogram is similar as TBA^+ , which are explained by Micro-ITIES theory, for spherical diffusion during the forward scan and linear diffusion during the backward scan are observed.

Condition (B): $\log P - pKa < pH < pH_{aq}^{lim}$, neutral AME spontaneous transfer into the organic solution due to its lipophilicity. Consequently, proton would transfer firstly to an organic solution during the forward scan, AME then get protonated and would diffuse linearly inside the capillary. This process is described as TIC (Transfer by Interfacial Complexation). On the reverse scan, AME presents linear diffusion across the W|DCE interface. Its current peak is limited by AME concentration in organic phase.

Condition (C): $pH_{aq}^{lim} < pH$, AME would have same transfer than for condition (B) but the transfer current is limited by proton concentration in aqueous phase.

In order to comprehend and verify this particular mechanism, we did scan rate study. The mixed solution of 50 μM AME and 50 μM TBA^+ was applied by cyclic voltammetry at 10 $mV \cdot s^{-1}$ and 20 $mV \cdot s^{-1}$. The ion transfer of TBA^+ displayed asymmetric peak

current both at pH 1 and pH 3 aqueous solution in voltammogram as Figure 3.7 shown. The forward peak current was about 0.6-0.7 nA as indicated with blue dotted curve for both scan rates. At the same time, AME had simple ion transfer as TBA^+ at pH 1. Nevertheless, the peak current of AME increased at pH 3 with showing symmetric current response for both scan rate $10 \text{ mV} \cdot \text{s}^{-1}$ and $20 \text{ mV} \cdot \text{s}^{-1}$. It means that neutral AME would transfer continuously from aqueous solution to organic solution at pH 3. Thus, proton assist with neutral AME in the organic solution at the ITIES.

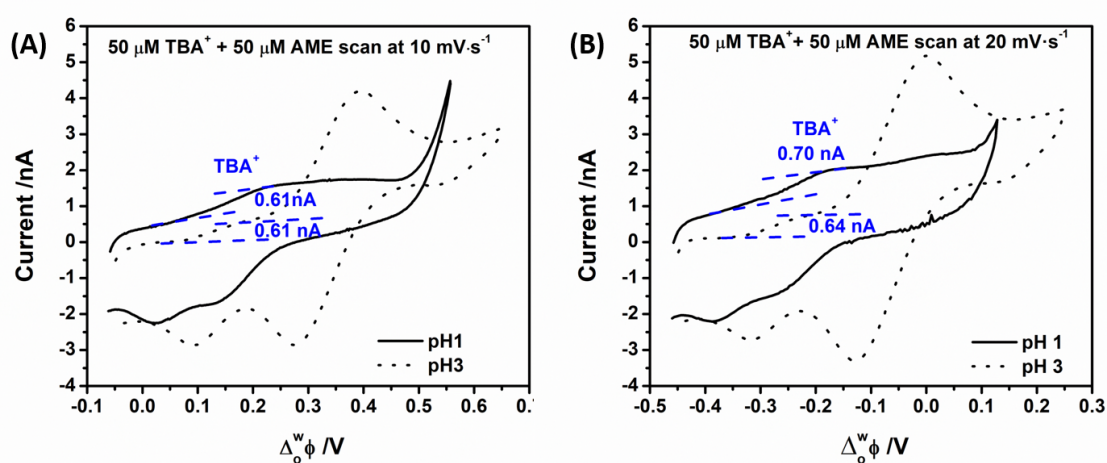


Figure 4.7: Cyclic voltammograms obtained for mix solution of $50 \mu\text{M}$ AME and $50 \mu\text{M}$ TBA^+ at different scan rate: (A) $10 \text{ mV} \cdot \text{s}^{-1}$, (B) $20 \text{ mV} \cdot \text{s}^{-1}$.

Furthermore, a smaller pore capillary which the radius equal to $12.5 \mu\text{m}$ was employed to detect $40 \mu\text{M}$ and $80 \mu\text{M}$ AME at pH 3 by following the same process. The result is illustrated in Figure 3.8. The repeatable symmetric peak current response are found in voltammogram confirming that AME possess a linear diffusion for over pH 1 aqueous solution during forward scan and backward scan regardless the geometry of single pore at Micro-ITIES. Thus, facilitated ion transfer mechanism for AME detection based on pH modulation have been appropriately found.

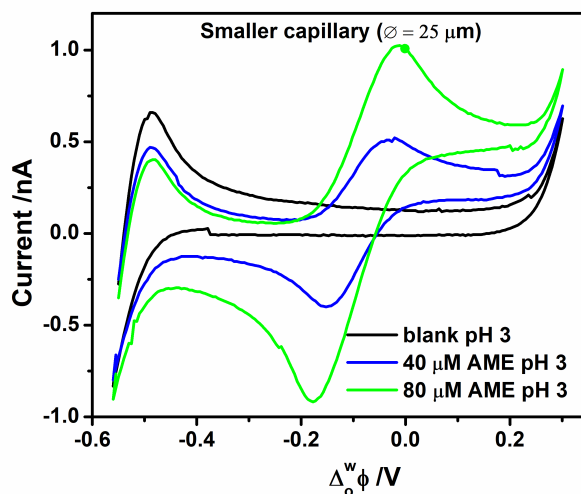


Figure 4.8: Cyclic voltammograms obtained for the absence of Ametryn at pH 7 (black solid line), 40 μM Ametryn at pH 3 (blue solid line) and 80 μM AME at pH 3 (green solid line) at Micro-ITIES using smaller capillary with diameter = 25 μm .

Moreover, Scan rate studies of 320 μM AME at pH 1 from 10 mVs^{-1} to 30 mVs^{-1} and 70 μM AME at pH 2 from 10 mVs^{-1} to 25 mVs^{-1} . The results are illustrated in Figure 3.9a and 3.9b respectively. From this comparison, it could be distinguished that the forward peak current of 320 μM AME at pH 1 was kept 4 nA for different scan rate. Briefly, this diffusion limited steady state current at single pore of Micro-ITIES pipet electrodes can be expressed in equation 4.10:

$$I_{ss} = 4zFD[\text{AMEH}^+]_{aq}r \quad (4.10)$$

where I_{ss} is the steady-state current, z is the number of transferred charges and equal to 1, F is Faraday's constant, r is the radius of the μITIES and equal to 25 μm , D is the diffusion coefficient of AME ($\text{cm}^2 \cdot \text{s}^{-1}$), here we estimated ca. $1\text{e-}6 \text{ cm}^2 \cdot \text{s}^{-1}$ according to the report,¹⁹⁹ and $[\text{AMEH}^+]_{aq}$ is the concentration of protonated AME in the aqueous phase ($\text{mol} \cdot \text{cm}^{-3}$). Thus, on the pore ingress, the mass transfer is enhanced by hemispherical diffusion and it should show a sigmoidal shape of current during CVs. On the pore egress, the mass transfer inside the pore is dominated by linear diffusion and hence it should show a tail finished peak current during CVs. The results of AME at pH 1 aqueous

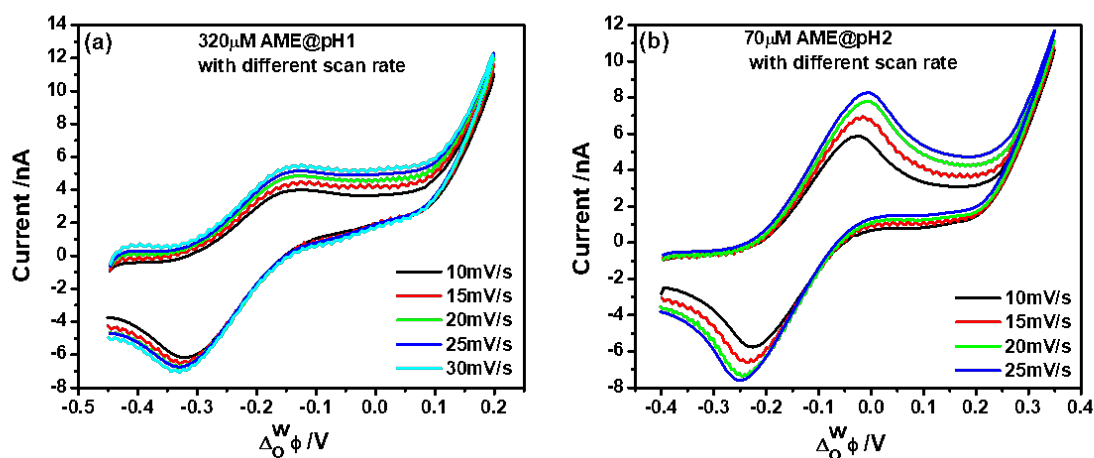


Figure 4.9: (a) Cyclic voltammograms obtained for variable scan rate (from 10 mV/s to 30 mV/s) of aqueous solution within 320 μM AME at pH1. (b) Cyclic voltammograms obtained for variable scan rate (from 10 mV/s to 25 mV/s) of aqueous solution within 70 μM AME.

solution present this phenomenon where the forward peak current remain unchanged from scan $10 \text{ mV} \cdot \text{s}^{-1}$ to $30 \text{ mV} \cdot \text{s}^{-1}$. However, AME at pH 2 did not conform to this restriction and present more like a process controlled by linear diffusion which as Randles–Sevcik equation 4.11 described.

$$I_p = 2.69 \times 10^5 z^{3/2} AD^{1/2} cv^{1/2} \quad (4.11)$$

where I_p is the peak current, z is the number of transferred charges and equal to 1 in our work, F is Faraday's constant, A is the interfacial area, D is the diffusion coefficient of AME, c is the concentration of AME and v is the scan rate. Thereby, the forward peak current of 70 μM AME at pH 2 was 5.2 nA at 10 mVs^{-1} and was up to 8.2 nA at 10 mVs^{-1} . Statics of the forward peak current and the backward peak current possess a linear regression with the square root of scan rate when pH over $\text{pKa} - \log P$. It shows that AME get protonated in the organic phase rather than in aqueous phase and obtain a facilitated proton transfer in organic phase. Consequently, the modulation of different concentration scale for AME can be realized and the favorable mode for ametryn detection is proton assisted ion transfer if we check the sensitivity.

A quantitative detection of AME from 2 μM to 100 μM was firstly tested at pH 3. The peak current responses showed a proportional relationship with AME concentration as the black dotted curves in Figure 3.11A.

Secondly, if pH_{aq}^{lim} calculated value as equation 4.12 expressed, pH_{aq}^{lim} depends on the initial ametryn concentration in the aqueous solution and the volumetric ratio. If the ratio is low enough as equation 4.13 expresses, pH_{aq}^{lim} is constant. Thus, there is a conclusion: when the ration V_{org}/V_{aq} get smaller, the bigger of pH_{aq}^{lim} will be. It means that less organic phase volume would improve the peak current in the condition of proton limited ion transfer .

$$[H^+]_{aq}^{lim} = \frac{-Ka(PV_{org} + V_{aq}) + \sqrt{Ka^2(PV_{org} + V_{aq})^2 - 4npKaV_{aq}}}{2V_{aq}} \quad (4.12)$$

$$[H^+]_{V_{org} \rightarrow 0}^{lim} = \frac{-KaV_{aq} + \sqrt{Ka^2V_{aq}^2 - 4npKaV_{aq}}}{2V_{aq}} \quad (4.13)$$

From this viewpoint, we will prepare an experiment where $[\text{AME}]_{org}$ is the greater but remains smaller than pH_{aq}^{lim} , then we could get the highest signal than the direct proton assisted ion transfer mode after voltammetry. This leads us to design the two-step detection with accumulation at high pH for the first step and detection at low pH for the second step. As an example, AME will become protonated at pH 3 rather than at pH 6. Thus, a capillary would contain neutral AME at pH 6 aqueous solution. Later, this preconcentration capillary could transfer into an much more acidic aqueous solution and be better analyzed.

In our work, we accumulated diluted AME into the organic solution by spontaneous partition reaction after 30 mins agitation at pH 6 in the aqueous solution. The experiment results are illustrated in Figure 3.10 for 8 μM AME. The blue dotted curve was measured using two-step method and the black dotted curve was measured using direct proton assisted measurement which AME was in aqueous solution. It showed evidently an improvement about 3 times for peak current in CVs applying two-step method. In order to obtain maximum concentration of organic AME concentration in capillary, AME at pH 8 aqueous phase were also done in two measurement way from 20 μM to 100 μM . Each capillary was ultrasonic washed in ethanol solution for 5 mins and then replaced with the

organic solution. The agitation time was set at 10 mins for each capillary. Calibration line of two step method was traced through preconcentration treatment at pH 8 aqueous solution and analysis at pH 3 aqueous solution (orange point). Calibration line of direct measurement for AME in aqueous solution was traced in black point with error bar $n = 4$. Both lines are showed in Figure 3.11B. Due to the first step of preconcentration, the improvement of AME detection is achieved by its hydrophobic property with its protonation process using micro pipette.

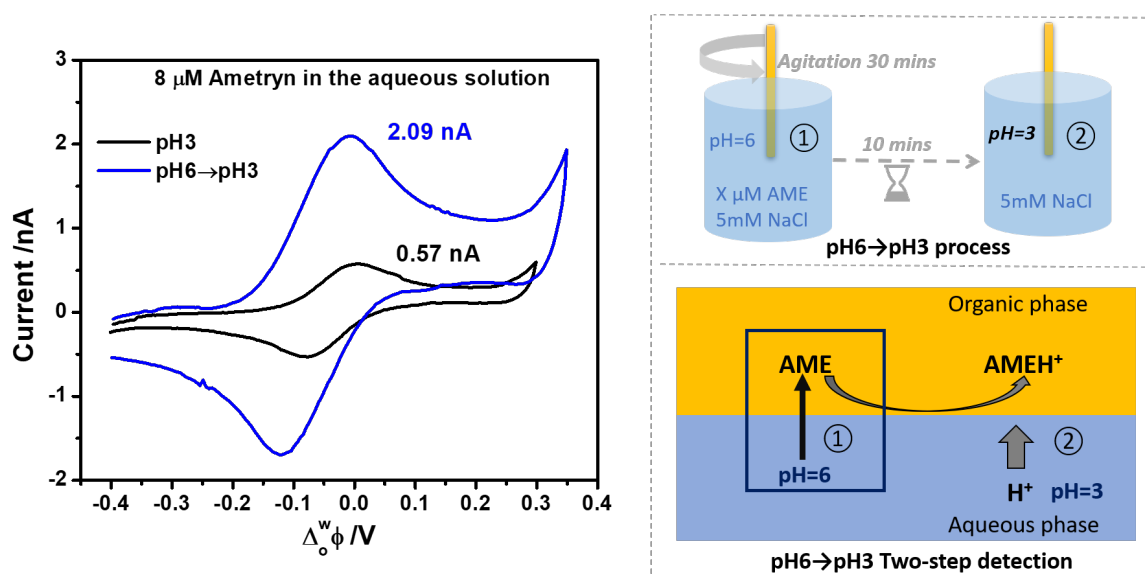


Figure 4.10: Cyclic voltammogram comparison of 8 μM AME with 2 kinds measurement : two-step measurement by agitating 30mins at pH 6 and testing at pH 3 in blank NaCl solution (blue curve), direct measurement at pH 3 in NaCl solution (black curve).

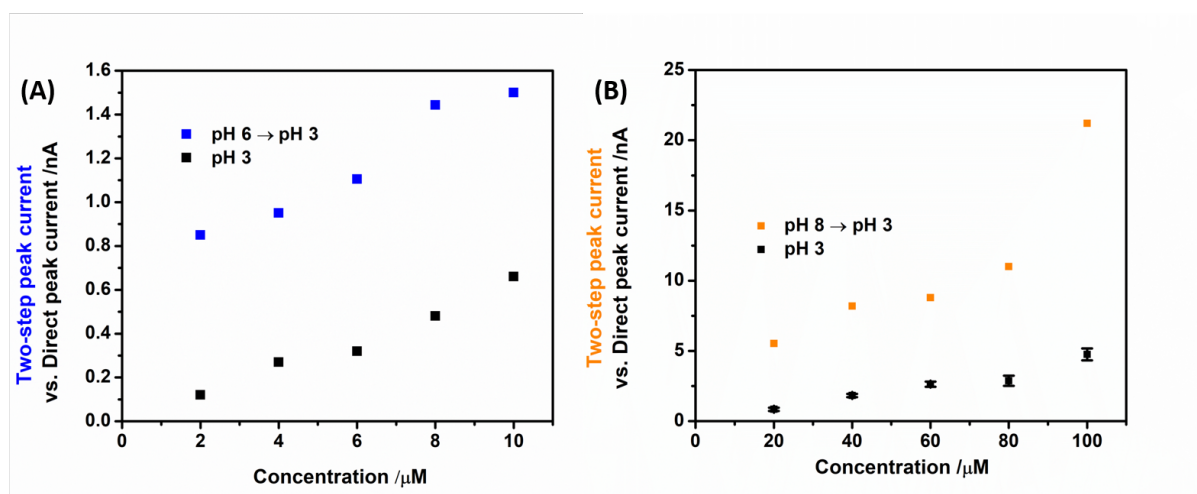


Figure 4.11: (A) Calibration line for two-step measurement by employing preconcentration treatment at pH 6 aqueous solution and testing at pH 3 aqueous solution (blue point); Calibration line of direct measurement for AME in aqueous solution (black point). (B) Calibration line for two-step measurement by employing preconcentration treatment at pH 8 aqueous solution and testing at pH 3 aqueous solution (orange point); Calibration line of direct measurement for AME in aqueous solution (black point with error bar $n = 4$).

Nevertheless, there was still a big problem with this preconcentration method. The maximum value of AME in the aqueous solution was normally detected for first cycle voltammetry as Figure 3.12 illustrated. Moreover, two-step detection did not improve the sensitivity. And this method has a larger error bar for each concentration. We did 5 consecutive cyclic voltammetry for large concentration from 20 micro molar to 100 micro molar. We can see the peak current is decreased strongly from the first cycle to the third cycle. This is the reason that we get larger error bar and did not get a linear regression. Protonated AME was dissolved in the second aqueous phase after the new equilibrium. Protonated AME was dissolved in the second aqueous phase after the new equilibrium and then AME concentration in the organic phase was decreased. Thus, the peak current was also decreased in cyclic voltammetry.

It is thus impossible to have an average value and standard deviation to detect the initial AME concentration by this two-step method. Obviously, the accumulation process also depends on other parameters and need improve. For this reason, even the the measured peak current int the first cyclic voltammogram was not correct if comparing the ion

transfer behavior to the direct measurement.

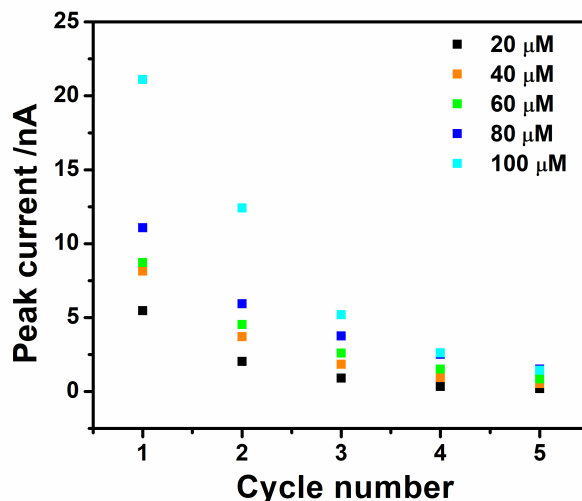


Figure 4.12: Cyclic evolution of the experimental peak currents for preconcentration of 20 μM , 40 μM , 60 μM , 80 μM and 100 μM . All experiments were for preconcentration at pH 8 aqueous phase, analyzed at pH 3 to aqueous phase.

Thus, we think about a method using acidic organic solution in the capillary by providing proton.²⁰⁰ With proton direct assistance in capillary, the test can be simply without modify the pH value of the aqueous solution. Subsequently, we have tested a capillary contained 300 mM octanoic acid with 10 mM BTPPA⁺TPBCl⁻ in 1,2 DCE solvent while keeping the pH value at pH 6 for the aqueous phase. The result was presented in Figure 3.13 and we can clearly see this kind of capillary work well to detect AME in neutral aqueous solution.

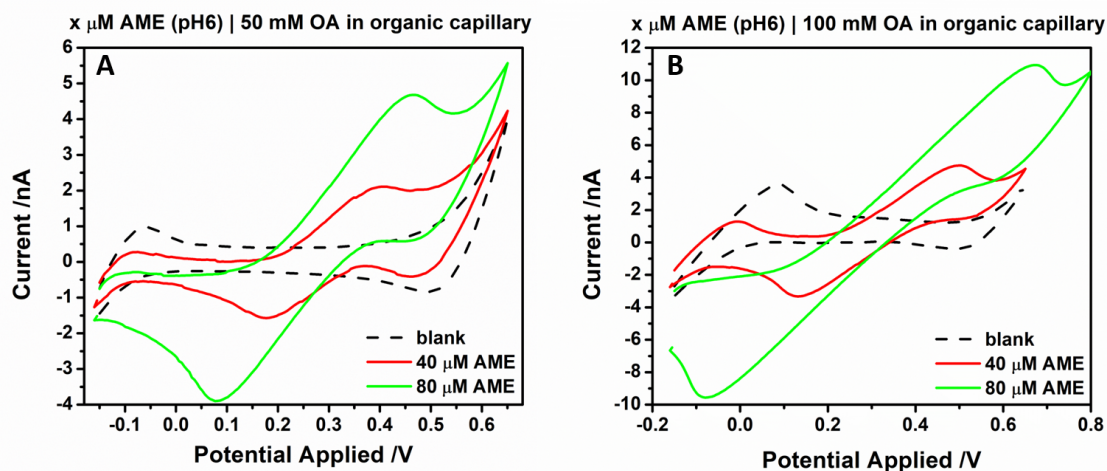


Figure 4.13: Cyclic voltammetry for AME detection using (A) 50 mM OA in organic capillary; (B) 100mM OA in organic capillary.

We obtained a linear interaction between AME concentration and its peak current. However, the organic acid used method would bring the new problem of large resistance due to the presence of octanoic acid in the organic phase. Previous results have demonstrated that both accumulation and peak current for the proton assisted transfer are pH-dependent. Accumulation will be optimal at $\text{pH} \gg \text{pK}_a$, and ametryn detection will be optimal at $\text{pH} < \text{pH}_{\text{lim}}$. Such contradictory conditions would require a time-consuming two-step protocol. Furthermore, detection conditions would vary greatly with the nature of the target analytes pK_a and P . To circumvent these limitations, we have investigated the effect of the addition of buffer to the aqueous solution. The presence of buffer in the aqueous solution ensures a constant concentration of protons available for the transfer across the interface. Figure 3.14 shows the cyclic voltammograms of 8 μM ametryn initially dissolved in the aqueous phase at pH 6.8, 0.1, 1, and 10 mM phosphate buffer. At 0.1 mM phosphate buffer, the proton transfer assisted by ametryn was not observed. The buffer concentration was not high enough and limited the transfer reaction. However, when the phosphate buffer concentration was 1 mM, a peak for the transfer of 8 μM ametryn was observed, and thus allowing the one-step detection of ametryn. Increasing the concentration of phosphate buffer to 10 mM resulted in a loss of ametryn signal due to the rise of background current (inset of Figure 3.14). All subsequent experiments were

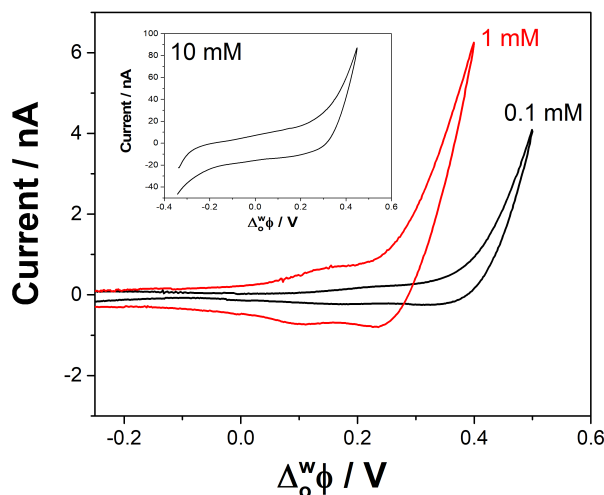


Figure 4.14: Cyclic voltammograms of 8 μM AME in a 10 mM LiCl aqueous solution containing 0.1 (red curve), 1 (black curve) and 10 mM (inset) phosphate buffer. Scan rate was 10 mV s^{-1} . The CVs were recorded after the electrochemical cell was left 30 min at open-circuit potential to reach equilibrium.

done in the presence of 1 mM phosphate buffer (pH 6.8).

Besides, a more sensitive electrochemical method was required to overcome the mediocre limit of detection reached with cyclic voltammetry. Recently, AC voltammetry was described by Suárez-Herrera and Scanlon as an quantitative analytical method at the ITIES.²⁰¹ Thereby, it was used here to improve the sensitivity of the ametryn detection. We assumed that the electrochemical cell behaves as a Randles circuit. The analytical signal Y , used to plot the AC voltammograms was determined and was expressed as:

$$Y = -\frac{10^6}{\omega Z_{Im} A} - C_d$$

where ω is the angular frequency (rad s^{-1}), Z_{Im} is the imaginary part of the impedance (Ω), A is the surface area of the interface ($A = 1.96 \times 10^{-5} \text{ cm}^2$) and C_d is the double layer capacitance ($\mu\text{F cm}^{-2}$) determined in the absence of analyte. The frequency of the AC signal was set at a value of 1 Hz, which favoured the Faradaic response of the proton assisted transfer limited by AME diffusion in the organic phase. AC voltammetry experiments were also measured with the amplitude was 10 mV, and the step potential was 10 mV. An electrochemical cell was set with 10 mM LiCl + 1 mM phosphate buffer

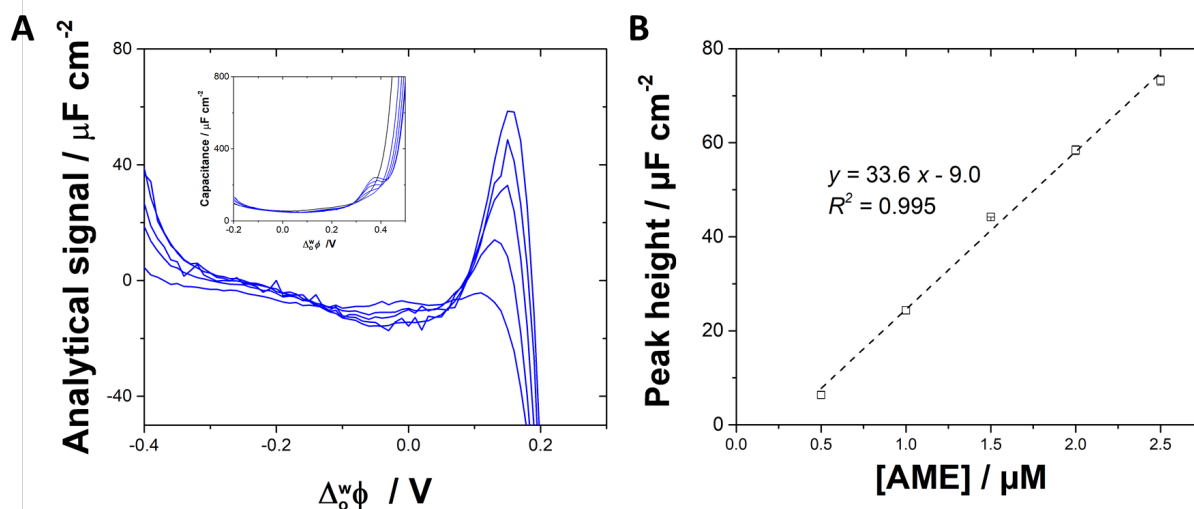


Figure 4.15: . (A) Background subtracted AC voltammograms for increasing concentrations of AME (0.5 – 2.5 μM) in the aqueous phase (10 mM LiCl + 1 mM phosphate buffer, pH 6.8). Experiments were done in triplicate. Inset: AC voltammograms before background subtraction. (B) Calibration curve for AME obtained from the AC voltammograms. Error bars are smaller than symbols when not visible.

as an aqueous phase. A blank cyclic voltammogram and a blank AC voltammogram were recorded prior to additions of ametryn to the aqueous phase. After each ametryn addition, AC voltammograms were recorded after 30 minutes of waiting time at open-circuit potential to allow the partition of neutral lipophilic ametryn to reach equilibrium. AC voltammograms for ametryn concentrations ranging from 0.5 to 2.5 μM are shown in Figure 3.15. A peak at 0.16 V, corresponding to the proton transfer assisted by AME, was measured and its height increased linearly with the concentration of AME (Figure 3.15B). The sensitivity of $33.6 \mu\text{F} \cdot \text{cm}^{-2} \cdot \mu\text{M}^{-1}$ allowed to reach a limit of detection of 0.2 μM (calculated as 3 times the standard deviation divided by the sensitivity). Such a limit of detection is 40 times lower than with cyclic voltammetry.

Three river water samples (CS3, CS4 and SG) were then analyzed by AC voltammetry. The ionic composition of the three river samples was determined by ion chromatography. Phosphate concentration was measured at 27.7 μM for CS3 and below the limit of detection for ion chromatography for the other two samples (CS4 and SG). Since the phosphate concentration in the samples was naturally insufficient, 1 mM phosphate buffer was added,

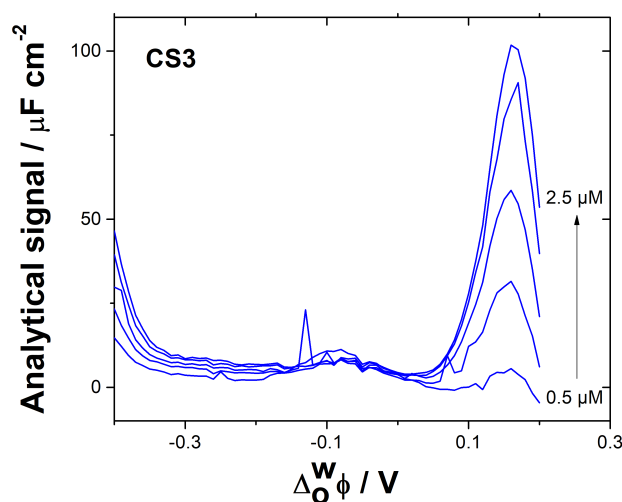


Figure 4.16: AC voltammograms for increasing spiked concentrations of AME (0.5 – 2.5 μM) in real sample CS3 from the Strengbach river (Vosges, France). 1 mM phosphate buffer (pH 6.8) was added to the sample. 30 minutes of waiting time after each addition prior to AC voltammetry run. The voltammograms were background subtracted.

and the pH was set 6.8. AC voltammograms for increasing concentrations are shown after subtraction of the blank seen Figure 3.16.

As for the model solution, the analytical signal increased linearly with the concentration of AME in the aqueous phase for all three real samples investigated. Analytical figures of merit for the real samples are gathered in Table 3.4.

Concentrations of Li^+ , Na^+ , NH_4^+ , K^+ were also determined by ion chromatography since the presence of those ions could interfere with proton assisted transfer. Their concentrations in the samples tested are given in Table 3.4. Among those four cations found naturally in the river samples, NH_4^+ has the lowest standard transfer potential with $\Delta_o^w \phi_{\text{NH}_4^+}^0 = 0.531 \text{ V}$ and is hence the most likely to interfere with the proton assisted transfer. The standard transfer potential of K^+ is slightly higher with $\Delta_o^w \phi_{\text{K}^+}^0 = 0.542 \text{ V}$, followed by Na^+ ($\Delta_o^w \phi_{\text{Na}^+}^0 = 0.606 \text{ V}$) and Li^+ ($\Delta_o^w \phi_{\text{Li}^+}^0 = 0.620 \text{ V}$).²⁰² For Li^+ , K^+ and NH_4^+ , the concentrations are between 3.6 and 37.2 μM . The natural concentrations of these three ions did not significantly alter the limits of detection achieved as they were comprised in the range $0.2 < \text{LOD} < 0.31 \mu\text{M}$. The real samples tested were naturally

Table 4.3: Analytical performance and chemical composition of the river solution analyzed

Analytical performance and chemical composition of the river solution analyzed.				
	Model solution	CS3 ^b	CS4 ^b	SG ^b
Sensitivity / $\mu\text{F cm}^{-2} \mu\text{M}^{-1}$	33.6	46.3	26.9	22.3
Dynamic range / μM	0.5 – 2.5	0.5 – 2.5	0.5 – 2.5	0.5 – 2.5
R^2	0.995	0.994	0.994	0.988
LOD ^a / μM	0.20	0.22	0.31	0.27
[Li ⁺]	10 mM	– ^c	– ^c	37.2 μM
[Na ⁺]	1.49 mM	96.6 μM^{d}	96.1 μM^{d}	104.7 μM^{d}
[NH ₄ ⁺]	0	– ^c	– ^c	5.2 μM
[K ⁺]	0	3.6 μM	11.6 μM	3.7 μM

^a: Limit of detection was calculated as 3 times the standard deviation of the intercept divided by the sensitivity. ^b: These sample names correspond to sampling points on the Strengbach river. ^c: concentration below the limit of detection of ion chromatography. ^d: determined by IC before addition of phosphate buffer.

more concentrated in Na⁺, but the concentration was artificially increased to 1.5 mM due to the addition of the sodium salt of the phosphate buffer. The proximity of the proton transfer assisted by AME with the Na⁺ transfer may hamper the limit of detection.

4.2.2 Imidacloprid

The imidacloprid would become cationic in an acidic environment below pKa₁(1.56),²⁰³ and become anion a basic environment of pH 12.3, which is above pKa₂ (11.12). Thus, we tested imidacloprid at pH 1.1 for its cation transfer and pH 12.3 for its anion transfer. The cyclic voltammograms were presented in Figure 3.17. The cationic imidacloprid in Figure 3.17A presented positive peak with proton together at the edge of potential window because proton concentration was larger than sodium concentration ($[\text{H}^+] = 0.1 \text{ M} \gg 5 \text{ mM LiCl}$). Therefore, if we check the negative peak current, the peak current was increased due to the augmentation of imidacloprid concentration. However, no peak was detected for anionic imidacloprid in the potential window as Figure 3.17B illustrate. The possible reason is that the transfer potential of imidacloprid is more negative than

the transfer potential of Cl^- . Thereby, its characteristic peak is outside of the potential window.

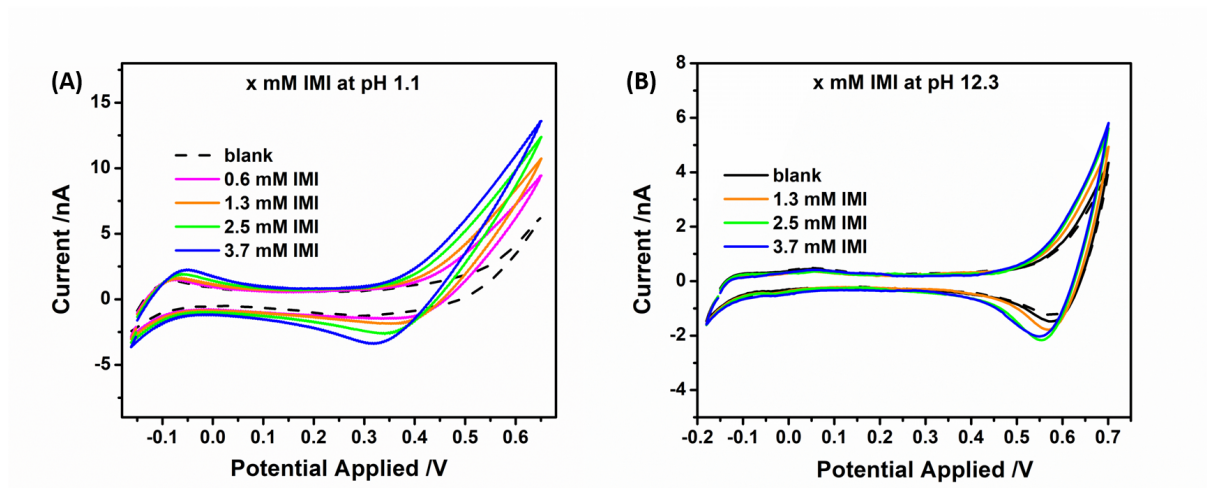


Figure 4.17: Cyclic voltammetry of IMI (A) at pH 1.1 from 0.6 mM to 3.7 mM; (B) at pH 12.3 from 1.3 to 3.7 mM. $\nu = 10 \text{ mV} \cdot \text{s}^{-1}$.

4.2.3 Metam sodium

The metam would become cation in an acidic environment below its pK_a is 2.89.²⁰⁴ We then tested metam at pH 2.3. However, we did not see any signal peak in the potential window after increasing metam sodium concentration as Figure 3.18 shown.

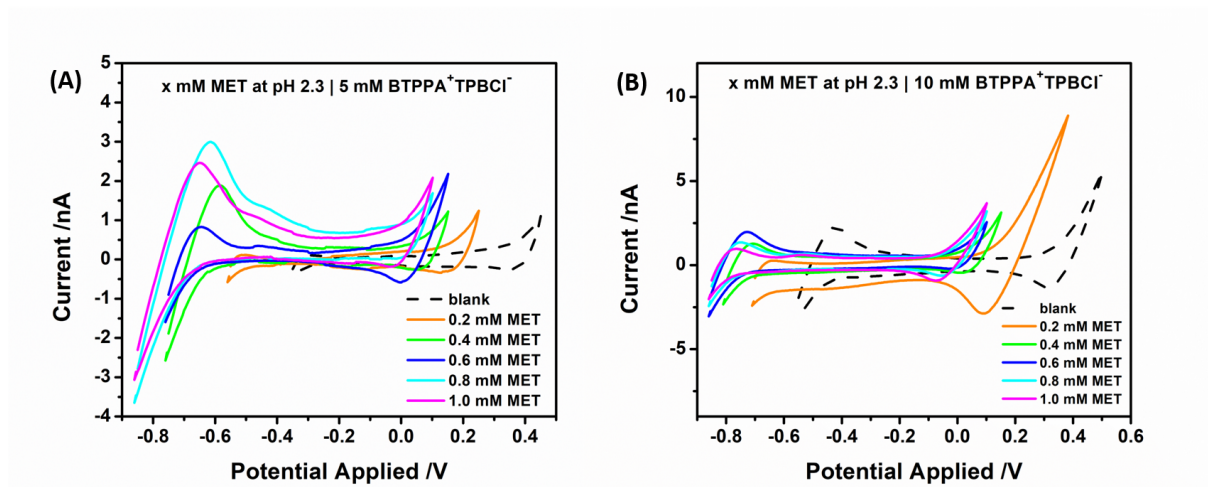


Figure 4.18: Cyclic voltammetry of MET: (A) at pH 2.3 from 0.2 mM to 1.0 mM MET using 5 mM BTPPA⁺TPBCl⁻; (B) at pH 2.3 from 0.2 mM to 1.0 mM MET using 10 mM BTPPA⁺TPBCl⁻. $\nu=10\text{mVs}^{-1}$

Besides, we saw the negative shift of potential window when the MET concentration was increased for different organic electrolyte concentrations: 5 mM mM BTPPA⁺TPBCl⁻ and 10 mM mM BTPPA⁺TPBCl⁻. To quantify this movement, The first peak current was selected with considering Cl^- ion transfer potential and the curve was traced as a function of the MET concentration. As Figure 3.19A illustrated, the transfer potential of chloride ion would be more negative as increasing the concentration of metam sodium. In Figure 3.19A, even the organic electrolyte concentration of BTPPA⁺TPBCl⁻ were augmented up to 10 mM but the result showed same tendency. In Figure 3.19B, the scales of ITIES potential windows were mostly stable and had no link to the MET concentration.

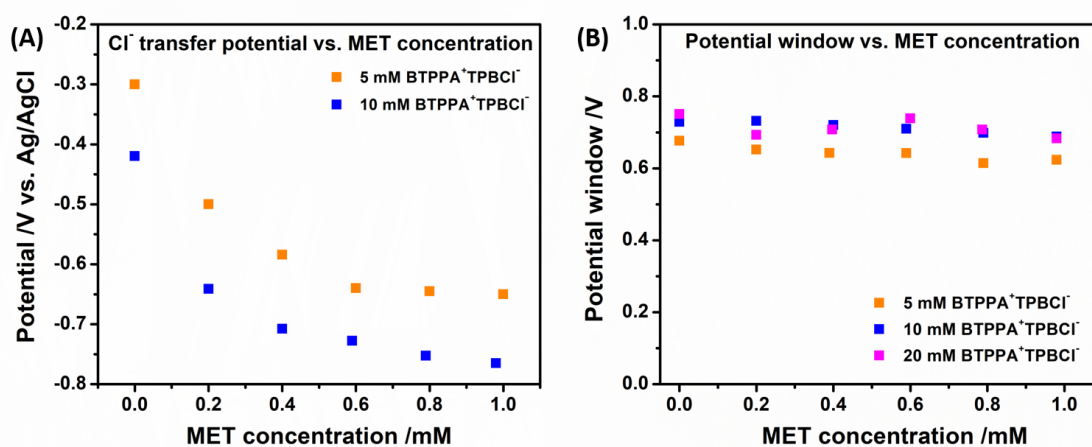


Figure 4.19: (A) Decay of Cl^- transfer potential with increasing the concentration of MET from 0.2mM to 1.0 mM under 5 mM BTPPA⁺TPBCl⁻ and 10 mM BTPPA⁺TPBCl⁻ two conditions; (B) the potential window scale was stable and had no direct link to the concentration of organic electrolyte BTPPA⁺TPBCl⁻.

We estimated there was a possible decomposition happened for MET in acidic solution as described in the introduction. MET would decompose into methylamine(MA). Thus, we tested different concentrations of methylamine in the aqueous solution. As Figure 3.20 shown, there was no potential windows shift while adding MA. Thereby, the shift of potential window was not caused by the decomposition of MET. It would probably Ag reference electrode in the organic phase has reaction with MET.

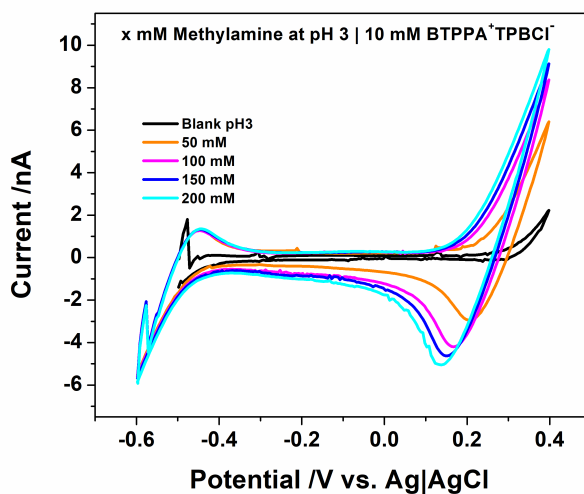


Figure 4.20: Cyclic voltammetry for Methylamine at pH 3 from 50 mM to 200 mM. $\nu=10\text{mVs}^{-1}$

4.3 Conclusions

Firstly, we have investigated the ion transfer mechanism of AME at Micro ITIES. It would not only help us to detect AME concentration in different scale mM and μM by pH modulation, but also it could improve the current peak by optimizing the spontaneous transfer AME into the capillary at Micro ITIES scale. The method is based on the hydrophobic property of AME in the organic solution. We accomplished a quantitative measurement for AME with a single pore capillary at Micro-ITIES. Detection would be optimized based on pH and preconcentration in the organic capillary. We demonstrated firstly the combination between protonation and preconcentration at Micro-ITIES pipet electrodes. It indicated that linear diffusion would also happen for Micro-ITIES during the forward scan if protonation process starts in the organic solution and followed TIC facilitated process. In our experiments, AME detective range would be mM at pH=1 (simple ion transfer) and be μM at pH=3 (proton assisted transfer and preconcentration in capillary). We further demonstrated the improvement of AME detection at Micro-ITIES by integrating an organic acid for protonation of AME and by stirring in the pH > pKa

aqueous solution for preconcentration in the organic solution. So, it makes the measurement range differently. This strategy would be not only applicable for hydrophobic ion detection at ITIES, but also for hydrophilic ion detection if we use aqueous electrolyte capillary. The new strategy also presented the complexity of ITIES, which allows us to design the electrochemical sensor based on ITIES in a distinctive angle which makes it more competitive than traditional electrochemical sensors. What is more, this strategy would be not only applicable for lipophilic ion detection at ITIES, but also hydrophilic ion detection if micro-capillary is filled aqueous phase.

Base on this principle, we improved the detection using phosphate buffer at pH 6.82. The buffer medium can provide sufficient proton during proton assisted transfer. Meanwhile, neutral medium can also improve spontaneous transfer into organic phase for AME. Thus, we tested 3 different types phosphate buffer. All the buffers can make the ametryn to be detectable. But only 1 mM phosphate buffer can optimize the current signal comparing background. And it offered a good sensitivity while 10 mM phosphate buffer has enough proton but too large background current and 0,1 mM phosphate buffer cannot provide enough proton. We also applied this method for 3 different spiked river samples. And the result showed that each calibrations had a linear regression using AC voltammetry. All the tests can achieve a limit of detection around 0.3 μM .

Secondly, the detection of IMI and MET was not good unfortunately. Still, the result of MET is interesting duo to the unique shifting of potential window. This phenomena has not been studied precisely. We din not get the right answer.

In summary, the quest for new pesticides to measure accurately at ITIES is a great impetus to research efforts to understand their individual transfer.

Chapter 5

Silica electrodeposition study

5.1 Introduction

The silica electrodeposition is highlight work of ELAN group at LCMPE. Electrodeposition of mesoporous silica at solid electrodes (ITO) was firstly reported by Walcarius et al.²⁰⁵ This mesoporous silica films with high symmetry and controlled pore orientation is achievable by the bottom-up method of Electrochemically Assisted Self-Assembly (EASA).²⁰⁶ Using such an approach, the condensation of silica precursor can be catalyzed by OH⁻ electrogeneration at cathodic potential. Under these conditions, cetyltrimethylammonium cations (CTA⁺) present in the reaction media plays a role in the formation of hexagonal structure of silica film perpendicular to the electrode surface. Such films deposited on an electrode surface can be of great interest in sensing applications if likely to interact with target analytes in an environment ensuring great accessibility and fast mass transfer rates.

The electrochemically controlled formation of a silicate film at ITIES is firstly reported by Mareček et al.²⁰⁷ This study shows that the separation of template and precursor ions through the interface between two immiscible electrolyte solutions opens up a new avenue to prepare silicate films at the liquid-liquid interface. Furthermore, the thickness of the silicate layer can be easily controlled by the amount of charge. Specifically, the time and current magnitude of the electrodeposition can be modulated to control the electrodeposited film. Also, template ions can be removed from this thin film layer by reverse voltage during the reverse process. The authors also note that the silicate layer can also be co-grown on other porous materials or membranes that support a liquid-liquid interface. The formation of this co-grown film can be initiated both chemically or by taking advantage of the interfacial potential difference caused by suitable ions in the liquid-liquid interface.

Latter, Poltorak et al. developed mesoporous silica electrodeposition at the liquid-liquid interface by galvanostatic deposition using surfactant CTA⁺ as the suitable ions.¹²⁶ The macroscopic liquid – liquid interface electrochemical modification is achieved with silica material structured as the formation of Si-O-Si bond. The cationic surfactant as the surface driving agent to catalyze silica in the aqueous phase and as the templating agent in the organic phase during cyclic voltammetry. In detail, the CTA⁺ ion transfer

was facilitated by hydrolyzed TEOS species in the aqueous phase and the formation of silica at the ITIES is limited by CTA^+ . Latter, silica deposits were also found to stabilize the liquid-liquid interface and can act as membrane to improve the selectivity for ion detection.

In order to improve the electrochemical performance of the mesoporous silica thin films at liquid-liquid interface, the surface of the silica walls can be modified with a particular organo functional group. The schematic presented below shows the two main strategies used for surface silica modification: co-condensation and post-synthesis grafting. The co-condensation approach is bottom-up way. It means that the organosilane reagent of the desired organo-functional group is included in the precursor solution with the sol gel precursors. This method obtains a balanced distribution of functional groups on the channel wall and few channel blockages. It is important to note that if the concentration of the organosilane reagent is too high in comparison to the sol-gel precursor solution, the resulting structure will be disorder and nonporous.^{208, 209}

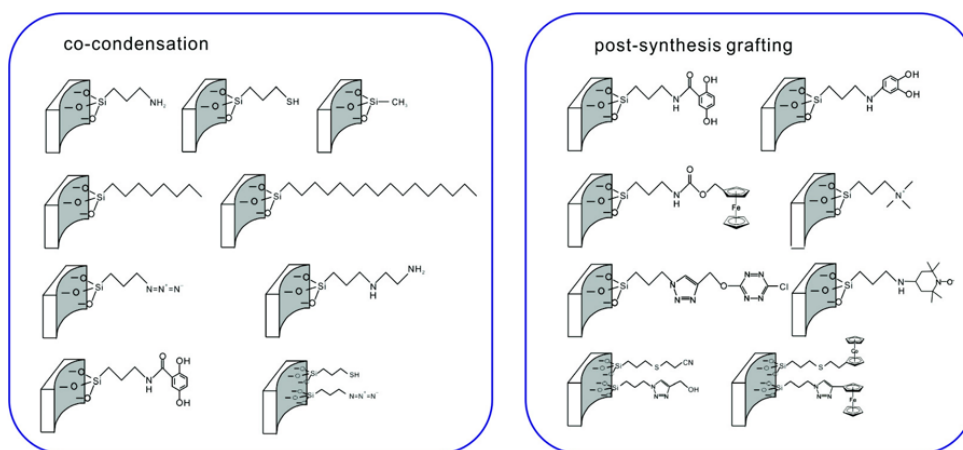


Figure 5.1: Co-condensation and post-synthesis grafting routes for for the functionalization of silica mesochannel walls.²⁰⁹

Therefore to maintain the highly ordered and vertically aligned structure, one must keep the percentage of organosilane reagent relative to the sol-gel precursor below the threshold amount which is different for every functional group. The optimization of silica film thickness at ITIES is needed. In the following part, we worked on the influence of the parameters such as the electrodeposition time and geometry i.e. at miniaturized ITIES.

5.2 Results and discussion

5.2.1 Macro scale electrogeneration of silica film

Firstly, we followed silica modification choosing CTA^+ as the cationic surfactant as the surface driving agent. It has been shown that silica deposits can be formed only in the presence of silica precursor in the aqueous phase and positively charged surfactant template in the organic phase from Lukasz Poltorak's thesis. He indicates that the CTA^+ ion transfer was facilitated by negative charge of hydrolyzed polynuclear TEOS species in the aqueous phase. The shape of voltammetric response has suggested the interfacial adsorption process of CTA^+ , as abrupt drop in current was always observed on the reverse peak. This formation process of cyclic voltammetry is illustrated in Figure 4.3. Additionally, TEOS was hydrolysis in aqueous solution at pH 3 and this precursor was adjusted by NaOH at pH 9 during the electrodeposition.

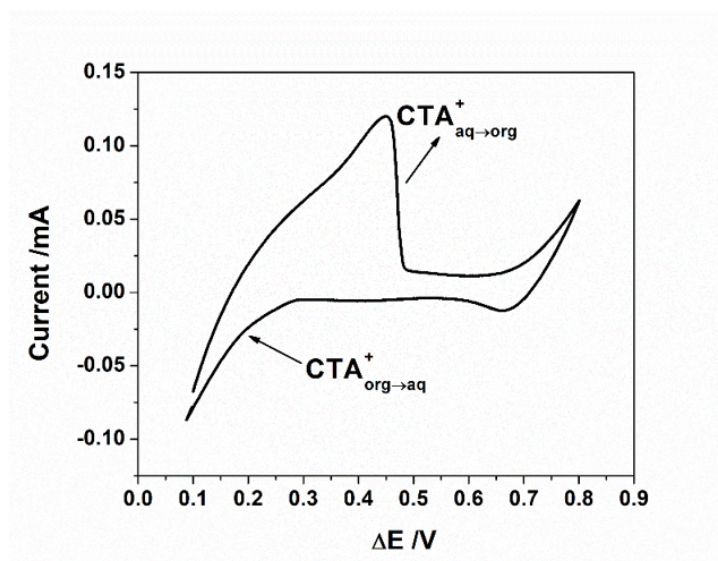


Figure 5.2: Black solid line was recorded in the presence of TEOS (50 mM, hydrolysis at pH3) and in the presence of CTA^+ in the organic phase (14 mM). Scan rate = $5 \text{ mV} \cdot \text{s}^{-1}$.

Moreover, it was concluded that the formation of silica at the ITIES is strictly limited by the concentration of CTA^+ in the organic solution, as the charge above the reverse peak was increasing linearly with its concentration. Thereby, we always kept the CTA^+

concentration as 14 mM with galvanostatic deposition at $-13.4 \mu\text{A}$ and studied only the electrodeposition time. For example, chronopotentiometry with 300, 600, 700 seconds were individually applied, and their signals were recorded in Figure 4.4. The current is decreasing due to the silica generation at the liquid-liquid interface.

The current curves indicate that the electro-generated films would be different in a view of that the initial starting potential, but the absolute value of potential are relatively similar ca. 0.1 V. Thus, the electrodeposited film would be reproducible as the potential tendency is quite resemblant from 0 to 100 seconds. The variation of initial potential is probably due to the reference electrode used for organic phase.

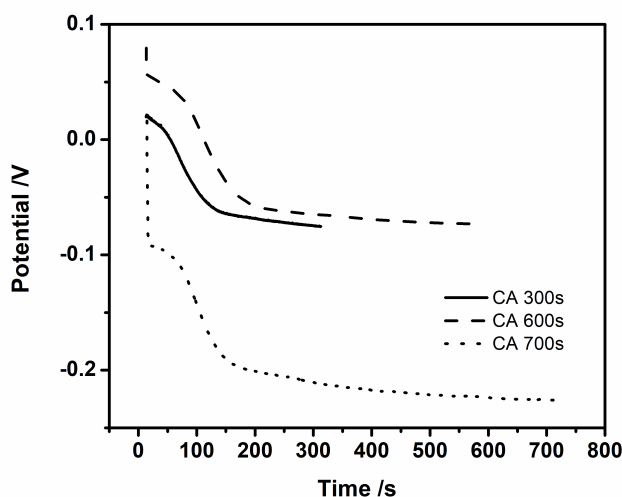


Figure 5.3: Galvanostatic deposit at $-13.4 \mu\text{A}$ for silica film at macro ITIES lasting different time period: 300s (solid line), 600s (dashed line), 700s (dotted line).

To characterize the influence of the silica membrane for ion transfer, TMA^+ was used as the model analyte to study the silica membrane's permeability. These results were presented in Figure 4.5 for different silica deposition time. TMA^+ concentration from 0.2 mM to 1.0 mM were tested by cyclic voltammetry and the current response were adjusted at same scale. At the same TMA^+ concentration, the peak current of silica 100s film and silica 300s film is smaller than the peak current of other silica films. For instance, the silica 100s film limited 1 mM TMA^+ as 0.08 mA and the silica 300s film restricted at 0.075 mA. However, the silica 50s film detected it as 0.1 mA, and the silica 500s film presented

0.12 mA. As a result, the silica membrane reduced the ion transfer at the liquid-liquid interface due to its narrow channel. With shorter electrodeposition (50 s), the thin silica membrane could enhance ion transfer. However, the capacitance is increased. For longer deposition times, the silica membrane is growing thicker (500 s). Such a membrane offers a particular ion transfer at ITIES and provides a good modulation for ion detection. However, massive resistance at the liquid-liquid interface exists for all the silica deposit since the difference potential between the forward peak and the backward peak are all over 0.1 V. The silica-modified interface worsen ion diffusion. Besides, the adsorption of TMA^+ at silica film is apparent in the cases of silica 50s film and silica 500s film when we check the cyclic voltammogram form. The current signal shape is asymmetric, where the forward peak currents are wave-like, and the backward peak is tail-finished for 0.8 mM and 1.0 mM. Both the silica 50s film and the silica 500s film are present symmetric shape all the time.

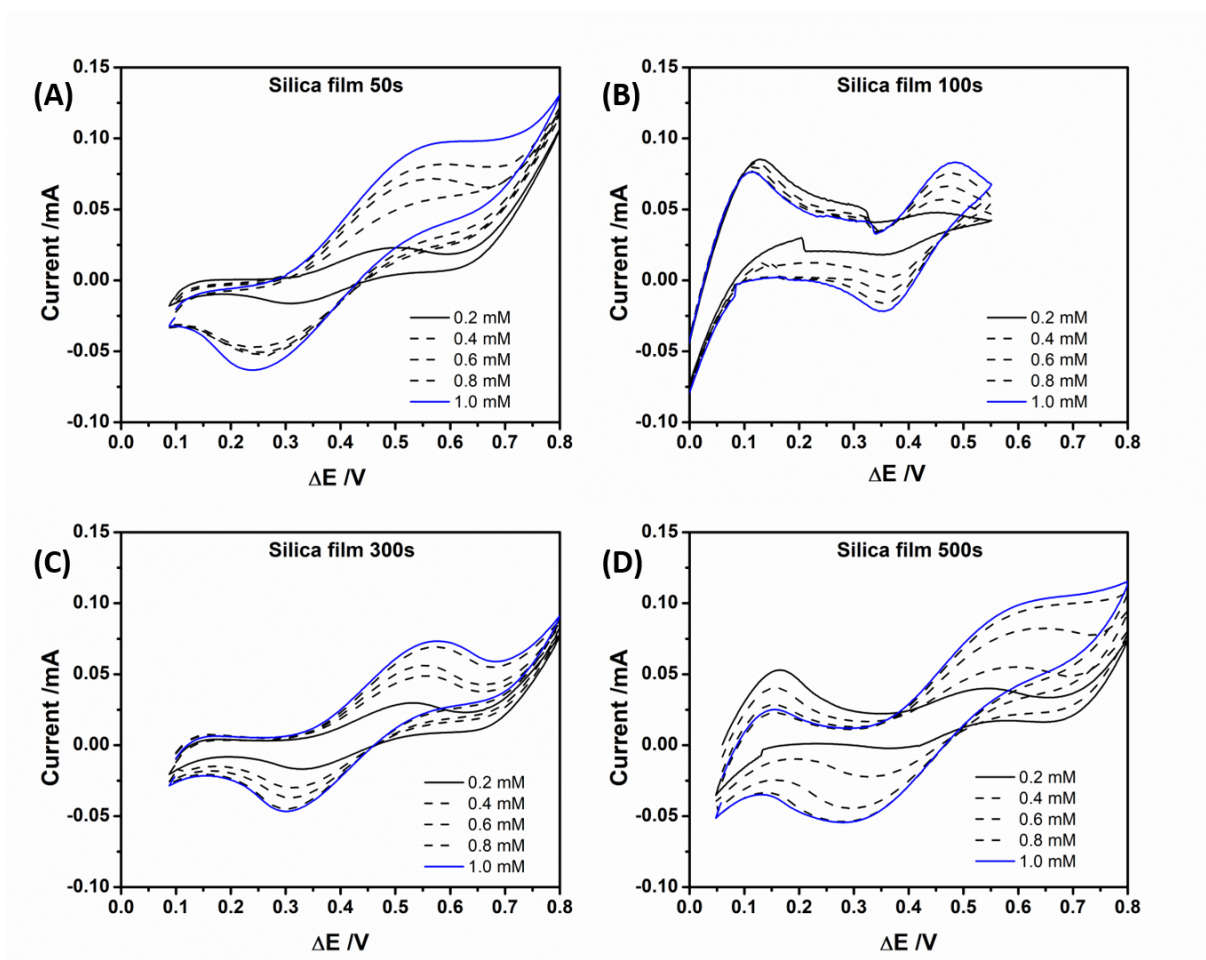


Figure 5.4: CVs of 1 mM TMA^+ crossing the silica interface with different deposit time.

To understand this influence deeply, we introduced the variable deposit time for the same condition from 0s to 900s and selected the peak current as a function of deposit time. Figure 4.6 illustrated the peak current for different TMA^+ concentration in the role of the electrodeposit time. Additionally, 0s is the condition without applying the potential but still contain the silica precursor TEOS in the aqueous solution. Precisely, the calibrations between the analyte concentration and peak current for each silica film are illustrated in Figure 4.7A. The sensitivity of each silica film is extracted from the calibration curves and presented in Figure 4.7B. As a consequence, the presence of deposited silica has an impact on both the current intensity and the slope for ion transfer. For a fixed analyte concentration, its current signal relatively depends on the deposited silica membrane.

Silica layer at the liquid-liquid interface can be optimized through controlling the time in the galvanostatic deposition. Thereby, the silica membrane's property is changed by the inside channel thickness.

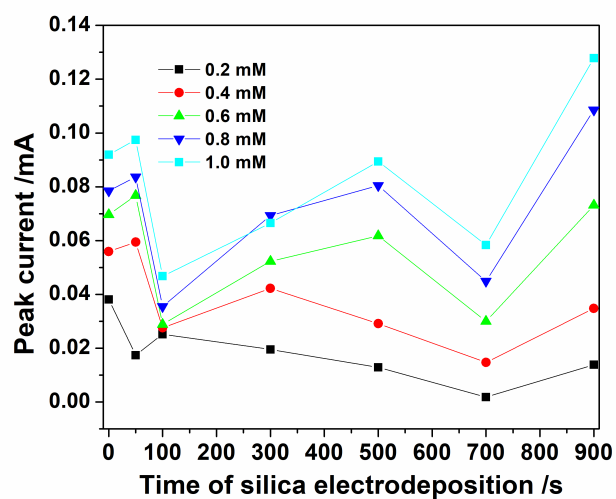


Figure 5.5: Forward peak current of TMA⁺ from 0.2 mM to 1.0 mM as a function of silica electrodeposition time. Obtained from previous cyclic voltammograms using same electrochemical cell 1, $\nu = 5 \text{ mV} \cdot \text{s}^{-1}$.

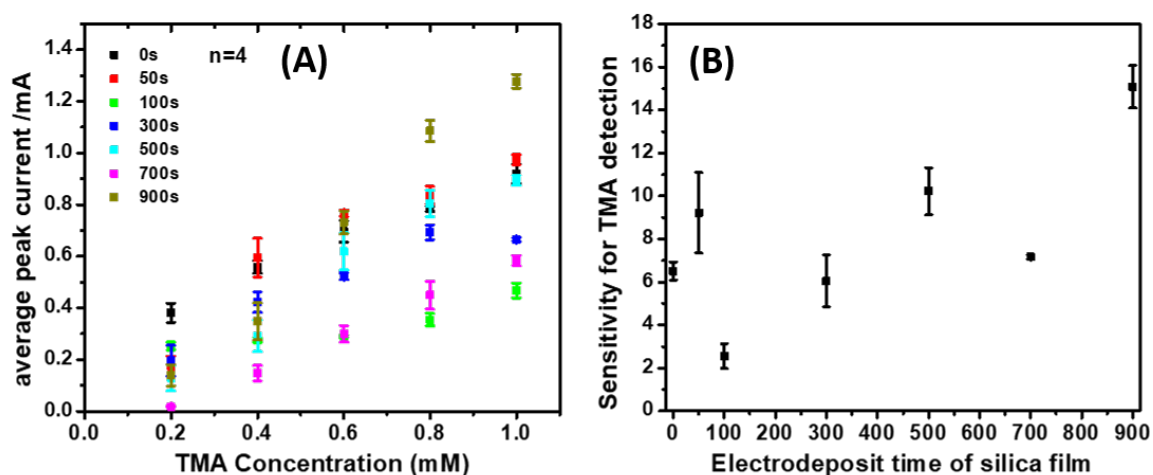


Figure 5.6: (A) the detective peak current as a function of TMA⁺ concentration with different time deposit silica membrane. (B) the calculated sensitivity (i.e. slope of the calibration curve) of TMA⁺ detection with different time silica membranes.

In detail, the silica membrane of the 50s and 900s have a larger electrochemical signal than the blank test 0s. As supposed, silica membrane could adsorb TMA⁺ and give obvious feedback for high analyte concentration such as 1 mM. The thin silica 50s did not absorb more than the thick silica 900s. Still, the thin silica layer with high TMA⁺ concentration at the interface plays a key role as important as the thick silica layer. Other silica membranes are limiting the ion transfer due to the unclear concentration in the film by comparing the peak current of 50s silica film and 900s silica film.

We could see that silica film deposited for 50s, 500s and 900s showed higher TMA⁺ transfer peak than blank test 0s. Silica film 300s and 700s have similar peak currents, but 700s are much more reproducible. Silica film 100s is more likely linked to block ion transfer across the liquid-liquid interface. From the optimization of silica membrane, we could see than obstruction or facilitation of ion transfer can be both possible from the silica membrane. One possible reason for that may not only from the thickness of the silica membrane but also come from the pores inside the membrane which make it adsorption possible for ion transfer.

Since that, silica membrane could be used for accumulation while forming the silica

film 50s and 900s at the interface. However, all the silica membranes were fragile due to the absence of curing in the oven comparing the silica film electrodeposit at ITO. When we change the aqueous phase, the in-situ film was damaged as Figure 4.8 illustrated. Three major mechanic faults of fissure, rupture and bubble are not easy to avoid during the manipulation of changing the organic phase using the pipette. When we removed the aqueous solution of silica precursor TEOS at the top cell, the pressure difference between the aqueous phase and the organic phase would push the in-situ silica to move up. Because the connection of the glass wall with silica film is not mechanical strong, silica film then is damaged by this force.

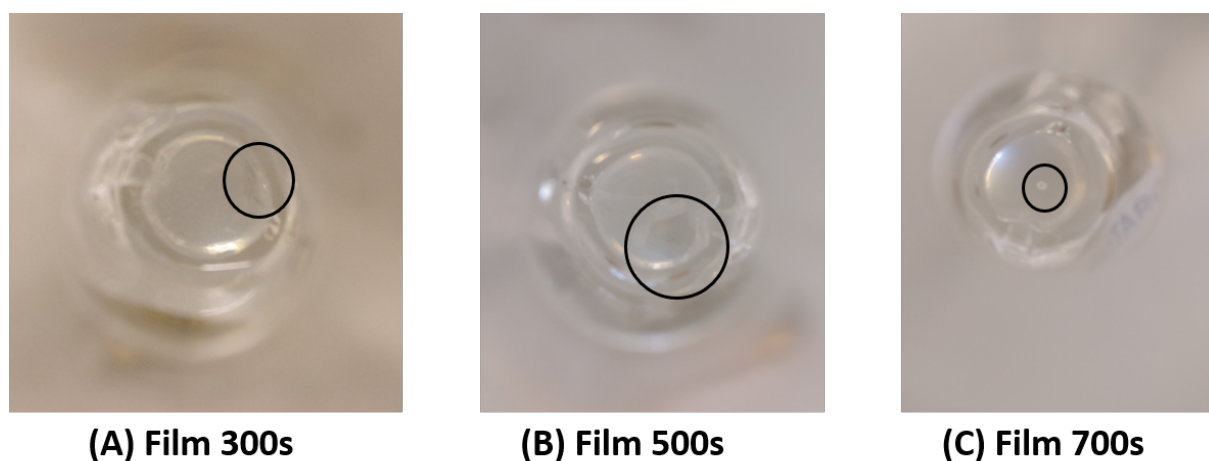


Figure 5.7: The mechanical problem noted in cycle for macro silica membrane: (A) fissure from film 300s, (B) rupture from film 500s, (C) Bubble from film 700s.

5.2.2 Micro scale electrogeneration of silica film

In order to avoid these mechanical issues, we introduced the silica electrodeposition at single pore capillary. Miniaturization of ITIES at single pore capillary can offer lots of advantages such as iR drop and improved mass transfer. Still, it also can solve the mechanical problems by curing in oven. Thus, the first step before electrodeposition is to make sure these capillaries function well after following the fabrication process in the experimental section. Figure 4.9 shows the typical cyclic voltammograms recorded at single pore μ ITIES which have asymmetric current peaks from an asymmetrical diffusion zone

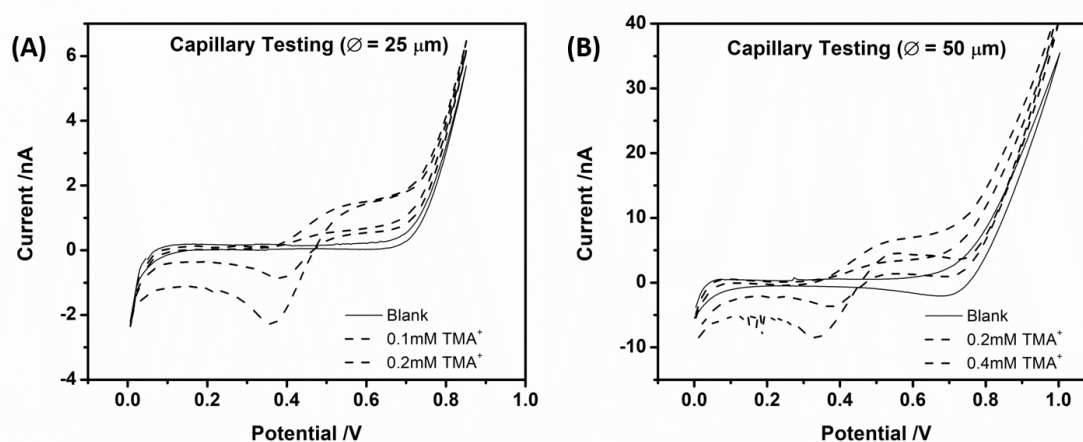


Figure 5.8: Single pore capillary testing by using TMA^+ ion transfer: (A) pore diameter $\text{Ø} = 25 \mu\text{m}$, (B) pore diameter $\text{Ø} = 50 \mu\text{m}$. Scan rate = $5 \text{ mV} \cdot \text{s}^{-1}$.

profile. The capillary detection was straightforward by assuming a direct experimental relation between the concentration of model ion (TMA^+) and the peak current during the forward scan. This relation is following by the equation:

$$i_p = 4nFDcr$$

where n is the charge number ($n=1$ for TMA^+), F is the Faraday constant, D is the diffusion coefficient, c is the concentration, r is the pore radius. Since the TMA^+ diffusion coefficient keep same in both phases, the peak current would have a linear relation with its concentration and the pore radius which have demonstrated in Figure 4.10. Table 4.2 lists all the concentration with measured peak current and both types of capillaries fit well with the current formula. Thus, the capillary can be used at next stage for silica modification.

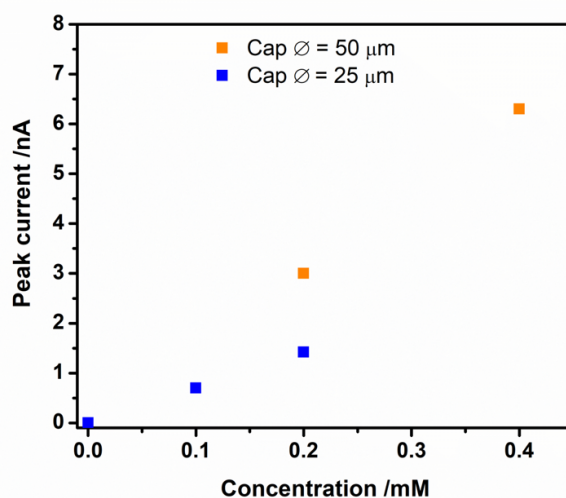


Figure 5.9: The calibration dotted line for the capillary with diameter 25 μm and the capillary with diameter 50 μm . Other experimental parameters are unchanged.

Table 5.1: Calibration points of forward peak current as the electrochemical response at unmodified μITIES .

c /mM	r / μm	Peak current /nA
0.1	12.5	0.7
0.2	12.5	1.4
0.2	25	3.0
0.4	25	6.4

We start to identify the behavior of CTA^+ transfer across micro-interface during silica film electrogeneration. Figure 4.11 illustrated the typical cyclic voltammogram of silica electrodeposition at μITIES as the capillary was filled with the organic phase $\text{CTA}^+\text{TPBCl}^-$. Simultaneously, the current of CTA^+ transfer from the organic phase to the aqueous phase is negative and ca. -5 nA.

After identifying the surfactant transfer, we could apply the galvanostatic deposition for micro pore capillary. However, cyclic voltammetry from 0.4 V to 0.8 V was employed to enforce all the CTA^+ in the aqueous phase back to the organic phase in order to have unified all the CTA^+ ions transfer from the organic phase to the aqueous phase. The

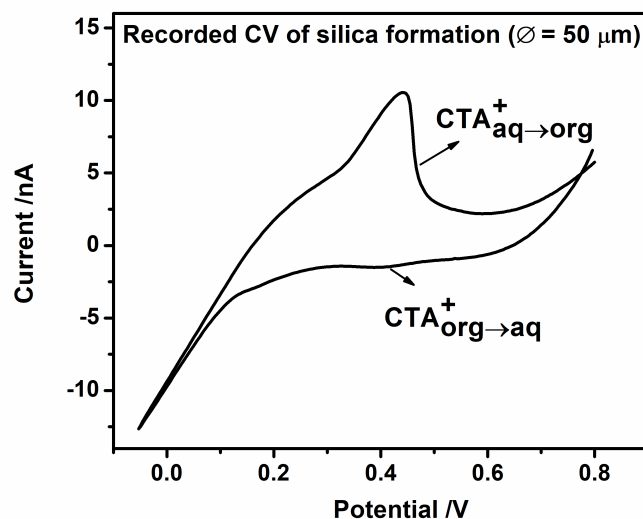


Figure 5.10: Recorded cyclic voltammogram of surfactant-template CTA^+ silica film electrodeposition at single pore capillary. 50 mM TEOS(aq, pH=9) | 14 mM $\text{CTA}^+\text{TPBCl}^-$ (org). Scan rate = 5 mV s^{-1} .

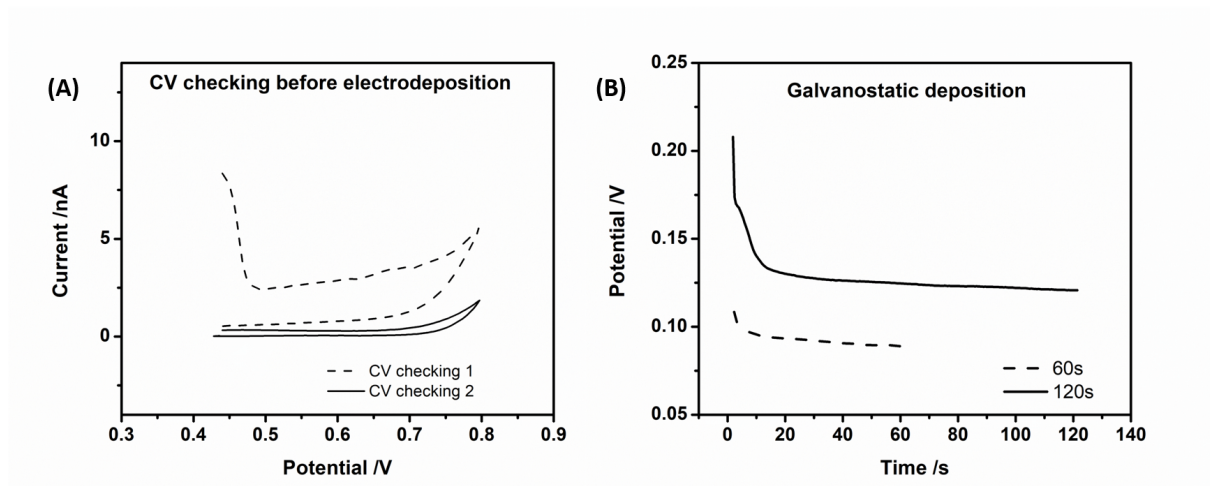


Figure 5.11: (A) CV checking to sure all the CTA^+ ion rest in the organic phase before silica electrodeposition. (B) Potential transient during the galvanostatic deposition of silica film at -5.2 nA . Ag | 50mM TEOS(aq, pH=9) || 14mM $\text{CTA}^+\text{TPBCl}^-$ (org) | AgCl | Ag.

first CV always has the the positive current at initial potential at 0.4 V caused by a mount of CTA^+ was contained in the aqueous phase in the beginning. If obtained CV like checking 2 as Figure 4.12A shown, it means all the CTA^+ are polarized into the organic phase. Consequently, chrono potentiometry with a fixed negative current (-5.2 nA) was used to electro-generate the silica film at the pore of capillary for ensuring CTA^+ are transferred. In this work, we controlled the deposit time for two conditions: 60s and 120s. Their galvanostatic voltammograms were presented in Figure 4.12B. The potential window was shifted from positive to more negative potentials for both conditions. The electrodeposit of 120s was initial taking place at +0.2 V which is more positive than the 60s electrodeposition (starting potential is 0.1V). Additionally, the tendency of current from 0s and 10s is recorded similar for both cases. After 20 seconds, both currents keep at constant. Thus, the silica mesoporous membrane at micro capillary is reproducible at the electrodeposition stage.

With the support of capillary, silica membrane can be held at the interface while micro-ITIES is established. The optical captures were shown in Figure 4.13.

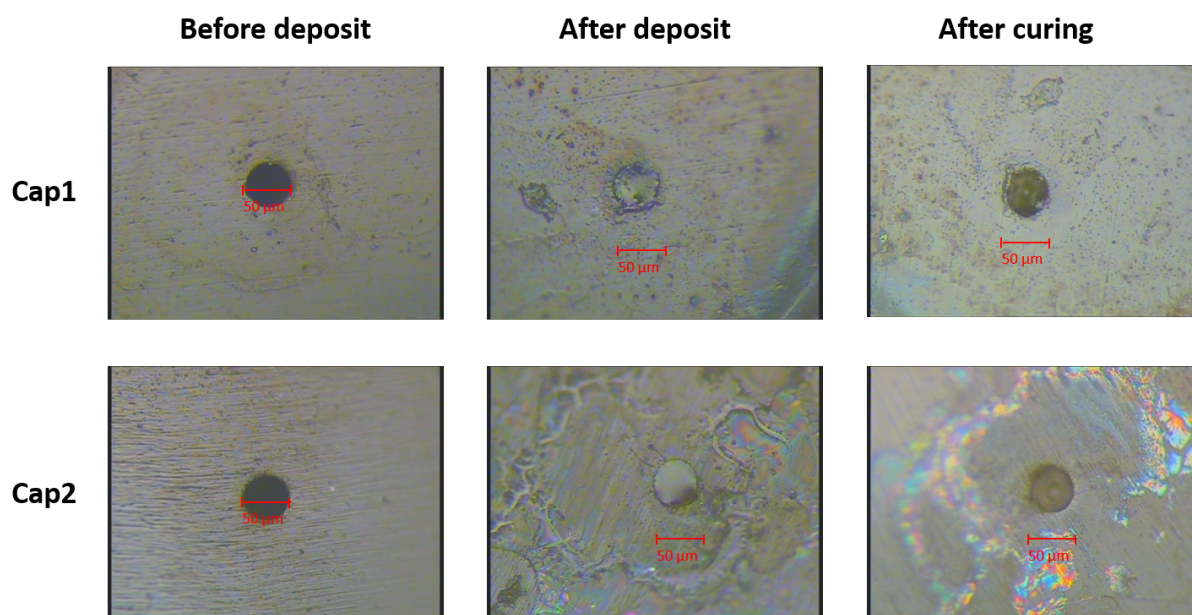


Figure 5.12: Optical capture for micro silica film at the single pore capillary at the experimental step before electrodeposition, after electrodeposition and after curing.

We could see the silica films were located at the pore of capillaries and the silica films can be solidified after the curing in oven at 110 °C for 24 hours. Furthermore, these silica modified capillaries were characterized by cyclic voltammetry with recording the model ion TMA⁺ transfer. The electrochemical responses for two types of capillaries 60s and 120s are shown in Figure 4.14. Both silica modified capillaries have limited TMA⁺ transfer across the water-DCE interface. For example, the peak current of 0.4 mM TMA⁺ measured at an unmodified capillary, silica modified (60 s) capillary and silica modified (120 s) capillary were 6.4 nA, 2.2 nA, 5.8 nA respectively. In other words, lower amount of TMA⁺ was transferred from the aqueous phase to the organic phase as a consequence of silica film presented at the tip of capillary. Comparing these two kinds of silica deposit, capillaries modified for 60 s have strong limitation for model in transfer and less noise from capillary itself. It has to be mentioned that a new current peak was located for the black testing with capillaries modified for 120 s. This result pointed out that the residual surfactant CTA⁺ would adhere to silica film during the galvanostatic deposition and presented electrochemical response in latter characterization testing of capillary. This signal can be decreased as long as keeping the tip of capillary into the aqueous solution. In this study, the high concentration characterization of model ion was done latter than the low concentration. As a result, this surfactant peak dwindled as the model ion concentration increased and this trend is illustrated in Figure 4.14. In this scenario, it can be concluded that the longer time silica deposit at the single pore capillary worsened the ion transfer across the liquid-liquid interface due to the surfactant residue at the film and the relatively increased interfacial capacitance.

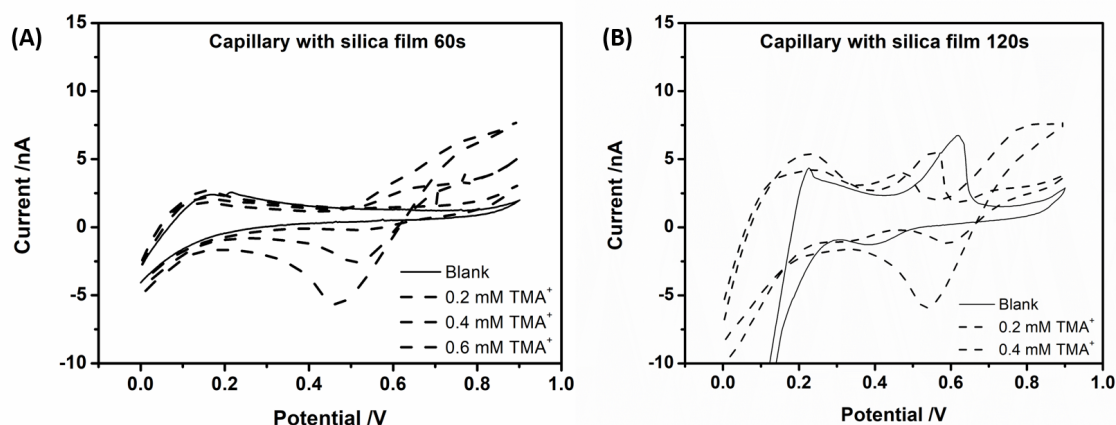


Figure 5.13: Recorded cyclic voltammograms in the presence of TMA^+ ion transfer at μITIES using the silica modified capillary: (A) capillary with the galvanostatic electrodeposit 60s of silica, (B) capillary with the galvanostatic electrodeposit 120s of silica. Scan rate = $5 \text{ mV} \cdot \text{s}^{-1}$.

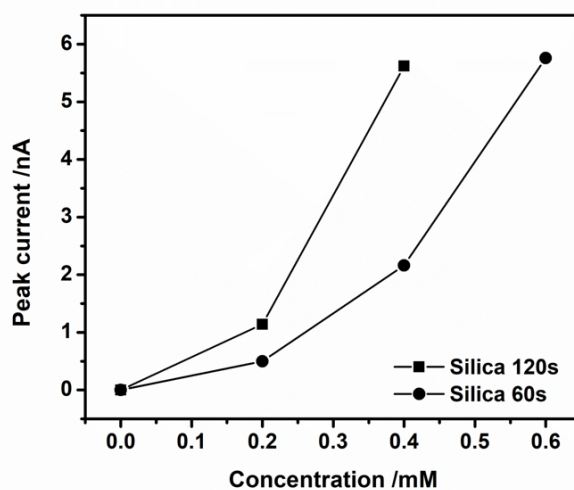


Figure 5.14: The calibration of TMA^+ using the modified capillary 60s and 120s.

From the calibration illustrated in Figure 4.15, the ion transfer would be enhanced in the presence of thick silica film due to the adsorption. However, silica membrane at the tip of capillary would bring the inconvenience at the stage of adding organic solution during

the model ion characterization. Figure 4.16 present the recorded cyclic voltammetry from the failed capillaries. The capillary with silica 60s was more likely restricted the ion transfer but still could establish the polarized liquid-liquid interface. For the silica 120s capillary, the recorded cyclic voltammetry indicated that ITIES was not built since the thick silica film at the tip of capillary, as Figure 4.16D illustrated.

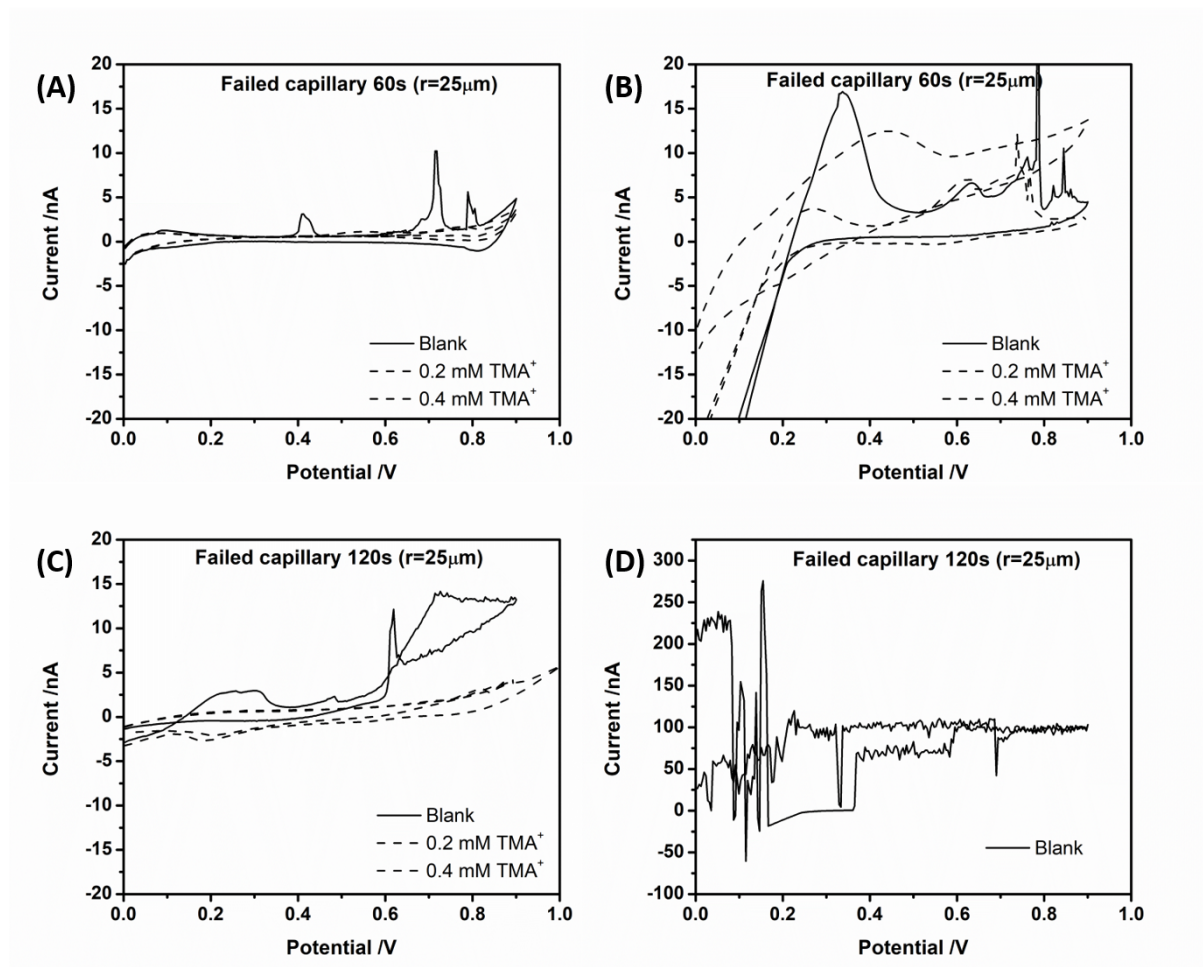


Figure 5.15: Cyclic voltammograms recorded from the failed capillaries with modified silica membrane: (A) the capillary with silica 60s, (B) the capillary with silica 60s, (C) the capillary with silica 120s, (D) the capillary with silica 120s.

Other possible reason is the absence of organic phase in capillary. This kind of capillaries can not be used in electrochemical characterization. Our experimental reproducibility is only 25%, i.e. 3 capillaries succeed but 9 capillaries failed. Thus, we also established

a digital simulation performed by finite element method using the COMSOL software to compare predict the experimental results of cyclic voltammetry. However, this model just allowed us analyze the mass transport at modified membranes by varying the diffusion coefficient and the thickness of membrane. It can not predict the geometry for mesoporous structure of deposited silica membrane.

5.3 Conclusions

The silica membrane at the Macro-ITIES was optimized through electrodeposition time. The property such as ion selectivity of these films was really dependent on the process of electrodeposition. At the same time, the in-situ macro membrane can not avoid the disadvantage from mechanical view since the curing and solidification were not achieved. Thus, we moved to micro electrodeposition at single pore capillary. From the optical captures of the tip capillary, we can be sure that the silica membranes were formed at the outlet of the tip even after curing in oven.

However, the electrochemical characterization by analyte ion failed as no current detection and large resistance during measurement. Complication in cyclic voltammetric measurements have been occurred for silica modified interface as a result from the resistance of silica membrane and the hardly addition of organic solution into capillary. These rendered voltammetric analysis difficult and ambiguous. We can conclude that both the thickness and the diffusion coefficient inside the silica membrane play a critical role for ion transfer which would limit clearly the ion transfer. That is the reason hardly get the current signal from micro-capillary after silica deposition.

In details, the modified capillary lost the electrochemical signal in later experiment when we use silica modified capillary to study its membrane selectivity. There are two reasons: the first is the surfactant CTA^+ still attained in the film and in most cases, the second is the mesoporous silica film at the tip block solution and then ITIES can not be established. Comparing the large scale, the characteristic signal of TMA^+ was hindered in Macro-ITIES. Despite this, the electrochemical signal presented was clearly to indicate the silica membrane at the interface. Because of the miniaturized interface, the reproducibility of experiment was still a big issue. Meanwhile, the experimental

measurement of thickness for micro silica membrane was hardly achieved because of the limitations of experiment at micro scale. A reliable characterization method for ex-situ characterization of silica deposition remains to be established.

Chapter 6

Chitosan electrodeposition at ITIES

6.1 Introduction

As natural bio-control active ingredients to defend against fungal infections, chitin or chitosan, are found in the shells of crustaceans, such as lobsters, crabs, and shrimp, and many other organisms, including insects and fungi. It is an abundant source of renewable, natural polymer material. It has a number of commercial and possible biomedical uses due to bio-compatible, easily degradable, non-toxic properties. Thus, chitosan and its derivatives have a huge demand for application, especially in the biomedical field, can be used as a drug carrier, artificial soft tissue materials such as artificial skin, etc. Chitosan is rich in hydroxy and amino groups, which can be modified to develop specific functional polymers materials according to field of application.

6.1.1 The structure and properties of chitosan

Cellulose and chitin are, two important and structurally related polysaccharides that provide structural integrity and protection to plants and animals, respectively in nature. Chitin may be regarded as cellulose with hydroxyl at position C-2 replaced by an acetamido group seen in Figure 5.1B. Both are polymers of monosaccharide made up of glucosamine units ($-(1-4)\text{-}2\text{-acetamido-}2\text{-deoxy-}\beta\text{-D-glucose}$) and glucose units ($-(1-4)\text{-}2\text{-deoxy-}\beta\text{-D-glucopyranose}$ units as Figure 5.1A shown. Thus, chitin is poly ($-(1-4)\text{-N-acetyl-d-glucosamine}$). In fact, as in the case of cellulose, chitin exists in three different polymorphic forms (α , β and γ). Recent studies have reported that the form is a variant of family.²¹⁰

Because of its insolubility in the vast majority of common solvents, chitin was recognized an intractable condensation polymer, and for many years it remained mainly a laboratory curiosity. The chemical structure of completely acetylated chitin is represented in Figure 5.1C. However, chitosan is a linear polysaccharide obtained by extensive deacetylation of chitin. The chemical structure of an entirely deacetylated chitosan is represented in Figure 5.1D. Moreover, since it is virtually impossible to deacetylate chitin completely, which is usually known as chitosan is a family of chitins with different but always low degrees of acetylation (the commercial product contains 15% approximately).

The capacity of chitosan to dissolve in dilute aqueous solutions is the commonly accepted criterion to differentiate it from chitin. Thus, chitosan is a linear polysaccharide composed of randomly distributed β -linked D-glucosamine and N-acetyl-D-glucosamine.

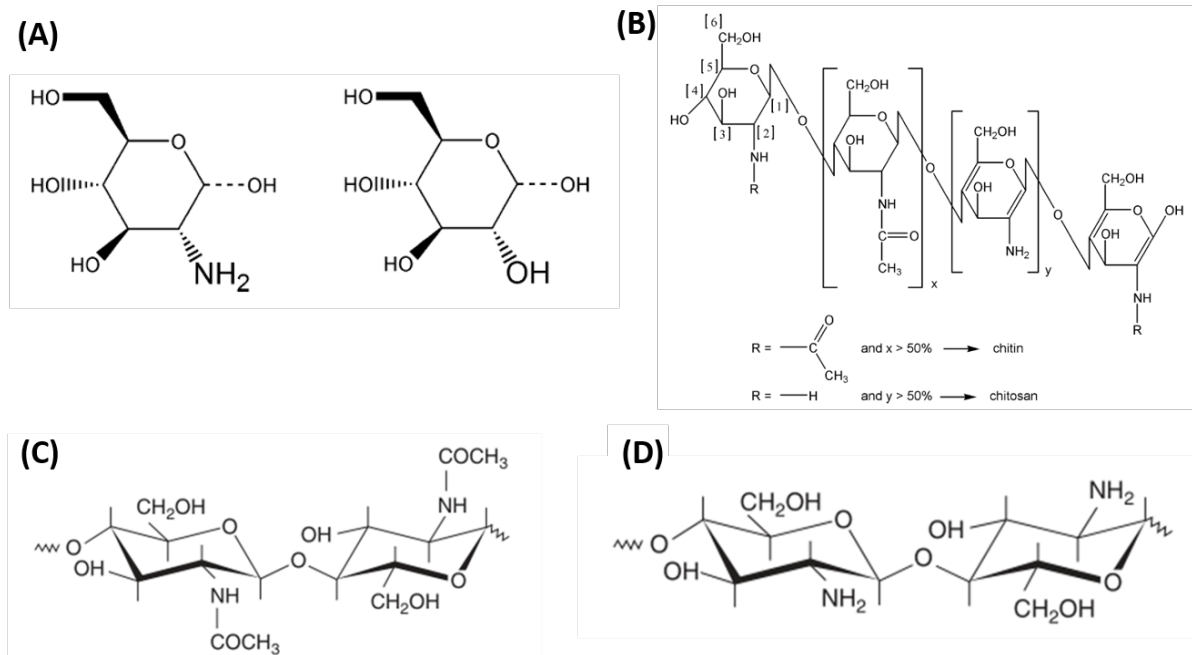


Figure 6.1: (A) Structure of glucosamine (monomer of chitosan) and glucose (monomer of cellulose), (B) Structure of chitin and chitosan (C) Schematic representation of completely acetylated chitin, (D) Schematic representation of completely deacetylated chitosan.²¹⁰

Chitosan dissolves in dilute acid. The higher the degree of deacetylation, the more free amines in the molecular chain, the higher the ionization strength and the easier it is to dissolve in dilute acids. However, the higher the molecular weight, the slower the dissolution. The degree of deacetylation of typical commercial chitosan is usually between 70% and 95%, and the molecular weight between 10 and 1000 kDa (The dalton, symbol Da, is also sometimes used as a unit of molar mass, especially in biochemistry, with the definition $1 \text{ Da} = 1 \text{ g} \cdot \text{mol}^{-1}$).²¹¹ Polysaccharides are soluble in dilute hydrochloric acid, dilute acetic acid, etc.²¹² Chitosan is pH-responsive to the environment, and this property can be exploited to form membranes, fibers, particles, and different forms such as gels and solids. Through further surface modification and cross-linking, chitosan can be used as a matrix to achieve versatility. For example, it has significant potential as a biomedical

material in drug controlled and extended-release cell culture carriers or tissue engineering material.²¹³

Table 6.1: Chemical and biological properties of chitosan.²¹³

Chemical properties of chitosan	Biological properties of chitosan
Cationic polyamine	Biocompatibility
High charge density at pH 6.5	Natural polymer
Adheres to negatively charged surfaces	Biodegradable to normal body constituents
Forms gels with polyanions	Safe and non-toxic
High molecular weight linear polyelectrolyte	Hemostatic, bacteriostatic, and fungistatic
Viscosity, high to low	Spermicidal
Chelates certain transitional metals	Anticancerogen
Amiable to chemical modification	Anticholesteremic
Reactive amino/hydroxyl groups	Reasonable cost

As Figure 5.2 shows, in acidic solution ($\text{pH} < 6.2$), amine groups of glucosamine units are protonated. This protonation allows the polymer dissolution by the establishment of both, electrostatic repulsive forces between polymer chains and hydrogen bonds between water and chitosan. At higher pH, the deprotonation of amine groups, i.e. the decrease in repulsive potential between polymer chains, favors polymer-polymer interactions rather than the polymer-solvent ones. Therefore, chitosan becomes insoluble. The soluble-insoluble transition occurs at pH around 6 to 6.5 depending on the degree of acetylation and molar mass.^{214,215} The amine group has a pKa value around 6.5 depending of the DA.²¹⁶ At DA below 20 %, chitosan shows strong polyelectrolyte behavior (the linear charge density is high) in acidic aqueous solutions that favors expansion of the polymer chain and solubility.²¹⁷ The occurrence of entanglements decreases solubility (polymer-solvent interactions) and enhances polymer-polymer interactions. The formation of interchain entanglements occurs when overpassing a critical concentration and molar mass of chitosan.^{218,219}

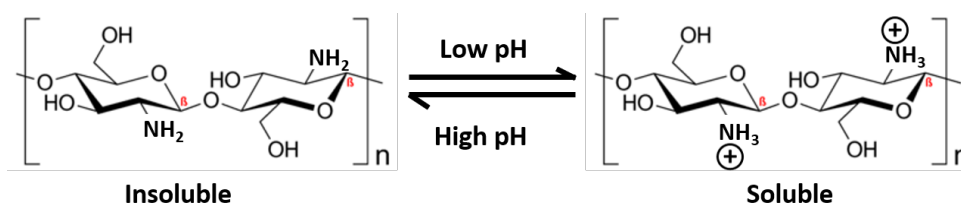


Figure 6.2: Schematic illustration of chitosan's versatility. At low pH (less than about 6), chitosan's amine groups are protonated conferring polycationic behavior to chitosan. At higher pH (above about 6.5), chitosan's amines are deprotonated and reactive.²²⁰

Thus, chitosan became a great promise as next generation membrane materials because its fundamentally sustainable, bio-degradable, recyclable, inexpensive and intrinsically low molecular weight. organics are easily functionalised or engineered, allowing researchers to tune their electrochemical properties and improve their performance in terms of stability and efficiency.

6.1.2 Cross-linking modification

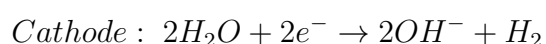
After the dilution of chitosan in an acid environment, it becomes as hydrophilic hydrogels generally consist of a large number of water molecules but keep their structure that does not dissolve in the liquid. Since then, it needs to cross-link to form the stable structure of the film. In particular, CS membranes exhibit higher hydrophilicity due to the presence of hydroxyl and amino groups on the main chain backbone. In particular, CS membranes exhibit higher hydrophilicity due to the presence of hydroxyl and amino groups on the main chain backbone, which would be beneficial to re-functionalize its groups. For example, poly(4-styrenesulfonic acid-co-maleic acid) (PSSA-MA), as a cross-linker and a proton conductor can be employed to synthesis CS film through the esterification reaction between $-OH$ of CS and $-COOH$ of PSSA-MA and the complex formation of NH_3^+ of CS and SO_3^- of PSSA-MA.²²¹ Ordered poly(3,4-ethylenedioxythiophene) (PEDOT) was successfully prepared by electrochemical polymerization of 3,4-ethylenedioxythiophene in lyotropic liquid crystal phase formed by chitosan in an acetic acid solution by Meng et al..²²² Recently, a facile approach for the formation of microporous (chitosan) hydrogel scaffolds based on self-crosslinking using N-(b-maleimidopropoxy)succinimide ester

(BMPS) is reported by Chen et al.²²³ To date, many approaches for the generation of cross-linker chitosan film have been reported and the porogen-based strategy is probably the most well-known. However, the use of electrified immiscible interface for chitosan film in the fabrication process, and the controlling of reaction through another phase in the scaffold have not reported. Thus, in this chapter, and we demonstrated this strategy could be a novel and facile approach for the formation of chitosan film, which relies on the crosslinking reactions of the polymeric materials in organic phase and separate aqueous precursor solutions.

6.1.3 Electrodeposition for chitosan film

Due to the excellent electrical response and biocompatibility of chitosan, there are more and more reports about the research and development of electro-modification for chitosan. Through the electrical signal, the chitosan molecule selectively completes the self-assembly process on the electrode surface and form a thin film. The structure and properties of the electrodeposited film can be adjusted to meet the deposition conditions, such as the concentration of chitosan solution, the deposition time and current. One can accurately control the self-assembly process of chitosan on the electrode surface. The deposition conditions are mild and carried out in an aqueous environment. As described before, chitosan is a weak electrolyte with exceptional pH responsiveness, and it is also considered the only natural electrified cationic polymer that forms hydrogels. In the external environment, when pH is smaller than its pKa value (approximately 6.3), the amine groups of chitosan will be protonated to form water-soluble cationic polyelectrolytes; when the pH is close to or greater than its pKa value, the amine groups will undergo deprotonation and chitosan will become insoluble. So if a reductive potential is applied, the electrolysis of water causes the pH at the working electrode surface to increase, which induces the deprotonation of chitosan molecules and produce chitosan film. The cathodic deposition process of chitosan generally uses a two-electrode system where the cathode uses sheet or rod-shaped gold, iron metal materials or ITO conductive glass and the anode usually uses a platinum mesh electrode. After applying a specific voltage difference between the positive electrode and the negative electrode such as 2.0V in the work of Wu

et al,²²⁴ the current passing through the chitosan solution will electrolyze water on the surface of the electrode, and the chitosan film will be formed at the cathodic electrode (the negative electrode). The reaction formula is followed as below:



The film can be easily removed from the electrode surface, remains relatively stable under natural conditions, and the deposited chitosan gel film can be readily washed away by acid or crosslinked with a crosslinking agent for stable storage. Furthermore, the gel film size prepared by electrodeposition can be controlled within a few micrometers to several millimeters, which is difficult to achieve with conventional sol-gel preparation methods. As Figure 3.1 shown, the chitosan co-electrodeposition process allows for the embedding of nanoparticles, protein cells, and other materials in the formed chitosan gel film.

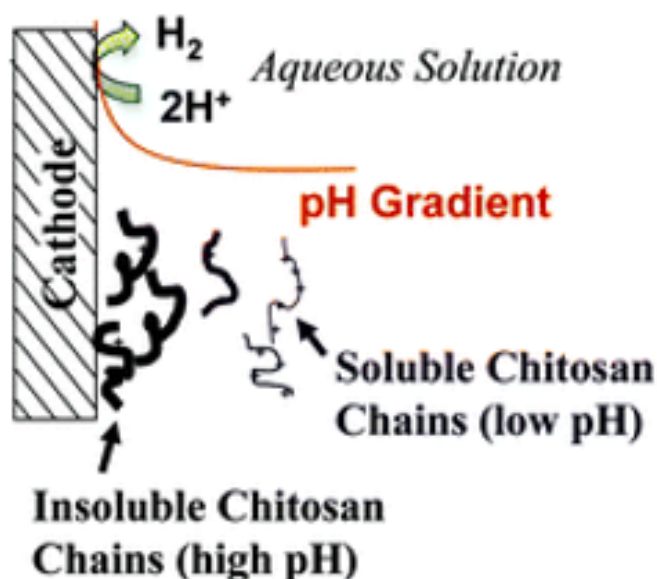


Figure 6.3: Chitosan assembly using the local gradient of pH at a cathode results in the deposition of a chitosan network from solution.²²⁵

6.1.4 Chitosan study at liquid-liquid interface

The ITIES study involving chitosan dates back to 2012 by Yudi et al.²²⁶ The aim of their paper is to study the interaction between chitosan and two different anions. The electrochemical analysis of chitosan at ITIES is based on the changes produced by the presence of chitosan on the voltammetric current corresponding to anion transfer. Due to the presence of amine groups in chitosan, protonated chitosan acts as anion carrier at low pH value. From their results, the binding of the anions to cationic chitosan is enhanced at low pH values due to chitosan exhibits a major fraction of protonated amine groups, thereby, obtaining insight into the effect of the charge, the pH and the concentration of the anion and the cationic polyelectrolyte on those interactions. Thus, it is concluded that electrostatic interactions are the main factor determining the extent of this kind of hydrophilic ions binding to the cationic polyelectrolyte.

Lately, the effect of chitosan on distearoylphosphatidylglycerol (DSPG) films was analyzed by cyclic voltammetry of model ion transfer TEA^+ across the liquid-liquid interface.²²⁷ In this report, the permeability of DSPG film increases when chitosan is present in the aqueous phase, minimizing the blocking effect of the film due to the interaction between DSPG and chitosan. Additionally, the interaction of chitosan with DSPG is proposed. At the stage of low pressure, this interaction is facilitated by Van der Waals forces between the DSPG hydrocarbon tails and the hydrophobic zones of chitosan. At the stage of high pressure, this interaction is probably through electrostatic interaction between phosphate and the amine groups because chitosan is partially expelled from the interface, but it remains at the interface interacting with DSPG mono-layer. Therefore, an enhancement of the permeability of film is achieved due to a channel expansion of the DSPG membrane in the presence of chitosan in the aqueous phase produces. Recently, a better characterization of the interaction between chitosan and phospholipid monolayers was reported by studying on a more compact monolayer of distearoylphosphatidic acid (DSPA) films formed at water|1,2-dichloroethane interface.²²⁸

Despite these previous studies, the electrodeposition of in-situ chitosan film at liquid-liquid interface has not been reported. For the sake of extending widely chitosan applications as films, we developed a new way to synthesize chitosan membrane at ITIES by introducing

electrodeposition. The chitosan film formation is controlled by adsorption of cationic chitosan at the interface. Number of characterization for this ex-situ film such as EDX, Raman analysis were investigated to reveal the formation mechanism.

6.2 Results and discussion

6.2.1 Macro-scale experiments

We prepared firstly a control group of experiment to understand the chitosan film formation mechanism by polarizing the interface potential with ions. The detailed conditions are listed in Table 5.2. The result for each condition after 24 hours was shown in Figure 5.4 and we can see only cell B has been generated a chitosan film. As a consequence, chitosan film was formed by protonated chitosan transfer to organic phase while we added the K^+TPBCl^- electrolyte to increasing the interfacial potential. The reaction can be described as:



As for the others, there were no hydrophobic anion transfer from the aqueous phase to the organic phase. Thereby, chitosan film can not be generated since cationic chitosan do not transfer into the organic phase. In addition, the color change of the DCE solution from transparent to white in the cell C is caused by K^+TPBCl^- precipitation due to its low solubility in the 1,2 DCE. Thus, the achievement of chitosan film at macro ITIES can be done by polarizing chemically the common ion. However, this method require the time, yet not control the thickness of chitosan film. Therefore, electrodeposition is introduced in this work. All the chitosan film including the cross linked chitosan latter were obtained by potentiostatic deposition with a specific potential and a period of time.

Initially, cyclic voltammetry was applied to characterize the transfer of protonated chitosan to ensure the cell is set and the successful cyclic voltammogram was shown in Figure 5.5A. We could see that positive chitosan transfer from the aqueous phase to the organic phase at ca. 1.0V. Since then, potentiostatic electrodeposition was employed at

Table 6.2: Polarized liquid-liquid interface by common ion transfer.

Cell	Composition	Condition	Result
A	1 wt% chitosan in 2 V% HAc solution	single phase	No film
B	2 mM K^+TPBCl^- + 1 wt% chitosan 1,2 DCE	positive polarization	Film
C	1 wt% chitosan 2 mM K^+TPBCl^- in 1,2 DCE	without polarization	No film
D	2 mM $BTPPA^+Cl^-$ + 1 wt% chitosan 1,2 DCE	negative polarization	No film
E	1 wt% chitosan 2 mM $BTPPA^+Cl^-$ + 1,2 DCE	without polarization	No film

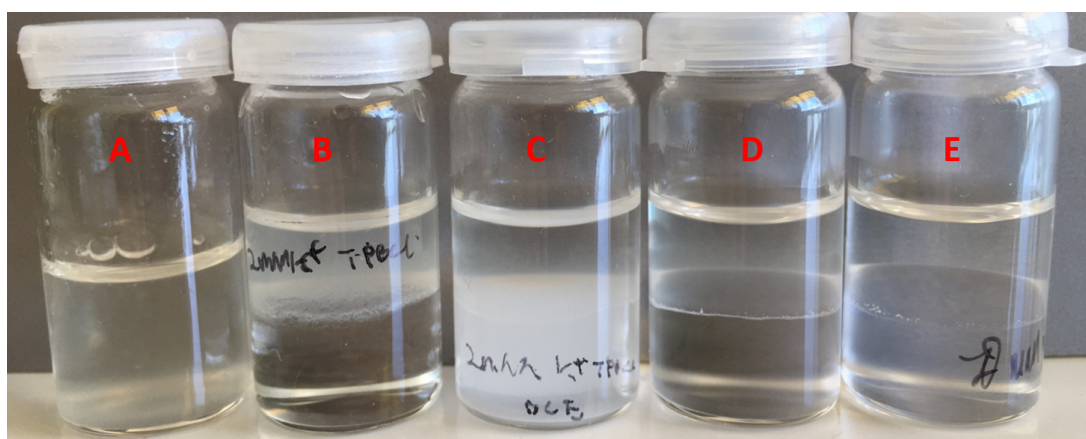


Figure 6.4: (A) model chitosan solution: 1 wt% Chitosan in 2 V% HAc solution used in cell B, C, D, E as the aqueous phase. Biphasic reaction controlled by common ion transfer: (B) 2 mM K^+TPBCl^- + 1 wt% chitosan solution || 1,2 DCE, (C) 1 wt% chitosan solution || 2 mM K^+TPBCl^- in 1,2 DCE, (D) 2 mM $BTPPA^+Cl^-$ + 1 wt% chitosan solution || 1,2 DCE, (E) 1 wt% Chitosan solution || 2 mM $BTPPA^+Cl^-$ + 1,2 DCE.

1.1 V and lasted 600 seconds and the current transient for this deposition was presented in Figure 5.5B. A white thick film was generated simultaneously. The film was clearly seen by comparing the interface before deposition and after deposition which was illustrated in Figure 5.6.

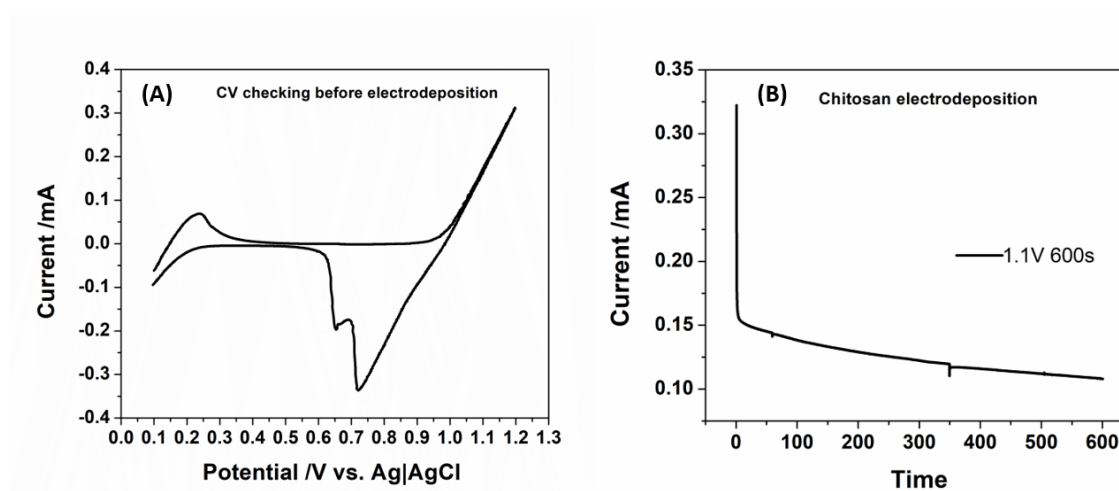


Figure 6.5: (A) Typical cyclic voltammograms obtained in the presence of CS solution in the aqueous phase. (B) Current transient for the potentiostatic deposition of chitosan membrane at 1.1 V lasting 600s.

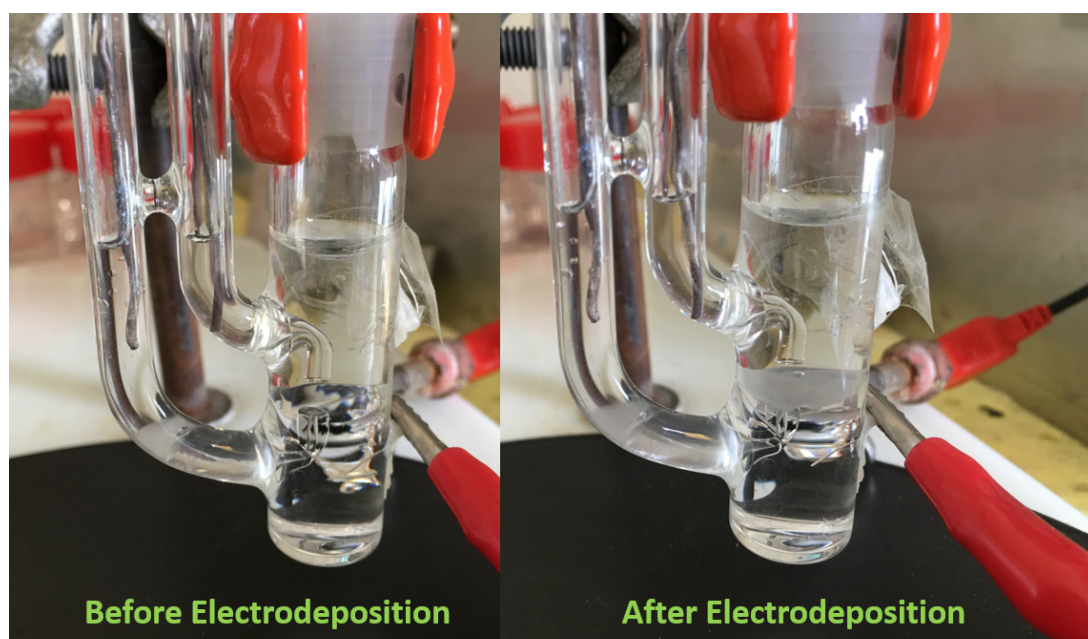


Figure 6.6: Chitosan film generated at macro-ITIES by electrodeposition with 1.1V and 600s.

With the remarkable phenomena, we successfully electrodeposited of chitosan film at a macroscopic water-DCE interface. However, the permeability of the the generated white chitosan film at the interface still remain unknown. Thus, this membrane was characterized by cyclic voltammetry using model ion transfer across the modified water-DCE interface. In this work, TEA^+ and TMA^+ were selected as the model ion and their transfer behaviors were recorded as Figure 5.7 shown. Both the electrochemical responses of TEA^+ and TMA^+ were presented nonlinear regression between the concentration and the peak current. It has to be mentioned that linear relationship is always established at unmodified liquid-liquid interface.

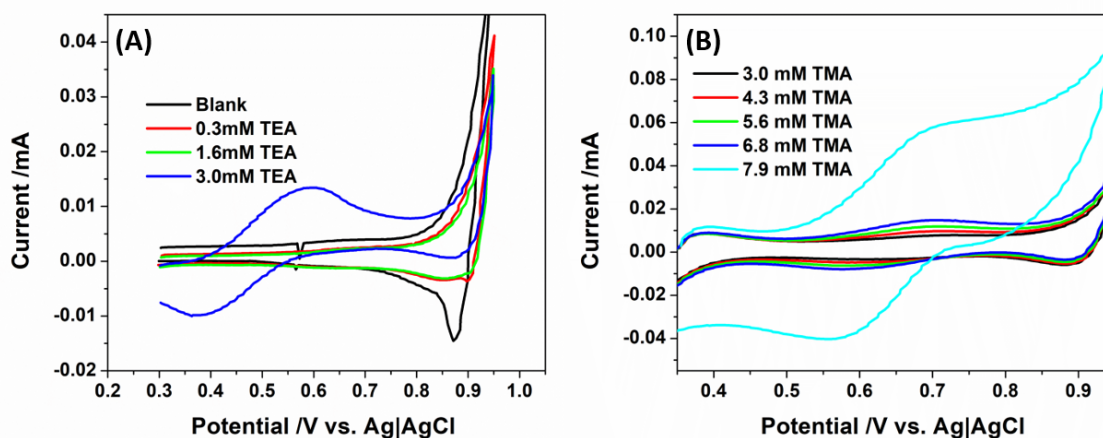


Figure 6.7: Cyclic voltammograms in the presence of TEA⁺ from 0.3 mM to 3.0 mM (A), and TMA⁺ from 3.0 mM to 7.9 mM (B). Scan rate = 5 mVs⁻¹.

Hence, it is necessary to study the electrochemical evolution of model ion as a function of the cycle number and deposition time. Firstly, the time response for a fixed concentration of model ion TMA⁺ was illustrated in Figure 5.8. We could see that the peak current increased with time for the same electrochemical cell. It remained stable after 7 hours as the calibration dotted curve present in Figure 5.8B. Secondly, numerous cyclic voltammetry was applied for the initial time, and this result was shown in Figure 5.9A. Each cycle voltammetry could improve the peak current. The calibration curve of peak current enhancement is shown in Figure 5.9B. Therefore, the electro-generated chitosan film at the liquid-liquid interface offers the blocking for ion transfer by the pores and the adsorption at the same time due to the electrostatic force. With waiting more time for diffusion through the film, it allowed ions to reach the interface.

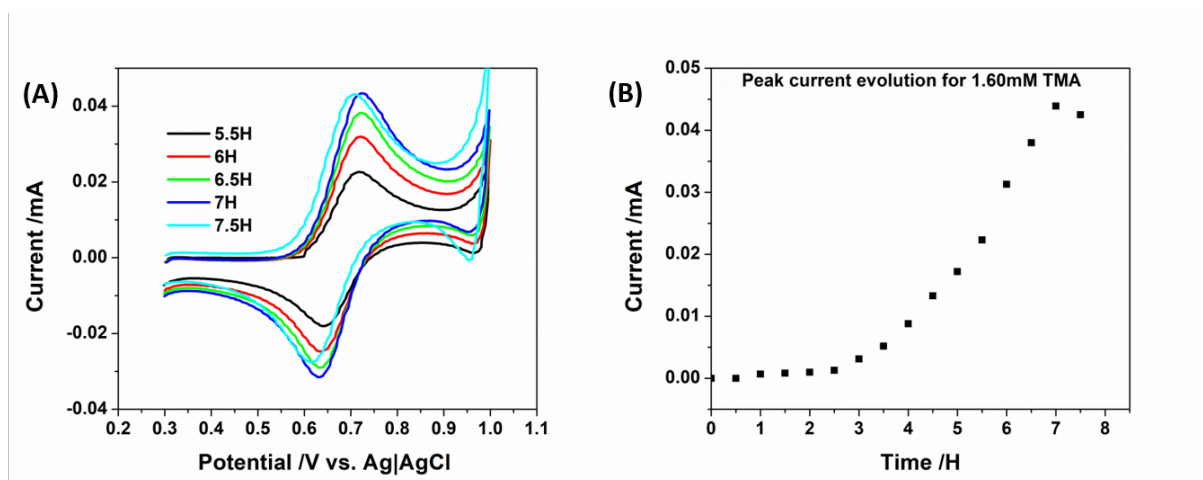


Figure 6.8: Cyclic voltammogram of different time period from the initial to 7.5 hours for same electrochemical cell and its calibration curve between the time and the peak current.

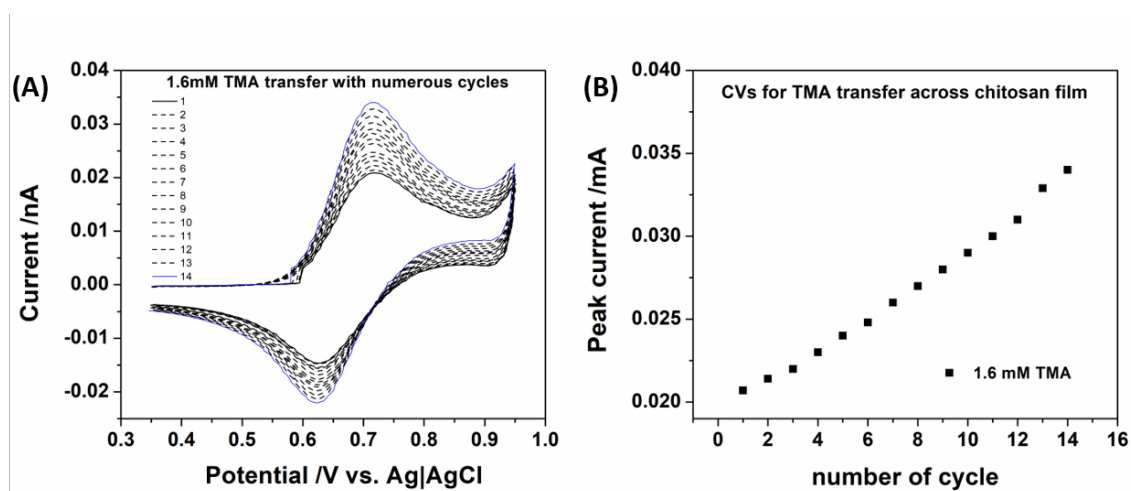


Figure 6.9: Cyclic voltammogram of numerous cycle study for the electrochemical cell contained 1.6 mM TMA⁺ and its dotted calibration curve between the number of cycle and the peak current.

Moreover, the permeability of chitosan film can be modified by the applied voltage and the deposition time. Figure 5.10 shows four types of potentiostat electrodeposition: 1.0V-600s, 1.1V-600s, 1.1V-60s, and 1.2V-600s. The deposited films with 1.0V-600s and 1.1V-600s were analyzed by TMA⁺. The deposited films with 1.1V-60s and 1.2V-600s were analyzed by TEA⁺. All the curves show a similar current response, a sharp decrease

at the beginning. Then it's a steady decline.

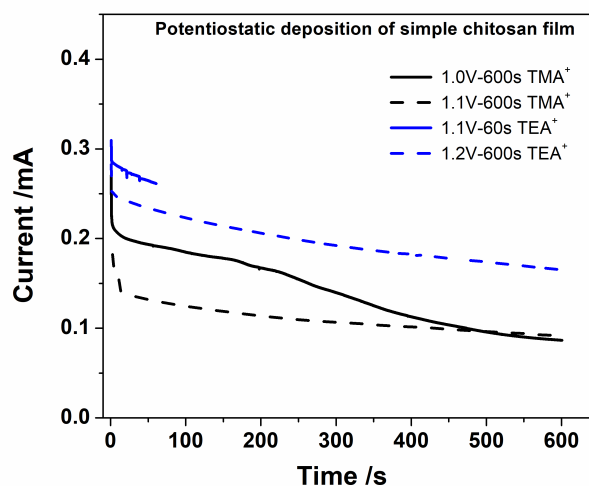


Figure 6.10: The potentiostatic deposition for simple chitosan film at liquid-liquid interface: TMA⁺ and TEA⁺ are the model ion for characterize the deposited film.

As Figure 5.11A shown, 1.1V-60s chitosan did not change the ion transfer at modified ITIES. The ion transfer voltammetry is reversible which is the same as at unmodified ITIES. With more deposition time and larger applied potential (1.2V-600s), chitosan film can block completely the ion transfer. For the same deposition time, the deposit chitosan film with a high potential is more compact and can limit the ion transfer at low concentration as Figure 5.11D shown.

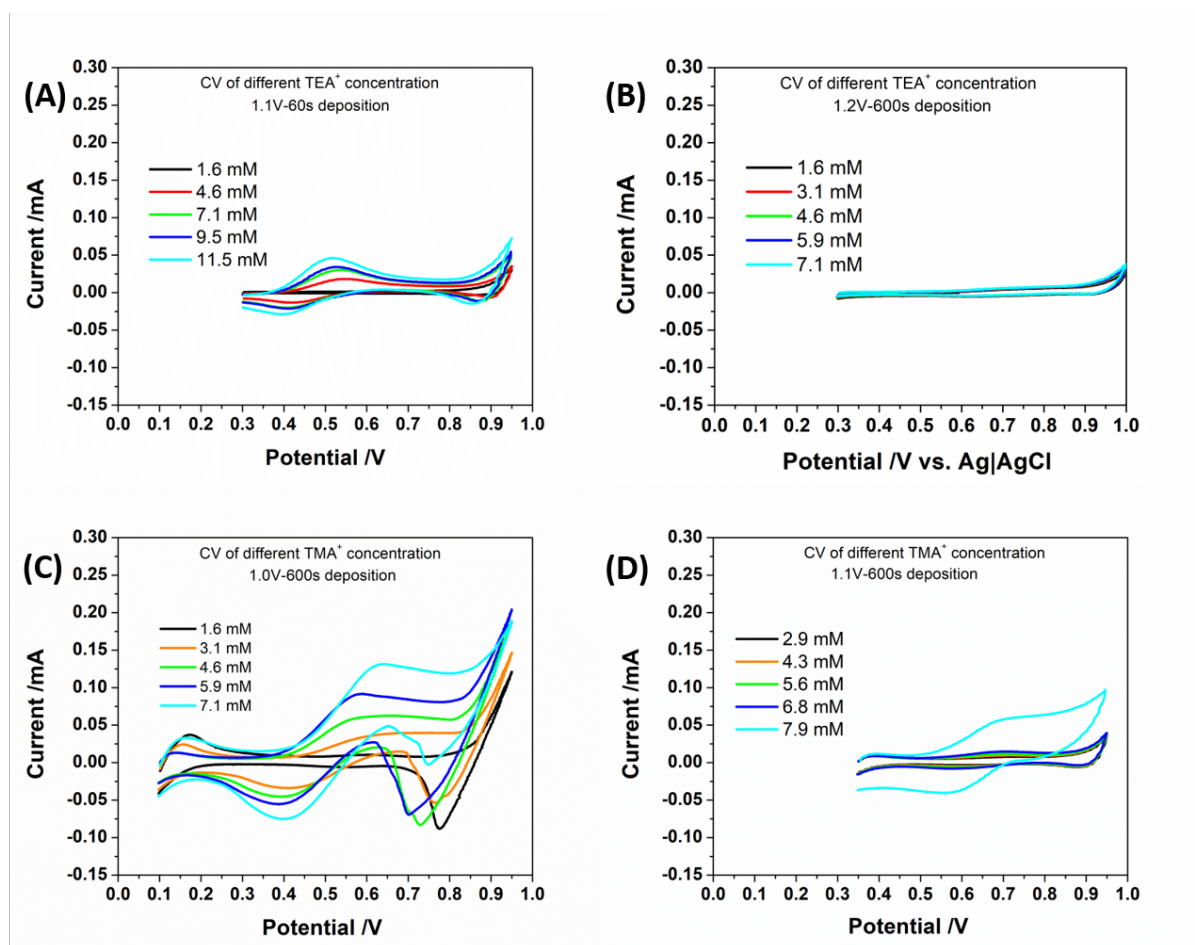
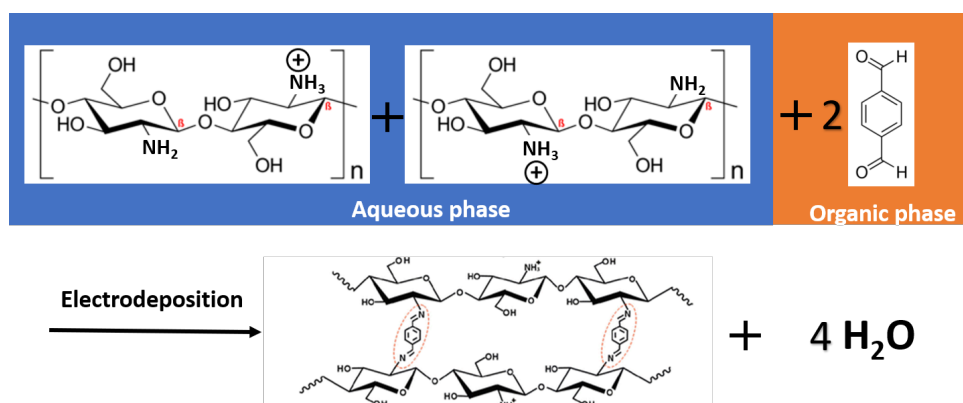


Figure 6.11: Electrochemical characterization by model ion TEA^+ and TMA^+ at the modified liquid-liquid interface: (A) recorded CVs of different TEA^+ through 1.1V-120s deposition chitosan film, (B) recorded CVs of different TEA^+ through 1.2V-600s deposition chitosan film, (C) recorded CVs of different TMA^+ through 1.0V-600s deposition chitosan film, (A) recorded CVs of different TMA^+ through 1.1V-600s deposition chitosan film. Scan rate = $5 \text{ mV} \cdot \text{s}^{-1}$.

Non-crosslinked chitosan film can not be kept stable in strong acidic environment because this kind of chitosan film is readily re-solubilized by washing with acids. In order to prepare stabilized structure with free-standing, chitosan films can be made acid-insoluble by covalent crosslinking. Herein, crosslinking agent of terephthalaldehyde (TPA) was selected and was used to solidify the bare chitosan film. As supposed, the aldehyde group in TPA would react to the amino group in chitosan to generate an imine bonding. Moreover, TPA contains double aldehyde group and is suitable as the crosslinking agent

for chitosan chain to form film. The proposed formation is illustrated below:



The reaction of aldehydes or ketones with ammonia or 1^o-amines forms imine derivatives, also known as Schiff bases (compounds having a C=N function) because Imines are sometimes called Schiff bases or Schiff's bases. Water is eliminated in the reaction and the dehydration of the carbinolamine is the rate-limiting step of imine formation. This imine formation is catalyzed by acids which is reversible in the same sense as acetal formation. Thereby, the pH of reactions to form imine compounds must be carefully controlled.^{229, 230}

However, the role of Terephthalaldehyde (TPA) in the chitosan film during electrodeposition is unclear since TPA was added into organic phase and chitosan precursor was in the aqueous phase. To reveal the reaction, a group of 4 different concentration from 0 mM to 10 mM TPA were studied by following same potentiostatic electrodeposit. Moreover, the water-DCE and the water-TFT were both employed. Figure 5.12 shows cyclic voltammetry of protonated chitosan with different concentration of TPA in water-DCE system and water-TFT system individually. We could see that all the deposits at the water-DCE interface present larger slope than the water-TFT interface. It means protonated chitosan are more easily transferred across the water-DCE interface than the water-TFT interface under same potential. In fact, stable chitosan film is only electro-generated for all the water-DCE interfaces. However, the effect of cross-linking and its influence on the functional properties of membranes and especially on ion transport is still unknown, and it is therefore necessary to understand the relationship between the performance and the concentration of the cross-linked films.

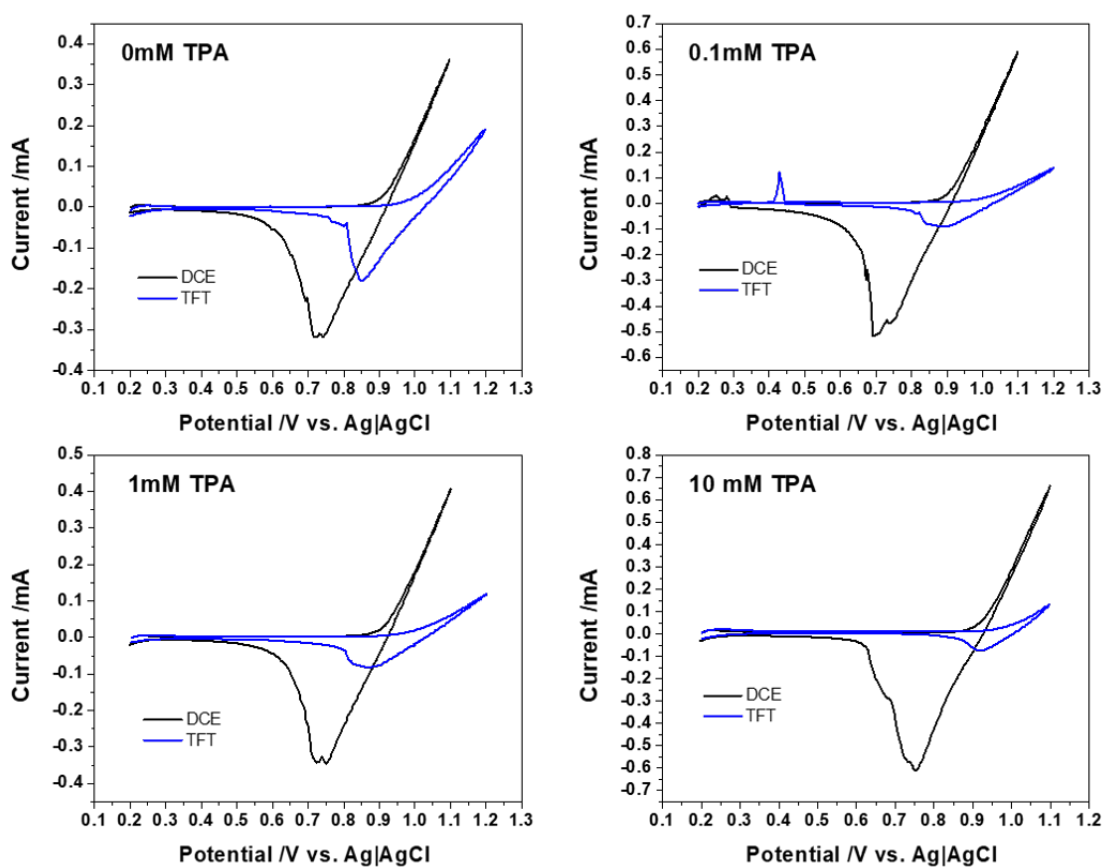


Figure 6.12: Cyclic voltammety of protonated chitosan with different concentration of TPA from 0 mM to 10 mM TPA in water-DCE system (black line) and water-TFT system (blue line) individually.

Thus, it is of importance to understand which TPA concentration is optimized. In order to identify and understand the influence of chitosan membrane at the interface, different potentiostatic processes were employed by varying the potential and the working time. TPA was added into organic phase to avoid the contact with chitosan precursor initially. After obtaining each electrodeposited chitosan film, model ion was used to characterize the diffusion profile in the membrane. From the measurement of each calibration from Figure 5.13, we obtained the tendency of each condition and were in Table 5.4 for TMA⁺ and Table 5.5 for TEA⁺. We could see that larger potential and more time help to generate more thick film and then present the channel in the film is less permissive.

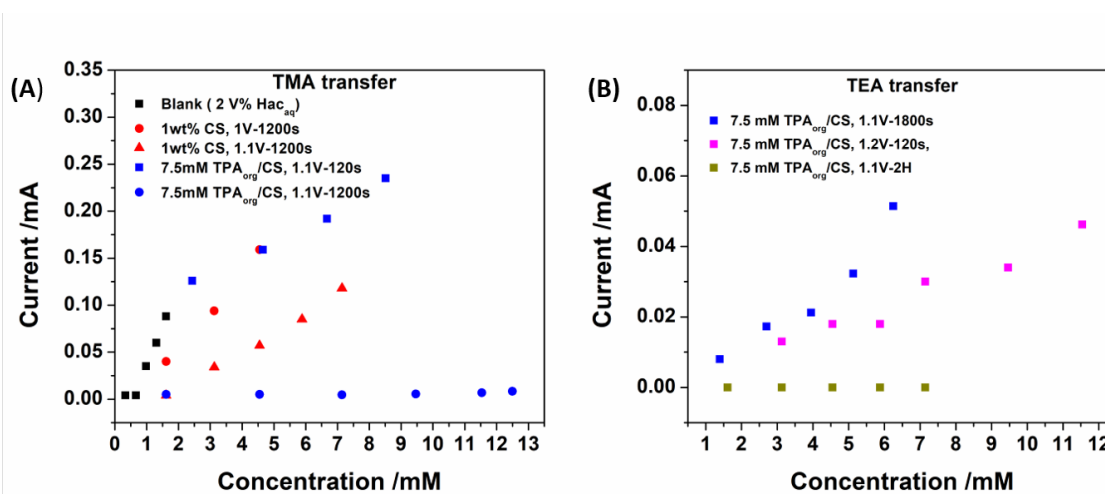


Figure 6.13: Calibration curves obtained of model ion TMA and TEA at chitosan modified interface with different potentiostat process.

Besides, the adding of TPA could help to control the size of pores in the film and would block the channel completely when applied more reaction time. Therefore, the addition of cross-linking agent can reduce the membrane permeability and accelerate the curing of the membrane with less time comparing the simple chitosan film.

Table 6.3: TMA⁺ transfer across electro-generated chitosan membrane by potentiostatic deposit in variable potential and time .

CS _{aq}	[TPA] _{Org}	Electrodeposition	Slope /A · M ⁻¹
0	0	0s	0.07
1wt%	0	1V-1200s	0.04
1wt%	0	1.1V-1200s	0.02
1wt%	7.5 mM	1.1V-120s	0.017
1wt%	7.5 mM	1.1V-1200s	0

Table 6.4: TEA⁺ transfer across electro-generated chitosan membrane by potentiostatic deposit in variable potential and time.

CS _{aq}	[TPA] _{Org}	Electrodeposition	Slope / A · M ⁻¹
1 wt%	7.5 mM	1.1V-1800s	0.008
1 wt%	7.5 mM	1.2V-120s	0.004
1 wt%	7.5 mM	1.1V-1200s	0

6.2.2 Ex-situ characterization of dried chitosan films

In order to know the detail difference of chemical composition and mechanical properties, we took film samples out from the electrochemical cell and put them on the glass by using tweezers. After drying in the ambient for each sample of 0 mM TPA, 0.1 mM TPA, 1 mM TPA and 10 mM TPA, we did EDX analysis with combining SEM capture firstly. The optical result of SEM was shown in Figure 5.14.

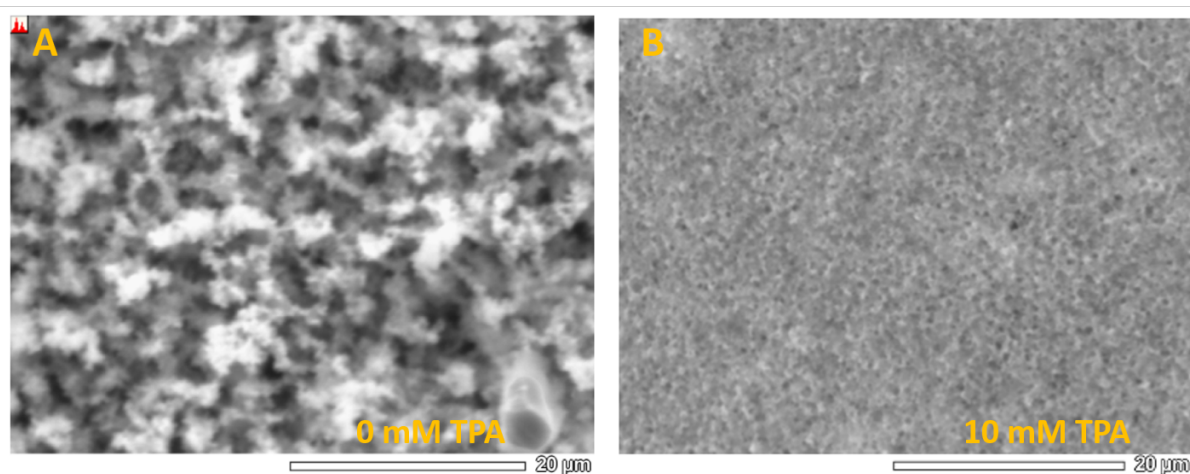
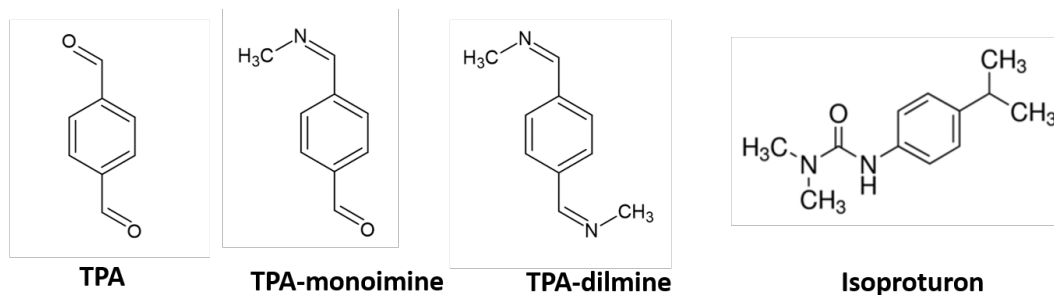


Figure 6.14: SEM image: (A) 0 mM TPA, (B) 10 mM TPA.

For 10 mM TPA concentrations, we observed the surface of chitosan membrane was affected by cross-linker. The film with 10 mM TPA presented more dense and more flat surface. Thus, TPA was added into the organic phase and can modify the surface of chitosan film during electrodeposition.

The elemental analysis showed both membranes contained Cl and C. Cl came from the aqueous electrolyte LiCl and C was definitively from the chitosan precursor. Since then, it can not confirm that TPA functioned as a cross-linker for chitosan film to modify the internal structure. Therefore, the characterization of Raman and infrared spectrum was taken and their results were presented in Figure 5.15 and 5.16. We could see phenyl ring from TPA was added into chitosan for 10 mM TPA set-up as the detailed Raman spectrum indicated. At the same time, the double carbon–nitrogen bond (C=N) was generated due to cross linking by electrodeposition. Lastly, the infrared spectrum could also confirm that new peak happened between 1350 cm^{-1} and 1400 cm^{-1} for C=O bond. Additionally, the phenyl ring of 10 mM TPA is moved. This variation is caused by a shift in the elongation frequency of the C=N function that remains. It means for 10 mM TPA film, TPA is partial cross-lined due to its over amount adding. Result of the calculations of the Raman spectra by DFT/ B3LYP is presented in Figure 3.15C and 3.15D owing to Manuel Dossot's work. The frequencies have been corrected for the shift induced by the DFT method using the same correction as for the isoproturon. What is more, the chemical structure of isoproturon with 3 different TPA is shown below:



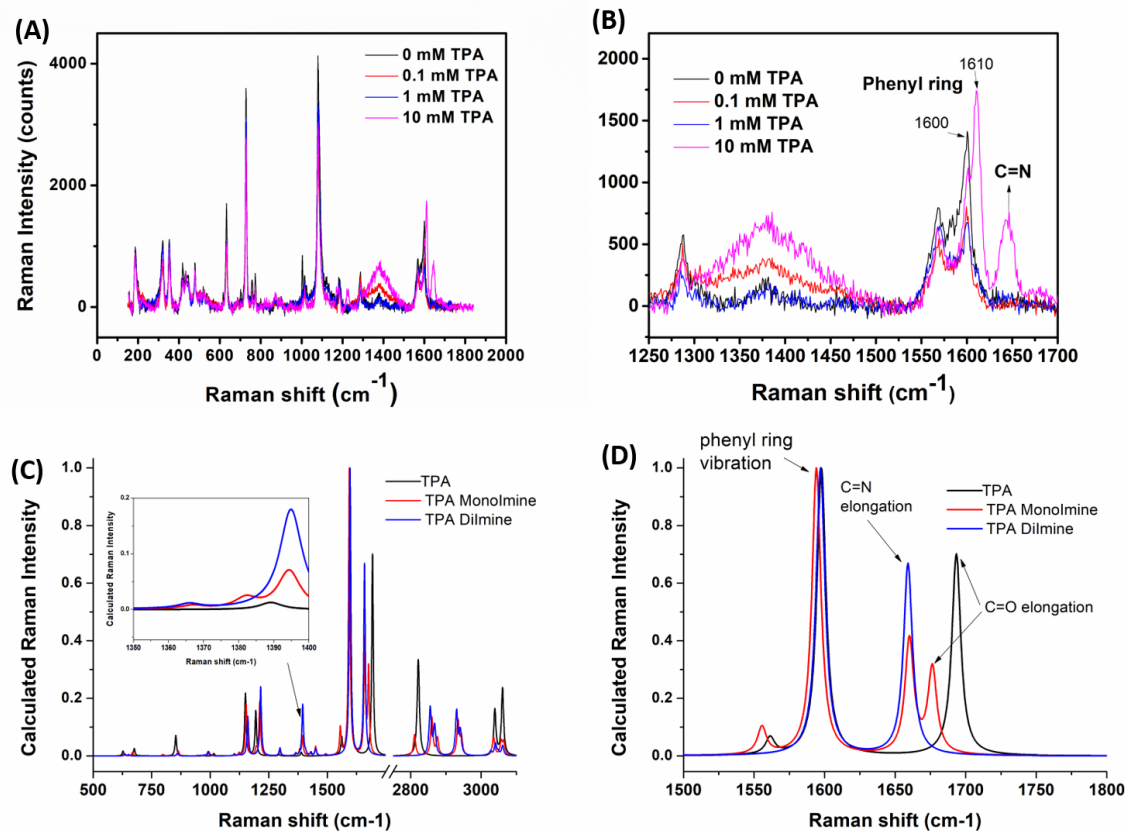


Figure 6.15: (A) Raman spectrum of chitosan electrodeposit following different TPA concentrations. (B) The detailed wave-number for raman spectrum. The most significant wavenumbers are indicated with the arrows.

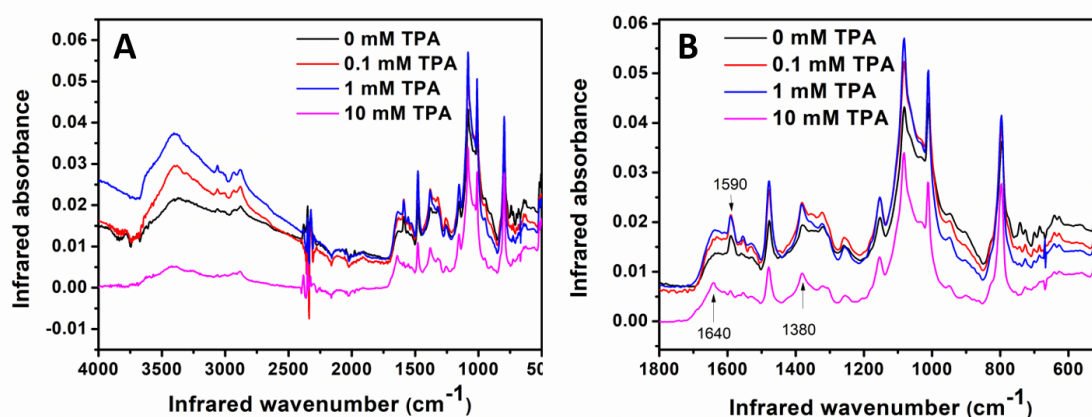


Figure 6.16: (A) Infra-red spectrum of chitosan electrodeposit following different TPA concentrations. (B) The detailed wave-number for Infra-red spectrum. The most significant wavenumbers are indicated with the arrows.

Based on the previous observations, we used DSC measurement to determine the acetylation degree for chitosan film by following the suggest calculated model.²³¹ The method is established on the exothermic degradation peak observed due to N-acetylation in chitin and chitosan samples, which changes in temperature, area and intensity depending on the the degree of N-acetylation (A). The use of DSC curves can help us to know the transformation of chitosan electro-generated film in considering the DA and their results were presented in Figure 5.17. The commercial chitosan power (CS-LM) was used as a reference for evaluating the peak area and peak height of the exothermic event regarding the temperature. The integration of the area is performed by the Gadgets in Origin® using baseline and its value is 16.67. Thus, its peak area in Jg^{-1} is calculated through the equation below:

$$16.67 * 60/5 = 200.4Jg^{-1}$$

where 5 is the heating flow ($5\text{ }^{\circ}C/min$) and 60 is 60 seconds in minute unit conversion. The peak height is measured by the difference between the heat flow at the peak and the baseline before the peak and the value was measured ca. $0.85\text{ }Wg^{-1}$. The degree of N-acetylation in a linear relationship with the DSC peak area and the DSC peak height respectively. As Figure 5.17B shown, the electro-generated chitosan films have lost the peak at the interval temperature from $264\text{ }^{\circ}C$ to $328\text{ }^{\circ}C$. Therefore, the acetyl functional

group of chitosan precursor has been used during the electrodeposition. However, the mechanism of the removal of an acetyl group in chitosan film is still undiscovered. This study need more sophisticated measurement such as Nuclear magnetic resonance (NMR).

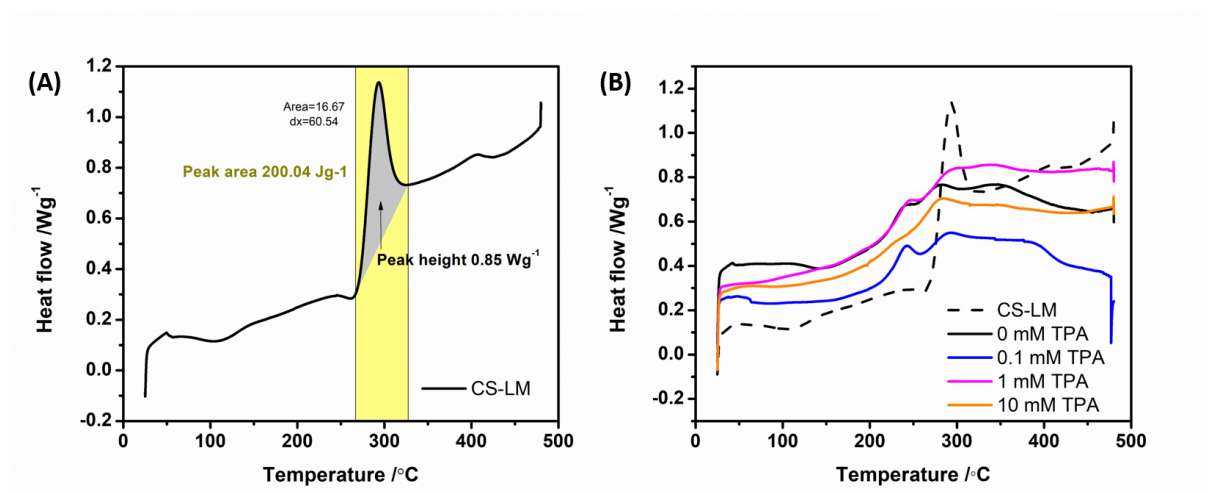


Figure 6.17: Under dynamic nitrogen atmosphere (50mLmin^{-1}), sample mass ca. 4 mg at heating rate of $5\text{ }^{\circ}\text{Cmin}^{-1}$, (A) DSC curve for chitosan power, (B) DSC curves for chitosan films with 0 mM TPA, 0.1 mM TPA, 1 mM TPA, 10 mM TPA.

Chitosan film offers a good mechanical property than silica film which can be served as a free-standing thin membrane at the immiscible interface. Since then, it is of importance to quantify mechanical properties such as the thickness and the stiffness. The first step was employed by profilometer to have a preliminary test. Their thickness was estimated from the position before and after deposit film, using the Dektak XT apparatus with Vision 64 software (Brüker). Table 5.6 gave us the thickness of the selected group of four types chitosan film. The effective film thickness was evaluated from the minimum $1.3\text{ }\mu\text{m}$ until the maximum $170.2\text{ }\mu\text{m}$. Each test group has a big issue from the variation. This large standard deviation originated mainly from the scratch sample due to ex-situ manipulation and desiccation process.

Table 6.5: Thickness measurement of four types TPA-chitosan film.

	Test 1 / μm	Test 2 / μm	Test 3 / μm	Test 4 / μm	Test 5 / μm	average / μm
0 mM	4.6	21	60	45.5	48	36 ± 20
0.1 mM	50.4	33.6	21.2	79.2	170.2	71 ± 53
1 mM	5.2	3.8	2	1.3	2.4	2.9 ± 1.4
10 mM	115.3	118.3	113.1	112.5	105	113 ± 4

Therefore, profilometer may not be a satisfactory technique because it monitors the local thickness of chitosan film but can not give the global stiffness of chitosan films. We then developed a macro-force set-up to measure the global thickness and the stiffness of the film and its process followed three steps as Figure 5.18 illustrated. The force sensor gain of set-up was calibrated as 0.5975 N/V by introducing the local gravity which is ca. $9.80885 \text{ N} \cdot \text{kg}^{-1}$ in Nancy (Latitude 48.664507, sea level altitude 212). In terms of load-displacement, the stress is linear related to the defection of materials. As long as the stress remains in the chitosan film, the sensor would give a feedback which is different in free loading condition. This contact moment was illustrated in Figure 5.18A and could help us measure the macro-thickness of chitosan film. In consequence, the deflection and the loading force is in the function of time and we could established the linear relation between the difference of force load and the difference of the deflection as:

$$k = \frac{\Delta F}{\Delta \varepsilon}$$

where k is stiffness ($\text{N} \cdot \text{m}^{-1}$), ΔF is the difference of loading force in Newton (N), $\Delta \varepsilon$ is the difference of deflection which is defined by the displacement on the z axis (μm). Therefore, we could get the stiffness of sensor probe from the bare calibration as Figure 5.18 shown including the global stiffness of chitosan film attached with sensor such as 0 mM TPA film and 0.1 mM TPA film.

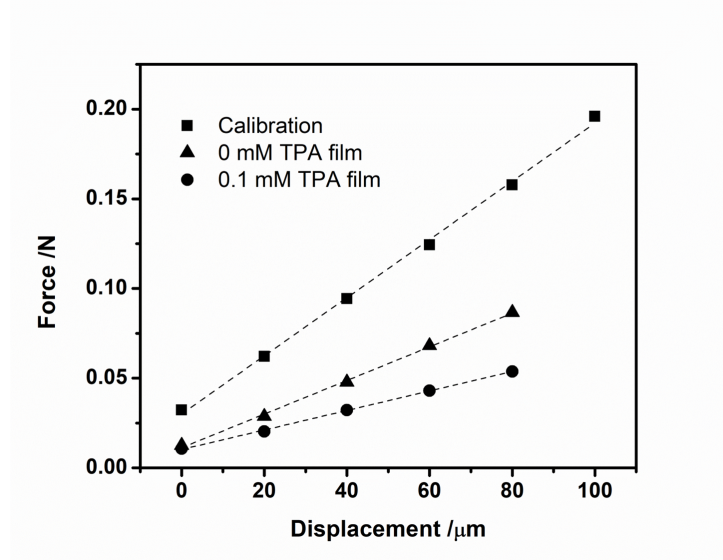


Figure 6.18: The macro force measurement for calibration, 0 mM TPA film, 0.1 mM TPA film.

With a view to getting the stiffness of the film, the spring in series model is introduced and can be written as:

$$\frac{1}{k_{all}} = \frac{1}{k_{cali}} + \frac{1}{k_{film}}$$

where k_{all} is the global stiffness, k_{cali} is the stiffness of sensor probe and k_{film} is the stiffness of film. Thus, the stiffness of film can be expressed as:

$$k_{film} = \frac{k_{cali} * k_{all}}{k_{cali} - k_{all}}$$

For a given uni-axial stress (compression in this work), Young's modulus is a more general approach and can be obtained from the stiffness k . The equation is written as:

$$E_{film} = \frac{k_{film} L_{film}}{A}$$

where A is the cross-sectional area of probe contact and is measure as 12.57 mm^2 , L is the initial thickness of film before compression. Thus, Young's modulus E of each can be obtained in Table 5.6. The film with TPA cross-liner have been strengthen in mechanical propriety.

Table 6.6: Stiffness k , thickness L and Young's modulus E obtained for each chitosan film.

Sample	$k_{\text{cali}} / \text{Nm}^{-1}$	$k_{\text{all}} / \text{Nm}^{-1}$	$k_{\text{film}} / \text{Nm}^{-1}$	$L_{\text{film}} / \mu\text{m}$	$E_{\text{film}} / \text{Pa}$
0 mM	1637	926	2132	10	1696
0.1 mM	1637	538	801	179	11431
1 mM	1637	378	492	260	10180
10 mM	1637	471	660	140	7352

6.2.3 Micro-scale experiments

The micro-scale set-up was similar to silica membrane which is described in the chapter 4. Initially, we only did simple electrodeposition for chitosan film as cyclic voltammetry presented in Figure 5.19A. Protonated chitosan transfer from the aqueous phase to the organic phase was at less positive potential ca. 0.1 V comparing the blank testing in the absence of chitosan precursor at single pore ITIES. Owing to the miniaturized interface of water|DCE, the film could be generated at the single pore without the potentiostatic deposition process. Chitosan film was located at the outlet of the capillary with the organic solution in seen in Figure 5.19B.

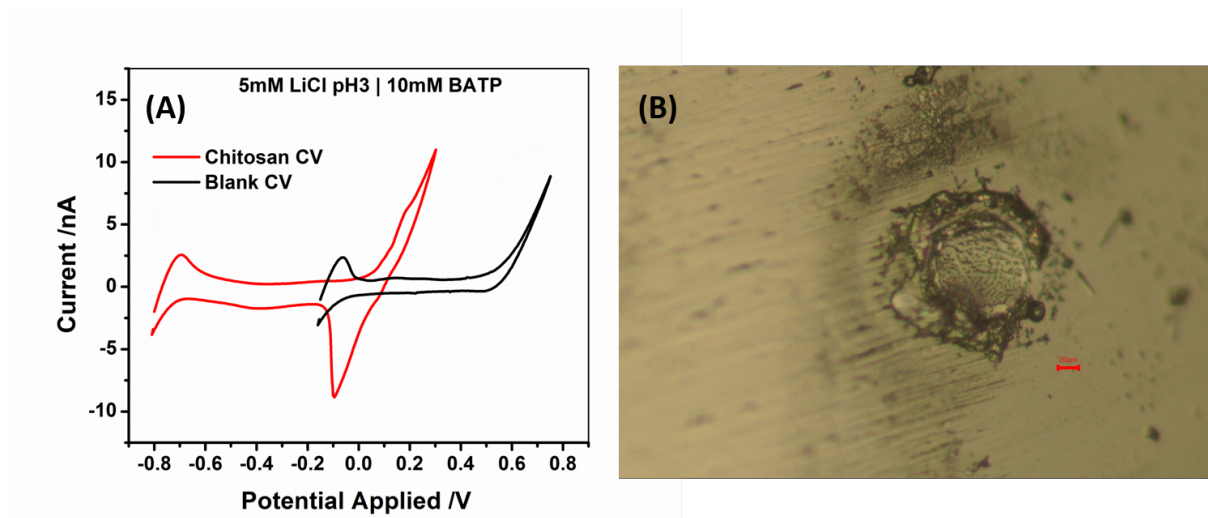


Figure 6.19: (A) Cyclic voltammograms recorded at micro ITIES using single pore capillary. Black solid line was recorded in the absence of chitosan solution and red solid line was recorded in the presence of chitosan solution (0.1 wt% diluted in HCl). Scan rate = 5 mV/s. (B) optical micrograph of single pore capillary after electrodeposition.

The chitosan film deposit at the tip of capillary will have influence on the electrochemical analysis due to its membrane functionality. We then selected TMA^+ as the model ion to study its transfer behavior at the micro water/1,2-DCE interface containing chitosan membrane and the result was present in Figure 5.20. Considering that TMA^+ has been successfully detected, the chitosan film remained porous for ion transfer.

In Figure 5.21, the measured values for interfacial capacitance are plotted versus Ag electrode potential for the presence and the absence of chitosan film. Our results confirm the increment of interfacial capacitance due to the generation of membrane. The values and the potential dependent features of capacitance are clearly influenced by chitosan membrane.

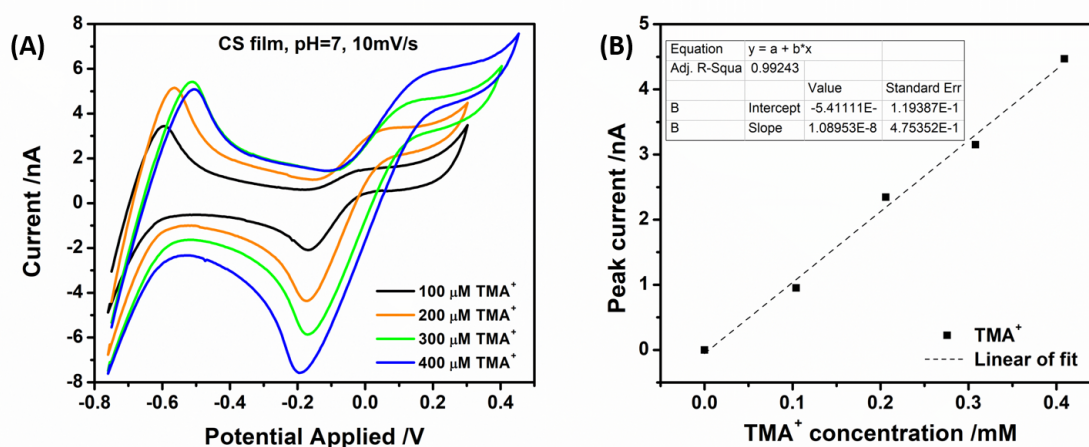


Figure 6.20: (A) Cyclic voltammograms for different concentration of TMA^+ in the aqueous phase: 100 μM ; 200 μM ; 300 μM ; 400 μM . Scan rate was 5 mV/s. (B) The calibration curve between TMA^+ concentration and peak current.

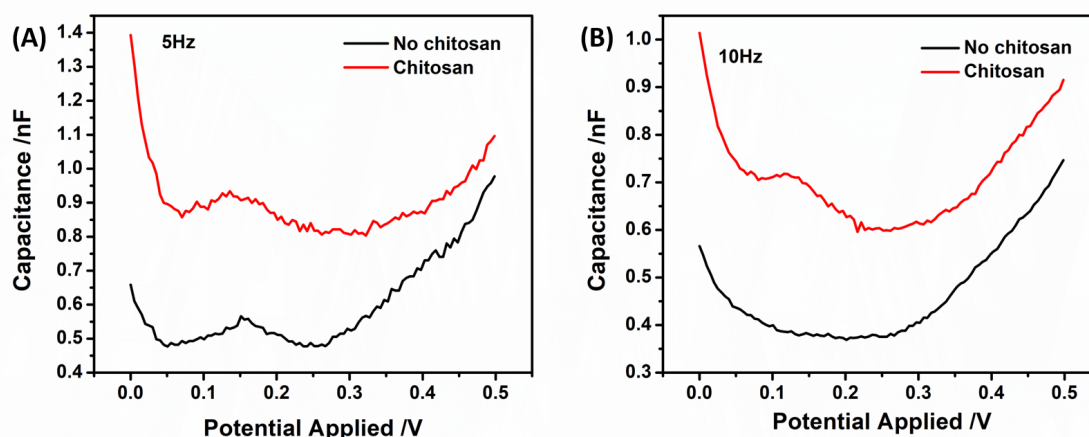


Figure 6.21: Potential dependence of the interfacial capacitance of the presence chitosan film (red curve) and the absence of chitosan film (black curve) (A) at 5Hz (B) at 10Hz

Moreover, cyclic voltammetry of the model ion TMA^+ across the unmodified interface in Figure 5.22A confirmed the interfacial capacitance of chitosan modified capillary is increased. Take the example of 100 μM TMA, the variance for positive peak with no EDOT chitosan modified capillary is ca. 2 nA which is larger than the variance with bare capillary (1 nA).

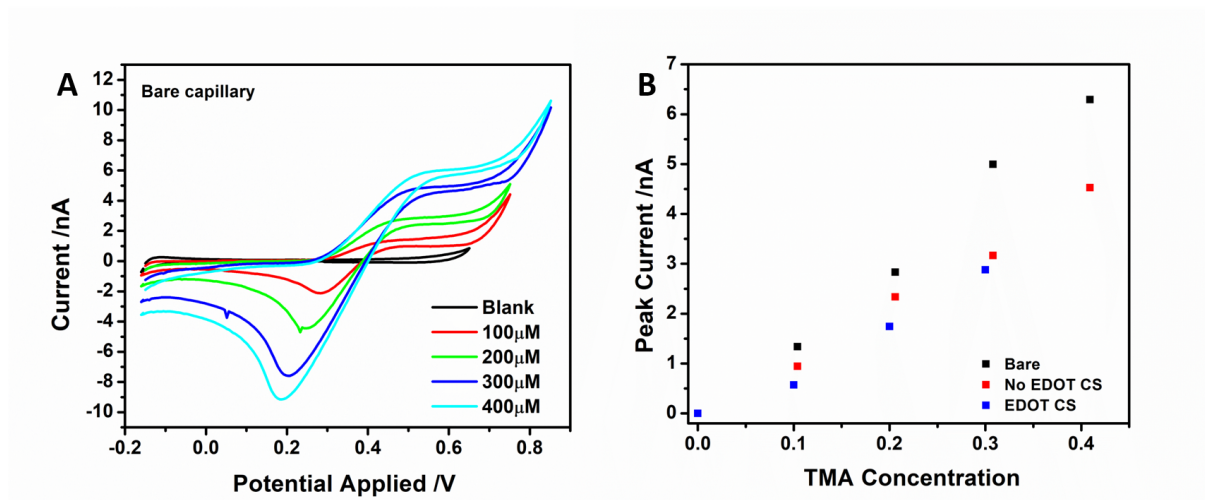


Figure 6.22: Comparison of Cyclic voltammograms for different concentration of TMA in the aqueous phase across different chitosan film (A) the blank test without chitosan film; (B) Plot of peak currents versus TMA concentration from 0.1 mM to 0.4mM obtained for the modified chitosan film.

To observe the effect of cross-linker for chitosan film, we measured two others chemicals EDOT and TPA into the organic solution to improve the mechanical property of film. After the electrodeposition, the outlet of capillary tip was closed by chitosan films and they were kinetically stable in solution or in air, and do not undergo spontaneous bulk aggregation in the concentration range of model ion during cyclic voltammetry. According to change of surface film as Figure 5.23 presented, we assumed that the cross linked film influence the ion transfer across the interface. Further, cyclic voltammetry with different concentrations of TMA^+ were applied using different capillaries. The Plot of peak currents versus TMA^+ concentration from 0.1 mM to 0.4mM were traced in Figure 5.22B with comparing the blank test of bare capillary. Hence, the surface of chitosan film played a important role for ion transfer since the slopes were changed. However, the chitosan film with TPA has no single due to the block at the tip of capillary as Figure 5.23B illustrated.

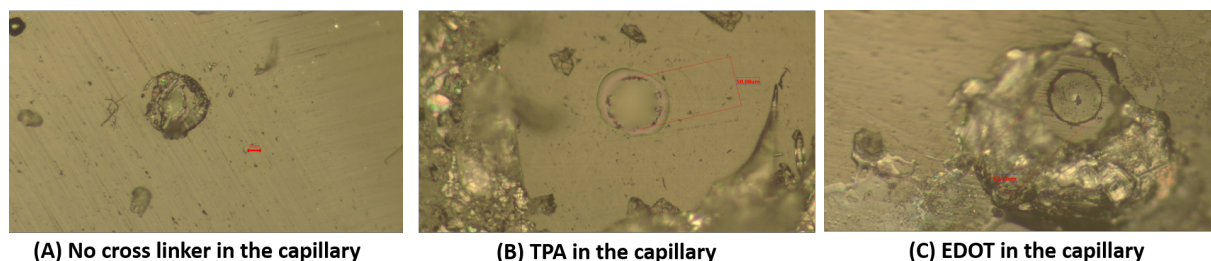


Figure 6.23: Optical images of the formation of cross-liner with chitosan film at the micro ITIES.

6.3 Conclusions

First of all, the materials for membranes should be non-toxic, abundant, low cost, and sufficiently stable. Due to these requirements, it is challenging to discover suitable biomaterials such as chitosan which, in combination with adapted electrodeposition at ITIES for film product formation. Secondly, in this work, we have developed a new method based on ion transfer at ITIES to form a free-standing chitosan film at LLI with its suitability for selective ion transfer applications, aiming to pesticide detection. The chitosan solution is prepared in the aqueous phase; the film is generated under chronoamperometry and is cross-linked with x mM TPA (Terephthalaldehyde) in the organic phase. The chitosan film properties are linked to variable electrodeposit time and TPA concentration. The charge transfer reactions recorded by cyclic voltammetry show reduced backwards current peak on the positive side of the potential window due to the chitosan film formation at LLI. All of the electro-generated chitosan films offer excellent mechanic property which can be pull out from the solution. After the total water evaporation, Stiffness of the film was measured ca. 30 under Micro force Sensing Probe of FEMTO. It further is characterized by infrared spectroscopy and Raman spectroscopy. The characterization results demonstrated covalent bond of C=N was introduced into chitosan film. This soft membrane of chitosan at LLI would give the selectivity for in-situ analyte detection. We tested with TMA^+ and TEA^+ and their cyclic voltammograms illustrated different respond for interfacial ion transfer. Thus, in-situ electrodeposited chitosan would be a novel synthesized membrane functioned as a soft membrane at LLI and allows for analyte adsorption with selective detection for ITIES sensor.

Chapter 7

Conclusions and Perspectives

This thesis contained two main research goals. The first was the improvement of pesticide detection at ITIES. The second was the development of membrane at ITIES to functionalised the interface which would make pesticide detection more selective.

Following this discipline, chapter 1 of this thesis gives a global and comprehensive review of state of the art about liquid-liquid interface electrochemistry from the fundamental to the achieved application. Chapter 2 summarizes the experimental and instrumentation details for electrochemical cell set-up with the synthesis of protocols. Chapter 3 is dedicated to the attempt of pesticide detection at Micro-ITIES due to its enhanced mass transfer for ion transfer across the interface. Chapter 4 to 5 in this thesis were the modification of electrified liquid-liquid interface using the bottom-up method. In details, chapter 4 was the base of sol-gel modification at ITIES, which were established by Poltorak et al. during his PhD and then developed by Gamero-Quijano et al. during his post-doc in LCMPE. Under their indications, we tried to optimize the silica deposition at Macro-ITIES by varying the time of chronoamperometry for electrodeposition. After having the sol-gel method experiment, the electrodeposition of chitosan polymer film at ITIES was realized and was described in Chapter 5.

The pesticide results presented in chapter 3 have shown the ametryn was succeeded to be enhanced analyzed at micro-ITIES. As proof-of-concept, the design scheme of our proposed approach is shown in Figure 6.1.

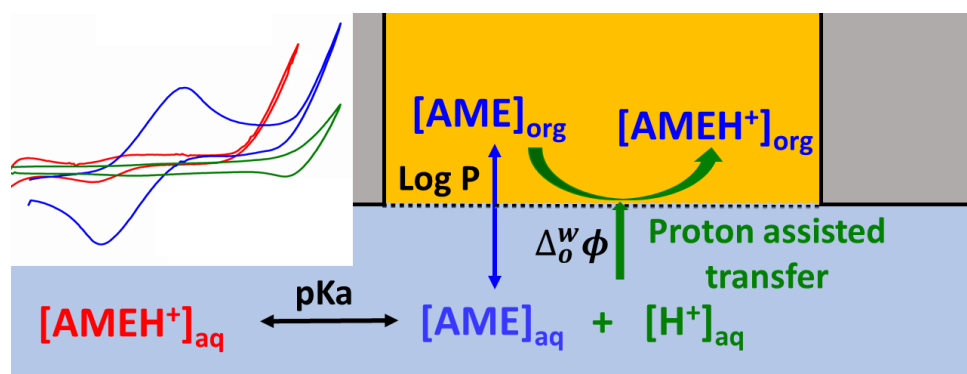


Figure 7.1: the concept of enhanced detective signal for ametryn.

It was shown that when the pH of the aqueous solution is 3, we got symmetric voltammogram for the single pore of micro-ITIES. In order to reveal this phenomenon, the proton

assisted transfer of ametryn was then introduced into its mechanism. At the same time, the partition coefficient ($\log P$) is considered because of the immiscible interface. Besides, the disassociation coefficient (pK_a) of ametryn is not negligible in the acidic aqueous solution. Thus, we took all the favorable parameters into account and established the modeling of proton assisted transfer, proton limited transfer and direct ion transfer in the function of the aqueous pH. We could then increase the peak current owing to its unique transfer on variable pH. Afterwards, the asymmetric geometry of micro ITIES would also play an important role to enhance the detection signal. The two-step protocol of the detection process was then proposed on the basis of unequal balance condition. After having the simple comparison proton assisted transfer, the two-step detection has an increased current signal ca. 3 times. However, this protocol has the limits of stability which cannot neglect. Octanoic acid in the organic phase was also tested to improve the proton concentration, which can be used as an enhanced factor for ametryn detection.

The electrochemical detection of Imidacloprid and Metam sodium was failed at micro-ITIES due to no correspond current peak during cyclic voltammetry. In details, IMI present no electrochemical signal in the potential window although it was protonated. One reason for this is the transfer potential of IMI was less notable than the proton; the proton was then transferred more quickly and previously than IMI. Thus, we cannot see its peak in the potential window. As for MET, it is more complicated since the potential window was shifting in the function of MET concentration. Furthermore, this shifting has no linear relationship with MET concentration. More factors influence the micro-interface, including the decomposition of MET and the breakdown products enhanced hydrophilic interface. Thus, the potential window was shifted to more negative potential versus the reference electrode. In brief, the breadth of practical applications of ITIES has been severely limited because it is still a great challenge to achieve simultaneously a larger potential window and a high reproducibility.

In chapter 4, we follow firstly previous work about in-situ silica membrane deposition at macro-ITIES. This method was also applied at micro-ITIES to obtain a miniaturized silica membrane adhering at the single pore of the capillary. The kinds of silica miniaturization can bring several advantages:

1. An easy and straightforward silica deposition with fewer materials used and simplified experimental set-up.
2. Improvement of the mechanical stabilization of silica deposits.
3. Possibility of multi-membrane for simultaneous deposition.
4. Ex-situ modification of silica film according to practical application.

However, as already noticed, modification caused the decrease of the Faraday current evidenced for studied ions, and its re-productivity was quite low for single pore capillary. The results present that the geometry of deposited silica film at the interface has affected the mass transfer significantly. Thereby, the diffusion profiles were different and were variable after deposition since silica film was not controlled well at the micro ITIES during electrodeposition. At this stage, it can be concluded that silica deposit on the micro liquid-liquid interface worsened the ion transfer due to the uncontrollable miniaturization process of silica membrane. Nevertheless, it was noteworthy for the miniaturized silica membrane since the problem was identified at the step of chronoamperometry. Thus, the solution in the future is about to figure out the stabilized silica electrodeposition method at micro-ITIES with the morphological trickling for each step.

We developed chitosan membrane electrodeposition at ITIES with better mechanical properties owing to the cross-linker in the organic solution that was described in chapter 5. To prepare free-standing chitosan film, we separated the reaction agent and cross-linker in each phase while chitosan was dissolved in the aqueous phase, and TPA (cross-linker) was dissolved in the organic phase. Thus, we could control TPA concentration to achieve the manipulation of the interfacial reaction of chitosan film at ITIES. The differential films were measured by a home-made mechanical instrument. The result shows all the films have an excellent stiffness as Young's modulus are ca. 10 kPa. Moreover, SEM study illustrated that each film has unique morphology owing to size scale is influenced by cross-linker. The characteristic ions TEA^+ , TMA^+ present their electrochemical response for chitosan membrane were really depended on the time of electrodeposition, TPA concentration. Therefore, the contribution of this film as serves as a new platform of ion immobilization. With functionality in the membrane, it could help to improve the

analyte selectivity through channel controlling and analyte adsorption at the interface by electrostatic interaction. Second approach dealing with chitosan electrodeposition was based on the single pore capillary. The electrochemical study presents the same mechanism of film formation at the liquid-liquid interface, which protonated chitosan adsorption at the interface and its film generated. Nevertheless, as the same problem found in micro silica deposition, chitosan film has the challenge for a precise process which leading a homogeneous film.

Further study is needed to improve the micro-structure properties of synthesized materials for chitosan and silica. The factors which affect the structure of these two kinds of the film can vary from the electrodeposit step and the initial chemical condition. Even the manipulation of the extraction film from the solutions can play an important role. To sum, it is worthy of reconsidering the micro-deposit film at liquid-liquid interface and optimizer its accuracy of the experimental set-up.

Bibliography

- [1] W. Ronald Fawcett. *Liquids, Solutions, and Interfaces: From Classical Macroscopic Descriptions to Modern Microscopic Details*. Oxford University Press, Oxford ; New York, 2004.
- [2] E. H. Riesenfeld. Concentrationsketten Mit Nichtmischbaren Lösungsmitteln. *Annalen der Physik*, 313(7):616–624, 1902.
- [3] C. Gavach. Cinétique de l'Electroadsorption et de la Polarisation à l'Interface Entre Certaines Solutions Ioniques Non Miscibles. In Giulio Milazzo, Peter E. Jones, and Liliana Rampazzo, editors, *Biological Aspects of Electrochemistry: Proceedings of the 1st International Symposium. Rome (Italy) Istituto Superiore di Sanità, May 31st to June 4th 1971*, Experientia Supplementum, pages 321–331. Birkhäuser, Basel, 1971.
- [4] C. Gavach and A. Savajols. Potentiels biioniques de membranes liquides fortement dissociées. *Electrochimica Acta*, 19(9):575–581, September 1974.
- [5] PATRICK SETA CLAUDE GAVACH and FRANÇOIS HENRY. A Study of the Ionic Transfer across an Aqueous Solution | Liquid Membrane Interface by Chronopotentiometric and Impedance Measurements. page 14.
- [6] Claude Gavach, Patrick Seta, and Bertrand D'epenoux. The Double Layer and Ion Adsorption at the Interface between Two Non Miscible Solutions. *Journal of Electroanalytical Chemistry and Interfacial Electrochemistry*, 83(2):225–235, October 1977.

- [7] Zdeněk Samec, Vladimír Mareček, and Jan Weber. Charge Transfer between Two Immiscible Electrolyte Solutions. *Journal of Electroanalytical Chemistry and Interfacial Electrochemistry*, 103(1):11–18, October 1979.
- [8] J. Koryta, L.Q. Hung, and A. Hofmanova. Biomembrane Transport Processes at the Interface of Two Immiscible Electrolyte Solutions with an Adsorbed Phospholipid Monolayer. *Stud. Biophys.*, 90, 1982.
- [9] Mauro Guainazzi, Giuseppe Silvestri, and Giovanni Serravalle. Electrochemical Metallization at the Liquid–Liquid Interfaces of Non-Miscible Electrolytic Solutions. *J. Chem. Soc., Chem. Commun.*, (6):200–201, 1975.
- [10] D. Yogev and S. Efrima. Novel Silver Metal Liquidlike Films. *J. Phys. Chem.*, 92(20):5754–5760, October 1988.
- [11] S. Kutuzov, J. He, R. Tangirala, et al. On the Kinetics of Nanoparticle Self-Assembly at Liquid/Liquid Interfaces. *Phys. Chem. Chem. Phys.*, 9(48):6351, 2007.
- [12] E.J.W. Verwey and K.F. Niessen. XL. The Electrical Double Layer at the Interface of Two Liquids. *The London, Edinburgh, and Dublin Philosophical Magazine and Journal of Science*, 28(189):435–446, October 1939.
- [13] Jonathan D Reid, Owen R Melroy, and Richard P Buck. DOUBLE LAYER CHARGE AND POTENTIAL PROFILES AT IMMISCIBLE LIQUID/LIQUID ELECTROLYTE INTERFACES. page 12.
- [14] Claude Gavach, Roger Sandeaux, and Patrick Seta. A Potentiostatic Study of Hydrophobic Ion Transfer across Lipid Bilayer: Part I. Case of Zero Ion Fluxes in Adsorption and Desorption Processes. *Journal of Electroanalytical Chemistry and Interfacial Electrochemistry*, 89(2):321–334, May 1978.
- [15] Z. Samec, V. Mareček, and D. Homolka. The Double Layer at the Interface between Two Immiscible Electrolyte Solutions. *Journal of Electroanalytical Chemistry and Interfacial Electrochemistry*, 126(1-3):121–129, September 1981.

- [16] Takashi Kakiuchi and Mitsugi Senda. Structure of the Electrical Double Layer at the Interface between Nitrobenzene Solution of Tetrabutylammonium Tetraphenylborate and Aqueous Solution of Lithium Chloride. *BCSJ*, 56(6):1753–1760, June 1983.
- [17] D. Homolka, P. Hájková, V. Mareček, and Z. Samec. The Double Layer at the Interface between Two Immiscible Electrolyte Solutions: Structure of the Water/Nitrobenzene Interface. *Journal of Electroanalytical Chemistry and Interfacial Electrochemistry*, 159(1):233–238, December 1983.
- [18] Takashi Kakiuchi and Mitsugi Senda. Polarizability and Electrocapillary Measurements of the Nitrobenzene–Water Interface. *BCSJ*, 56(5):1322–1326, May 1983.
- [19] Z. Samec, V. Mareček, and D. Homolka. The Use of the Mean Spherical Approximation in Calculation of the Double-Layer Capacitance for the Interface between Two Immiscible Electrolyte Solutions. *Journal of Electroanalytical Chemistry and Interfacial Electrochemistry*, 170(1):383–386, July 1984.
- [20] Zdeněk Samec, Vladimír Mareček, and Daniel Homolka. The Double Layer at the Interface between Two Immiscible Electrolyte Solutions: Part II. Structure of the Water/Nitrobenzene Interface in the Presence of 1:1 and 2:2 Electrolytes. *Journal of Electroanalytical Chemistry and Interfacial Electrochemistry*, 187(1):31–51, May 1985.
- [21] H. H. Girault and D. J. Schiffrin. Thermodynamic Surface Excess of Water and Ionic Solvation at the Interface between Immiscible Liquids. *Journal of Electroanalytical Chemistry and Interfacial Electrochemistry*, 150(1):43–49, July 1983.
- [22] H.H.J. Girault and D.J. Schiffrin. Theory of the Kinetics of Ion Transfer across Liquid/Liquid Interfaces. *Journal of Electroanalytical Chemistry and Interfacial Electrochemistry*, 195(2):213–227, November 1985.
- [23] Cheng Yufei, Vincent J. Cunnane, David J. Schiffrin, Lasse Mutomäki, and Kyösti Kontturi. Interfacial Capacitance and Ionic Association at Electrified Liquid/Liquid Interfaces. *J. Chem. Soc., Faraday Trans.*, 87(1):107–114, 1991.

- [24] Mitsugi Senda, Takashi Kakiuchi, and Toshiyuki Osaka. Electrochemistry at the Interface between Two Immiscible Electrolyte Solutions. *Electrochimica Acta*, 36(2):253–262, January 1991.
- [25] Ilan Benjamin. Theoretical Study of the Water/1,2-dichloroethane Interface: Structure, Dynamics, and Conformational Equilibria at the Liquid–Liquid Interface. *The Journal of Chemical Physics*, 97(2):1432–1445, July 1992.
- [26] Karl J. Schweighofer and Ilan Benjamin. Transfer of Small Ions across the Water/1,2-Dichloroethane Interface. *J. Phys. Chem.*, 99(24):9974–9985, June 1995.
- [27] Ilan Benjamin. Chemical Reactions and Solvation at Liquid Interfaces: A Microscopic Perspective. *Chem. Rev.*, 96(4):1449–1476, January 1996.
- [28] Ilan Benjamin. MOLECULAR STRUCTURE AND DYNAMICS AT LIQUID-LIQUID INTERFACES. *Annu. Rev. Phys. Chem.*, 48(1):407–451, October 1997.
- [29] Guangming Luo, Sarka Malkova, Jaesung Yoon, et al. Ion Distributions near a Liquid-Liquid Interface. *Science*, 311(5758):216–218, January 2006.
- [30] Lisa B. Dreier, Yuki Nagata, Helmut Lutz, et al. Saturation of Charge-Induced Water Alignment at Model Membrane Surfaces. *Science Advances*, 4(3):eaap7415, March 2018.
- [31] Cornelis Lütgebaucks, Carlos Macias-Romero, and Sylvie Roke. Characterization of the Interface of Binary Mixed DOPC:DOPS Liposomes in Water: The Impact of Charge Condensation. *J. Chem. Phys.*, 146(4):044701, January 2017.
- [32] Grégoire C. Gschwend, Astrid Olaya, and Hubert H. Girault. How to Polarise an Interface with Ions: The Discrete Helmholtz Model. *Chem. Sci.*, May 2020.
- [33] Frédéric Reymond, David Fermin, Hye Jin Lee, and Hubert H. Girault. Electrochemistry at Liquid/Liquid Interfaces: Methodology and Potential Applications. *Electrochimica Acta*, 45(15):2647–2662, May 2000.

- [34] Z. Samec. Electrochemistry at the Interface between Two Immiscible Electrolyte Solutions (IUPAC Technical Report). *Pure and Applied Chemistry*, 76(12):2147–2180, January 2004.
- [35] A. Sabela, V. Mareček, Z. Samec, and R. Fuoco. Standard Gibbs Energies of Transfer of Univalent Ions from Water to 1,2-Dichloroethane. *Electrochimica Acta*, 37(2):231–235, February 1992.
- [36] The ElectroChemical DataBase. <http://sbsrv7.epfl.ch/instituts/isic/lepa/cgi/DB/InterrDB.pl>.
- [37] Lukasz Poltorak. Modification Électrochimique de l'interface Liquide – Liquide Avec de La Silice Mésoporeuse. page 234.
- [38] R. A. Marcus. On the Theory of Ion Transfer Rates across the Interface of Two Immiscible Liquids. *The Journal of Chemical Physics*, 113(4):1618–1629, July 2000.
- [39] Renfa Cui, Qing Li, Dustin E. Gross, et al. Anion Transfer at a Micro-Water/1,2-Dichloroethane Interface Facilitated by β -Octafluoro-Meso-Octamethylcalix[4]Pyrrole. *J. Am. Chem. Soc.*, 130(44):14364–14365, November 2008.
- [40] Qing Li, Shubao Xie, Zhongwei Liang, et al. Fast Ion-Transfer Processes at Nanoscopic Liquid/Liquid Interfaces. *Angewandte Chemie International Edition*, 48(43):8010–8013, 2009.
- [41] J. Koryta. Electrochemical Polarization Phenomena at the Interface of Two Immiscible Electrolyte Solutions. *Electrochimica Acta*, 24(3):293–300, March 1979.
- [42] B. S. Zhorov and V. S. Ananthanarayanan. Structural Model of a Synthetic Ca²⁺ Channel with Bound Ca²⁺ Ions and Dihydropyridine Ligand. *Biophysical Journal*, 70(1):22–37, January 1996.
- [43] Ubald F. Kragten, Maarten F. M. Roks, and Roeland J. M. Nolte. Facilitated Ion Transport in a Biomembrane Model. Artificial Ion Channels as Pores in Dihexadecyl Phosphate Vesicles. *J. Chem. Soc., Chem. Commun.*, (19):1275–1276, January 1985.

- [44] D. Homolka, Le Quoc. Hung, A. Hofmanova, et al. Faradaic Ion Transfer across the Interface of Two Immiscible Electrolyte Solutions: Chronopotentiometry and Cyclic Voltammetry. *Anal. Chem.*, 52(11):1606–1610, September 1980.
- [45] Y. Shao, M.D. Osborne, and H.H. Girault. Assisted Ion Transfer at Micro-ITIES Supported at the Tip of Micropipettes. *Journal of Electroanalytical Chemistry and Interfacial Electrochemistry*, 318(1-2):101–109, November 1991.
- [46] François O. Laforge, Peng Sun, and Michael V. Mirkin. Shuttling Mechanism of Ion Transfer at the Interface between Two Immiscible Liquids. *J. Am. Chem. Soc.*, 128(46):15019–15025, November 2006.
- [47] Peng Sun, François O. Laforge, and Michael V. Mirkin. Role of Trace Amounts of Water in Transfers of Hydrophilic and Hydrophobic Ions to Low-Polarity Organic Solvents. *J. Am. Chem. Soc.*, 129(41):12410–12411, October 2007.
- [48] Shigeru Amemiya, Xiting Yang, and Tracy L. Wazenegger. Voltammetry of the Phase Transfer of Polypeptide Protamines across Polarized Liquid/Liquid Interfaces. *J. Am. Chem. Soc.*, 125(39):11832–11833, October 2003.
- [49] Yi Yuan and Shigeru Amemiya. Facilitated Protamine Transfer at Polarized Water/1,2-Dichloroethane Interfaces Studied by Cyclic Voltammetry and Chronoamperometry at Micropipet Electrodes. *Anal. Chem.*, 76(23):6877–6886, December 2004.
- [50] Antonín Trojánek, Jan Langmaier, Eva Samcová, and Zdeněk Samec. Counterion Binding to Protamine Polyion at a Polarised Liquid–Liquid Interface. *Journal of Electroanalytical Chemistry*, 603(2):235–242, May 2007.
- [51] W. Mickler, A. Mönner, E. Uhlemann, S. Wilke, and H. Müller. Transfer of β -Diketone and 4-Acylpyrazolone Anions across the Electrified Water | Nitrobenzene Interface. *Journal of Electroanalytical Chemistry*, 469(2):91–96, July 1999.
- [52] L M Yudi, A M Baruzzi, and V M Solis. Competitive Transfer of H⁺ and Li⁺ Ions

through the Water-1,2-Dichloroethane Interface Mediated by 1,10-Phenanthroline. page 12.

- [53] D. J. Fermin and R. Lahtinen. Dynamic Aspects of Heterogeneous Electron-Transfer Reactions at Liquid|Liquid Interfaces. *Liquid Interfaces in Chemical, Biological, and Pharmaceutical Applications*, pages 179–227, 2001.
- [54] Salvatore Daniele, M. Antonietta Baldo, and Carlo Bragato. A Steady-State Voltammetric Investigation on the Oxidation of Ferrocene in Ethanol–Water Mixtures. *Electrochemistry Communications*, 1(1):37–41, January 1999.
- [55] Manuel A. Méndez, Raheleh Partovi-Nia, Imren Hatay, et al. Molecular Electrocatalysis at Soft Interfaces. *Phys. Chem. Chem. Phys.*, 12(46):15163, 2010.
- [56] Andrew N. J. Rodgers, Samuel G. Booth, and Robert A. W. Dryfe. Particle Deposition and Catalysis at the Interface between Two Immiscible Electrolyte Solutions (ITIES): A Mini-Review. *Electrochemistry Communications*, 47:17–20, October 2014.
- [57] Fiona L. Thomson, Lesley J. Yellowlees, and Hubert H. Girault. Photocurrent Measurements at the Interface between Two Immiscible Electrolyte Solutions. *J. Chem. Soc., Chem. Commun.*, (23):1547–1549, January 1988.
- [58] Nicolas Eugster, Henrik Jensen, David J. Fermín, and Hubert H. Girault. Photoinduced Electron Transfer at Liquid|liquid Interfaces. Part VII. Correlation between Self-Organisation and Structure of Water-Soluble Photoactive Species. *Journal of Electroanalytical Chemistry*, 560(2):143–149, December 2003.
- [59] David J. Fermín, Henrik Jensen, Jacques E. Moser, and Hubert H. Girault. Organisation and Reactivity of Nanoparticles at Molecular Interfaces. Part II. Dye Sensitisation of TiO₂ Nanoparticles Assembled at the Water|1,2-Dichloroethane Interface. *ChemPhysChem*, 4(1):85–89, January 2003.
- [60] Naoya Nishi, Seiichi Imakura, and Takashi Kakiuchi. Wide Electrochemical Window at the Interface between Water and a Hydrophobic Room-Temperature Ionic Liquid

- of Tetrakis[3,5-Bis(Trifluoromethyl)Phenyl]Borate. *Anal. Chem.*, 78(8):2726–2731, April 2006.
- [61] Evgeny Smirnov, Pekka Peljo, Micheál D. Scanlon, and Hubert H. Girault. Interfacial Redox Catalysis on Gold Nanofilms at Soft Interfaces. *ACS Nano*, 9(6):6565–6575, June 2015.
- [62] Micheál D. Scanlon, Pekka Peljo, Manuel A. Méndez, Evgeny Smirnov, and Hubert H. Girault. Charging and Discharging at the Nanoscale: Fermi Level Equilibration of Metallic Nanoparticles. *Chem. Sci.*, 6(5):2705–2720, 2015.
- [63] Micheál D. Scanlon, Evgeny Smirnov, T. Jane Stockmann, and Pekka Peljo. Gold Nanofilms at Liquid–Liquid Interfaces: An Emerging Platform for Redox Electrocatalysis, Nanoplasmonic Sensors, and Electrovariable Optics. *Chem. Rev.*, 118(7):3722–3751, April 2018.
- [64] Frédéric Reymond, Guillaume Steyaert, Pierre-Alain Carrupt, Bernard Testa, and Hubert Girault. Ionic Partition Diagrams: A Potential-pH Representation. *J. Am. Chem. Soc.*, 118(47):11951–11957, January 1996.
- [65] Frédéric Reymond, Véronique Chopineaux-Courtois, Guillaume Steyaert, et al. Ionic Partition Diagrams of Ionisable Drugs: pH-Lipophilicity Profiles, Transfer Mechanisms and Charge Effects on Solvation. *Journal of Electroanalytical Chemistry*, 462(2):235–250, February 1999.
- [66] Véronique Gobry, Sorina Ulmeanu, Frédéric Reymond, et al. Generalization of Ionic Partition Diagrams to Lipophilic Compounds and to Biphasic Systems with Variable Phase Volume Ratios. *J. Am. Chem. Soc.*, 123(43):10684–10690, October 2001.
- [67] Annika Mälkiä, Peter Liljeroth, Anna-Kaisa Kontturi, and Kyösti Kontturi. Electrochemistry at Lipid Monolayer-Modified Liquid-Liquid Interfaces as an Improvement to Drug Partitioning Studies. *J. Phys. Chem. B*, 105(44):10884–10892, November 2001.

- [68] Maria A. Deryabina, Steen H. Hansen, and Henrik Jensen. Molecular Interactions in Lipophilic Environments Studied by Electrochemistry at Interfaces between Immiscible Electrolyte Solutions. *Anal. Chem.*, 80(1):203–208, January 2008.
- [69] F. M. Karpfen and J. E. B. Randles. Ionic Equilibria and Phase-Boundary Potentials in Oil-Water Systems. *Trans. Faraday Soc.*, 49(0):823–831, January 1953.
- [70] Takashi Kakiuchi. Limiting Behavior in Equilibrium Partitioning of Ionic Components in Liquid-Liquid Two-Phase Systems. *Anal. Chem.*, 68(20):3658–3664, January 1996.
- [71] Vladislav S. Markin and Alexander G. Volkov. Potentials at the Interface between Two Immiscible Electrolyte Solutions. *Advances in Colloid and Interface Science*, 31(1):111–152, February 1990.
- [72] Y. Shao, A. A. Stewart, and H. H. Girault. Determination of the Half-Wave Potential of the Species Limiting the Potential Window. Measurement of Gibbs Transfer Energies at the Water/1,2-Dichloroethane Interface. *J. Chem. Soc., Faraday Trans.*, 87(16):2593–2597, January 1991.
- [73] Astrid J. Olaya, Manuel A. Méndez, Fernando Cortes-Salazar, and Hubert H. Girault. Voltammetric Determination of Extreme Standard Gibbs Ion Transfer Energy. *Journal of Electroanalytical Chemistry*, 644(1):60–66, May 2010.
- [74] Zhifeng Ding, Bernadette M. Quinn, and Allen J. Bard. Kinetics of Heterogeneous Electron Transfer at Liquid/Liquid Interfaces As Studied by SECM. *J. Phys. Chem. B*, 105(27):6367–6374, July 2001.
- [75] Maizatul Najwa Jajuli, M. Hazwan Hussin, Bahruddin Saad, et al. Electrochemically Modulated Liquid–Liquid Extraction for Sample Enrichment. *Anal. Chem.*, 91(11):7466–7473, June 2019.
- [76] Allen J. Bard. *Electroanalytical Chemistry, 23 : A Series of Advances*. <https://cds.cern.ch/record/1319748>, 2010.

- [77] Grégoire Herzog. Recent Developments in Electrochemistry at the Interface between Two Immiscible Electrolyte Solutions for Ion Sensing. *Analyst*, 140(12):3888–3896, 2015.
- [78] Chapter 6 Sensitivity and Limit of Detection. In Desiré L. Massart, Auke Dijkstra, and Leonard Kaufman, editors, *Techniques and Instrumentation in Analytical Chemistry*, volume 1 of *Evaluation and Optimization of Laboratory Methods and Analytical Procedures*, pages 143–156. Elsevier, January 1978.
- [79] G. Taylor and H. H. J. Girault. Ion Transfer Reactions across a Liquid–Liquid Interface Supported on a Micropipette Tip. *Journal of Electroanalytical Chemistry and Interfacial Electrochemistry*, 208(1):179–183, August 1986.
- [80] J.A. Campbell and H.H. Girault. Steady State Current for Ion Transfer Reactions at a Micro Liquid/Liquid Interface. *Journal of Electroanalytical Chemistry and Interfacial Electrochemistry*, 266(2):465–469, July 1989.
- [81] A.A. Stewart, Y. Shao, C.M. Pereira, and H.H. Girault. Micropipette as a Tool for the Determination of the Ionic Species Limiting the Potential Window at Liquid/Liquid Interfaces. *Journal of Electroanalytical Chemistry and Interfacial Electrochemistry*, 305(1):135–139, April 1991.
- [82] Yuanhua Shao and Michael V. Mirkin. Fast Kinetic Measurements with Nanometer-Sized Pipets. Transfer of Potassium Ion from Water into Dichloroethane Facilitated by Dibenzo-18-Crown-6. *J. Am. Chem. Soc.*, 119(34):8103–8104, August 1997.
- [83] Yuanhua Shao and Biao Liu. Studying Ionic Reactions by a New Generation/Collection Technique. <https://pubs.acs.org/doi/pdfplus/10.1021/ja983154b>, December 1998.
- [84] Eva Alvarez de Eulate and Damien W. M. Arrigan. Adsorptive Stripping Voltammetry of Hen-Egg-White-Lysozyme via Adsorption–Desorption at an Array of Liquid–Liquid Microinterfaces. *Anal. Chem.*, 84(5):2505–2511, March 2012.

- [85] Eva Alvarez de Eulate, Shane O’Sullivan, Sharon Fletcher, Philip Newsholme, and Damien W. M. Arrigan. Ion-Transfer Electrochemistry of Rat Amylin at the Water–Organogel Microinterface Array and Its Selective Detection in a Protein Mixture. *Chemistry – An Asian Journal*, 8(9):2096–2101, 2013.
- [86] Eva Alvarez de Eulate, Lauren Serls, and Damien W. M. Arrigan. Detection of Haemoglobin Using an Adsorption Approach at a Liquid–Liquid Microinterface Array. *Anal Bioanal Chem*, 405(11):3801–3806, April 2013.
- [87] Courtney J. Collins and Damien W. M. Arrigan. Ion-Transfer Voltammetric Determination of the β -Blocker Propranolol in a Physiological Matrix at Silicon Membrane-Based Liquid|Liquid Microinterface Arrays. *Anal. Chem.*, 81(6):2344–2349, March 2009.
- [88] Grégoire Herzog, Amandine Roger, David Sheehan, and Damien W. M. Arrigan. Ion-Transfer Voltammetric Behavior of Protein Digests at Liquid|Liquid Interfaces. *Anal. Chem.*, 82(1):258–264, January 2010.
- [89] Hye Jin Lee. Voltammetric Studies of Anion Transfer Reactions Across a Microhole Array-Water/PVC-NPOE Gel Interface. *Bulletin of the Korean Chemical Society*, 33(5):1734–1740, May 2012.
- [90] Sang Hyuk Lee, Hyungi Kim, and Hye Jin Lee. Portable Amperometric Perchlorate Selective Sensors with Microhole Array-Water/Organic Gel Interfaces. *Bulletin of the Korean Chemical Society*, 34(9):2577–2582, September 2013.
- [91] Afef Mastouri, Sophie Peulon, Nizar Bellakhal, and Annie Chaussé. M(II) Transfer across a Liquid-Liquid Microinterface Facilitated by a Complex Formation with 8-Hydroxyquinoline: Application to Quantification of Pb(II), Cd(II) and Zn(II) Alone or in Mixture in Effluents. *Electrochimica Acta*, 130:818–825, June 2014.
- [92] A. Mastouri, S. Peulon, D. Farcage, N. Bellakhal, and A. Chaussé. Perfect Additivity of Microinterface Arrays for Liquid-Liquid Measurements: Application to Cadmium Ions Quantification. *Electrochimica Acta*, 120:212–218, February 2014.

- [93] Shane O’Sullivan and Damien W. M. Arrigan. Electrochemical Behaviour of Myoglobin at an Array of Microscopic Liquid–Liquid Interfaces. *Electrochimica Acta*, 77:71–76, August 2012.
- [94] Shane O’Sullivan and Damien W. M. Arrigan. Impact of a Surfactant on the Electroactivity of Proteins at an Aqueous–Organogel Microinterface Array. *Anal. Chem.*, 85(3):1389–1394, February 2013.
- [95] Shane O’Sullivan, Eva Alvarez de Eulate, Yiu Hang Yuen, Erik Helmerhorst, and Damien W. M. Arrigan. Stripping Voltammetric Detection of Insulin at Liquid–Liquid Microinterfaces in the Presence of Bovine Albumin. *Analyst*, 138(20):6192–6196, September 2013.
- [96] José A. Ribeiro, Inês M. Miranda, F. Silva, and Carlos M. Pereira. Electrochemical Study of Dopamine and Noradrenaline at the Water/1,6-Dichlorohexane Interface. *Phys. Chem. Chem. Phys.*, 12(46):15190–15194, November 2010.
- [97] José A. Ribeiro, F. Silva, and Carlos M. Pereira. Electrochemical Sensing of Ammonium Ion at the Water/1,6-Dichlorohexane Interface. *Talanta*, 88:54–60, January 2012.
- [98] José A. Ribeiro, F. Silva, and Carlos M. Pereira. Electrochemical Study of the Anticancer Drug Daunorubicin at a Water/Oil Interface: Drug Lipophilicity and Quantification. *Anal. Chem.*, 85(3):1582–1590, February 2013.
- [99] José A. Ribeiro, F. Silva, and Carlos M. Pereira. Electrochemical Sensing of Catecholamines at the Water/ 1,6-Dichlorohexane Interface. *Electroanalysis*, 25(10):2331–2338, 2013.
- [100] Masniza Sairi and Damien W. M. Arrigan. Electrochemical Detection of Racetopamine at Arrays of Micro-Liquid | Liquid Interfaces. *Talanta*, 132:205–214, January 2015.
- [101] Patricia Vazquez, Grégoire Herzog, Conor O’Mahony, et al. Microscopic Gel–Liquid

- Interfaces Supported by Hollow Microneedle Array for Voltammetric Drug Detection. *Sensors and Actuators B: Chemical*, 201:572–578, October 2014.
- [102] V. J. Cunnane, D. J. Schiffrin, and D. E. Williams. Micro-Cavity Electrode: A New Type of Liquid-Liquid Microelectrode. *Electrochimica Acta*, 40(18):2943–2946, December 1995.
- [103] Peng Sun. Cylindrical Nanopore Electrode and Its Application to the Study of Electrochemical Reaction in Several Hundred Attoliter Volume. *Anal. Chem.*, 82(1):276–281, January 2010.
- [104] Tom J. Stockmann and Zhifeng Ding. Hydrophobicity of Room Temperature Ionic Liquids Assessed by the Galvani Potential Difference Established at Micro Liquid/Liquid Interfaces. *Journal of Electroanalytical Chemistry*, 649(1-2):23–31, November 2010.
- [105] Tom J. Stockmann, Anne-Marie Montgomery, and Zhifeng Ding. Determination of Alkali Metal Ion Transfers at Liquid|liquid Interfaces Stabilized by a Micropipette. *Journal of Electroanalytical Chemistry*, 684:6–12, September 2012.
- [106] Dale A. C. Brownson, Dimitrios K. Kampouris, and Craig E. Banks. Graphene Electrochemistry: Fundamental Concepts through to Prominent Applications. *Chem. Soc. Rev.*, 41(21):6944–6976, October 2012.
- [107] Jacques Josserand, Jacques Morandini, Hye Jin Lee, Rosaria Ferrigno, and Hubert H Girault. Finite Element Simulation of Ion Transfer Reactions at a Single Micro-Liquid|liquid Interface Supported on a Thin Polymer Film. *Journal of Electroanalytical Chemistry*, 468(1):42–52, June 1999.
- [108] Sophie Peulon, Valery Guillou, and Maurice L’Her. Liquid |liquid Microinterface. Localization of the Phase Boundary by Voltammetry and Chronoamperometry; Influence of the Microchannel Dimensions on Diffusion. *Journal of Electroanalytical Chemistry*, 514(1):94–102, November 2001.

- [109] Shujuan Liu, Qing Li, and Yuanhua Shao. Electrochemistry at Micro- and Nanoscopic Liquid/Liquid Interfaces. *Chem. Soc. Rev.*, 40(5):2236, 2011.
- [110] Saito Yukio. A Theoretical Study on the Diffusion Current at the Stationary Electrodes of Circular and Narrow Band Types. *Review of Polarography*, 15(6):177–187, 1968.
- [111] Alan M. Bond, Darryl Luscombe, Keith B. Oldham, and Cynthia G. Zoski. A Comparison of the Chronoamperometric Response at Inlaid and Recessed Disc Microelectrodes. *Journal of Electroanalytical Chemistry and Interfacial Electrochemistry*, 249(1):1–14, July 1988.
- [112] Stefan Wilke and Tadesse Zerihun. Diffusion Effects at Microhole Supported Liquid/Liquid Interfaces. *Electrochimica Acta*, 44(1):15–22, September 1998.
- [113] Yvonne H. Lanyon, Gianluca De Marzi, Yvonne E. Watson, et al. Fabrication of Nanopore Array Electrodes by Focused Ion Beam Milling. *Anal. Chem.*, 79(8):3048–3055, April 2007.
- [114] Yang Liu, Jörg Strutwolf, and Damien W. M. Arrigan. Ion-Transfer Voltammetric Behavior of Propranolol at Nanoscale Liquid–Liquid Interface Arrays. *Anal. Chem.*, 87(8):4487–4494, April 2015.
- [115] M. C. Osborne, Y. Shao, C. M. Pereira, and H. H. Girault. Micro-Hole Interface for the Amperometric Determination of Ionic Species in Aqueous Solutions. *Journal of Electroanalytical Chemistry*, 364(1):155–161, January 1994.
- [116] Eva Alvarez de Eulate, Jörg Strutwolf, Yang Liu, Kane O’Donnell, and Damien W. M. Arrigan. An Electrochemical Sensing Platform Based on Liquid–Liquid Microinterface Arrays Formed in Laser-Ablated Glass Membranes. *Anal. Chem.*, 88(5):2596–2604, March 2016.
- [117] Vladimir Sladkov, Valery Guillou, Sophie Peulon, and Maurice L’Her. Voltammetry of Tetraalkylammonium Picrates at Water|nitrobenzene and Water|dichloroethane

- Microinterfaces; Influence of Partition Phenomena. *Journal of Electroanalytical Chemistry*, 573(1):129–138, November 2004.
- [118] Hye Jin Lee, Grégoire Lagger, Carlos M. Pereira, Antonio F. Silva, and Hubert H. Girault. Amperometric Tape Ion Sensors for Cadmium(II) Ion Analysis. *Talanta*, 78(1):66–70, April 2009.
- [119] Raul Zazpe, Cyrille Hibert, Joseph O’Brien, Yvonne H. Lanyon, and Damien W. M. Arrigan. Ion-Transfer Voltammetry at Silicon Membrane-Based Arrays of Micro-Liquid–Liquid Interfaces. *Lab Chip*, 7(12):1732–1737, November 2007.
- [120] Robert A. W Dryfe and Brett Kralj. Voltammetric Ion Transfer in the Presence of a Nanoporous Material. *Electrochemistry Communications*, 1(3):128–130, March 1999.
- [121] P. Yu Apel. Track-Etching. In *Encyclopedia of Membrane Science and Technology*, pages 1–25. American Cancer Society, 2013.
- [122] Micheál D. Scanlon, Jörg Strutwolf, Alan Blake, et al. Ion-Transfer Electrochemistry at Arrays of Nanointerfaces between Immiscible Electrolyte Solutions Confined within Silicon Nitride Nanopore Membranes. *Anal. Chem.*, 82(14):6115–6123, July 2010.
- [123] Mickaël Rimboud, Robert D. Hart, Thomas Becker, and Damien W. M. Arrigan. Electrochemical Behaviour and Voltammetric Sensitivity at Arrays of Nanoscale Interfaces between Immiscible Liquids. *Analyst*, 136(22):4674, 2011.
- [124] Jonathan S. Ellis, Gregoire Herzog, Barry Glynn, and Damien Arrigan. Electrochemical Characterization of Regularly-Aligned Nanopore Array Membranes Filled with Electrolyte Solutions and Their Use for Detection of Nucleic Acid Hybridization. *ECS Trans.*, 35(7):29, April 2011.
- [125] Nam-Trung Nguyen. Chapter 4 - Fabrication Technologies. In Nam-Trung Nguyen, editor, *Micromixers (Second Edition)*, Micro and Nano Technologies, pages 113–161. William Andrew Publishing, Oxford, January 2012.

- [126] Lukasz Poltorak, Grégoire Herzog, and Alain Walcarius. In-Situ Formation of Mesoporous Silica Films Controlled by Ion Transfer Voltammetry at the Polarized Liquid–Liquid Interface. *Electrochemistry Communications*, 37:76–79, December 2013.
- [127] Lukasz Poltorak, Grégoire Herzog, and Alain Walcarius. Electrochemically Assisted Generation of Silica Deposits Using a Surfactant Template at Liquid/Liquid Microinterfaces. *Langmuir*, 30(38):11453–11463, September 2014.
- [128] Lukasz Poltorak, Karima Morakchi, Grégoire Herzog, and Alain Walcarius. Electrochemical Characterization of Liquid-Liquid Micro-Interfaces Modified with Mesoporous Silica. *Electrochimica Acta*, 179:9–15, October 2015.
- [129] Lukasz Poltorak, Nienke van der Meijden, Sławomira Skrzypek, Ernst J.R. Sudhölter, and Marcel de Puit. Co-Deposition of Silica and Proteins at the Interface between Two Immiscible Electrolyte Solutions. *Bioelectrochemistry*, 134:107529, August 2020.
- [130] Robert A. W. Dryfe and Stuart M. Holmes. Zeolitic Rectification of Electrochemical Ion Transfer. *Journal of Electroanalytical Chemistry*, 483(1):144–149, March 2000.
- [131] Mark Platt, Robert A. W. Dryfe, and Edward P. L. Roberts. Controlled Deposition of Nanoparticles at the Liquid–Liquid Interface. *Chem. Commun.*, (20):2324–2325, October 2002.
- [132] Mark Platt, Robert A. W. Dryfe, and Edward P. L. Roberts. Voltammetry with Liquid/Liquid Microarrays: Characterization of Membrane Materials. *Langmuir*, 19(19):8019–8025, September 2003.
- [133] Mark Platt, Robert A. W. Dryfe, and Edward P. L. Roberts. Electrodeposition of Palladium Nanoparticles at the Liquid–Liquid Interface Using Porous Alumina Templates. *Electrochimica Acta*, 48(20):3037–3046, September 2003.
- [134] J. H. Yuan, F. Y. He, D. C. Sun, and X. H. Xia. A Simple Method for Preparation of Through-Hole Porous Anodic Alumina Membrane. *Chem. Mater.*, 16(10):1841–1844, May 2004.

- [135] Mark Platt and Robert A. W. Dryfe. Electrodeposition at the Liquid/Liquid Interface: The Chronoamperometric Response as a Function of Applied Potential Difference. *Journal of Electroanalytical Chemistry*, 599(2):323–332, January 2007.
- [136] Yong Chen, Shujuan Bian, Kui Gao, et al. Studies on the Meso-Sized Selectivity of a Novel Organic/Inorganic Hybrid Mesoporous Silica Membrane. *Journal of Membrane Science*, 457:9–18, May 2014.
- [137] Md. Mokarrom Hossain, Shaikh Nayeem Faisal, Chang Sup Kim, et al. Amperometric Proton Selective Strip-Sensors with a Microelliptic Liquid/Gel Interface for Organophosphate Neurotoxins. *Electrochemistry Communications*, 13(6):611–614, June 2011.
- [138] Jörg Strutwolf and Damien W. M. Arrigan. Optimisation of the Conditions for Stripping Voltammetric Analysis at Liquid–Liquid Interfaces Supported at Micropore Arrays: A Computational Simulation. *Anal Bioanal Chem*, 398(4):1625–1631, October 2010.
- [139] Jörg Strutwolf, Micheál D. Scanlon, and Damien W. M. Arrigan. The Performance of Differential Pulse Stripping Voltammetry at Micro-Liquid–Liquid Interface Arrays. *Journal of Electroanalytical Chemistry*, 641(1):7–13, March 2010.
- [140] Xiao Huang, Lisiqi Xie, Xingyu Lin, and Bin Su. Permselective Ion Transport Across the Nanoscopic Liquid/Liquid Interface Array. *Anal. Chem.*, 88(12):6563–6569, June 2016.
- [141] Paola Gramatica and Antonio Di Guardo. Screening of Pesticides for Environmental Partitioning Tendency. *Chemosphere*, 47(9):947–956, June 2002.
- [142] P. Gramatica, S. Pozzi, V. Consonni, and A. Di Guardo. Classification of Environmental Pollutants for Global Mobility Potential. *SAR and QSAR in Environmental Research*, 13(2):205–217, January 2002.
- [143] Melanie Kah and Colin D. Brown. LogD: Lipophilicity for Ionisable Compounds. *Chemosphere*, 72(10):1401–1408, August 2008.

- [144] John C. Westall, Christian. Leuenberger, and Rene P. Schwarzenbach. Influence of pH and Ionic Strength on the Aqueous-Nonaqueous Distribution of Chlorinated Phenols. *Environ. Sci. Technol.*, 19(2):193–198, February 1985.
- [145] Chad T. Jafvert, John C. Westall, Erwin Grieder, and Rene P. Schwarzenbach. Distribution of Hydrophobic Ionogenic Organic Compounds between Octanol and Water: Organic Acids. *Environ. Sci. Technol.*, 24(12):1795–1803, December 1990.
- [146] Chad T. Jafvert. Sorption of Organic Acid Compounds to Sediments: Initial Model Development. *Environmental Toxicology and Chemistry*, 9(10):1259–1268, 1990.
- [147] Kyösti Kontturi and Lasse Murtomäki. Electrochemical Determination of Partition Coefficients of Drugs. *Journal of Pharmaceutical Sciences*, 81(10):970–975, October 1992.
- [148] Ferhat Kaykal, Erdal Kocabas, Haluk Bingol, Emine G. Akgemci, and Ahmet Coskun. Selective Sodium Ion Transfer across a Water/1,2-Dichloroethane Micro-Interface by a Calix[4]Arene Derivative. *Journal of Electroanalytical Chemistry*, 654(1):96–101, May 2011.
- [149] Hye Jin Lee and Hubert H. Girault. Amperometric Ion Detector for Ion Chromatography. *Anal. Chem.*, 70(20):4280–4285, October 1998.
- [150] Shigeru Amemiya and Allen J. Bard. Scanning Electrochemical Microscopy. 40. Voltammetric Ion-Selective Micropipet Electrodes for Probing Ion Transfer at Bilayer Lipid Membranes. *Anal. Chem.*, 72(20):4940–4948, October 2000.
- [151] Muge Durmaz, Erhan Zor, Erdal Kocabas, Haluk Bingol, and Emine G. Akgemci. Voltammetric Characterization of Selective Potassium Ion Transfer across Micro-Water/1,2-Dichloroethane Interface Facilitated by a Novel Calix[4]Arene Derivative. *Electrochimica Acta*, 56(15):5316–5321, June 2011.
- [152] Dongping Zhan, Xiao Li, Wei Zhan, Fu-Ren F. Fan, and Allen J. Bard. Scanning Electrochemical Microscopy. 58. Application of a Micropipet-Supported ITIES Tip

- To Detect Ag⁺ and Study Its Effect on Fibroblast Cells. *Anal. Chem.*, 79(14):5225–5231, July 2007.
- [153] Sang Hyuk Lee, Jitapa Sumranjit, Pratoomrat Tongkate, Bong Hyun Chung, and Hye Jin Lee. Voltammetric Studies of Cu(II) Ion Transfer Reaction with Picolinamide-Phenylenevinylene across Liquid/Liquid Interfaces and Their Sensing Applications. *Electrochimica Acta*, 123:198–204, March 2014.
- [154] Md. Mokarrom Hossain, Sang Hyuk Lee, Hubert H. Girault, Valérie Devaud, and Hye Jin Lee. Voltammetric Studies of Hexachromic Anion Transfer Reactions across Micro-Water/Polyvinylchloride-2-Nitrophenyloctylether Gel Interfaces for Sensing Applications. *Electrochimica Acta*, 82:12–18, November 2012.
- [155] Quansheng Qian, George S. Wilson, Kristin Bowman-James, and Hubert H. Girault. MicroITIES Detection of Nitrate by Facilitated Ion Transfer. *Anal. Chem.*, 73(3):497–503, February 2001.
- [156] Hye Jin Lee, Carlos M. Pereira, António F. Silva, and Hubert H. Girault. Pulse Amperometric Detection of Salt Concentrations by Flow Injection Analysis Using Ionodes. *Anal. Chem.*, 72(22):5562–5566, November 2000.
- [157] Courtney J. Collins, Conor Lyons, Jörg Strutwolf, and Damien W. M. Arrigan. Serum-Protein Effects on the Detection of the β -Blocker Propranolol by Ion-Transfer Voltammetry at a Micro-ITIES Array. *Talanta*, 80(5):1993–1998, March 2010.
- [158] Dongping Zhan, Shuneng Mao, Qiang Zhao, et al. Electrochemical Investigation of Dopamine at the Water/1,2-Dichloroethane Interface. *Anal. Chem.*, 76(14):4128–4136, July 2004.
- [159] Alfonso Berduque, Raúl Zazpe, and Damien W. M. Arrigan. Electrochemical Detection of Dopamine Using Arrays of Liquid–Liquid Micro-Interfaces Created within Micromachined Silicon Membranes. *Analytica Chimica Acta*, 611(2):156–162, March 2008.

- [160] Hye Jin Lee, Carine Beriet, and Hubert H. Girault. Stripping Voltammetric Determination of Choline Based on Micro-Fabricated Composite Membrane. *Anal. Sci.*, 14(1):71–77, 1998.
- [161] Md Mokarrom Hossain, Chang Sup Kim, Hyung Joon Cha, and Hye Jin Lee. Amperometric Detection of Parathion and Methyl Parathion with a Microhole-ITIES. *Electroanalysis*, 23(9):2049–2056, 2011.
- [162] Bo Huang, Bazhang Yu, Peibiao Li, et al. Vitamin B1 Ion-Selective Microelectrode Based on a Liquid-Liquid Interface at the Tip of a Micropipette. *Analytica Chimica Acta*, 312(3):329–335, September 1995.
- [163] Hye Rim Kim, Carlos M. Pereira, Hye Youn Han, and Hye Jin Lee. Voltammetric Studies of Topotecan Transfer Across Liquid/Liquid Interfaces and Sensing Applications. *Anal. Chem.*, 87(10):5356–5362, May 2015.
- [164] Michelle L. Colombo, Jonathan V. Sweedler, and Mei Shen. Nanopipet-Based Liquid-Liquid Interface Probes for the Electrochemical Detection of Acetylcholine, Tryptamine, and Serotonin via Ionic Transfer. *Anal. Chem.*, 87(10):5095–5100, May 2015.
- [165] Risa Matsui, Toru Sakaki, and Toshiyuki Osakai. Label-Free Amperometric Detection of Albumin with an Oil/Water-Type Flow Cell for Urine Protein Analysis. *Electroanalysis*, 24(5):1164–1169, 2012.
- [166] Raymond A. Sierka. Activated Carbon Adsorption and Chemical Regeneration in the Food Industry. In José Coca-Prados and Gemma Gutiérrez-Cervelló, editors, *Economic Sustainability and Environmental Protection in Mediterranean Countries through Clean Manufacturing Methods*, NATO Science for Peace and Security Series C: Environmental Security, pages 93–105, Dordrecht, 2013. Springer Netherlands.
- [167] Analu Egydio Jacomini, Plínio Barbosa de Camargo, Wagner Eustáquio Paiva Avelar, and Pierina Sueli Bonato. Assessment of Ametryn Contamination in River Water, River Sediment, and Mollusk Bivalves in São Paulo State, Brazil. *Arch Environ Contam Toxicol*, 60(3):452–461, April 2011.

- [168] Ying Liu, Li Ya Ma, Yi Chen Lu, et al. Comprehensive Analysis of Degradation and Accumulation of Ametryn in Soils and in Wheat, Maize, Ryegrass and Alfalfa Plants. *Ecotoxicology and Environmental Safety*, 140:264–270, June 2017.
- [169] Penelope R. Whitehorn, Stephanie O’Connor, Felix L. Wackers, and Dave Goulson. Neonicotinoid Pesticide Reduces Bumble Bee Colony Growth and Queen Production. *Science*, 336(6079):351–352, April 2012.
- [170] A.R. Koohpaei, S.J. Shahtaheri, M.R. Ganjali, A. Rahimi Forushani, and F. Golbabaei. Optimization of Solid-Phase Extraction Using Developed Modern Sorbent for Trace Determination of Ametryn in Environmental Matrices. *Journal of Hazardous Materials*, 170(2-3):1247–1255, October 2009.
- [171] Yuan-Na Li, Hai-Long Wu, Xiang-Dong Qing, et al. Quantitative Analysis of Triazine Herbicides in Environmental Samples by Using High Performance Liquid Chromatography and Diode Array Detection Combined with Second-Order Calibration Based on an Alternating Penalty Trilinear Decomposition Algorithm. *Analytica Chimica Acta*, 678(1):26–33, September 2010.
- [172] Bin Xu, Nai-yun Gao, Hefa Cheng, et al. Ametryn Degradation by Aqueous Chlorine: Kinetics and Reaction Influences. *Journal of Hazardous Materials*, 169(1-3):586–592, September 2009.
- [173] Yao Chen, Zeng-Ping Chen, Jing-Wen Jin, and Ru-Qin Yu. Quantitative Determination of Ametryn in River Water Using Surface-Enhanced Raman Spectroscopy Coupled with an Advanced Chemometric Model. *Chemometrics and Intelligent Laboratory Systems*, 142:166–171, March 2015.
- [174] Benny Chefetz, Yitzhak I. Bilkis, and Tamara Polubesova. Sorption–Desorption Behavior of Triazine and Phenylurea Herbicides in Kishon River Sediments. *Water Research*, 38(20):4383–4394, December 2004.
- [175] Darlene Guse, Matthew J. Bruzek, Paul DeVos, and Jay H. Brown. Electrochemical Reduction of Atrazine: NMR Evidence for Reduction of the Triazine Ring. *Journal of Electroanalytical Chemistry*, 626(1-2):171–173, February 2009.

- [176] Motohiro Tomizawa and John E. Casida. NEONICOTINOID INSECTICIDE TOXICOLOGY: Mechanisms of Selective Action. *Annu. Rev. Pharmacol. Toxicol.*, 45(1):247–268, September 2005.
- [177] Motohiro Tomizawa, David L. Lee, and John E. Casida. Neonicotinoid Insecticides: Molecular Features Conferring Selectivity for Insect versus Mammalian Nicotinic Receptors. *J. Agric. Food Chem.*, 48(12):6016–6024, December 2000.
- [178] Takao Iwasa, Naoki Motoyama, John T. Ambrose, and R. Michael Roe. Mechanism for the Differential Toxicity of Neonicotinoid Insecticides in the Honey Bee, *Apis Mellifera*. *Crop Protection*, 23(5):371–378, May 2004.
- [179] Alberto Navalón, Antonio González-Casado, Rachid El-Khattabi, Jose Luis Vilchez, and Amadeo R. Fernández-Alba. Determination of Imidacloprid in Vegetable Samples by Gas Chromatography–Mass Spectrometry. *Analyst*, 122(6):579–581, 1997.
- [180] Amadeo R. Fernandez-Alba, Antonio Valverde, Ana Agüera, Mariano Contreras, and Serge Chiron. Determination of Imidacloprid in Vegetables by High-Performance Liquid Chromatography with Diode-Array Detection. *Journal of Chromatography A*, 721(1):97–105, January 1996.
- [181] Hirotaka Obana, Msahiro Okihashi, Kazuhiko Akutsu, Yoko Kitagawa, and Shinjiro Hori. Determination of Acetamiprid, Imidacloprid, and Nitenpyram Residues in Vegetables and Fruits by High-Performance Liquid Chromatography with Diode-Array Detection. *J. Agric. Food Chem.*, 50(16):4464–4467, July 2002.
- [182] A. I. Mandic, S. D. Lazic, Sz. N. Okresz, and F. F. Gaal. Determination of the Insecticide Imidacloprid in Potato (*Solanum Tuberosum* L.) and Onion (*Allium Cepa*) by High-Performance Liquid Chromatography with Diode-Array Detection. *J Anal Chem*, 60(12):1134, December 2005.
- [183] Eiki Watanabe, Heesoo Eun, Koji Baba, et al. Evaluation and Validation of a Commercially Available Enzyme-Linked Immunosorbent Assay for the Neonicotinoid Insecticide Imidacloprid in Agricultural Samples. *J. Agric. Food Chem.*, 52(10):2756–2762, May 2004.

- [184] Xiaoyan Zhang, Zhongyue Sun, Zhimin Cui, and Haibing Li. Ionic Liquid Functionalized Gold Nanoparticles: Synthesis, Rapid Colorimetric Detection of Imidacloprid. *Sensors and Actuators B: Chemical*, 191:313–319, February 2014.
- [185] A. Kumaravel and M. Chandrasekaran. Electrochemical Determination of Imidacloprid Using Nanosilver Nafion®/nanoTiO₂ Nafion® Composite Modified Glassy Carbon Electrode. *Sensors and Actuators B: Chemical*, 158(1):319–326, November 2011.
- [186] Parthena Chorti, Jan Fischer, Vlastimil Vyskocil, Anastasios Economou, and Jiri Barek. Voltammetric Determination of Insecticide Thiamethoxam on Silver Solid Amalgam Electrode. *Electrochimica Acta*, 140:5–10, September 2014.
- [187] Deborah E. Keil Stephen B. Pruettt, L. Peyton Myers. Toxicology of Metam Sodium. *Journal of Toxicology and Environmental Health, Part B*, 4(2):207–222, April 2001.
- [188] Marie Bretaudeau Deguigne, Laurence Lagarce, David Boels, and Patrick Harry. Metam Sodium Intoxication: The Specific Role of Degradation Products – Methyl Isothiocyanate and Carbon Disulphide – as a Function of Exposure. *Clinical Toxicology*, 49(5):416–422, June 2011.
- [189] M. Fátima Barroso, Paula Paíga, M. Carmo V. F. Vaz, and Cristina Delerue-Matos. Study of the Voltammetric Behaviour of Metam and Its Application to an Amperometric Flow System. *Anal Bioanal Chem*, 383(5):880–885, November 2005.
- [190] Ljubiša M. Ignjatović, Dragan A. Marković, Dragan S. Veselinović, and Borislav R. Bešić. Polarographic Behavior and Determination of Some S-Triazine Herbicides. *Electroanalysis*, 5(5-6):529–533, 1993.
- [191] J. Skopalová and M. Kotouček. Polarographic Behaviour of Some S-Triazine Herbicides and Their Determination by Adsorptive Stripping Voltammetry at the Hanging Mercury Drop Electrode. *Fresenius J Anal Chem*, 351(7):650–655, January 1995.

- [192] L. Pospíšil, R. Trsková, R. Fuoco, and M.P. Colombini. Electrochemistry of S-Triazine Herbicides: Reduction of Atrazine and Terbutylazine in Aqueous Solutions. *Journal of Electroanalytical Chemistry*, 395(1-2):189–193, October 1995.
- [193] Oriza Tavares, Simone Morais, Paula Paíga, and Cristina Delerue-Matos. Determination of Ametryn in Soils via Microwave-Assisted Solvent Extraction Coupled to Anodic Stripping Voltammetry with a Gold Ultramicroelectrode. *Anal Bioanal Chem*, 382(2):477–484, May 2005.
- [194] Kamrul Islam, Sandeep Kumar Jha, Rohit Chand, Dawoon Han, and Yong-Sang Kim. Fast Detection of Triazine Herbicides on a Microfluidic Chip Using Capillary Electrophoresis Pulse Amperometric Detection. *Microelectronic Engineering*, 97:391–395, September 2012.
- [195] Kamrul Islam, Rohit Chand, Dawoon Han, and Yong-Sang Kim. Microchip Capillary Electrophoresis Based Electroanalysis of Triazine Herbicides. *Bull Environ Contam Toxicol*, 94(1):41–45, January 2015.
- [196] Pascale M. L. Bonin, Dorin Bejan, Leah Schutt, Jalal Hawari, and Nigel J. Bunce. Electrochemical Reduction of Hexahydro-1,3,5-Trinitro-1,3,5-Triazine in Aqueous Solutions. *Environ. Sci. Technol.*, 38(5):1595–1599, March 2004.
- [197] Lubomír Švorc, Miroslav Rievaj, and Dušan Bustin. Green Electrochemical Sensor for Environmental Monitoring of Pesticides: Determination of Atrazine in River Waters Using a Boron-Doped Diamond Electrode. *Sensors and Actuators B: Chemical*, 181:294–300, May 2013.
- [198] Yaning Yang, Yuan Chun, Guangyao Sheng, and Minsheng Huang. pH-Dependence of Pesticide Adsorption by Wheat-Residue-Derived Black Carbon. *Langmuir*, 20(16):6736–6741, August 2004.
- [199] A. V. Juárez and L. M. Yudi. Electrochemical Study of S-Triazine Herbicides Transfer Across the Water/1,2-Dichloroethane Interface. *Electroanalysis*, 15(18):1481–1487, 2003.

- [200] Nicholas Toshio Iwai, Michelle Kramaric, Daniel Crabbe, et al. GABA Detection with Nano-ITIES Pipet Electrode: A New Mechanism, Water/DCE–Octanoic Acid Interface. *Anal. Chem.*, 90(5):3067–3072, March 2018.
- [201] Marco F. Suárez-Herrera and Micheál D. Scanlon. Quantitative Analysis of Redox-Inactive Ions by AC Voltammetry at a Polarized Interface between Two Immiscible Electrolyte Solutions. *Anal. Chem.*, 92(15):10521–10530, August 2020.
- [202] Min Zhou, Shiyu Gan, Lijie Zhong, et al. Improvement in the Assessment of Direct and Facilitated Ion Transfers by Electrochemically Induced Redox Transformations of Common Molecular Probes. *Phys. Chem. Chem. Phys.*, 14(10):3659, 2012.
- [203] Keith Chamberlain, Avis A. Evans, and Richard H. Bromilow. 1-Octanol/Water Partition Coefficient (Kow) and pKa for Ionisable Pesticides Measured by apH-Metric Method. *Pesticide Science*, 47(3):265–271, 1996.
- [204] Richard A. Kreuzer, David J. Hewitt, and William M. Draper. An Epidemiological Assessment of the Cantara Metam Sodium Spill: Acute Health Effects and Methyl Isothiocyanate Exposure. In William M. Draper, editor, *Environmental Epidemiology*, volume 241, pages 209–230. American Chemical Society, Washington, DC, May 1994.
- [205] A. Walcarius, E. Sibottier, M. Etienne, and J. Ghanbaja. Electrochemically Assisted Self-Assembly of Mesoporous Silica Thin Films. *Nature Materials*, 6(8):602–608, August 2007.
- [206] Aurélie Goux, Mathieu Etienne, Emmanuel Aubert, et al. Oriented Mesoporous Silica Films Obtained by Electro-Assisted Self-Assembly (EASA). *Chem. Mater.*, 21(4):731–741, February 2009.
- [207] Vladimír Mareček and Hana Jänchenová. Electrochemically Controlled Formation of a Silicate Membrane at a Liquid|liquid Interface. *Journal of Electroanalytical Chemistry*, 558:119–123, October 2003.

- [208] Fei Yan, Yayun He, Longhua Ding, and Bin Su. Highly Ordered Binary Assembly of Silica Mesochannels and Surfactant Micelles for Extraction and Electrochemical Analysis of Trace Nitroaromatic Explosives and Pesticides. *Anal. Chem.*, 87(8):4436–4441, April 2015.
- [209] Fei Yan, Xingyu Lin, and Bin Su. Vertically Ordered Silica Mesochannel Films: Electrochemistry and Analytical Applications. *Analyst*, 141(12):3482–3495, June 2016.
- [210] C. K. S. Pillai, Willi Paul, and Chandra P. Sharma. Chitin and Chitosan Polymers: Chemistry, Solubility and Fiber Formation. *Progress in Polymer Science*, 34(7):641–678, July 2009.
- [211] Meera George and T. Emilia Abraham. Polyionic Hydrocolloids for the Intestinal Delivery of Protein Drugs: Alginate and Chitosan — a Review. *Journal of Controlled Release*, 114(1):1–14, August 2006.
- [212] Christine Dufes, Andreas G. Schätzlein, Laurence Tetley, et al. Niosomes and Polymeric Chitosan Based Vesicles Bearing Transferrin and Glucose Ligands for Drug Targeting. *Pharm Res*, 17(10):1250–1258, October 2000.
- [213] Radi Hejazi and Mansoor Amiji. Chitosan-Based Gastrointestinal Delivery Systems. *Journal of Controlled Release*, 89(2):151–165, April 2003.
- [214] Nadège Boucard, Christophe Viton, and Alain Domard. New Aspects of the Formation of Physical Hydrogels of Chitosan in a Hydroalcoholic Medium. *Biomacromolecules*, 6(6):3227–3237, November 2005.
- [215] Alberto Di Martino, Michael Sittinger, and Makarand V. Risbud. Chitosan: A Versatile Biopolymer for Orthopaedic Tissue-Engineering. *Biomaterials*, 26(30):5983–5990, October 2005.
- [216] Pierre Sorlier, Anne Denuzière, Christophe Viton, and Alain Domard. Relation between the Degree of Acetylation and the Electrostatic Properties of Chitin and Chitosan. *Biomacromolecules*, 2(3):765–772, September 2001.

- [217] Christophe Schatz, Christian Pichot, Thierry Delair, Christophe Viton, and Alain Domard. Static Light Scattering Studies on Chitosan Solutions: From Macromolecular Chains to Colloidal Dispersions. *Langmuir*, 19(23):9896–9903, November 2003.
- [218] Jaepyoung Cho, Marie-Claude Heuzey, André Bégin, and Pierre J. Carreau. Viscoelastic Properties of Chitosan Solutions: Effect of Concentration and Ionic Strength. *Journal of Food Engineering*, 74(4):500–515, June 2006.
- [219] Gao Qun and Wan Ajun. Effects of Molecular Weight, Degree of Acetylation and Ionic Strength on Surface Tension of Chitosan in Dilute Solution. *Carbohydrate Polymers*, 64(1):29–36, April 2006.
- [220] M. Dash, F. Chiellini, R. M. Ottenbrite, and E. Chiellini. Chitosan—A Versatile Semi-Synthetic Polymer in Biomedical Applications. *Progress in Polymer Science*, 36(8):981–1014, August 2011.
- [221] Jin Ah Seo, Joo Hwan Koh, Dong Kyu Roh, and Jong Hak Kim. Preparation and Characterization of Crosslinked Proton Conducting Membranes Based on Chitosan and PSSA-MA Copolymer. *Solid State Ionics*, 180(14):998–1002, June 2009.
- [222] Xue Meng, Zhen Wang, Luyan Wang, et al. Electrosynthesis of Pure Poly(3,4-Ethylenedioxythiophene) (PEDOT) in Chitosan-Based Liquid Crystal Phase. *Electron. Mater. Lett.*, 9(5):605–608, September 2013.
- [223] Yin Chen, Lu Huang, Xin Dai, et al. Facile Formation of a Microporous Chitosan Hydrogel Based on Self-Crosslinking. *J. Mater. Chem. B*, 5(47):9291–9299, December 2017.
- [224] Li-Qun Wu, Anand P. Gadre, Hyunmin Yi, et al. Voltage-Dependent Assembly of the Polysaccharide Chitosan onto an Electrode Surface. *Langmuir*, 18(22):8620–8625, October 2002.
- [225] Gregory F. Payne and Srinivasa R. Raghavan. Chitosan: A Soft Interconnect for Hierarchical Assembly of Nano-Scale Components. *Soft Matter*, 3(5):521–527, April 2007.

- [226] Julieta Soledad Riva, Ana Valeria Juarez, Dante M. Beltramo, and Lidia Mabel Yudi. Interaction of Chitosan with Mono and Di- Valent Anions in Aqueous Solution Studied by Cyclic Voltammetry at a Water/1,2-Dichloroethane Interface. *Electrochimica Acta*, 59:39–44, January 2012.
- [227] Candelaria I. Cámara, Mónica V. Colqui Quiroga, Natalia Wilke, Alvaro Jimenez-Kairuz, and Lidia M. Yudi. Effect of Chitosan on Distearoylphosphatidylglycerol Films at Air/Water and Liquid/Liquid Interfaces. *Electrochimica Acta*, 94:124–133, April 2013.
- [228] Candelaria I. Cámara, Julieta S. Riva, Ana V. Juárez, and Lidia M. Yudi. Interaction of Chitosan and Self-Assembled Distearoylphosphatidic Acid Molecules at Liquid/Liquid and Air/Water Interfaces. Effect of Temperature. *Journal of Physical Organic Chemistry*, 29(11):672–681, 2016.
- [229] Li Liu, Jian-Ping Yang, Xiao-Jie Ju, et al. Monodisperse Core-Shell Chitosan Microcapsules for pH-Responsive Burst Release of Hydrophobic Drugs. *Soft Matter*, 7(10):4821, 2011.
- [230] Clément Brasselet, Guillaume Pierre, Pascal Dubessay, et al. Modification of Chitosan for the Generation of Functional Derivatives. *Applied Sciences*, 9(7):1321, January 2019.
- [231] Luciana Simionatto Guinesi and Éder Tadeu Gomes Cavalheiro. The Use of DSC Curves to Determine the Acetylation Degree of Chitin/Chitosan Samples. *Thermochimica Acta*, 444(2):128–133, May 2006.